MEASUREMENT OF OIL-WATER FLOWS IN DEVIATED PIPES USING THERMAL ANEMOMETRY AND OPTICAL PROBES

Sam Simonian M.Eng

A thesis
submitted for the degree of
Doctor of Philosophy

Department of Mechanical Engineering and Aeronautics
City University, London.

Fluid Mechanics Department
Schlumberger Cambridge Research

September 1993

Contents

List of Figures

Acknowledgements

The author would like to express his gratitude to Schlumberger Cambridge Research for financial support and use of their experimental facilities during the research. I am indebted to the scientists employed at Schlumberger who were concerned with this work and in particular to Dr. I. Atkinson, Dr. S. Mobbs and Dr. C. Lenn for their help and suggestions.

Sincere thanks to Dr. R. Neve for being my academic supervisor at City University.

I would also like to express special thanks to Mr. R. Boardman and Mr. P. Faupel for their help in electrical and mechanical design.

My deepest thanks to my wife, Amanda, for her patience, love and understanding over the past four years.

Declaration

The author hereby grants powers of discretion to the University Librarian to allow this thesis to be copied in whole or in part without further reference to the author.

It should be noted that this thesis has been placed on restricted access for the next five years from the date of submission.

Abstract

Two phase flow investigations have been undertaken for some time involving either liquid-gas or liquid-liquid flows. In spite of the growing interest in inclined (deviated) oil-water flows, only a small number of experimental data exist. This thesis describes an experimental study into deviated oil-water flows using thermal anemometry and optical probes. Two novel measuring techniques have been designed and tested in a 78mm diameter multiphase flow loop. The measuring devices are known as the *dual probe* and the *dual split-film probe*. The dual probe is a combination of a hot-film anemometer and two optical probes. One of the optical probes was used to simplify the analysis of hot-film signals. The dual split-film probe is similar to the dual probe except that it uses a split-film anemometer instead of a hot-film anemometer. The dual probe and the dual split-film probe are both capable of measuring, locally at the same time, the continuous phase velocity, the dispersed phase velocity and the volume fraction.

The results from testing the dual probe were satisfactory except when used to measure the water velocity in deviated flow. The hot-film anemometer was not capable of measuring back flows which can be encountered on the bottom part of pipes. The dual split-film probe was successfully tested in deviated flows and was capable of measuring back flows. Local slip velocities and droplet cut chord length profiles were investigated. It was shown that as the oil volume fraction increases, the slip velocity decreases, for all flow conditions investigated. The droplet cut chord length was seen to vary from $2 - 4$mm in vertical flow; however in deviated flow, the droplet cut chord length remained constant at approximately 5mm, in regions where oil was present. As a part of the continuing research into deviated oil-water flows, the data gathered were compared to a two phase model with some success. Both the dual probe and the dual split-film probe are patented by Schlumberger Cambridge Research (Simonian [1991]).

Nomenclature

A	Constant in hot-wire calibration
A	Cross sectional area
$\mathcal{A}$	Constant in hot-film calibration
A_g	Area under gas PDF curve
A_j	Annular area associated with position j
A_l	Area under liquid PDF curve
A_o	Area occupied by oil
a	Length
a	Radius
B	Constant in hot-wire calibration relation
$\mathcal{B}$	Constant in hot-film calibration
C	Constant
C_{px}	Integrated value of quantity x from probe
C_{rx}	Integrated value of quantity x from reference meter
D	Diameter
d	Diameter
E	Output voltage from hot-film anemometer
$E(t)$	Output voltage from hot-film anemometer from time series
e_a	Error voltage
e_x	Error of reading or relative error of quantity x ($e_x = \frac{(C_{px}-C_{rx})100}{C_{rx}}$)
g	Gravitational constant
H	Heat loss from hot-film sensor
H	Height
h	Length

h	Film thickness
I	Electrical current
i	Angle of incidence
i	The i^{th} data point
j	Measuring position within pipe
k	Thermal conductivity of water
k	von Kármán's constant 0.41
L	Latency length
l	Length
f	Friction factor
m_a	Mass of air
m_l	Mass of liquid
N	Number of data points
NA	Numerical aperture
Nu	Nusselt number
n	Refractive index
n_a	Refractive index of air 1.00
n_f	Refractive index of optical fibre 1.4805
n_o	Refractive index of oil 1.436
n_w	Refractive index of water 1.33
P	Pressure
P_l	Pressure loss
PDF	Population density function
p	Pressure
ΔP	Differential pressure
ΔP_s	Flowing differential pressure
ΔP_{ls}	Flowing pressure loss
ΔP_{0s}	Static differential pressure
∇p	Pressure gradient
Q_l	Liquid volumetric flowrate
Q_o	Oil volumetric flowrate

Q_w	Water volumetric flowrate
Q_{wp}	Water volumetric flowrate as calculated by the probes
R	Electrical resistance
$\mathcal{R}$	Reflectance
R_e	Reynolds number
R_f	Feedback resistance
R_v	Variable resistance
R_w	Sensor resistance
R_o	Resistance at ambient temperature
R_{20}	Resistance at 20°C
r	Radius
r	Amplitude of reflection coefficient
T	Total time
$\mathcal{T}$	Transmittance
T_o	Ambient temperature
T_r	Rise time
T_{di}	Residence time for optical probe
T_{gi}	Residence time
ΔT	temperature difference
t	Time
t_a	Time at point a
t_b	Time at point b
U	Velocity
U_i	Instantaneous droplet velocity
U_l	Liquid velocity
U_m	Mixture velocity
U_o	Oil velocity
U_s	Slip velocity
U_t	Terminal rise velocity
U_w	Water velocity
U_{os}	Oil superficial velocity

U_{ws}	Water superficial velocity
U_{hom}	Homogeneous velocity
$\overline{U}_A^c$	Mean continuous phase velocity over the cross section
$\overline{U}_A^d$	Mean dispersed phase velocity over the cross section
$\overline{U}_j^c$	Mean actual continuous phase velocity at position j
$\overline{U}_j^{cs}$	Mean superficial continuous phase velocity at position j
$\overline{U}_j^{ds}$	Mean superficial dispersed phase velocity at position j
$\overline{U}_j^x$	Mean cross correlation velocity at position j
V	Voltage
V_{av}	Average voltage
V_{out}	Output voltage
X	Quality ($X = \frac{m_a}{m_l+m_a}$)
$X(t)$	Output signal from leading optical probe
x	Distance
$Y(t)$	Output signal from trailing optical probe
y	Axial distance
z	Length

Greek Symbols

α	Volume fraction
$\bar{\alpha}_A$	Oil volume fraction integrated over cross section
α_g	Gas volume fraction
$\bar{\alpha}_j$	Mean volume fraction at position j
α_l	Local volume fraction
$\bar{\alpha}_o$	Mean oil volume fraction
α_r	Temperature coefficient of resistivity
$\bar{\alpha}_w$	Mean water volume fraction
δ	Length
δt_i	Time delay
δx	Lateral distance

δy	Axial distance
δz	Tangential distance
γ	Overheat ratio
ν	Kinematic viscosity of water $10^{-6}\mathrm{m}^2\mathrm{s}^{-1}$
λ_{xy}	Cross correlation function
λ_o	Free space wavelength
μ	Dynamic viscosity
π	Constant (3.141592654)
ρ	Density
ρ	length
ρ_m	Mixture density
ρ_o	Density of oil $790\mathrm{kgm}^{-3}$
ρ_w	Density of water $1000\mathrm{kgm}^{-3}$
τ	Time delay
τ_{max}	Mean transit time
τ_w	Wall shear stress
θ	Temperature
θ	Angle
θ_{cr}	Critical angle
θ_{max}	Maximum angle of acceptance

Subscripts

1	Point 1
2	Point 2
A	Cross sectional area
a	Ambient
a	Air
a	Position a
av	Average
b	Position b

cr	Critical
f	Feedback
g	Gas
hom	Homogeneous
i	Number of events
i	Critical
j	Number of positions
l	Liquid
l	Local point in the flow
m	Mixture
max	Maximum
min	Minimum
o	Oil
o	Ambient
os	Oil superficial
oil	Oil
s	Slip
t	Transition
v	Variable
w	Water
w	Wall
ws	Water superficial

Superscripts

$-$	Mean value

Chapter 1

Introduction

The aim of this work was to develop an instrument to measure local velocities and oil volume fractions (the volume of oil relative to the total volume of the test section) in inclined (deviated) oil-water flows. The instrument was to be used as an investigative tool to measure primarily steady state parameters describing deviated oil-water flows. It can also be used to measure time dependent parameters e.g. proportional to turbulence intensities, however time dependent parameters were not investigated within this thesis. As will be seen in Section 1.1, the instrument will be used to measure deviated oil-water flows similar to those encountered in oil wells. The information describing deviated oil-water flows can be used to calibrate new instrumentation and generate data for modelling deviated oil-water flows. The instrument is known as the *Dual Probe* and another version of this instrument is known as the *Dual Split-Film Probe.* The dual probe is based on the combination of a hot-film anemometer and two optical probes. Similarly, the dual split-film probe is the combination of a split-film anemometer and two optical probes. The instruments had a requirement to measure local velocities of up to $1 ms^{-1}$ in bubbly oil-water flows and to measure the volume fraction distribution across the pipe section. The mean values from the instruments should be compared to reference meters in order to assess the performance of the instruments.

1.1 Multiphase flow in the oil industry

Multiphase flows occur frequently in both the natural and industrial environments, from rainfall to oil extraction and from blood flow to flow in nuclear reactor systems. Understanding the mechanisms of multiphase flow is therefore of prime importance in many engineering applications. These include oil and gas extraction processes, where many examples of multiphase flows occur and where the related industry has contributed much to the present knowledge of the subject. Multiphase flow is an exceedingly complex phenomenon and consequently, nearly all the research to date has been limited to the study of *two phase* flows (liquid-gas). Within this thesis, two component flows (liquid-liquid) will be referred to as two phase flows since this term is commonly used in the oil industry.

Within the petroleum industry, both oil wells and pipelines have variable deviation angles from the vertical. Figure 1.1 shows a diagram of a North Sea oil rig with several deviated oil wells stemming from a single platform. The structure of deviated two phase flows are influenced by gravity driven buoyancy effects and turbulent mixing effects. Within deviated oil-water flows, the less dense phase (oil) gathers at the upper part of the pipe. This segregation of the two fluids causes a non-uniform velocity profile across the pipe. Knowledge of these phase stratification effects and their dependence on deviation angles are necessary in order to understand the flow behaviour. In spite of the growing interest in deviated oil-water flows, only a limited number of experimental data exist.

Most of the worlds' oil wells are water continuous wells i.e. water is the continuous phase and oil is the dispersed phase. The challenging area of interest has been to measure low flow rate wells. A low flow rate well is one that is producing between 1000BPD to 5000BPD (Barrels per Day). In terms of flow velocity, these values are $0.1 ms^{-1}$ to $0.5 ms^{-1}$ in a 150mm diameter well (standard size for oil well casing). These flows are of interest since they are indicative of water back flows. Figure 1.2 shows a schematic diagram of a deviated oil-water flow in an oil well. Oil and water flow into a well through perforations made in the casing. The flow of oil and water into a well is driven by the pressure difference between the oil reservoir and the well. If the pressure difference is small, then low flow rates will develop within the oil well and possible water back flow may occur.

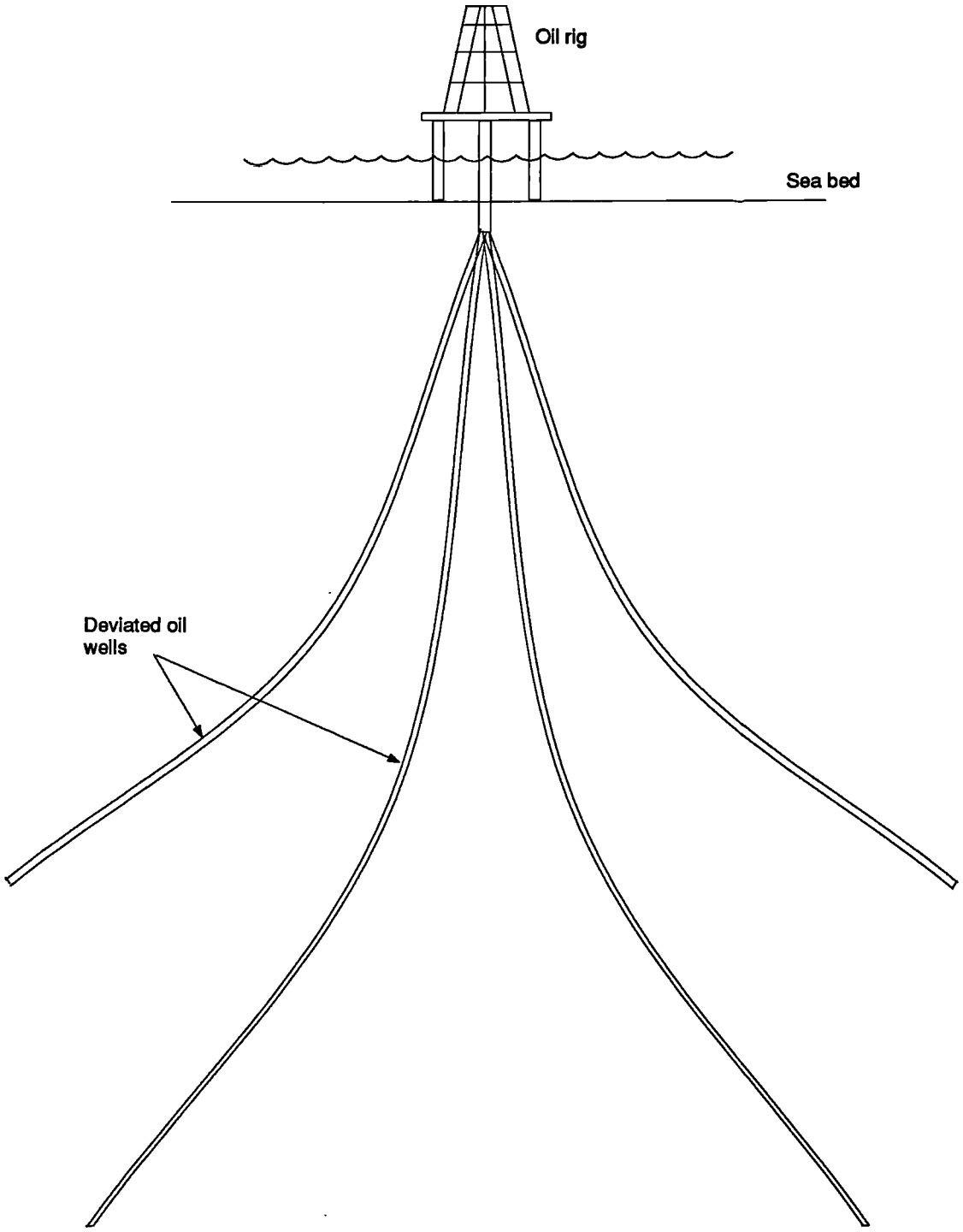

Figure 1.1: Typical North Sea oil rig

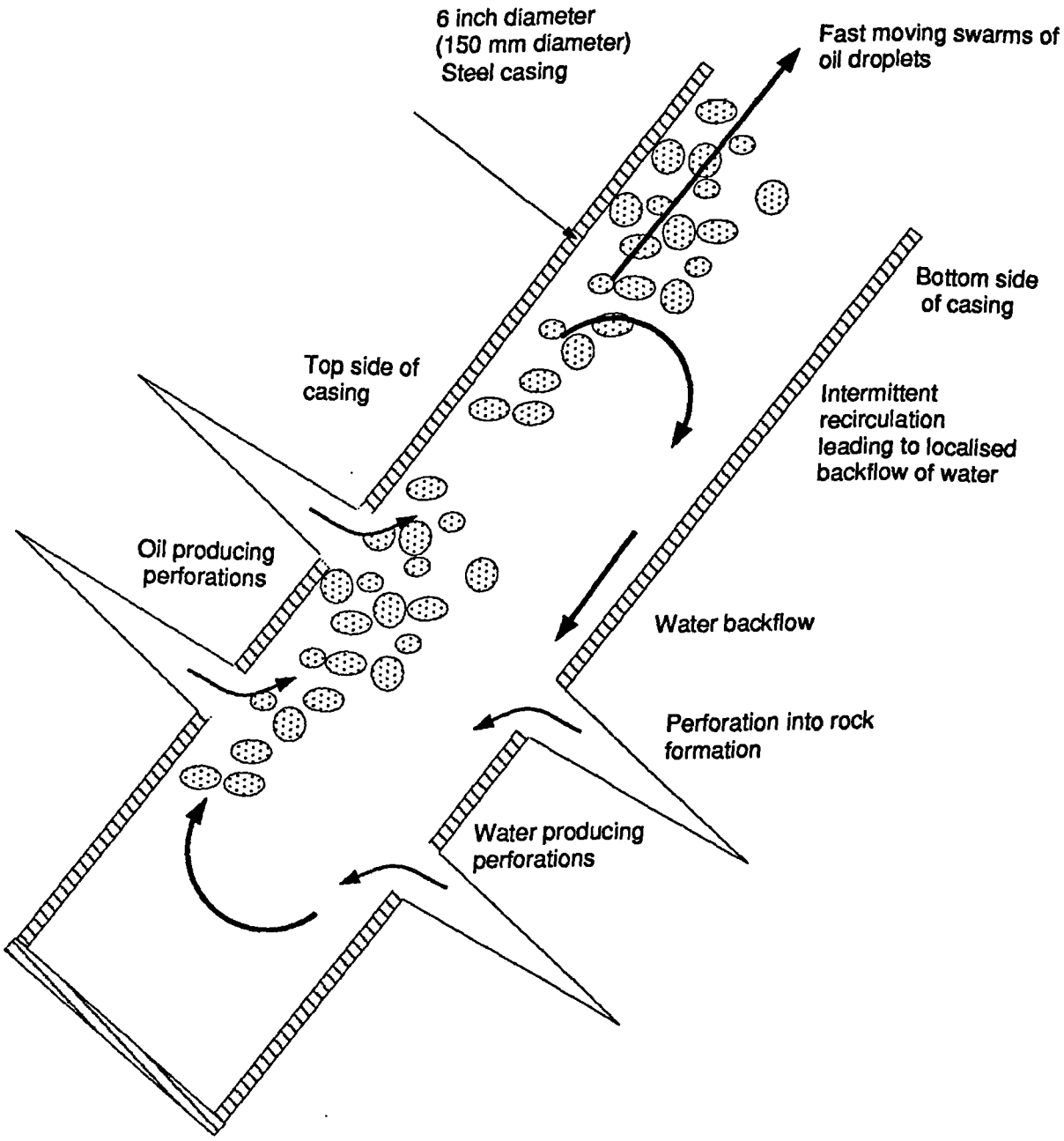

Figure 1.2: Deviated oil-water flow in an oil well

The majority of the work carried out to date has been addressed at measuring vertical liquid-gas and liquid-liquid flows. Instrumentation has been developed to measure quantities such as the volume fraction and the continuous phase velocity. In the 1950's the hot-film anemometer was developed which consists of an electrically heated film. When applied to a flowing thermally conducting media, the heat loss from the film is related to the flowing velocity. This instrument has been extensively used to measure local parameters such as continuous phase velocity and volume fraction. One of the limitations of using such instrumentation in two phase flows, was that complex analysis algorithms had been utilised to de-convolve the hot-film signal. The signals from hot-film anemometers consist of a fluctuating background signal corresponding to the continuous phase (the continuous phase is the water phase). The passage of the dispersed phase (oil droplets or gas bubbles) leads to a large change in the output signal. The algorithms had to cope with following the fluctuating background signal and decide where the start and finish points of the dispersed phase occurred. Alternative instrumentation such as Laser Doppler Anemometry (LDA) (see Boerner *et al.* [1982]) have been utilised in measuring velocities in two phase flows. LDA utilises external light sources penetrating the flowing mixture to measure flow velocity. Above volume fractions of approximately 10%, for both oil-water or air-water flows, the two phase flow mixture becomes opaque. If the flow becomes opaque, then the LDA system will not function correctly since the external light sources will not be able to penetrate into the flowing mixture.

In the late 1960's optical probes were developed to measure the local void fraction (volume fraction) in liquid-gas flows. Using the principles of total internal reflection and the fact that water and air have contrasting refractive indices, the optical probe proved to be a successful measuring instrument in air-water flows. The majority of optical probes have been prism or cone shaped optical tips. A simple 'on-off' signal was seen when the optical probe tip was immersed in air-water flows. One signal level corresponded to water and the other to air. To date, optical probes have not been used in oil-water flows due to the poor contrast between oil-water refractive indices. However, by choosing an alternative optical tip geometry, a contrast between oil and water is seen. Alternative instrumentation such as the Resistivity (RF) or the Radio Frequency probe (see Vigneaux [1988]) have been utilised in measuring volume fraction distributions in oil-water flows. The function of the RF probe is similar

to the optical i.e. it produces an 'on-off' signal. The RF probe functions on the principle of distinguishing between the dielectric constants of oil and water. One of the limitations of the RF probe is that of its large size compared with the optical probe. Typically the RF probe has a diameter of 1mm whereas the optical probe has a diameter of 0.1mm.

1.2 Layout of the thesis

The early use of hot-wire and hot-film anemometry in single and two phase flows is reviewed in Chapter 2. The use of optical probes in two phase liquid-gas flows is also reviewed. In Chapter 3 the principles of operation of hot-film anemometers and optical probes are discussed. A review of signal analysis techniques to analyse hot-film signals in two phase flows is made. Hot-film anemometers have been extensively used to measure continuous phase velocities in two phase flows. The limitation of the hot-film anemometer is that the signal analysis techniques used to identify the dispersed phase can be complex and may be inaccurate especially in deviated flows. The signal analysis techniques used to analyse optical signals in liquid-gas flows are discussed. An alternative optical probe tip is proposed for the use in oil-water flows.

Chapter 4 introduces the dual probe and the dual split-film probe. A considerable portion of the effort expended in this work was devoted to the design and construction of both probes. The construction of the dual probe is discussed with the view of choosing the types of hot-film anemometers and optical fibres. The final design of the dual probe was reached after carrying out a number of initial tests and computing the sources of errors. The calibration of the hot-film anemometer is also discussed. This is followed by the construction, design and calibration of the dual split-film probe.

Chapter 5 describes the experimental apparatus and procedure. The multiphase flow loop in which the experiments were conducted is described. In order to compare the probe results to the reference meter results, determination of superficial velocities and oil volume fraction in the working section are discussed. The acquisition procedure and implementation of the hardware are described. Initial dual probe tests are described where the number of measuring positions were determined in order to map the working section. Finally, the experiments carried out are tabulated.

The results from the dual probe and dual split-film probe tests are discussed in Chapter 6. Firstly, an in depth explanation of how the signals from the probes were analysed is described. Calculation of global mean quantities over the working section, from the local mean quantities, are described. These global mean quantities were required in order to compare the probe results to the reference meter results. The results from both probes are discussed at each deviation angle of the flow loop. Comparison is made between the dual probe and the dual split-film probe results.

A comparison of experimental results with those predicted by a two phase flow model is made in Chapter 7. In Chapter 8 the conclusions and suggestions for further work are discussed.

Chapter 2

Review of thermal anemometry and optical probes

2.1 Introduction

This chapter has two main sections. The first deals with previous work carried out using both hot-wire and hot-film anemometry in single phase and two phase flows. The second section deals with previous work carried out using optical probes in two phase flows.

A hot-wire anemometer is a device which relates the fluid velocity at the wire to the heat loss from the wire. This heat loss is a function of the current required to flow through the wire in order to maintain the wire at a constant temperature. Hot-wire and hot-film anemometers require calibration against a known velocity. Figure 3.1 in Chapter 3 shows a diagram of a modern cylindrical hot-film anemometer.

2.2 Early use of thermal anemometry

The initial work carried out on hot-wire anemometry, is mainly due to King [1914, 1915]. This work was firstly to establish the general laws for the convection of heat from small platinum wires in an air stream. Secondly, King wanted to produce portable hot-wire anemometers with standard instrumentation which required no calibration to measure air speed accurately. The platinum wires used were 0.025mm to 0.15mm diameter and 20mm to 40mm

in length. These wires were very much larger than the wires found on modern hot-wire probes (typically 0.005mm diameter and 1.25mm in length). The reason for using large wires was that platinum was too weak to use in smaller diameters and larger diameter wires had a lower resistance per unit length. Hence, longer wires were used to provide sufficient sensitivity. The wires were calibrated using a whirling arm and a stationary wire was used to correct for swirl created by the arm. During calibration, the wires were heated to 1100°C and tested at velocities of up to $9ms^{-1}$. The hot-wire probes were constant current anemometers i.e. the current supply to the wire was kept constant and the temperature of the wire varied as the heat loss from the wire changed.

King [1914, 1915] suggested that the heat loss, H from the wire would vary with the square root of the velocity. He plotted his experimental results in the form $H = \mathrm{A} + B\sqrt{U}$ where U is the velocity and the constants A and B are functions of temperature and the dimensions of the wire. The curve fit was good over a range of velocities, but some non-linearity was noticed at both ends of the curve, implying that a slightly lower power law may be better. From his results, King produced the following equation:

$$I^2R = A + \mathrm{B}\sqrt{\mathrm{U}} \tag{2.1}$$

where R is the wire resistance at ambient temperature, I is the current through the wire and the constants A and B are given by :

$$A = 2.5 * 10^{-4}(1 + 70d)\left[1 + 1.14 * 10^{-3}(\theta_w - \theta_a)\right](\theta_w - \theta_a) + C \tag{2.2}$$

where $C = 2\pi d * 0.514(\theta_w/1000)^{5.2}$ and

$$B = 1.432 * 10^{-3}(\sqrt{d})\left[1 + 8 * 10^{-5}(\theta_w - \theta_a)\right](\theta_w - \theta_a) \tag{2.3}$$

where d is the wire diameter in centimetres. Both A and B contain the term $(\theta_w - \theta_a)$ which is the temperature difference between the wire and the surroundings in degrees Celsius. Typical values for R and θ_a were 0.5Ω and 17°C. The current I could be varied from 0 to 5 Amps, however during his experiments the current varied between 1 to 2 Amps. Figure 2.1 shows typical variations of the constants A and B at different wire temperatures (θ_w) for a 0.0283mm diameter wire. King did not succeed in producing a standard hot-wire anemometer requiring no calibration. The reason for this is because at different wire temperatures (θ_w) and different wire diameters, there are individual values for both A and B. The calibration of individual wires is still regarded as the best method of calibration today.

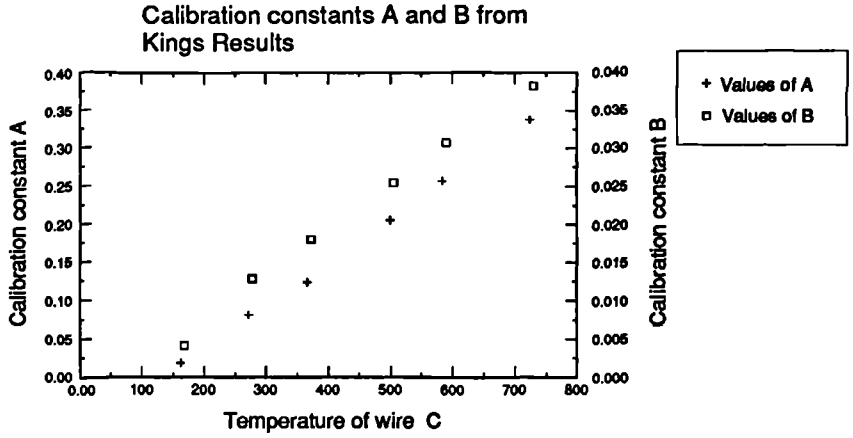

Figure 2.1: Typical values for A and B from King's experiments

Constant temperature anemometry came about when Weske [1943] adjusted the current supply to the wire in order to maintain the wire at constant temperature. This implied that as the heat loss from the wire increased, the current supply to the wire was increased so as to maintain its temperature. The constant current anemometer (used by King [1914, 1915]) is supplied with a constant heating current so that the temperature of the sensing element varies as the surrounding heat loss changes. If there was a sharp decrease in velocity, the wire could overheat and consequently burn out. Constant temperature anemometry began to convey more and more advantages and it is the most common type of anemometer used today. Typically, modern hot-wire anemometers have a frequency response of 30kHz.

Hot-wire anemometers had, by the 1950's, been developed to a stage where they were capable of making accurate and reliable measurements in turbulent gas flows. However, the use of hot-wire anemometers in liquid flows was seriously hampered. Attempts were made to use hot-wire anemometry in water flows but, the fragile wires were easily broken, and small bubbles (Middlebrook and Piret [1950]) formed on the surface of the wire causing erratic signals from the anemometer. Other problems were encountered due to build up of scale and algae resulting in calibration drifts. The most serious problem encountered was the use of hot-wire anemometers in electrically conducting media, such as water. The potential drop across the wire caused electrolysis of the water and this resulted in a very slight reduction in the wire diameter (e.g. cathode in electrolytic cell), causing a continual drift in the calibration of the probe. The hot-wire anemometer was rendered useless in conducting media.

Middlebrook and Piret [1950] tested the hot-wire anemometer, in water flows, to investigate the appearance of these small bubbles. They came to the conclusion that the main cause of the bubble formation was due to electrolysis. To eliminate this problem, they tested the hot-wire in distilled water with small amounts of sodium chloride (to increase the conductivity of the water). They observed that a smaller number of bubbles were being formed for the same operating temperature of the hot-wire. To overcome the problem of electrolysis, they suggested coating the wire with a resin. The layer of resin was 0.013mm thick which solved the problem of bubbles; however, the wire became insensitive to velocity fluctuations because this reduced the heat transfer and decreased the thermal conductivity between the wire and the fluid. This led them to suggest using a shorter wire to overcome the problems of electrolysis. A shorter wire will have a lower resistance and potential drop across the wire, if the wire is maintained at the same temperature. They claimed that a minimum potential drop exists below which electrolysis will not take place. In fact it was the coating of the wires which solved the problem of electrolysis, provided that a thin resin coating was applied to the wire.

The use of thermal anemometry in conducting liquids came about when Ling and Hubbard [1956] developed the hot-film anemometer. This consisted of a very thin platinum film, 1mm long and 2mm wide, deposited on a wedge shaped glass support. The platinum film was then covered with a thin quartz coating (about 0.001mm thick). Since the probe was robust compared to the earlier fragile hot-wire probes, it was thought that the probe would be better suited to liquid flows. The authors claimed that the hot-film anemometer was less sensitive to surface contamination (e.g. dirt) because most particles adhere to probes around the stagnation point; this claim has been confirmed by many users.

The manufactures of hot-film and hot-wire anemometers [Dantec], recommend the use of a velocity-voltage relationship to calibrate a hot-film anemometer. Equation 2.4 shows the modern Kings Law equation which is similar to Equation 2.1:

$$E^2 = \mathcal{A} + \mathcal{B}\sqrt{U} \tag{2.4}$$

where E is the hot-film anemometer voltage output, $\mathcal{A}$ and $\mathcal{B}$ are the calibration constants and U is the velocity. Farrar [1988] discusses the evolution of Equation 2.4 from the Kings Law Equation 2.1.

2.3 Thermal anemometry in gas-liquid flows

The first application of hot-film anemometry in two phase flow measurements was made by Hsu *et al.* [1963]. They attempted to study all the possible measurement applications of a single wire hot-film anemometer in steam-water flows. A high speed camera was used to check the reliability of the results attained from the hot-film anemometer. Non-dimensional empirical relationships, describing the behaviour of heated cylinders in a cross-flow, showed that the heat loss from the cylinder was dependent on the velocity and properties of the flowing fluid. In single phase flow, there is a unique relationship between fluid velocity and heat transfer, but in two phase flows, the relationship breaks down. Since the properties of the two fluids are so different, the heat transfer in the liquid phase is two or three times greater than in the gaseous phase. Hence, the fluctuations of the anemometer signal due to the passage of the gaseous phase are clearly distinguishable from those due to the velocity fluctuations within the liquid phase. Hsu *et al.* used a cylindrical hot-film probe which was 0.075mm in diameter and 3.2mm in length. To insulate the probe from its surroundings, the probe was 'dipped' into epoxy resin. The probe was operated as a constant temperature anemometer and was placed in a vertical glass heating tube where water-steam flows were investigated. From the experiments carried out, it was suggested that hot-film anemometry could be used to determine the local void fraction, local bubble rise velocity and local turbulence levels. However, no results were published other than void fraction values, nor was there any indication of how the bubble rise velocity could be obtained.

Delhaye [1969] investigated the use of hot-film anemometry in both steam-water and air-water flows. Delhaye utilised a conical hot-film anemometer (see Figure 2.2) which he claimed to have advantages over the cylindrical hot-film. The advantages were that:

1. Particles of dirt do not adhere to the film.

2. The conical probe has less influence on the trajectory of bubbles than a cylindrical probe.

It should be noted that the last claim was based on results taken at low velocities ($0.2ms^{-1}$ - $0.5ms^{-1}$). Delhaye reported on the choice of operating temperatures for the hot-film anemometer. He suggested that an operating

temperature should be chosen which is neither too high, to form bubbles on the sensor, nor so low as to be sensitive to the ambient temperature fluctuations. Delhaye chose an operating temperature of about 17°C above the ambient temperature. Rasmussen [1967] had shown that bubbles on the sensor, when operating in water, are not produced provided that the sensor temperature is less than 20°C above the ambient temperature.

Serizawa *et al.* [1974] carried out an experimental study into the behaviour of air-water two phase bubbly flows. The aim of the study was to measure local parameters (e.g. water velocity, turbulence intensities) in vertical air-water flows using a conical hot-film anemometer (see Figure 2.2). A Resistivity probe (RF) (Akagawa [1963], Neal and Bankoff [1963], Serizawa *et al.* [1974], Vigneaux [1988]) was also used to measure the local void fraction and the bubble velocity. A 2100mm long test section was used with an internal diameter of 60mm. The probes were traversed radially every 1 to 2mm across the pipe diameter and the range of flow variables covered in the study was: water superficial velocity $U_{ws} = 0.30$ to 1.03ms^{-1} and quality $X = 0.0085\%$ to 0.09% ($X = \frac{m_a}{m_l+m_a}$ where m_a is the mass of air and m_l is the mass of liquid). From the experimental study, it was shown that as the quality increased in a low bubble density region (near the pipe wall), the water velocity profile changes from the turbulent velocity profile i.e. $\frac{1}{7}$ power law, to a plug-shaped profile. An example of the velocity profiles measured by the hot-film anemometer can be seen in Figure 2.3. The water velocity was calculated using an interpretation suggested by Delhaye [1969]. This interpretation technique is discussed in Section 3.3. A similar trend in the velocity profiles was reported by many other investigators (e.g. Neal and Bankoff [1963], Nassos and Bankoff [1967], Kobayashi and Irino [1973], Sekoguchi and Sato [1975]). Also, Serizawa mentions that, when applying hot-film anemometers to two phase flows, some questions arise in relation to the calibration procedure. He calculated the total liquid flow rate by integrating the velocity and void fraction profiles over the pipe section. The total liquid flow rate was then compared to the reference turbine flowmeters, which indicated good agreement. Therefore, the calibration of the hot-film anemometer obtained in single phase water flow was considered valid for air-water flows.

Toral [1981], studied the performance of a constant temperature hot-wire anemometer as a local void fraction meter, with freely rising bubbles of air and vapour, in ethanol. The anemometer was used to measure the local void

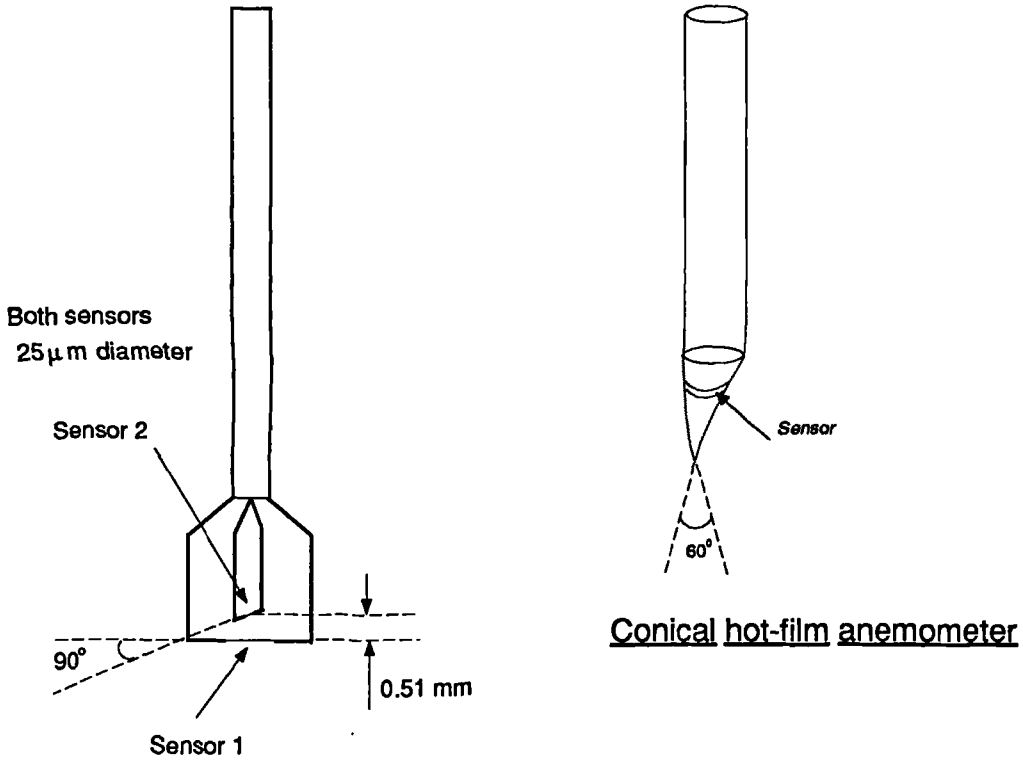

Figure 2.2: A diagram of both the conical and dual sensor hot-film anemometers. Serizawa *et al.* [1974], [1983]

fraction at different radial positions in a vertical tube. The test section (1m vertical glass tube with an internal diameter of 0.03m) contained liquid ethanol into which bubbles of air and ethanol vapour were injected. The hot-wire anemometer was a standard Dantec probe with a 0.005mm diameter platinum plated tungsten wire. An amplitude threshold method (see Section 3.3.1) was implemented to detect the part of the signal associated with the dispersed phase. The local void fraction, α_l, was given by (taken from Serizawa *et al.* [1974]):

$$\alpha_l = \frac{\sum T_{gi}}{T} \tag{2.5}$$

where T_{gi} is the period in which the probe spends in the gaseous phase and T is the total time. This assumes that for a long observation period, α_l tends towards the ratio of gas contact time (residence time when probe is immersed in the gaseous phase) to total observation time. Since Toral was studying freely rising bubbles, the above equation would lead to counteracting effects on the time ratio, i.e. the velocity of larger bubbles will be greater than smaller ones

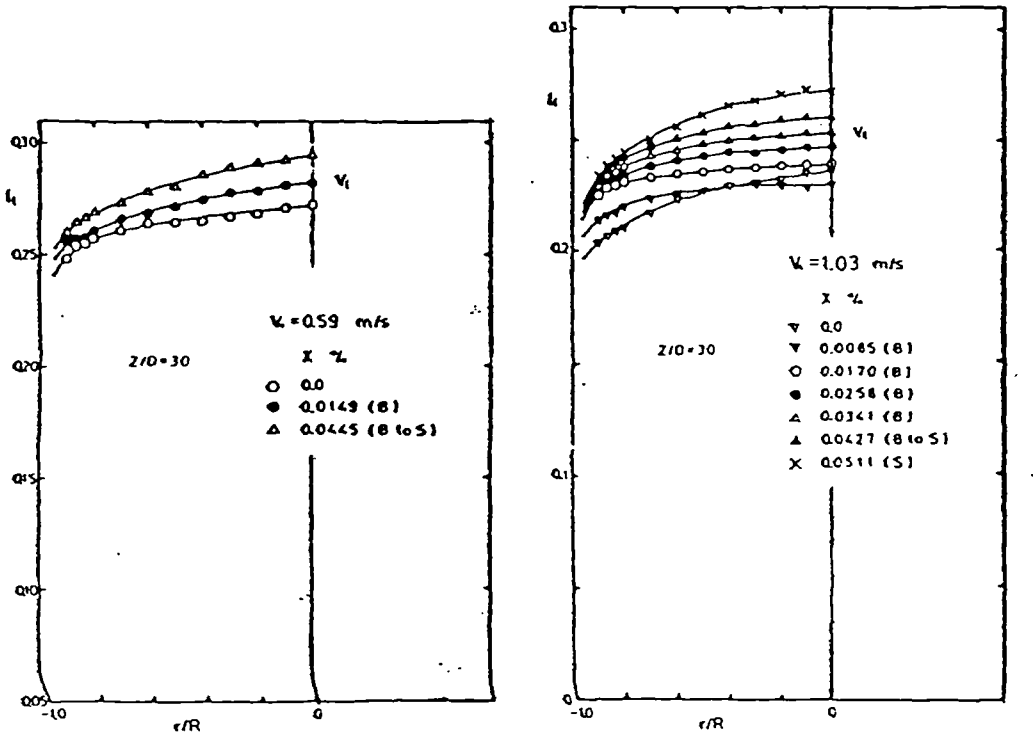

Figure 2.3: Velocity profiles for air-water flows from Serizawa *et al.* [1974]

resulting in under estimation of T_{gi} for larger bubbles. The sampling period varied between 30 seconds and 5 minutes, which was thought to provide an adequate statistical treatment of effects such as those arising from variations in bubble velocity and size. As a check, the void fractions were compared using two different sampling periods and it was noticed that there was negligible difference between the results. Analysis of the anemometer output waveform, on an oscilloscope, showed that the exact time interval which the probe spends in the bubble is obscured by three factors:

1. The evaporation of the liquid film remaining on the wire, and/or its shedding by shear or capillary forces,

2. The deformation of the bubble on impact with the wire due to a surface tension effect,

3. The deflection of some bubbles which approach the probe at an oblique angle.

Toral investigated the effect of surface tension on bubble shape and motion using high speed filming. The bubbles were observed to be retarded by 33% of the free rise velocity causing an overestimation of the void fraction.

Deformation of the bubble into an ellipsoidal shape, due to wire impingement, caused an underestimation of the void fraction. Bubbles approaching the wire at oblique angles may be deflected causing underestimation of the void fraction. He reports that the overall effect leads to an underestimation of the void fraction by up to 9% of reading.

Serizawa *et al.* [1983] carried out experiments in two phase air-water flows using a dual sensor hot-film anemometer and a conical hot-film anemometer (see Figure 2.2). A vertical circular tube with a 60mm inside diameter and length of 2150mm was used for the investigation. A comparison of the velocity profiles was demonstrated between the dual sensor hot-film and the conical hot-film. Both hot-film anemometers indicated a good agreement of the measured velocity profiles. This result was interesting since the thermal frequency response varies from sensor to sensor. Generally, larger substrate sensors have a slower frequency response than smaller sensors. Typically the frequency response of a conical hot-film anemometer was 3kHz in water whereas a cylindrical hot-film anemometer has a better (typically 30kHz) frequency response. The reason for this good agreement was that the practical range of turbulence in bubbly flows is smaller than 1kHz; also the liquid velocities investigated were less than $1 ms^{-1}$.

2.3.1 Split-film anemometry in gas-liquid flows

The split-film anemometer comprises of two sensors mounted on a single cylinder (see Figure 2.4). Calibration of such probes was investigated by Boerner and Leutheusser [1984]. The calibration and use of the split-film anemometer will be discussed in more detail in Section 4.6. The split-film anemometer is capable of providing the magnitude and the sign of one component of the velocity.

An investigation into the use of split-film anemometry was carried out by Franz *et al.* [1984] to measure three dimensional flow fields in a bubble column. The fluid velocities in the axial, radial and tangential directions were investigated. To compare and clarify the results obtained by the split-film anemometer, a Laser Doppler Anemometer (LDA) was used (see Boerner *et al.* [1982]). A vertical tube of 0.15m inside diameter and 2.58m in length was used for the investigation. Air was injected at the base of the test section through a sieve plate in order to produce a uniform distribution of air bubbles across

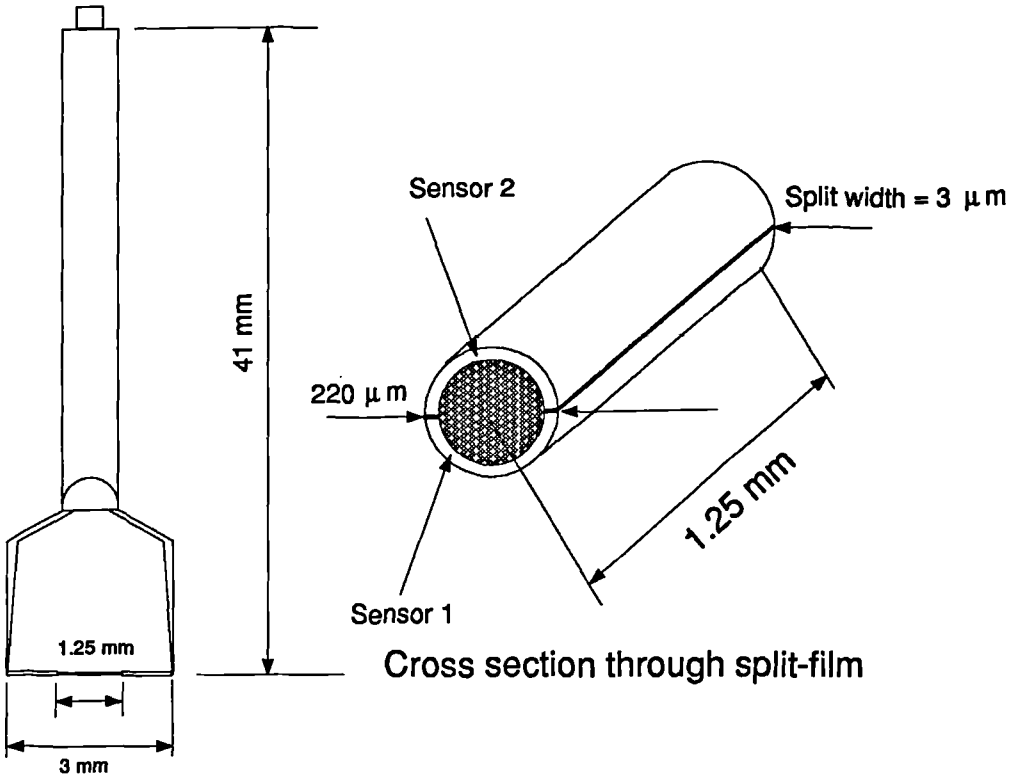

Figure 2.4: A diagram of a split-film anemometer. Dantec 55R55

the pipe cross-sectional area. Franz *et al.* [1984] showed the development of axial liquid velocities along the height of the test section. These measurements showed that downward liquid velocities exist near the pipe walls. The split-film anemometer proved to be an accurate measuring device especially in flows with negative axial velocity component.

2.4 Thermal anemometry in liquid-liquid flows

Farrar [1988] investigated the use of hot-film anemometry in vertical oil-water flows. An initial investigation was carried out to characterise the response of a hot-film anemometer in two phase air-water and oil-water flows. This was required since exact locations of the first contact point (start) and the last contact point (finish) between the probe and the bubble/droplet had to be identified. From the tests, Farrar stated that as a bubble enters the hot-film probe, a thin film of water exists on the sensor and will not break, in most cases, until the back of the bubble arrives. However, if the water film was to break within the bubble a sharp spike (overshoot) in the signal would be seen. Further

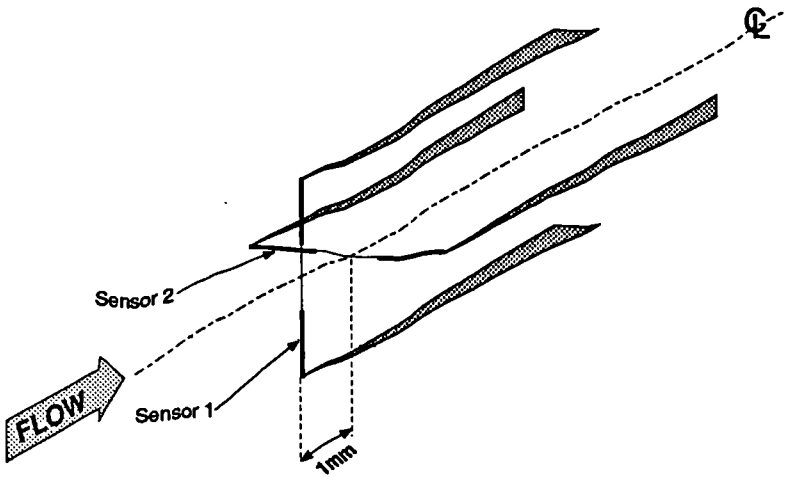

Figure 2.5: A dual sensor hot-film anemometer. Dantec 55R62

discussion of this can be found in Section 3.3. A two phase flow loop was built for the investigations which was capable of delivering air-water and oil-water flows. The vertical test section used for the investigation was a 0.078m inside diameter perspex tube which was 3.25m in length. A traversing mechanism was used to traverse the hot-film anemometer across the pipe section. Experiments were performed with varying oil volume fractions of 5% to 30%. Profiles for the oil volume fraction, bubble cut cord length, continuous phase (water) velocity and turbulence intensities were presented. Unfortunately, there were no comparison of the measured values to the reference values e.g. comparison of the mean continuous phase velocity, as measured by the hot-film, to the mean velocity as measured by the water turbine meter.

More recently, Smits [1991] investigated the use of hot-film anemometry in two phase deviated oil-water flows. The study was carried out in an inclinable flow loop with a 15m long test section having an inside diameter of 0.150m. A dual sensor hot-film anemometer (see Figure 2.5 and Figure 2.2) was traversed over the entire pipe section so as to compute the continuous phase (water) velocity, the dispersed phase (oil) velocity and the oil volume fraction. The dual sensor hot-film anemometer was used in order to determine the dispersed phase velocity. Using 'time of flight' or 'cross correlation' (Beck and Plaskowski [1987]) processing techniques, the dispersed phase velocity can be calculated. These processing techniques will be discussed in Section 6.2.2. Flow profiles for the different inclinations and flowrates were presented; Smits did not compare any of the results with reference meter results.

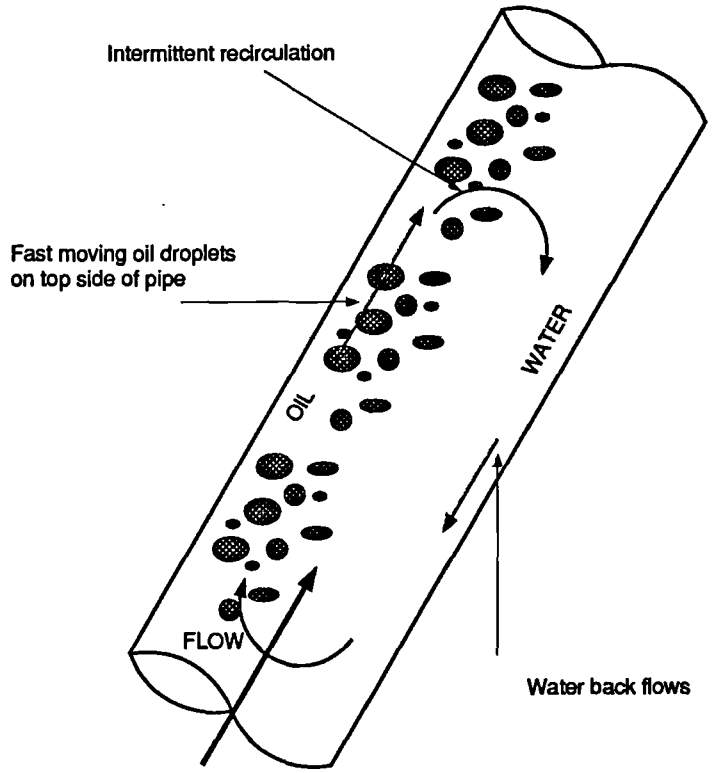

Figure 2.6: An illustration of deviated oil-water flows

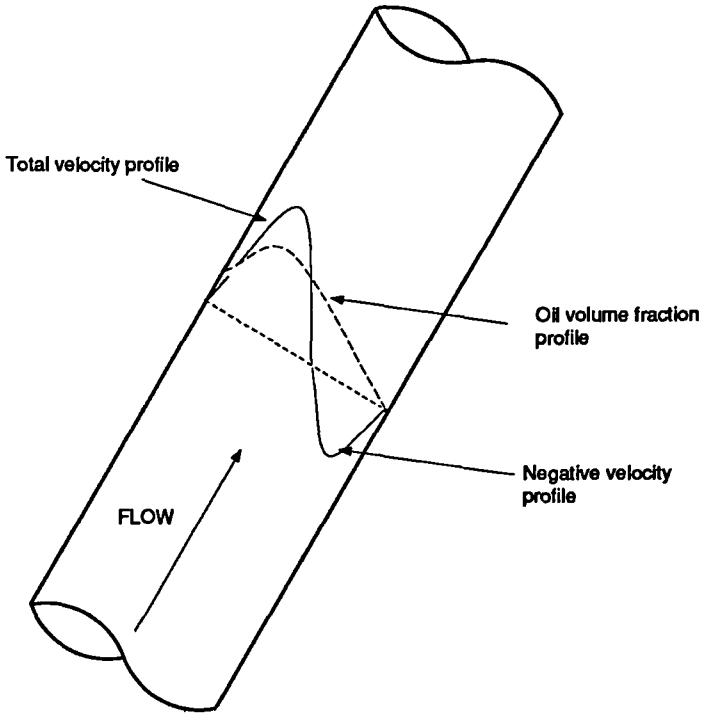

Figure 2.7: Measured velocity profiles in deviated oil-water flows. Vigneaux [1988]

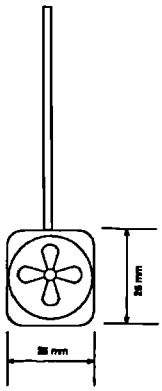

Figure 2.8: A diagram of a micro-spinner

Within deviated oil-water flows, the dominant parameter influencing the structure of such flows is the presence of gravity driven buoyancy effects. The less dense phase (oil), gathers at the top side of the pipe and the water flows along the bottom side of the pipe. The fluid velocity profile is non-uniform across the pipe and water *back flow* may be encountered. Figure 2.6, shows a deviated pipe with oil-water flow where water is the continuous phase and oil is the dispersed bubbly phase. Vigneaux [1988] carried out tests in a 0.2m inside diameter pipe, with a length of 15m, using a micro-spinner (a micro-spinner is a small turbine which revolves when placed in a flowing fluid and the revolutions of the turbine are converted to produce velocity information (see Figure 2.8)) and a Resistivity probe. The 0.025m diameter micro-spinner was traversed across a single diameter to produce velocity profiles for highly deviated pipes. For high deviations (greater than 30° to the vertical), they found that the back flows were not intermittent over a long time average at the bottom side of the pipe; the velocity profile was negative in this part of the pipe (see Figure 2.7). At deviation angles less than 30°, they found that water back flows were intermittent.

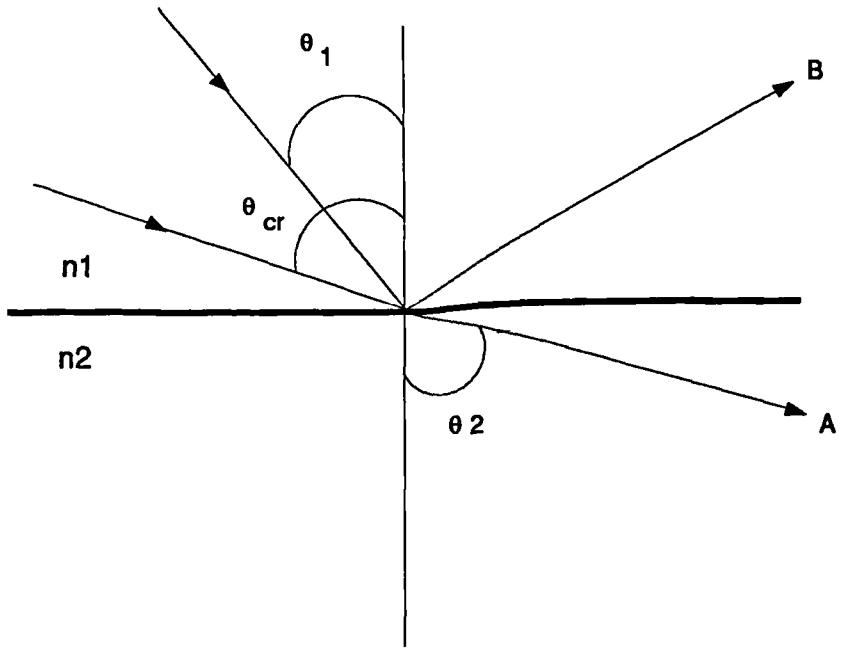

Figure 2.9: Light path for ordinary refraction A, and total internal reflection B

2.5 Introduction to fibre optics

Refraction is an effect which occurs due to the difference of the speed of light in different optical media. The refractive index n of a medium, is defined as the ratio of the velocity of light in a vacuum to the velocity of light in that medium.

There are two laws of refraction:

1. The incident and the refracted rays and the normal to the interface all lie in the same plane and the incident and refracted rays lie on opposite sides of the normal,

2. The deviation of a beam of light in a medium of refractive index n_1 when striking an interface at an angle of θ_1, to the normal is given by Snell's law (Born and Wolf [1980]):

$$n_1 \sin\theta_1 = n_2 \sin\theta_2 \tag{2.6}$$

where n_2 is the refractive index of the second medium and θ_2 is the new angle of light propagation (see Figure 2.9).

As light passes from a dense medium (high n) to a less dense medium (lower n), the light is always refracted away from the normal as shown in

Figure 2.9 (A). When θ_2 is equal to 90°, θ_1 is known as the critical angle (θ_{cr}). By rearranging Equation 2.6, we get:

$$\theta_{cr} = \sin^{-1}(n_2/n_1) \tag{2.7}$$

For angles greater than the critical angle, no light will be refracted i.e. all the light will be internally reflected (B). This effect is known as total internal reflection (TIR) and forms the basis of light transmission through optical fibres. As will be seen in Section 3.6, when optical probes are exposed to air-water (or oil-water) flows, they produce two distinct signal levels corresponding to each of the phases.

2.6 Past use of optical probes in two phase flows

The first application of optical probes in gas-liquid flows was made by Miller and Mitchie [1969]. They used a 2mm diameter glass rod, with a refractive index of 1.62, that was heated and drawn down to 0.3mm diameter tip. The tip of the fibre was shaped according to Figure 2.10. When the right-angled tip is immersed in the gaseous phase, total internal reflection occurs and light is reflected back to a receiver or photo-diode. This is further discussed in Section 3.5.

Hinata [1972] designed a fibre bundle system for measuring void fraction in air-mercury flows. The optical probe was constructed from several hundred glass fibres each 0.03mm in diameter. All of the fibres were tied together in a '*Y*' shaped bundle. An illustration of the optical probe is given in Figure 2.11. A glass rod 1mm long and 0.5mm diameter was glued onto the end of the fibre bundle to form the active tip which was ground and polished. The operation of the probe was similar to Miller and Mitchie's optical probe i.e. total internal reflection occurs at the tip when the tip is exposed to air.

One of the disadvantages of the optical probes mentioned above, is that they have large tip dimensions. Danel and Delhaye [1971] developed an alternative tip design with a significant reduction in tip size. The optical fibre was heated and drawn down to 0.04mm diameter. This was then bent into a 'U' shape (see Figure 2.12). Danel and Delhaye claimed that the probe had an active tip size of 0.1mm. This *two fibre* arrangement has an advantage

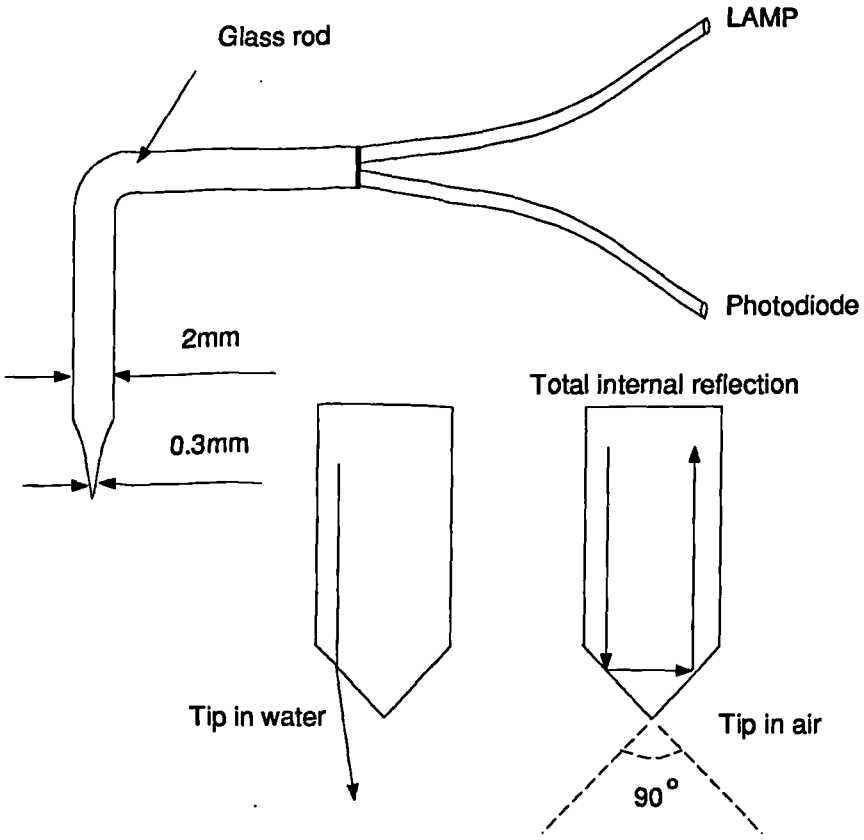

Figure 2.10: Diagram of optical probe used by Miller and Mitchie [1969]

over single fibres in that light is sent out through one path of the fibre and returns along a different path. Although this probe is commercially available from Dantec, it has been found to be very fragile above moderate velocities ($\approx 3ms^{-1}$).

Abuaf *et al.* [1978] investigated the use of a conical ended probe (see Figure 2.13) in air-water flows to measure the local void fraction and interface velocities. Two optical fibres, 0.076mm in diameter, were fused together with a mini torch and then drawn into a hypodermic needle (0.5mm outside diameter); finally the tip was chamfered to 90°. The test section used for their investigation was a 6.4mm internal diameter glass tube which was 830mm in length. Air bubbles were injected at the base covering the entire cross-section of the tube. The air velocities investigated ranged from $0.007ms^{-1}$ to $2.8ms^{-1}$. The velocity of a bubble was measured before it reached the probe tip by means of two diametrically opposed light sources and detectors. The bubble velocity was calculated using a counter and knowing the separation between the two detectors. They observed that as the air bubble velocity increased, the

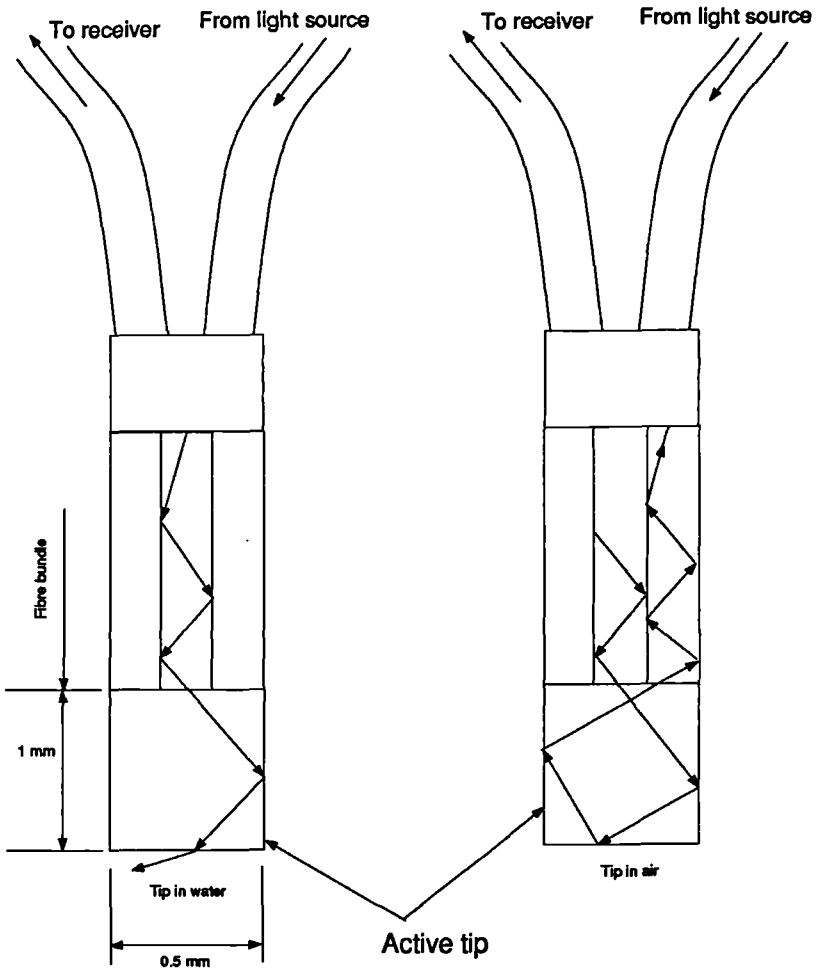

Figure 2.11: Diagram of optical probe used by Hinata [1972]

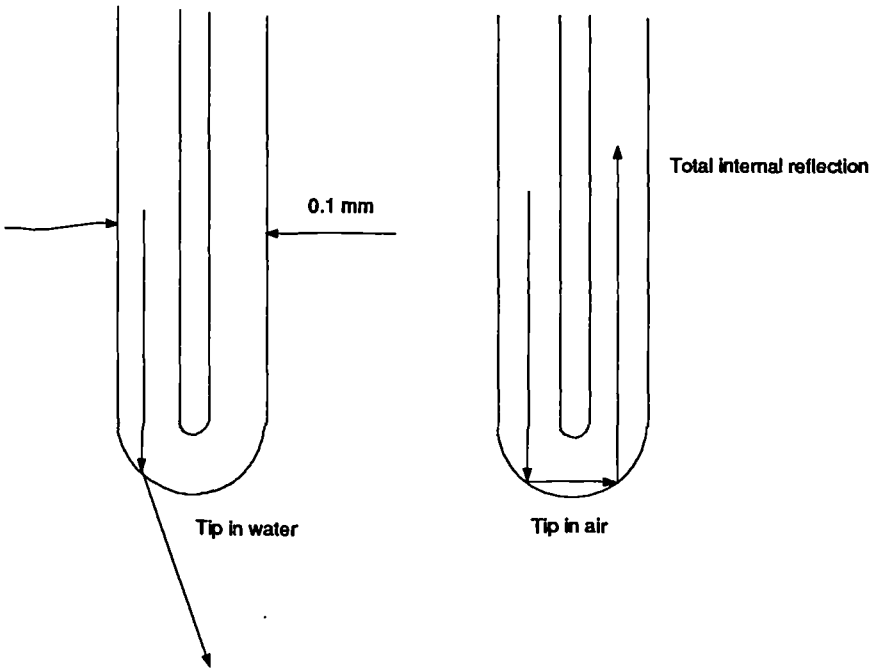

Figure 2.12: Diagram of optical probe used by Danel and Delhaye [1971]

amplitude of the signal from the optical probe decreased. At high air velocities i.e. greater than $1ms^{-1}$, the signal to noise ratio was greatly reduced due to a layer of water which was present on the probe tip. A plot of the ratio between the maximum and minimum amplitudes against the bubble velocity (see Figure 2.14) caused the authors to conclude that the optical probe can measure the local void fraction and the bubble velocity after proper calibration within a certain velocity range. They concluded that the change in signal amplitude as the air velocity increases was due to the presence of a liquid film on the probe tip which has different thicknesses at different velocities. This implied that the thickness of the water film present on the probe tip is increasing with air velocity i.e. the conical ended optical probe seems to preserve a water film on the tip.

Morris *et al.* [1987], investigated the use of optical probes in air-water flows. The optical probe used for their investigations was a cleaved tip fibre with a diameter of 0.15mm. The tip surface was cut (cleaved) at right angles to the fibre axis (see Figure 2.15). They claimed that this type of fibre tip improves spatial resolution because of its small size. They used Fresnel's Law (Born and Wolf [1980], Hecht and Zajac [1980]) to measure the reflection coefficient at the probe tip (see Section 4.3.1).

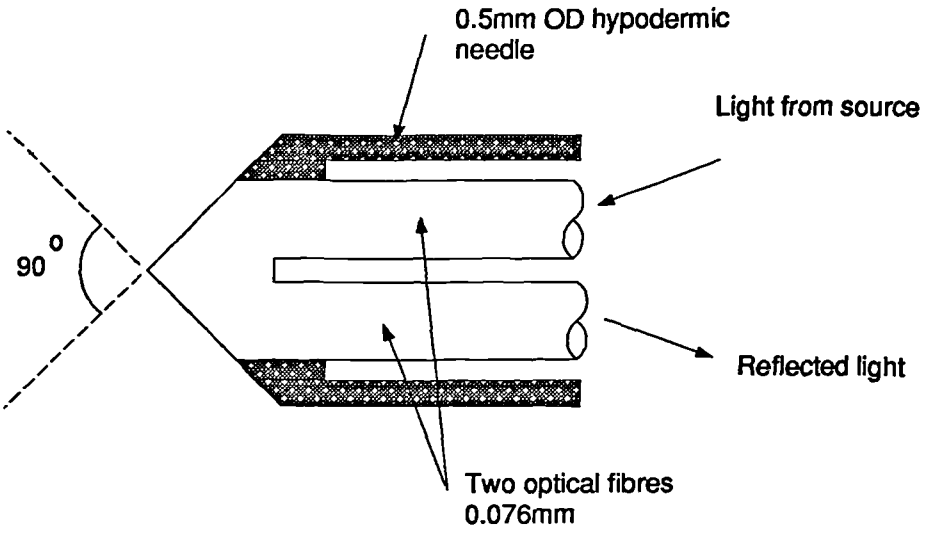

Figure 2.13: Diagram of optical probe used by Abuaf *et al.* [1978]

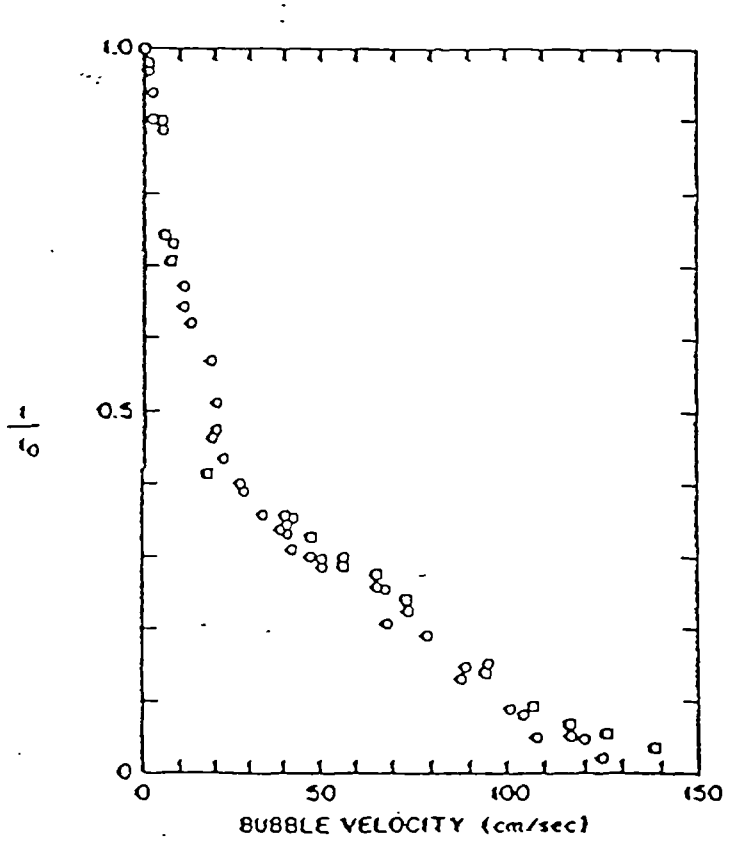

Figure 2.14: Non-dimensional signal intensity versus air velocity. Abuaf *et al.* [1978]

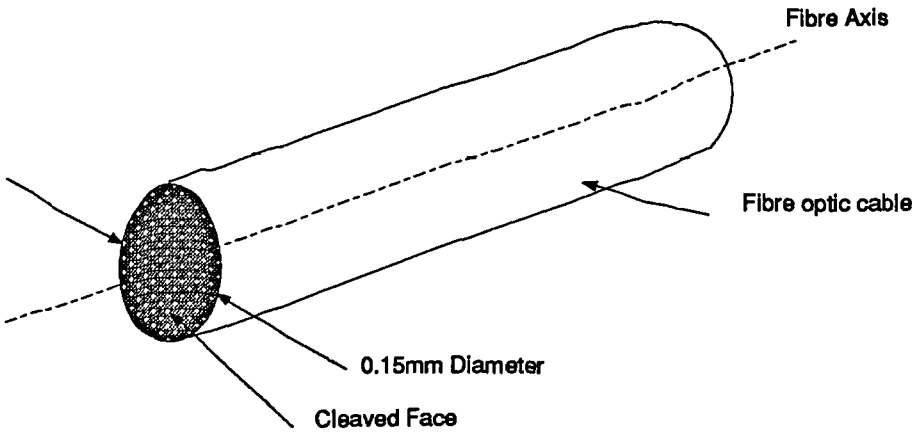

Figure 2.15: Optical probe used by Morris *et al.* [1987]

They carried out a series of tests, in air-water flows, using the cleaved optical probe in a vertical 18.9mm inside diameter tube with a length of 1104.9mm. To compare the results obtained from the optical probe, a Resistivity probe (RF) (Akagawa [1963], Neal and Bankoff [1963], Serizawa *et al.* [1974], Vigneaux [1988]) and Quick Closing Valves (QCV) (Morris *et al.* [1987]) were employed. From the results obtained using just the optical probe and the RF probe, they concluded that both techniques provide similar void fraction profiles at low void fraction values (less than 40%). Above this value, the optical probe was a better measuring instrument. Comparison of the average void fraction as measured by the optical probe was made with the QCV technique. They showed that the maximum relative error of reading between the QCV and the optical probes was 7%. This maximum error occurred at low void fractions and it could have been due to deflection of bubbles by the probe tip.

Moujaes and Dougall [1987] investigated the use of optical probes in vertical air-water flows. A dual spherical tipped optical probe was used to measure the local void fractions, the air velocity and the bubble sizes. A wedge shaped hot-film anemometer was used to compare the results from the optical probe and to measure the liquid velocity. It must be stressed that the data from the optical probes were taken in 1979 and the hot-film data were taken in 1980 i.e. the two measuring devices were not tested together at

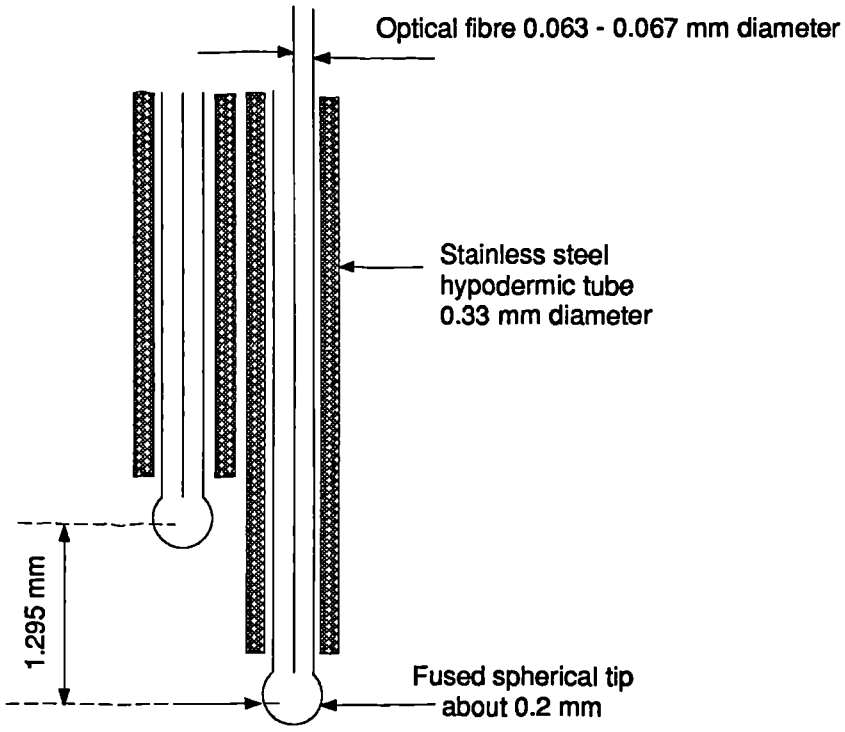

Figure 2.16: Optical probes used by Moujaes and Dougall [1987]

the same time. The investigations were carried out in a rectangular channel (12.7mm by 76.2mm cross-section) made of perspex. Figure 2.16 shows a diagram of the optical probe arrangement. The spherical tips were manufactured by fusing the two optical fibres together using a mini torch. Profiles were presented for void fraction, air velocity and water velocity. The measured air and water flowrates as calculated from the venturi meters and those found by integrating the results from the hot-film and the optical probes over the cross section, were compared. Moujaes and Dougall stated that the error range for the air flowrates were 5% to 18% and the error range for the liquid flowrates were 3% to 21%. These numbers include combined errors of void fraction and air or liquid flowrate. The error in the void fraction measurement could have been due to bubbles being deflected from the tip of the probe.

More recently, Moujaes [1990] compared the spherical tipped optical probes to Abuafs' [1978] conical probe. Moujaes constructed a conical optical probe and an experimental rig similar to that of Abuafs'. The non-dimensional signal intensities (ratio of maximum amplitude to minimum amplitude) were plotted for both the conical tipped probe and the spherical tipped probes. A similar shaped curve given by Abuaf *et al.* [1978] was obtained by Moujaes [1990]

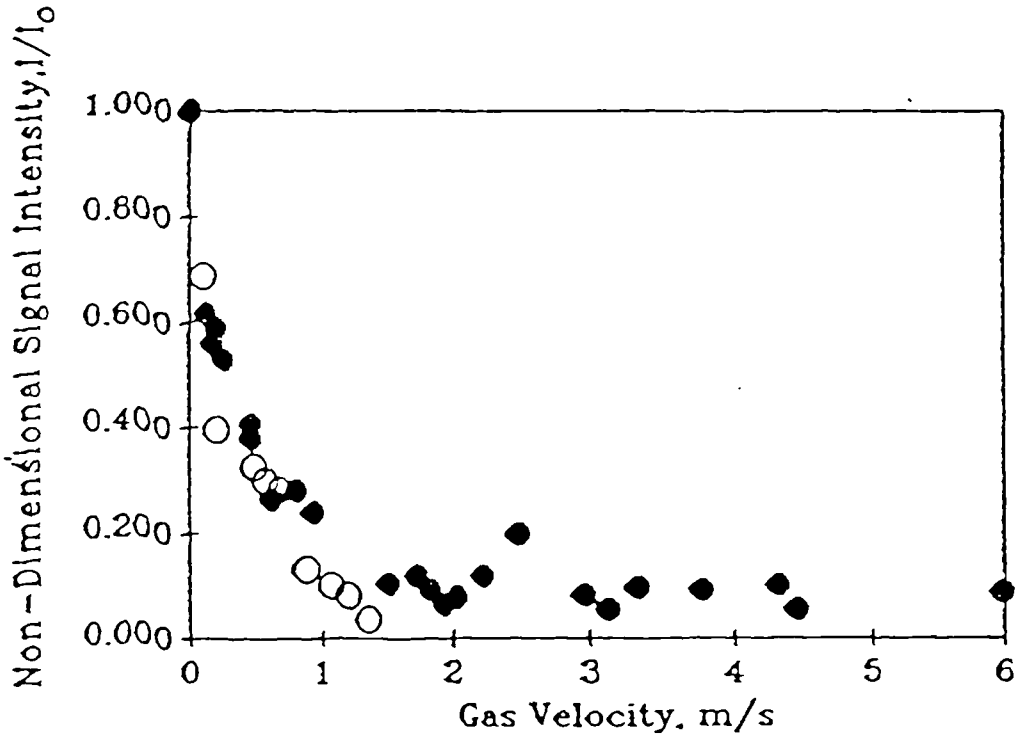

Figure 2.17: Signal intensity plot for a conical tipped optical probe. Moujaes [1990]

for the conical optical probe (see Figure 2.17). However, a major difference in the signal intensity plot was seen between the conical optical probe and the spherical tipped probes. With reference to Figure 2.18, it was shown that for the spherical tipped probes, the signal decreases linearly in a slow fashion down to a value of 0.5 and will continue to produce an output signal which has a large signal to noise ratio. Moujaes stated that a more 'blunt' tip of a small sensing area (0.2mm or less) will maintain a thinner layer of liquid around the tip surface helping it to maintain a high signal to noise ratio. The conical probe has a tendency to 'slice' the liquid and bubbles alike and tends to preserve a thicker layer of liquid around the tip which decreases the amount of reflected light. A qualitative model was presented which describes the forces around the liquid film, on the spherical tipped optical probe, after a bubble has been penetrated. The model showed that as the air velocity increases, the thickness of the liquid film on the tip increases which reduces the signal amplitude. However, Moujaes stated that the model would have to be verified by taking high-speed photography in order to obtain the shape of the liquid film around the probe tip as a function of air velocity. Moujaes concluded that the spherical tipped optical probe provided accurate results in air-water flows

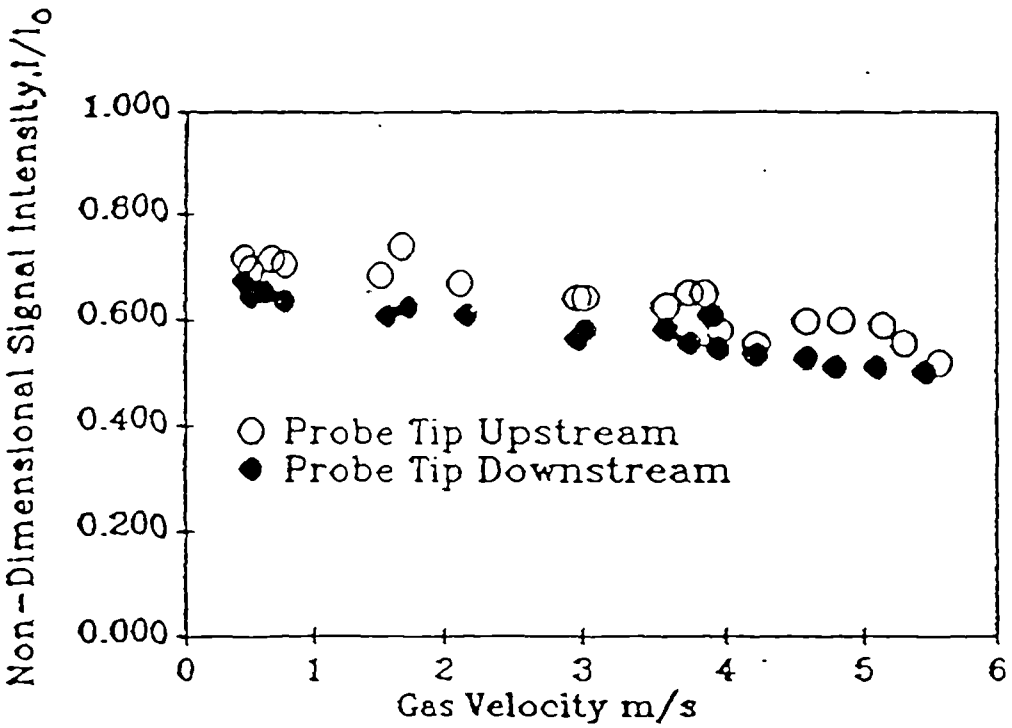

Figure 2.18: Signal intensity plot for spherical tipped optical probes. Moujaes [1990]

to measure the bubble velocity. However, he states that more work is required to improve the response and the sensitivity of the optical fibres. Use of smaller diameter probes will allow the user to sense smaller bubbles and hence provide a more accurate result.

Cartellier [1989], investigated the use of different tipped optical fibres in air-water flows. A flat interface consisting of air and water was swept across a stationary optical probe to investigate the piercing effects of the probe tip. A selection of different optical probe tip geometries were investigated to extract the interface velocity from the rise time of the signal. Cartellier [1990], [1992] claimed that the latency length L, defined as the product of the rise time T_r and the interface velocity V_i, remained constant above a critical velocity of $0.1 ms^{-1}$ for a conical tipped optical fibre. Hence, the determination of the rise times could provide the velocity of each bubble which interacted with the probe.

2.7 Summary

It has been seen that hot-film anemometers have been used in vertical and deviated oil-water flows. However, there has been no report of their accuracy in measuring water velocity in deviated or vertical oil-water flows.

Optical probes have not been used in oil-water flows, but have been extensively used in air-water flows. By using one optical probe, one can measure the local void or volume fraction. By using two optical probes, the bubble velocity can be computed (assuming that there is an offset between the two probes).

Chapter 3

Principles of operation of hot-film anemometers and optical probes

3.1 Introduction

This chapter describes the principles of operation of a hot-film anemometer and previous work carried out in developing signal analysis techniques in two phase flows. The principles of operation of optical probes will be described with the view to applying this technique to measure volume fraction and dispersed phase velocity.

3.2 Hot-film anemometers

Hot-film anemometers are used for measuring flows in water or other thermal conducting media. The sensor material is platinum which is deposited onto a 0.07mm diameter quartz fibre. The fibre is usually cylindrical but common alternatives are wedge and conical shapes. The probe shown in Figure 3.1 would have a total fibre length of 3mm with the ends gold and copper plated to leave an effective sensing length of 1.25mm. An additional quartz coating (typically 0.002mm) is applied to protect the film from electrochemical effects. Commercially available Dantec constant temperature anemometer (CTA) equipment was used with the hot-film probe. The specific CTA equipment serial numbers are given in Section 4.2.1.

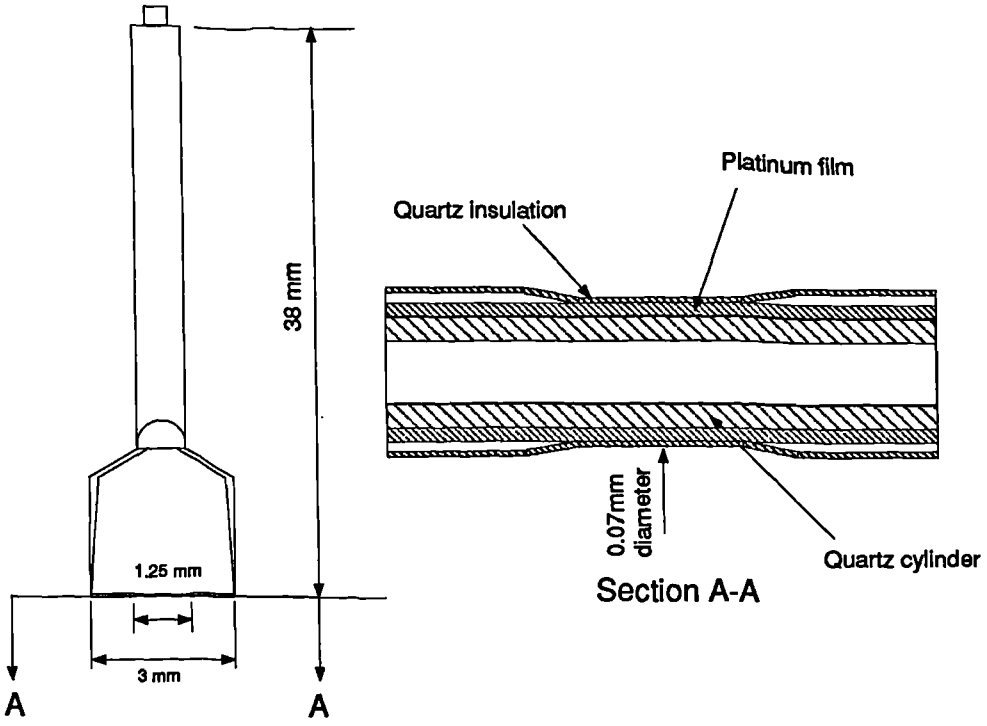

Figure 3.1: Diagram of a modern cylindrical hot-film anemometer. Dantec 55R11

3.2.1 Principles of operation

The sensor is heated by an electric current to a temperature T above the ambient temperature T_o of the fluid. Increased convection due to an increased flow velocity causes heat loss from the sensor at a rate depending upon the fluid velocity. In the normal mode of operation, the sensor is kept at constant temperature and the increase of current required to maintain this temperature is a measure of the heat loss from the probe. If the temperature of the fluid remains constant, then one can measure the fluid velocity with suitable calibration of the probe. The calibration of hot-film anemometers is discussed in Section 4.5.

Figure 3.2 shows a schematic diagram of the bridge circuit for the constant temperature anemometer (CTA). The probe sensor is electrically connected to form part of one arm of a Wheatstone bridge R_p. In stationary flow, the bridge is adjusted for balance such that the voltage difference between the two arms of the bridge is zero when the probe is heated to its normal operating temperature T i.e. the error voltage $e_a = 0$. A servo amplifier whose gain and bandwidth is programmable, controls the voltage across the bridge and thus

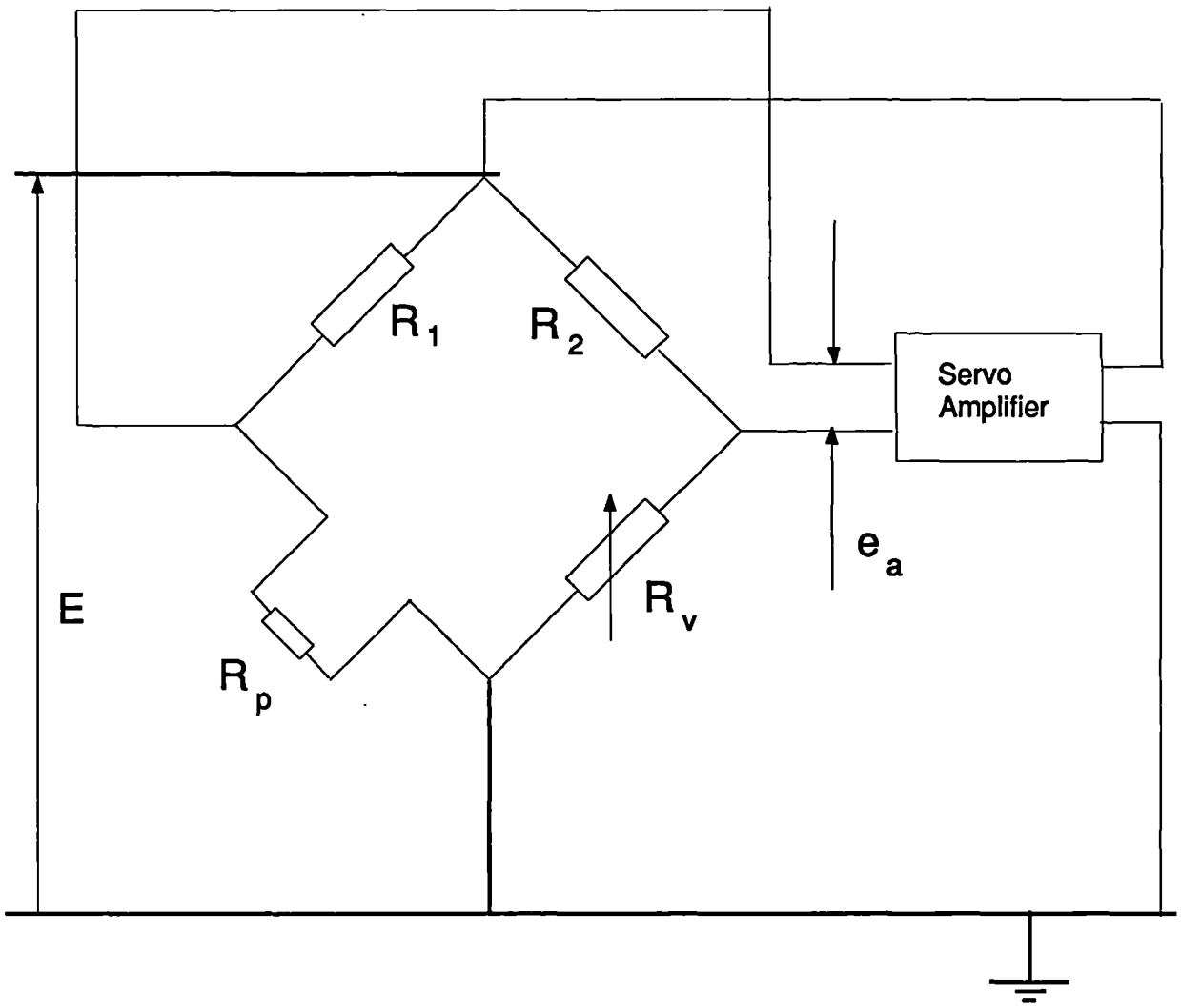

Figure 3.2: A schematic diagram of bridge circuit for hot-film anemometer

the current through the probe in such a way that the probe resistance remains almost constant. When the heat loss from the sensor is increased, e.g. by increased flow velocity, the resulting temperature change of the sensor causes an imbalance of the bridge error voltage e_a. The error signal from the bridge causes the servo amplifier to change its output voltage in such a way that the probe resistance (or equivalent average probe temperature) is restored to its former value, hence the designation constant temperature anemometer. The bridge voltage E is fed to the output as a measure of the effective cooling velocity.

3.3 Interpretation of hot-film signals

Delhaye [1969] studied the response of a conical hot-film anemometer in vertical air-water flows. Utilising a high speed camera and oscillograms of the anemometer output, he analysed the bubble/probe interaction. With reference to Figure 3.3, Delhaye reported that as the bubble approached the probe tip there is an increase in the value of E (the voltage output from the probe). This is illustrated by the points B to C. A reverse of this effect was observed when the bubble leaves the probe (points E to F). A bubble has a greater velocity than the mean liquid velocity. However, the liquid neighbouring the bubble has a slightly higher velocity than that of mean liquid velocity. As the bubble approaches the anemometer, the anemometer will sense this larger liquid velocity causing an increase in the output E (points B to C in Figure 3.3). As the probe enters the bubble there is a decrease in the anemometer output E. This is due to heat transfer properties of the two fluids (heat transfer in the liquid phase is two to three times greater than in the gaseous phase). When the probe is in contact with the rear interface of the bubble, a sharp increase in the voltage output E, can be seen (points D to E). As the probe leaves the bubble, it entrains liquid in its wake at a greater velocity than that of the mean liquid velocity (points E to F).

Bremhorst and Gilmore [1976] investigated the response of the cylindrical hot-film anemometer in two phase air-water flows. They used high speed photography coupled with simultaneous recordings of the hot-film signal. They found that the signals from the hot-film were repeatable and that the 'shapes' of the signals can be characterised into four different types of bubble/probe interactions.

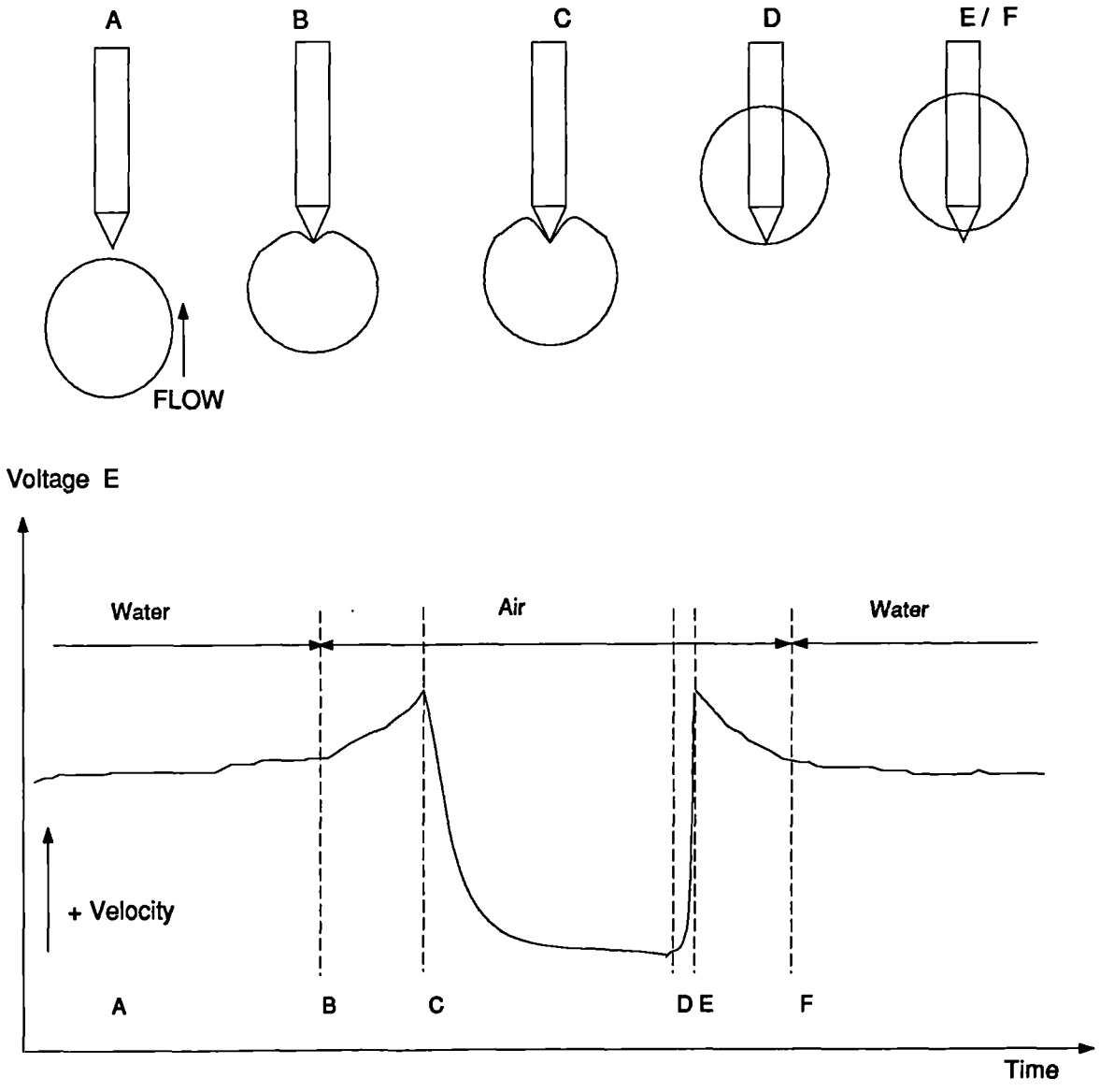

Figure 3.3: Conical hot-film signal response. Delhaye [1969]

With reference to Figure 3.4:

1. A direct hit is where the air bubble completely covers the sensing area of the hot-film. This is shown as curve 1 (solid line)

2. A glancing hit is where the bubble hits the wire off centre, but covers the sensing area completely. This is shown as curve 2

3. A partial hit is where the bubble strikes the wire off centre and the bubble does not cover the sensing area completely. This is shown as curves 3 and 4

In the case of a direct hit (curve1), the points A to B represent the bubble contact time. The part of the signal from points B to C represents the detachment of the bubble from the sensor, also known as the 'detachment tail'. From this interpretation, Bremhorst and Gilmore identified that part of the signal associated with the dispersed phase (bubble) and the continuous phase.

With reference to Figure 3.5, a method for modelling the bubble/probe interaction for a hot-film anemometer was developed by Bruun and Farrar [1988]. This was carried out using high speed photography and a theoretical and experimental study of surface tension effects around a hot-film sensor. The stages of bubble/probe interactions are given below:

1. As the bubble approaches the sensor, there is an increase in output from the sensor (points A to B). This is due to velocity of the liquid being greater than the mean liquid velocity in the vicinity of the bubble. This was also reported by Delhaye [1969].

2. The signal continues to increase until the bubble front reaches the sensor. At this point, B, a peak will occur.

3. As the bubble interface 'wraps' itself around the sensor, the heat transfer from the sensor is suppressed (point C). This effect is due to the velocity of the liquid approaching zero and hence the output voltage will tend to that of still water. The two menisci (a1 and a2) will then wrap themselves around the sensor leaving a thin film of water on the sensor.

4. The two menisci will coalesce behind the sensor. The thin film of water will slowly evaporate from the sensor (point D).

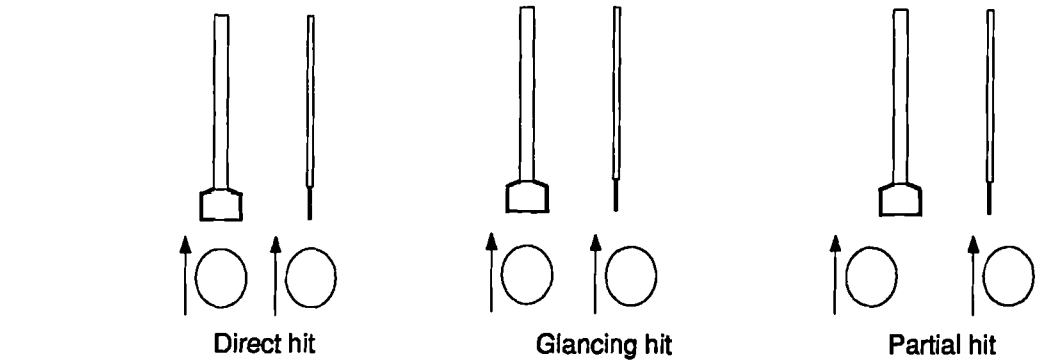

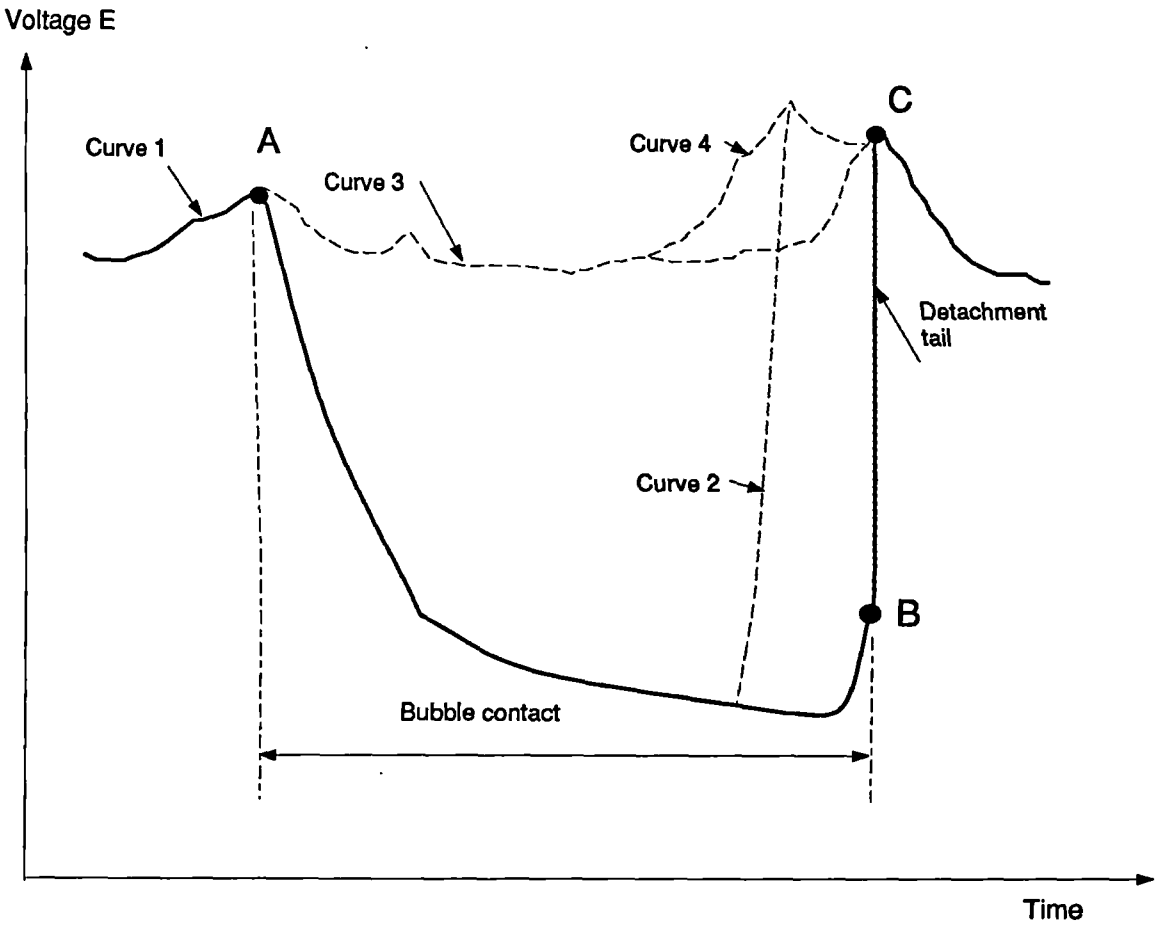

Figure 3.4: Cylindrical hot-film signal response to a bubble passage. Bremhorst and Gilmore [1976]

5. If this thin film breaks, a sharp peak is observed in the signal. This can be seen as point E.

6. As the back of the bubble starts to make contact with the sensor, there is a sharp rise in the sensor output until the sensor comes into contact with the liquid (points F to G).

7. At the point of contact with the liquid, the liquid forms a meniscus around the sensor causing rapid heat convection from the sensor hence producing a steep curve. The peak H is reached. This is thought to be related to dynamic meniscus effects and not to turbulent intensities.

8. The output signal then drops towards the average velocity of the liquid phase (point I), where points A and I are the same level.

3.3.1 Signal analysis

There are three basic methods for analysing hot-film signals:

1. The population density function (PDF), Delhaye [1969]. This is where the PDF of the output signal is evaluated to provide volume fraction estimates.

2. The amplitude method (Toral [1981]). A threshold voltage is chosen (often manually) just below the lowest value corresponding to the continuous phase. Any part of the signal below this threshold is associated with the dispersed phase and any part of the signal above the threshold is associated with the continuous phase. This method is used to compute the volume fraction and to identify the start and finish points associated with the dispersed phase, so that the continuous phase velocity can be calculated.

3. The slope threshold method (Serizawa *et al.* [1983], Smits [1991]). The slope threshold method calculates the first derivative of the hot-film signal. A chosen threshold level is then applied to the first derivative of the signal. This method is used to compute the volume fraction and to identify the start and finish points associated with the dispersed phase, leading to the calculation of the continuous phase velocity. It is usual to use a combination of the amplitude and slope threshold methods to analyse hot-film signals in two phase flows e.g. Farrar [1988].

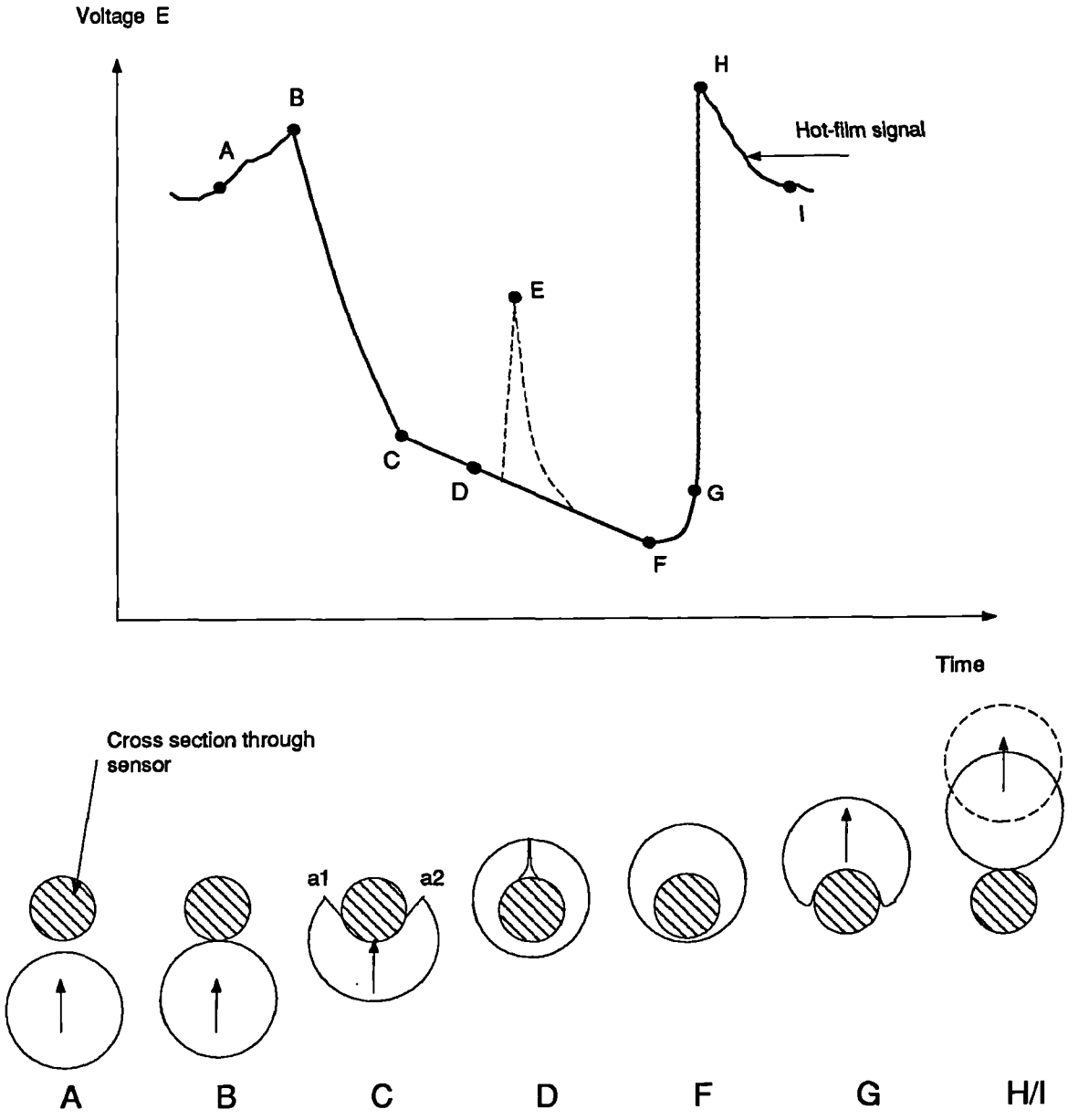

Figure 3.5: Hot-film signal response to a bubble passage. Bruun and Farrar [1988]

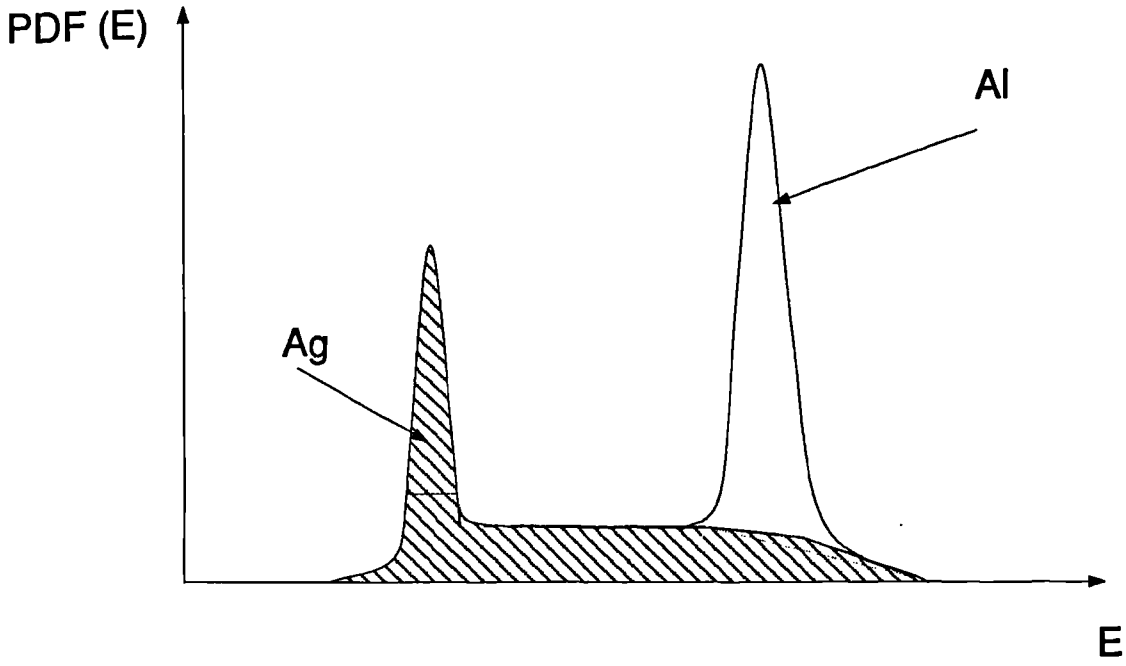

Figure 3.6: Population density function analysis. Delhaye [1969]

Population density function method

Delhaye [1969], developed a population density function method for analysing the hot-film data in air-water flows. An 800 channel analyser was used to count the number of times a certain voltage output was detected. By plotting the number of counts in each of the 800 channels against the voltage output from the hot-film, a PDF curve was produced (see Figure 3.6). The local void fraction, α_g, was related to the area of the distribution under the curve hence:

$$\alpha_g = \frac{A_g}{A_g + A_l} \tag{3.1}$$

where A_g is the area under the gas PDF curve and A_l is the area under the liquid PDF curve.

Amplitude threshold method

The amplitude threshold method is usually used to compute the volume fraction. The time averaged local volume fraction is given by Equation 2.5 in Section 2.3. Having chosen a threshold voltage, the part of the signal associated with the dispersed phase can be detected (see Figure 3.7). In practice, some bubbles are not detected using this method since a partial hit will produce a smaller amplitude output signal. This is shown as droplet XYZ which

will not be detected since the threshold voltage level, PQ, falls below that signal. Another drawback of using this method is that, the points A and C (which correspond to the droplet start and finish points) will not have been correctly identified. With reference to Figure 3.7, the true residence time should be $Td + \Delta t_1 + \Delta t_2$ instead of the estimated residence time Td. The outcome of this will be, underestimation of the volume fraction and incorrect identification of the start and finish points associated with the dispersed phase; this would lead to underestimation of the continuous phase velocity.

Slope threshold method

Applying the slope threshold technique, to the hot-film signals, can yield a better estimate of the points A and C. With reference to Figure 3.7, the point A can be estimated on the first derivative curve as point $A1$. Similarly, the points B and C are estimated as points $B1$ and $C1$. This technique does have its drawbacks. The peak RST is encountered on the hot-film signal when film breakage occurs within a bubble. This phenomenon was reported by Bremhorst and Gilmore [1976], Serizawa *et al.* [1983] and Farrar [1988]. Applying the slope threshold method, this would imply that there were two bubbles instead of one. This would result in underestimating the volume fraction and it would be interpreted as the passage of the rear of the bubble; the points between $S1$ and $C1$ will now be considered as part of the continuous phase.

One of the limitations of using a hot-film anemometer in two phase flows is that, the background signal due to the continuous phase is not stable and it is difficult to distinguish the start and the finish points of passing droplets. Authors in the past (e.g. Delhaye [1969], Farrar [1988]) have attempted to use sophisticated software to de-convolve the signals from the hot-film anemometer to provide information of the flow.

All of the above analysis methods have their advantages and disadvantages, but it seems that a more robust technique is required to correctly identify the start and the finish points associated with the dispersed phase. If the identification of the dispersed phase can be carried out independently of the hot-film signal, then none of the above analysis methods need to be used.

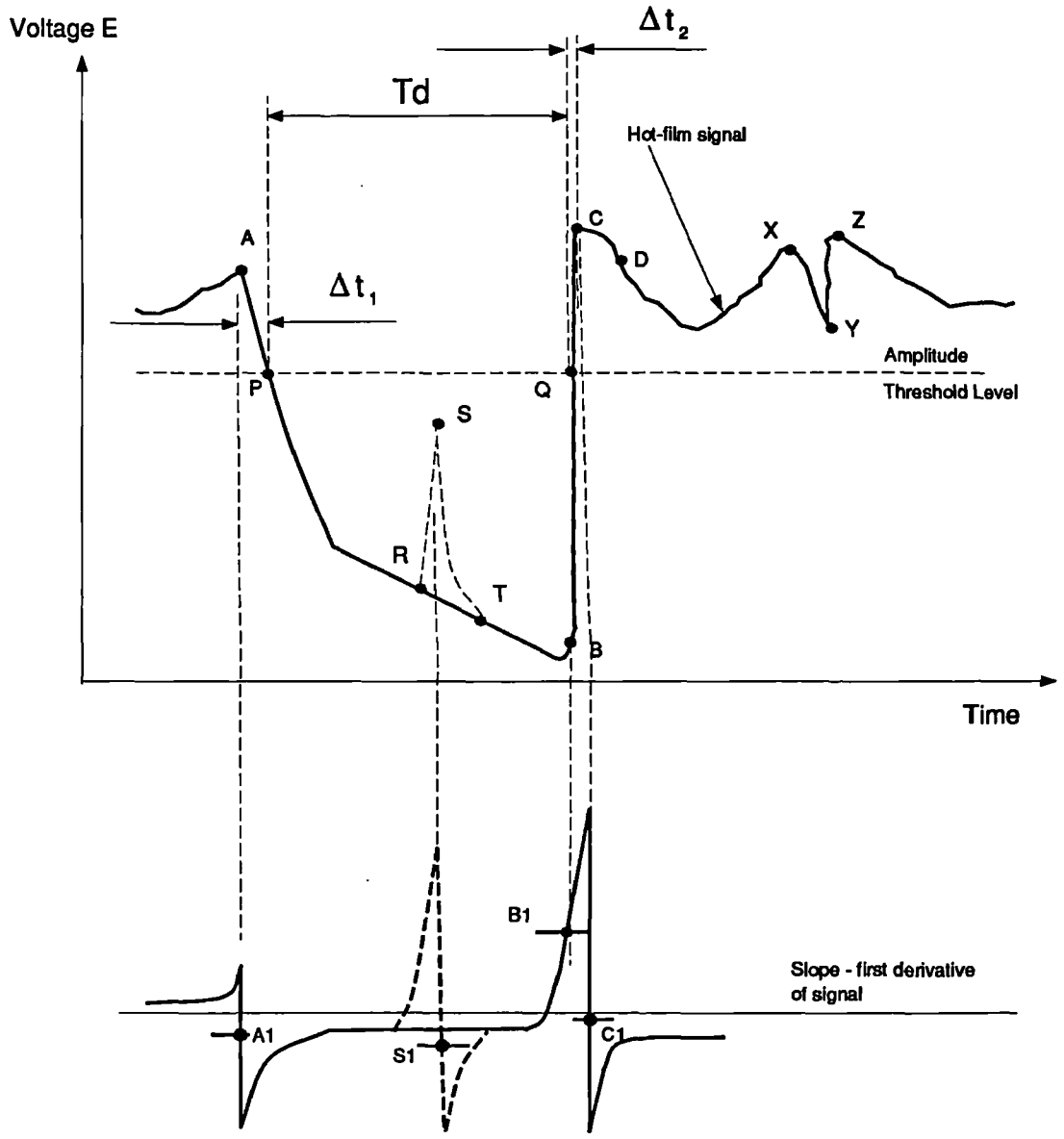

Figure 3.7: Hot-film bubble detection and analysis technique. Farrar [1988]

3.4 Optical probes

There are two basic forms of optical fibres. These are the step-index and graded (gradient) index fibres. Fibres are classified in this manner to provide the user with the refractive index profile of the fibre i.e. how the refractive index varies across the cross-section of the fibre.

1. Step index fibres: (see Figure 3.8) This type of fibre consists of a glass/silica core surrounded by a cladding. The refractive indices of the core and cladding are n_1 and n_2 respectively. The cladding is usually another glass material, but the core and the cladding have different refractive indices, the refractive index of the core being higher than that of the cladding. The main purpose of the cladding is to provide a constant refractive index at the core-cladding interface which in turn will guide the light down the core by total internal reflection; it also provides structural support to the fibre.

2. Graded index fibres: (see Figure 3.8) Graded index fibres are similar to step index fibres except for their refractive index profiles. In the core, the graded index fibre has a parabolic refractive index profile as opposed to the step index fibre which has a constant refractive index profile. The refractive index varies as a function of radial distance across the fibre core.

Light is guided through the fibre by total internal reflection at the core-cladding interface. The numerical aperture of a fibre indicates its light collecting ability and optical sensors are characterised by their numerical aperture. The numerical aperture (NA) is defined as the maximum angle of acceptance, θ_{max} (see Figure 3.8), of the fibre for light guidance. With reference to Figure 3.8 and using Snell's law (Section 2.5 Equation 2.6), it can be shown that:

$$NA = n \sin \theta_{max} = \sqrt{(n_1^2 - n_2^2)} \tag{3.2}$$

where n is the refractive index of the medium outside the fibre, n_1 and n_2 are the core and cladding refractive indices.

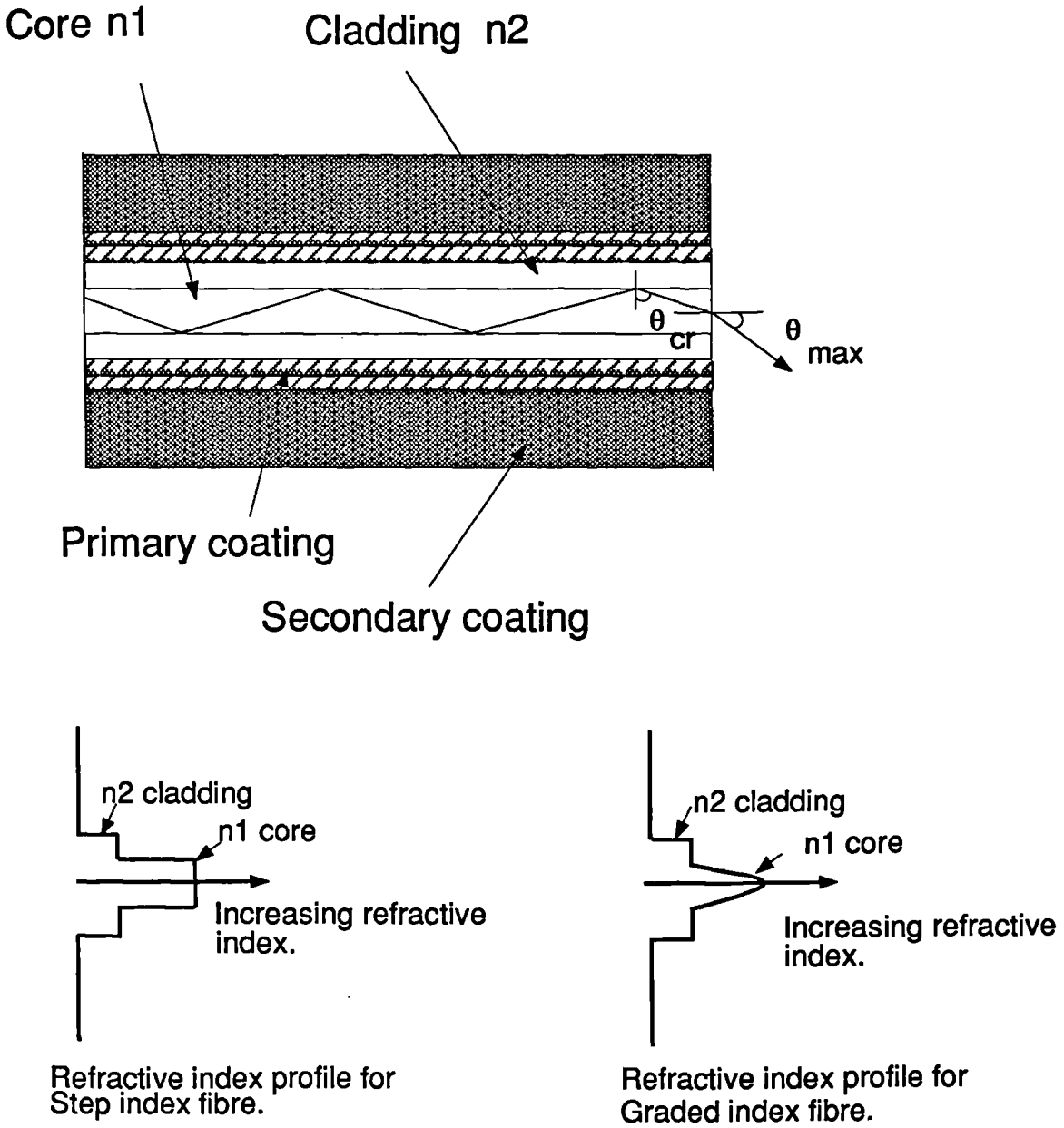

Figure 3.8: Step index fibre and Graded index fibre

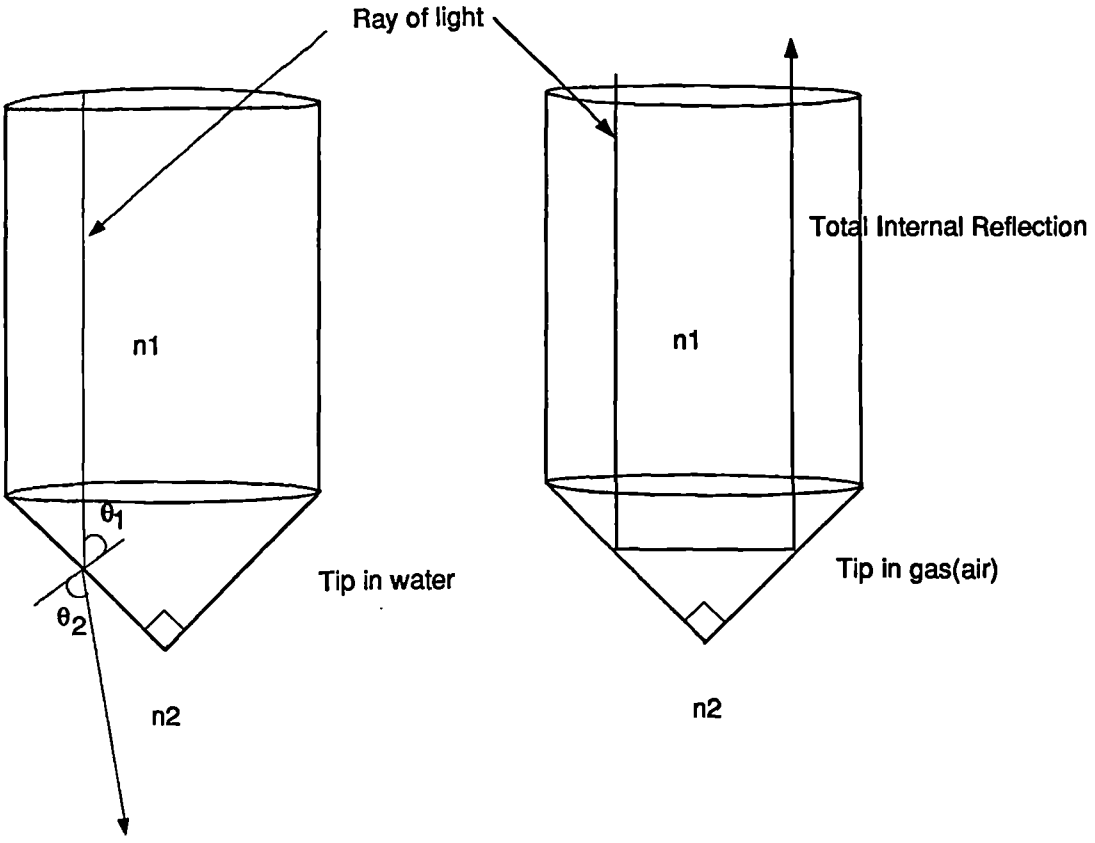

Figure 3.9: Operating principle for cone/prism ended optical probe

3.5 Principles of operation

Optical probes have been used in the past to identify the phase present at a point in the flow and function on the principle of total internal reflection. Cone tipped optical probes have been used (Miller and Mitchie [1969], Abuaf *et al.* [1978]) to distinguish between air and liquid phases using the principles as shown in Figure 3.9. When the probe tip is immersed in the liquid phase, the light ray is refracted out of the probe tip and when the probe tip is surrounded by the gaseous phase, total internal reflection occurs and a significant amount of the light is reflected back through the fibre.

With reference to Figure 3.9, for total internal reflection to occur, θ_1 must be $\geq 45°$ and the tip angle must be 90°. From Snell's law, Equation 2.6 we get that $\sin\theta_1 \geq \frac{1}{2}\sqrt{2}$ and $n_1 \geq n_2\sqrt{2}$. Using $n_1 = 1.48$ (the refractive index for silica), the refractive index of the medium must be less than 1.05. Hence, total internal reflection will occur if $n_2 \leq 1.05$.

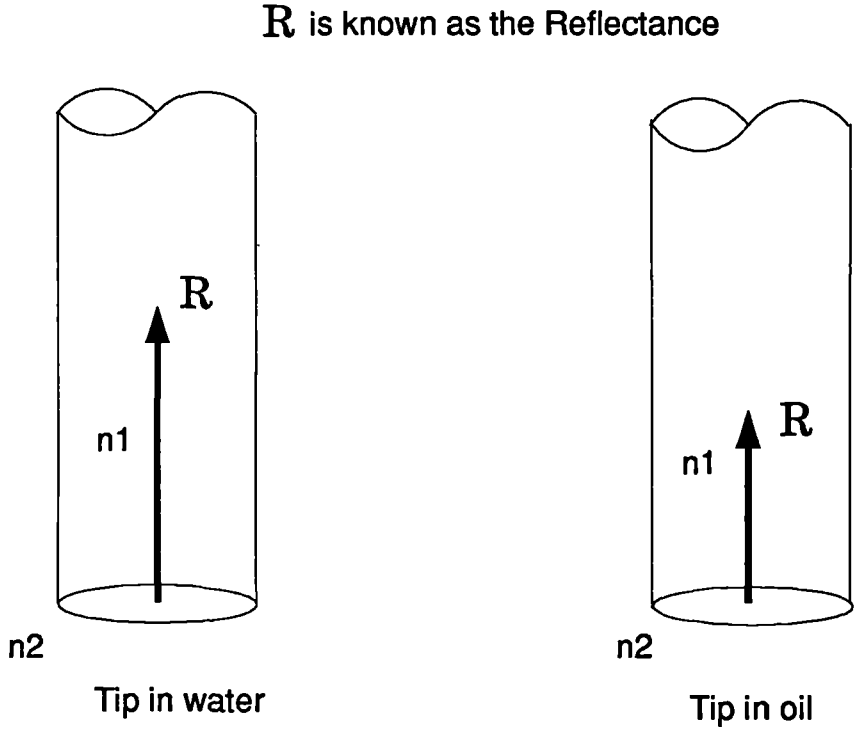

Figure 3.10: Operating principle for cleaved ended optical probe

Water has a refractive index of 1.33 and air has a refractive index of 1.00. By using the above calculation, one can see that a cone ended optical probe (90° tip angle) will function satisfactorily in liquid-air flows. However, the aim of this project is to measure oil-water flows. Oil has a refractive index of 1.436 and water 1.33. Clearly, a cone ended probe will not function satisfactorily in oil-water flows since total internal reflection occurs when $n_2 \leq 1.05$.

A cleaved (straight cut) optical probe was found to discriminate between oil and water (Morris *et al.* [1987]). A schematic diagram of the cleaved probe is shown in Figure 3.10. This type of optical probe functions on the principles of reflected intensities (reflectance). For further details see Section 4.3.1.

3.6 Signal analysis techniques

This section is sub-divided into two parts. Firstly, how past users calculated void fraction from the optical signals and secondly how bubble velocities were calculated.

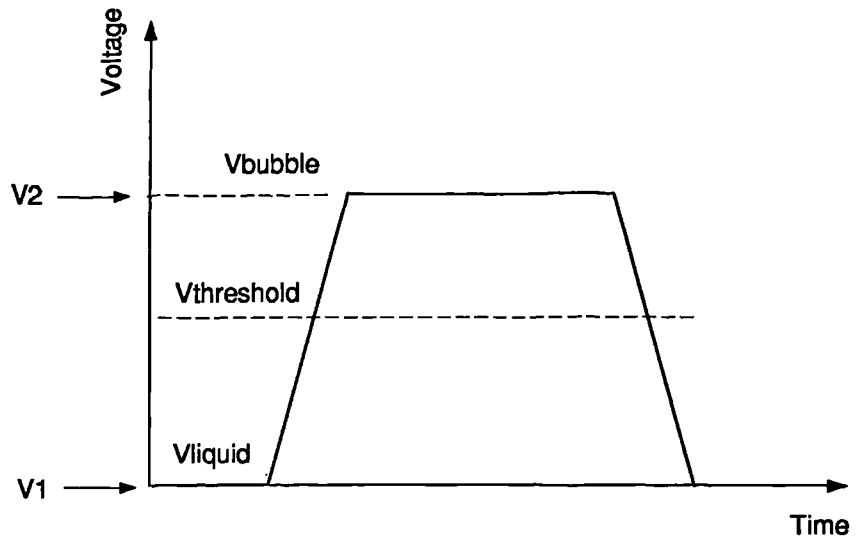

Figure 3.11: Detection threshold level used by Moujaes and Dougall [1987]

3.6.1 Void fraction analysis

The signal analysis used by Moujaes and Dougall [1987] was based on chosing a suitable threshold level to distinguish between the air bubbles and the continuous phase. Figure 3.11 shows a schematic optical signal in vertical air-water flow. The problem encountered by Moujaes and Dougall was the choice of the threshold level. They observed that there was a finite rise and fall time in the optical signal, for the probe to penetrate the film thickness of the bubble and to overcome the surface tension effects. This effect was not due to how fast the electronics responded to a change in signal, but it was due to hydrodynamic effects and the speed at which the bubble interacted with the optical probe. The threshold level was calculated by taking the average of the sum of the two voltage levels V_1 and V_2.

$$V_{av} = \frac{(V_1 + V_2)}{2} \tag{3.3}$$

The void fraction was given as:

$$\alpha = \frac{\sum_{V>V_{av}} N_d}{\sum_{N_{total}} N} \tag{3.4}$$

where N_d is the number of data points associated with the bubble phase and N is the total number of data points in the signal trace.

Cartellier [1989] reported on the characterisation and performance of an optical probe in air-water flows. In his report, he describes two different techniques for analysing the optical probe signal. The first technique that

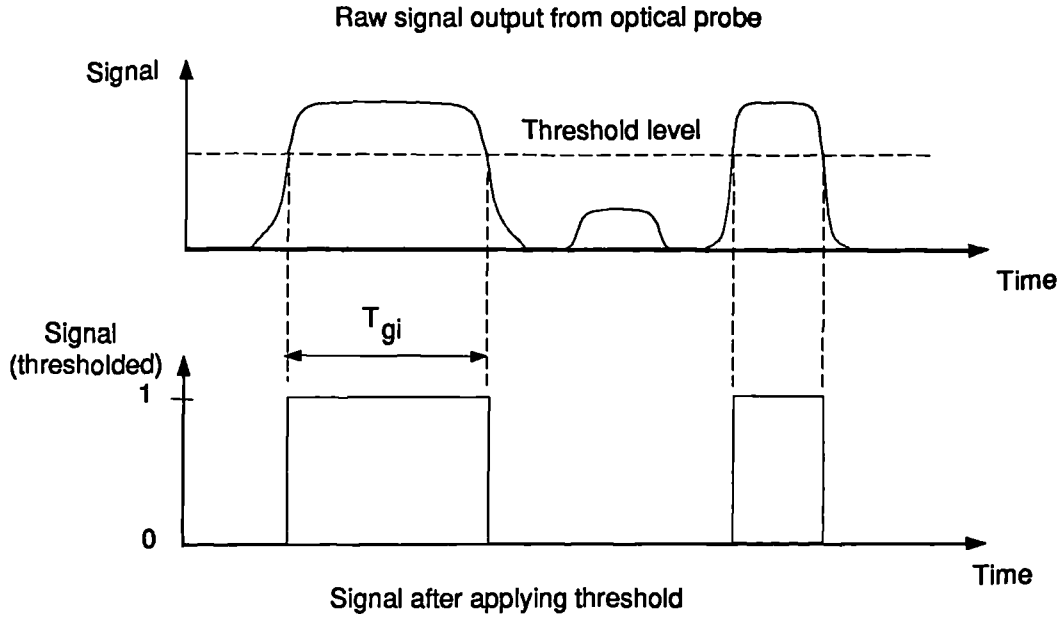

Figure 3.12: Threshold detection level used by Cartellier [1989]

he described was the use of a single detection threshold level. This is the most common method where a single threshold level is set. With reference to Figure 3.12, the intersection of the threshold level with the optical signal determines the start and finish points of a bubble. The second technique involves two distinct threshold levels. With reference to Figure 3.13, the first threshold level is applied to the rising slope of the signal and defines the start of a bubble. The second threshold acts on the falling slope and defines the end of a bubble. In order to calculate the local void fraction, Cartellier used Serizawa's definition given by Equation 2.5 in Section 2.3.

Other authors have used the same definition of the void fraction as given by Moujaes (see Equation 3.4) and Serizawa (see Equation 2.5). However, the choice of threshold level varies from author to author.

3.6.2 Dispersed phase velocity analysis

Moujaes and Dougall [1987] used a cross-correlation technique to measure the dispersed phase velocity. With reference to Figure 3.14, the penetration of a bubble will give rise to output signals $X(t)$ and $Y(t)$ from the upstream probe1 and the downstream probe2 respectively. The cross correlation function, $\lambda_{xy}(\tau)$, derived from the two signals $X(t)$ and $Y(t)$ is given

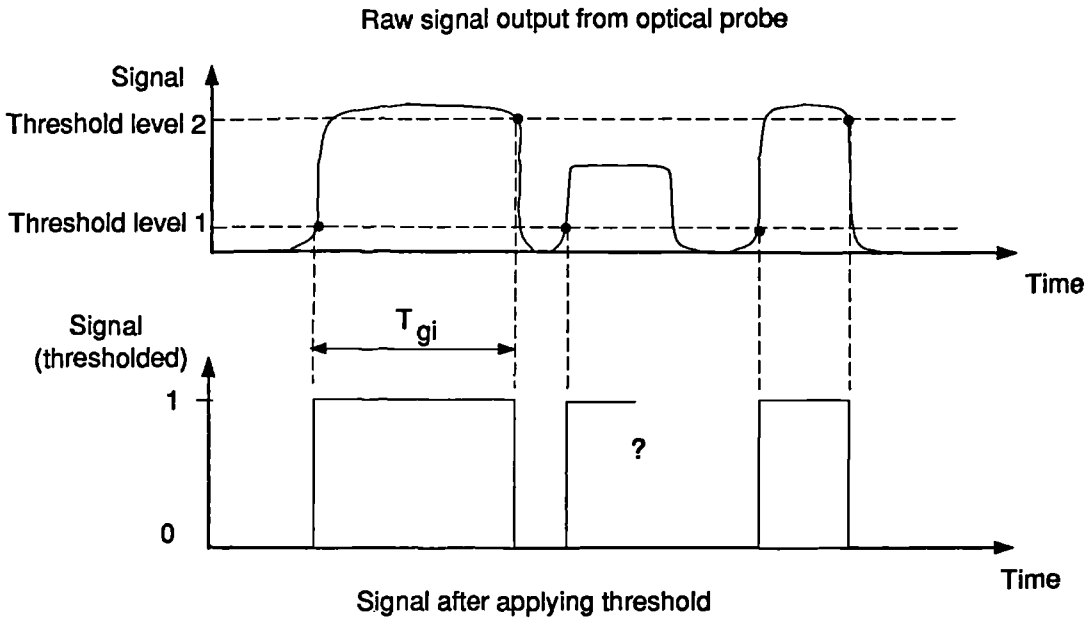

Figure 3.13: Double threshold level detection used by Cartellier [1989]

by Equation 6.5 in Section 6.2.2. Knowing the axial distance between the two optical probes, the dispersed phase velocity was calculated using Equation 6.6. Figure 6.12 in Section 6.2.2 shows a measured cross correlation curve obtained from the two optical signals in oil-water flow.

Cartellier and Achard [1990] proposed that a single optical probe can measure the bubble velocity by using the rise time of the optical signal. Cartellier investigated a number of different probe tip geometries and calculated a latency length L for each probe. The latency length is a characteristic length scale which describes individual optical fibres. The latency length of the optical probe was calculated in a calibration velocity rig. Knowing L, the bubble velocity was calculated by using:

$$U_i = \frac{L}{T_r} \tag{3.5}$$

where U_i is the instantaneous bubble velocity and T_r is the rise time as calculated from the optical signal. The threshold levels were chosen locally for each droplet from the local maximum and minimum of the signal. Figure 3.15 shows the calculation of the rise time. The bubble velocity as calculated by this method is questionable since it is dependent on the choice of thresholds marking the start and finish points of the rise time; Cartellier chose 10% and 90% for the threshold levels. To use this method, calibration of the optical probes are required to determine the latency length for a particular optical probe.

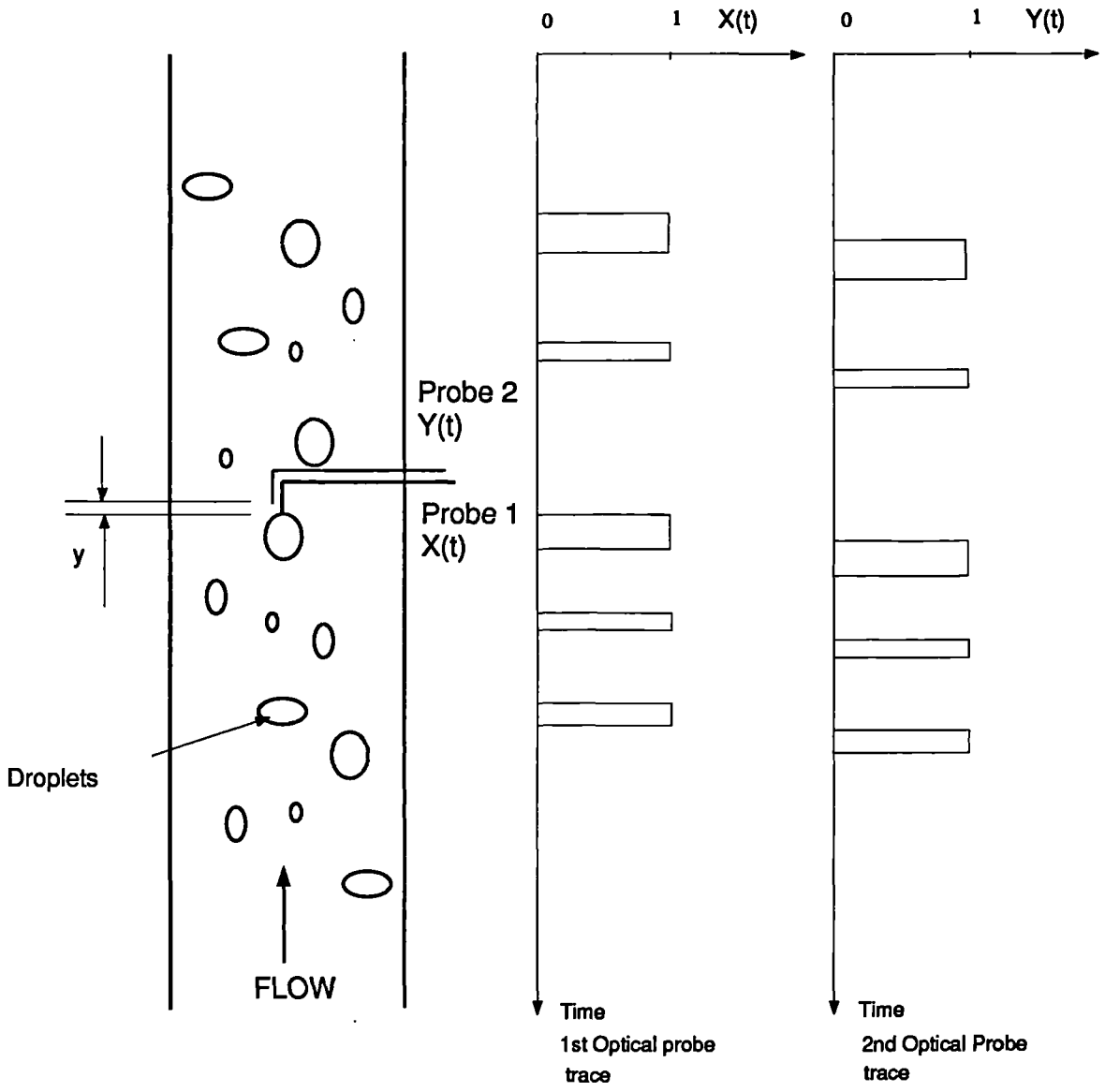

Figure 3.14: Idealised dispersed phase signals from two optical probes. Moujaes [1990]

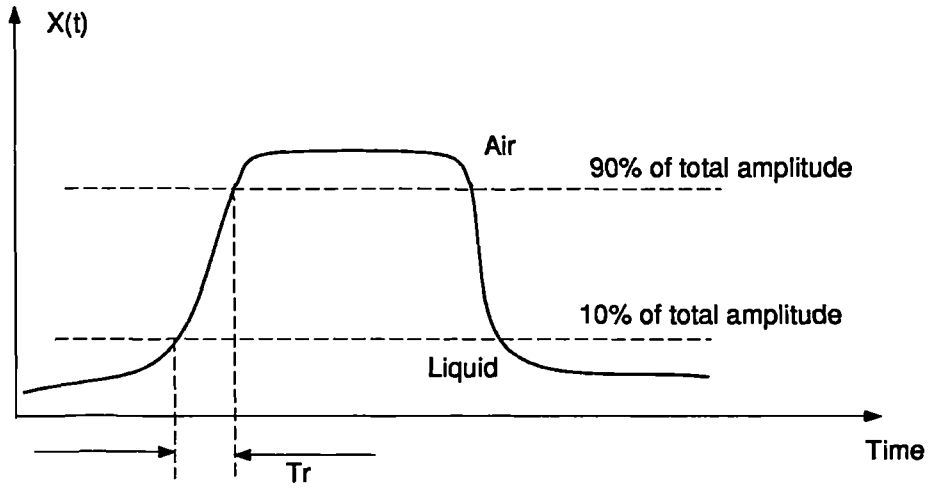

Figure 3.15: Rise time calculation from optical signal. Cartellier and Achard [1990]

3.7 Summary

In this chapter, it has been seen that analyses routines to analyse hot-film signals have been developed and used in oil-water flows. These techniques have been shown to be quite complex in identifying the start and finish points of a droplet. One of the objectives of this work is to produce instrumentation which will identify the start and finish points of a droplet independent of the hot-film signal, hence simplifying the analysis of hot-film signals in oil-water flows.

Optical probes have been developed and used in gas-liquid flows. Simple analysis techniques (thresholding) have been used to analyse the optical signal. The simplicity comes from having 'stable' signal levels which correspond to either of the phases. However, there seems to be no accepted method in the choice of threshold levels to analyse the signals. Calculation of void fraction and bubble velocity have been discussed.

The aim of this work is to provide local flow information in oil-water flows. The hot-film anemometer can provide the continuous phase velocity, and two optical probes (similar to Moujaes and Dougall [1987]) can provide the volume fraction and the dispersed phase velocity.

Chapter 4

The dual probe and the dual split-film probe - Assembly and initial tests

4.1 Introduction

The aim of this project is to determine the continuous phase velocity, the dispersed phase velocity and the volume fraction distribution for vertical and deviated oil-water flows. A hot-film anemometer was employed to measure the continuous phase velocity (after proper calibration see Section 4.5) once that portion of the hot-film anemometer signal associated with the dispersed phase had been identified and removed. Novel instrumentation and signal analysis techniques have been proposed by the author to produce a much simplified technique for measuring locally, two phase flow parameters. It is the purpose of one optical probe to distinguish the start and finish points of passing droplets. By positioning this optical probe in line with the hot-film anemometer, the start and finish points can be 'mapped' onto the hot-film signal. By extracting that part of the signal associated with the dispersed phase, on the hot-film signal, the background continuous phase signal can be analysed to determine the continuous phase velocity. The optical probe not only provides analysis of the hot-film signal, but it is also used to determine the volume fraction. To complete the objectives, the dispersed phase velocity had to be calculated. This is performed by siting another optical probe downstream, at a known

distance, from the upstream optical probe. Using cross correlation and time of flight analysis techniques (see Section 6.2.2) between the upstream and the downstream optical probe signals, the dispersed phase velocity can be calculated.

4.2 The dual probe

This section is divided into three parts. The choice of hot-film anemometers and optical probes will be discussed first. The initial testing of the dual probe to develop the final design of the probe will be discussed. Finally, the calibration of the hot-film anemometer will be described.

4.2.1 Choice of hot-film anemometer

A cylindrical hot-film anemometer was chosen because of its small size and high frequency response (bandwidth of the electronics was 50kHz). The hot-film anemometer was the 55R11 type (see Figure 3.1) which is commercially available from Dantec. Commercially available constant temperature anemometer (CTA) equipment was used with the hot-film probe. The CTA system used for all experiments was the 56C system comprising a $56B10$ main frame, $56C01$ CTA with a $56C17$ plug in bridge (Dantec). A diagram of the hot-film anemometer and its holder can be seen in Figure 4.1.

4.2.2 Choice of optical probes

The optical probes chosen for this investigation had a core diameter of 0.1mm and a cladding diameter of 0.14mm, with a numerical aperture (NA) of 0.29 (see Equation 3.2). This fibre was chosen because of its small size and its ability to transmit sufficient light power. The optical fibre was a multi-mode fibre with a graded refractive index profile (see Section 3.4). These types of optical fibres are commercially available and not expensive. The optical fibre was used as a mono-fibre i.e. light is transmitted and received through the same fibre. A photo-coupler (beam splitter) which connects this mono-fibre to the light source and photo-diode was implemented. The photo-coupler used is commercially available from Canstar. Figure 4.2 shows the optical fibre equipment.

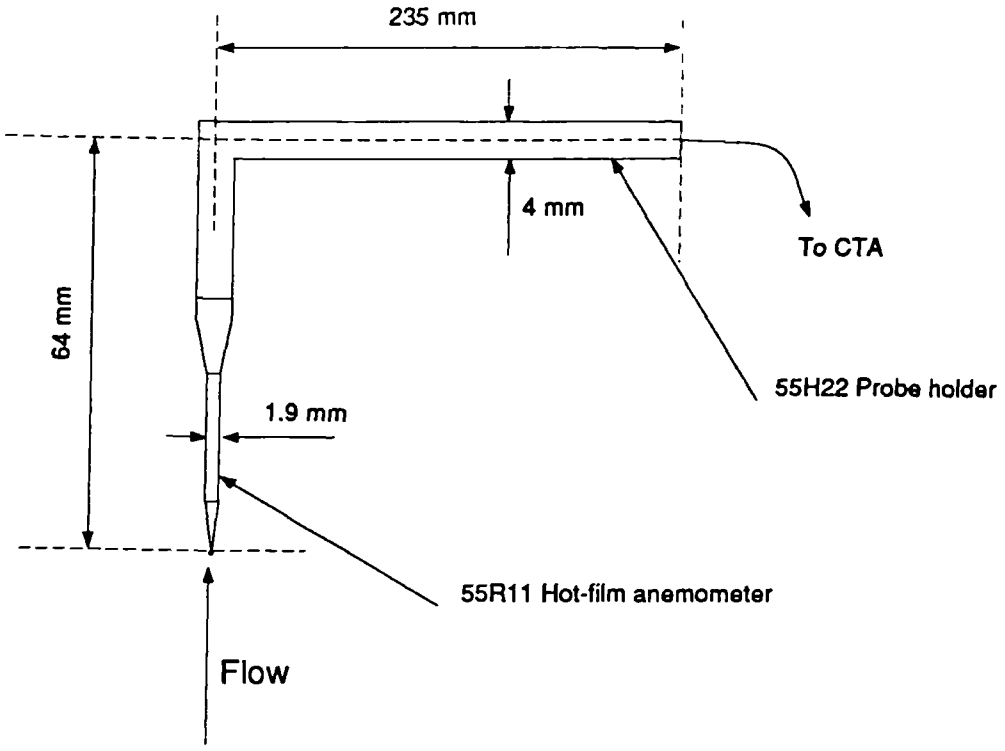

Figure 4.1: Diagram of a hot-film anemometer

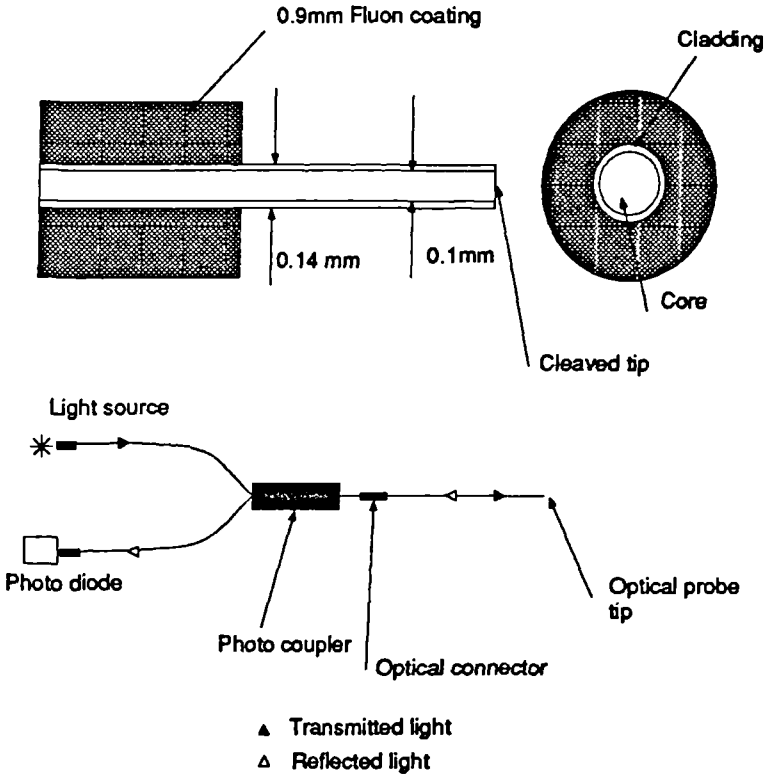

Figure 4.2: Diagram of optical probe equipment

Electronics for the optical probes

The electronics used for the optical probes was a simple circuit derived from Horowitz and Hill [1989]. With reference to Figure 4.3 and Figure 4.2, a high power (160μW) light emitting diode (LED) supplies the fibre with an infra-red light source at a wavelength of 830nm-850nm. This light is transmitted through the photo-coupler down to the fibre tip. Reflected light from the probe tip, is transmitted back through the same fibre to the photo-coupler. This reflected light power is then split with a ratio of 1 : 1 through the photo-coupler. This implies that 50% of the total light reflected back through the fibre is detected. With reference to Section 4.3.1, the reflectance $\mathcal{R}$ (see Equation 4.3) (assuming that the optical probe tip is not 'wetted') for air,water and oil are 0.04, 0.0028 and 0.0002 respectively. This implies that the reflected intensity from the fibre/water interface is of the order of 0.28% of the incident intensity; use of the photocoupler reduces the intensity at the detector to a maximum value of 0.14% of the source intensity. This necessitates the use of a high power emitter. The reflected light intensity is converted into a current via a photo-diode. Stage 1 is a current to voltage converter and stage 2 is a voltage amplifier. A potential divider was used to set the baseline level signal when the probe tip was immersed in water (water signal level Figure 4.8). The feed back resistor R_f had to be chosen such that there was sufficient amplitude difference between oil and water. A simple bench test was carried out to determine a suitable value for R_f. The optical fibre tip was immersed into oil and then water and their associated voltages were recorded at different values of R_f. An amplitude difference of approximately 2 volts between oil and water was produced with a gain of 560.

In order to quantify the bandwidth of the electronics, a frequency analyser was utilised. A frequency range of 0.1Hz to 60kHz (60kHz was the maximum for the frequency analyser) was tested. The electronics had a large bandwidth which was well over 60kHz. In order to investigate the noise content produced by the total system (optical fibre, electronics and ADC), the noise was recorded at a sampling rate of 160kHz (maximum for ADC) with the analogue to digital converter (ADC) (see Section 5.4). Figure 4.4 shows a plot of the population density function (PDF) of the noise signal from the total system

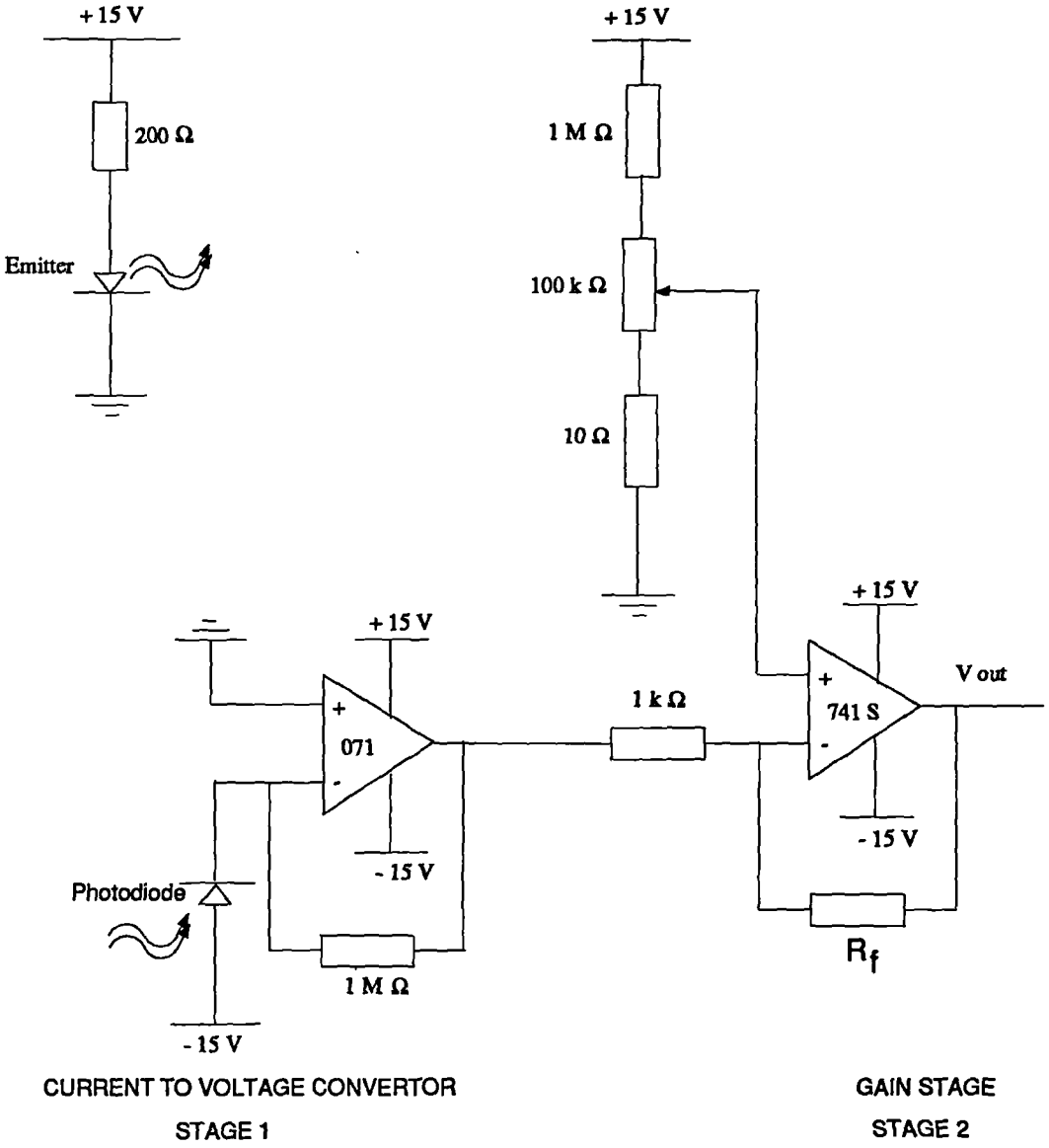

Figure 4.3: Electronics for one optical probe

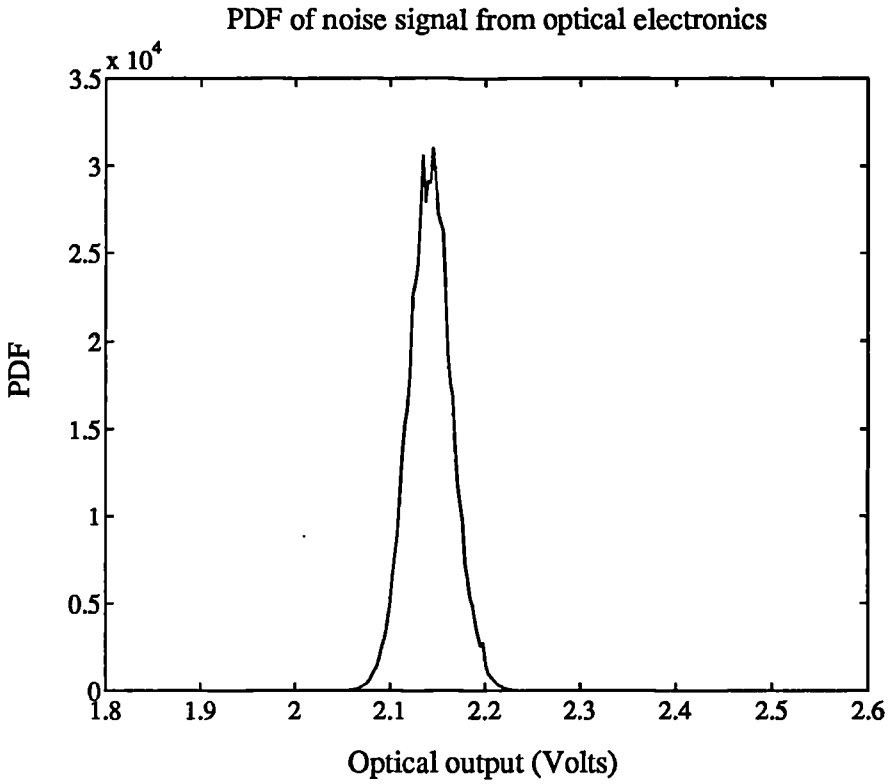

Figure 4.4: Optical electronic noise signal

when the optical probe tip was immersed in water. This was necessary since the analysis of the optical signal requires an estimate of the total noise signal. The maximum band of the noise level was 0.2volts and the signal to noise ratio between the oil and water level was 10. This was adequate to distinguish between oil and water.

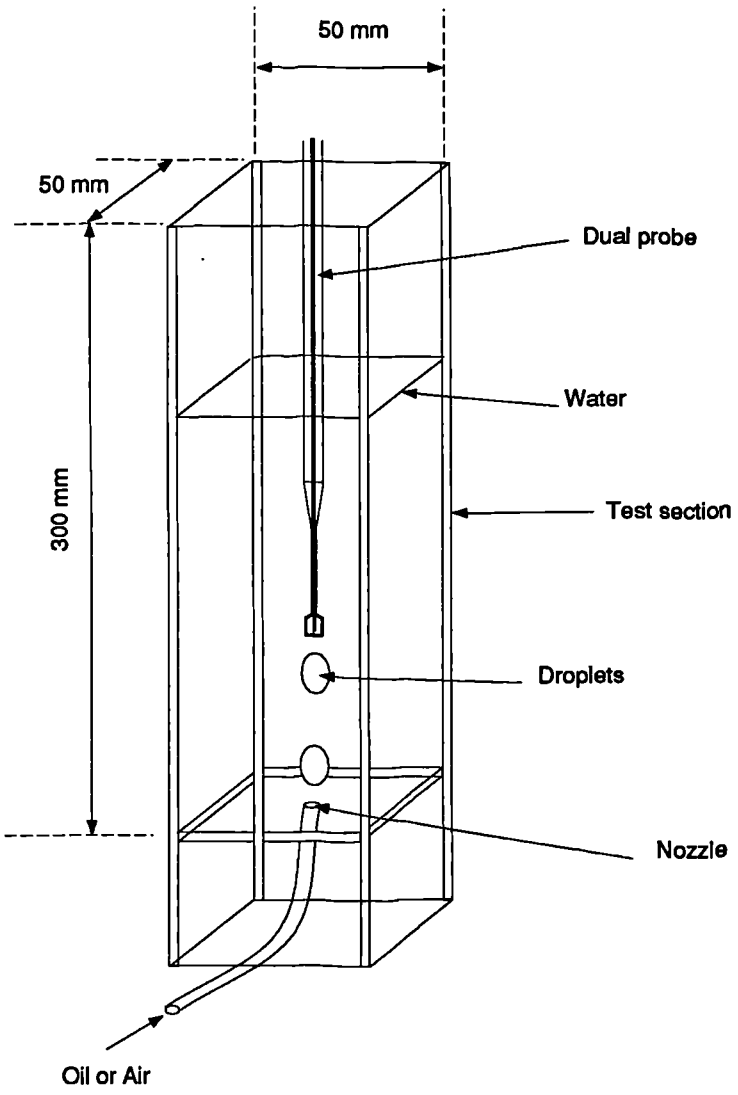

Figure 4.5: Small scale test section

4.3 Initial tests using the dual probe

In order to gain experience using hot-film anemometers and optical probes, a small test section was built to carry out visual low velocity tests. These tests allowed the assessment of errors in the positioning of the optical probes in relation to the hot-film sensor. A vertical perspex square section was built with a 3mm nozzle located at the base (see Figure 4.5). The section was water filled with oil or air being injected at the base. The photographs shown in Figure 4.6 and Figure 4.7 illustrate the motion and interaction of an oil droplet on the dual probe.

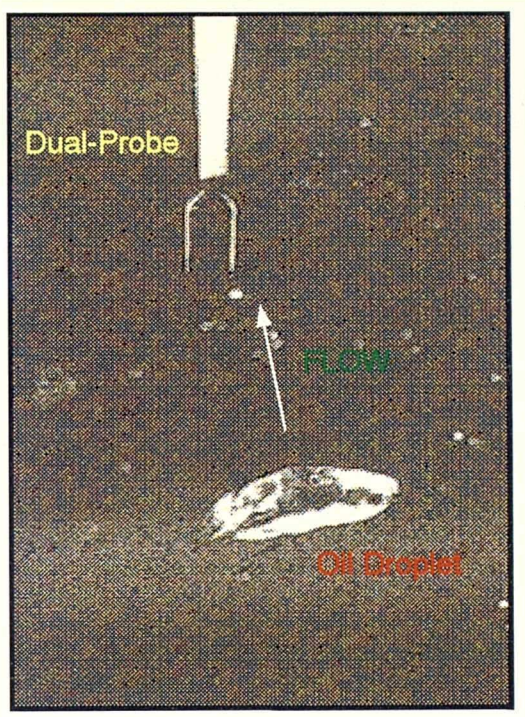

Figure 4.6: Motion of an oil droplet in the small test section

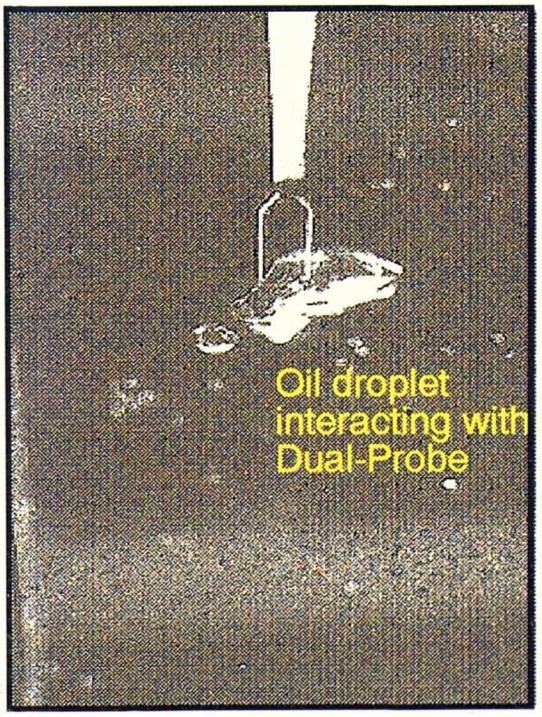

Figure 4.7: Interaction of an oil droplet with the dual probe

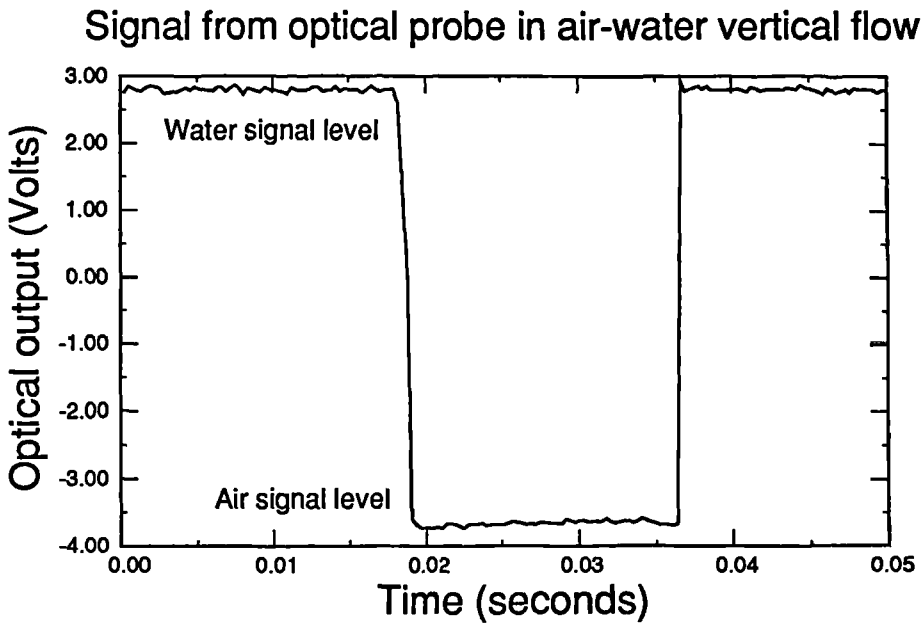

Figure 4.9: Detection of an air bubble passing an optical probe

From the two optical signals presented, both the oil and air levels fall below the water level. The optical fibre core, oil, water and air have refractive indices of 1.4805, 1.436, 1.33 and 1.00 respectively. With reference to Figure 4.10, by examining the refractive indices of the these fluids, one would assume that the levels detected by the optical probe should be oil, water and air respectively instead of water, oil and air. In order to investigate the reason for the oil and air signal levels falling below the water signal level, the 'wetting' effects on the optical probe tip were investigated. When a fibre tip is wetted by a fluid, it is assumed that a thin layer of fluid is always present on the tip which alters the reflective properties at the fibre tip.

The optical probe distinguishes between oil,water and air by the reflective properties of the surrounding fluid. The basic theory of reflectance is given in Born and Wolf [1980] which will be described below. Consider a single interface i.e. the fibre tip is not wetted by any fluid. The amplitude of the reflection coefficient, r_{12} is given by:

$$r_{12} = \frac{(p_1 - p_2)}{(p_1 + p_2)} \tag{4.1}$$

where $p_1 = n_1 \cos\theta_1$ and $p_2 = n_2 \cos\theta_2$. At normal angle of incidence, $\theta_1 = 0$ hence $\cos\theta_1 = 1$ and $p_1 = n_1$. Equation 4.1, then becomes:

$$r_{12} = \frac{(n_1 - n_2)}{(n_1 + n_2)} \tag{4.2}$$

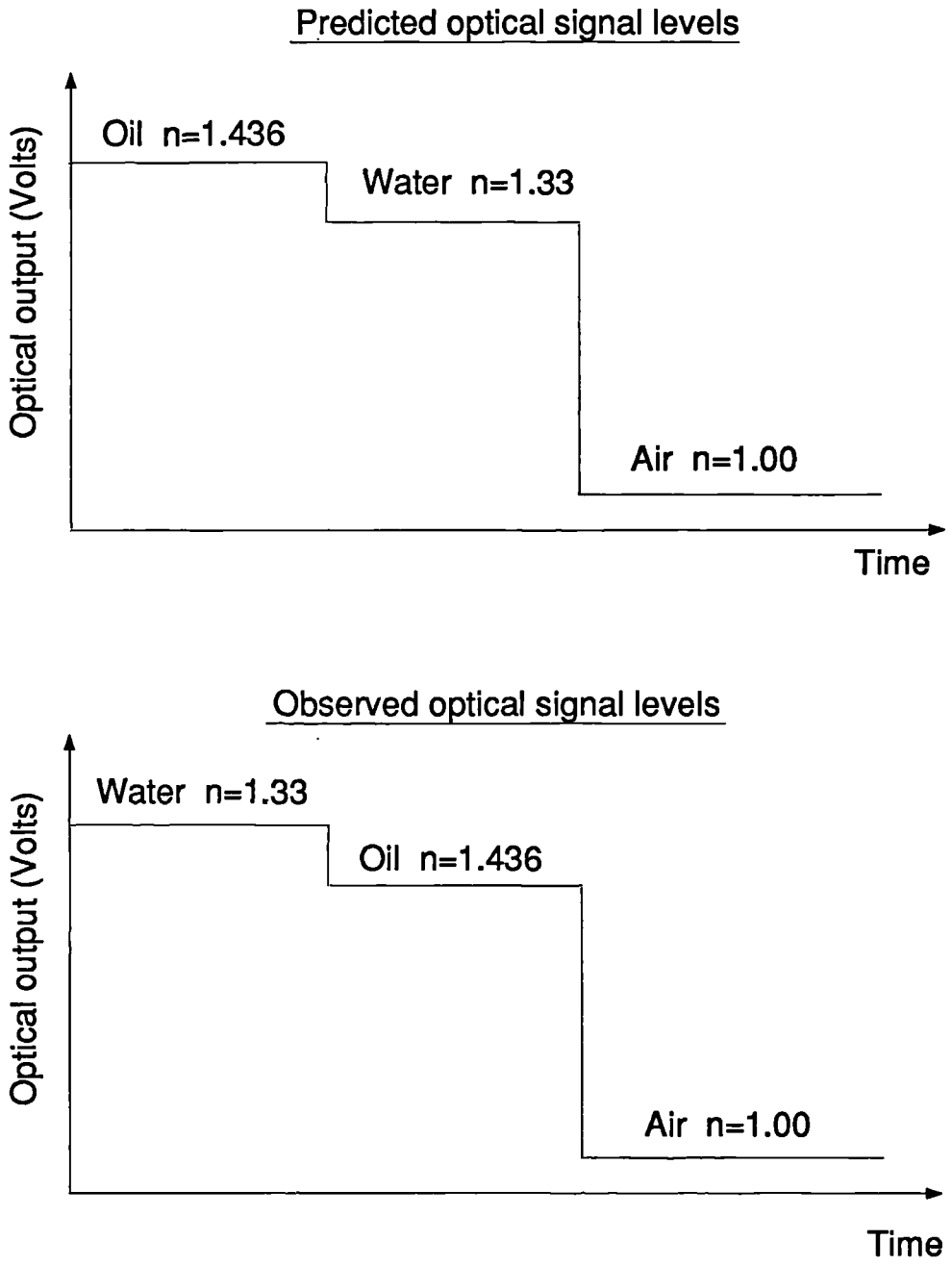

Figure 4.10: A schematic diagram showing observed and predicted signal levels corresponding to different refractive indices

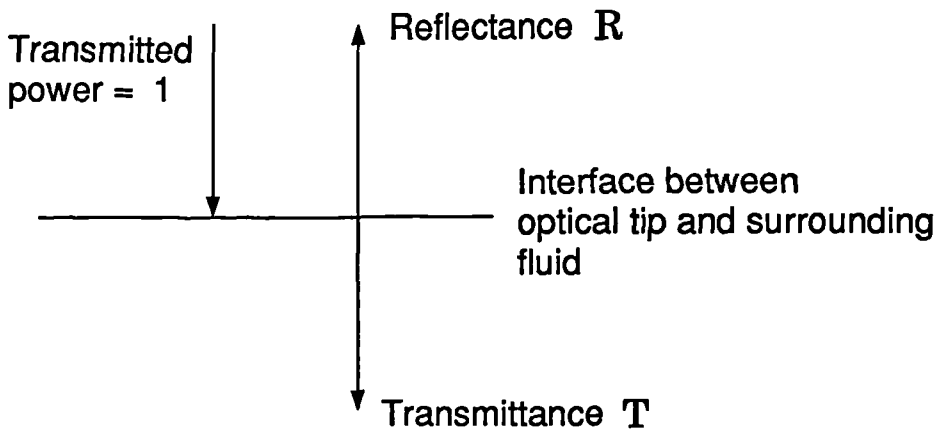

Figure 4.11: Diagram to explain reflectance

The reflectance $\mathcal{R}$ is given by the square of the modulus of the reflection amplitude i.e. $\mathcal{R} = |r|^2$; hence the reflectance for normal incidence is given by:

$$\mathcal{R}_{12} = \left(\frac{(n_1 - n_2)}{(n_1 + n_2)}\right)^2 \tag{4.3}$$

This is known as Fresnels Law (Born and Wolf [1980], Hecht and Zajac [1980]). With reference to Figure 4.11, consider that the power transmitted through the fibre is unity. Then the reflectance $\mathcal{R}$ is given by $1 - \mathcal{T}$, where $\mathcal{T}$ is the transmitted intensity or transmittance.

Now consider a thin film of fluid wetting the optical probe tip (see Figure 4.12). The amplitude of the reflection coefficient between the wetting fluid and the fluid, r_{23}, is given by:

$$r_{23} = \frac{(p_2 - p_3)}{(p_2 + p_3)} \tag{4.4}$$

where $p_2 = n_2 \cos\theta_2$ and $p_3 = n_3 \cos\theta_3$. At normal angle of incidence, $\theta_2 = 0$ hence $\cos\theta_2 = 1$ and $p_2 = n_2$. Equation 4.4, then becomes:

$$r_{23} = \frac{(n_2 - n_3)}{(n_2 + n_3)} \tag{4.5}$$

From Born and Wolf [1980], the reflectance $\mathcal{R}$ when a thin film is present on the optical tip, is given by:

$$\mathcal{R} = \frac{r_{12}^2 + r_{23}^2 + 2r_{12}r_{23}\cos 2\beta}{1 + r_{12}^2 r_{23}^2 + 2r_{12}r_{23}\cos 2\beta} \tag{4.6}$$

where β is given by:

$$\beta = \frac{2\pi n_2 h \cos\theta_2}{\lambda_0} \tag{4.7}$$

where h is the thickness of the wetting fluid and λ_0 is the wavelength of the light source.

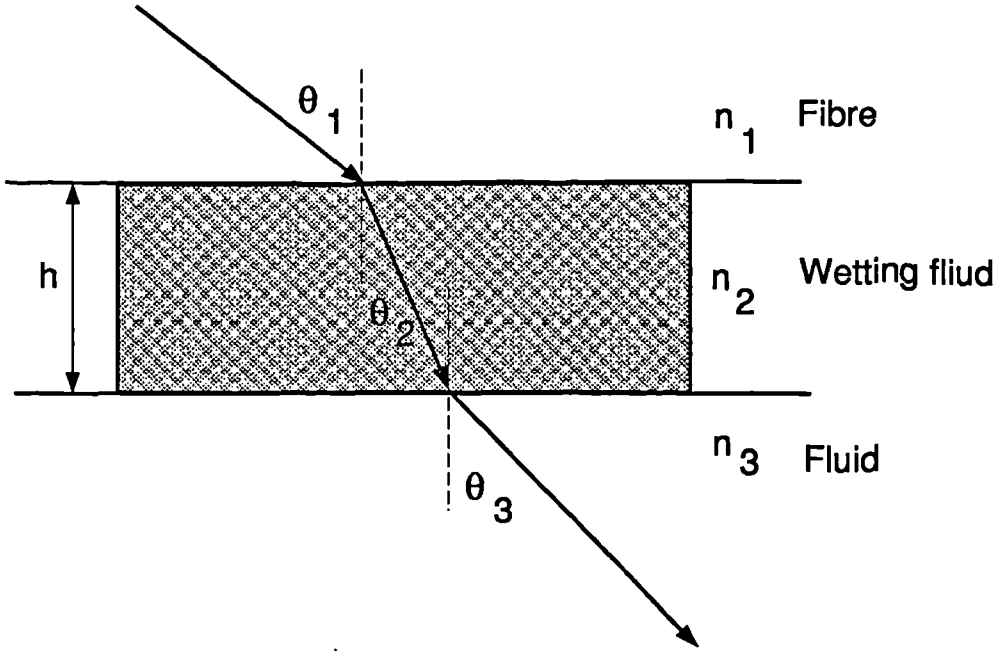

Figure 4.12: Diagram to show thin wetting film on optical tip

In order to understand why the optical signal levels decreased in the order of water, oil and air, (see Figure 4.10) the reflectance $\mathcal{R}$ was plotted against β using Equation 4.6. Figure 4.13 shows a plot of the reflectance $\mathcal{R}$ against β for a thin film of oil wetting the probe tip. The graph shows the different values of reflectance for the different media surrounding the oil wet probe tip. From the graph one can see that the reflectance increases as the refractive index of the media decreases. Hence from this plot, the probe tip is not oil wetted since the reflectance increases in the order of oil, water and air.

A similar exercise was carried out with a thin film of water wetting the optical probe tip (see Figure 4.14). From the graph, one can see that observation from experiments and theory are valid for values of $\pi/4 \leq \beta \leq 3\pi/4$ i.e. the reflectance between these values increase in the order of water, oil and air. An interesting observation from this plot is that, for values of $\beta \leq \pi/4$ and $\beta \geq 3\pi/4$, the reflectance increases in the order of oil, water and air. Hence, critical values for β exist where the signal levels could reverse. It must be mentioned here, that this reversal of signal levels was not seen in any of the experimental data.

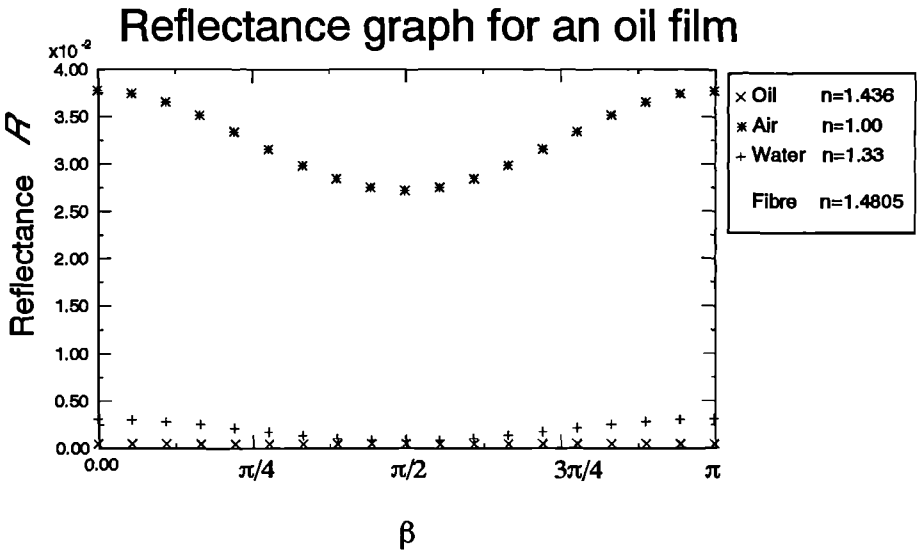

Figure 4.13: Plot of reflectance $\mathcal{R}$ against β for an oil wet probe tip

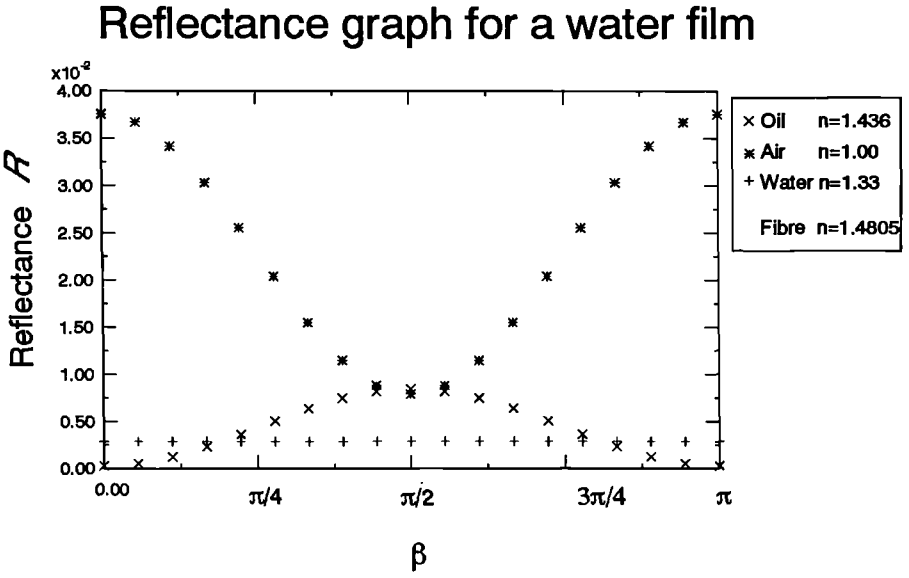

Figure 4.14: Plot of reflectance $\mathcal{R}$ against β for a water wet probe tip

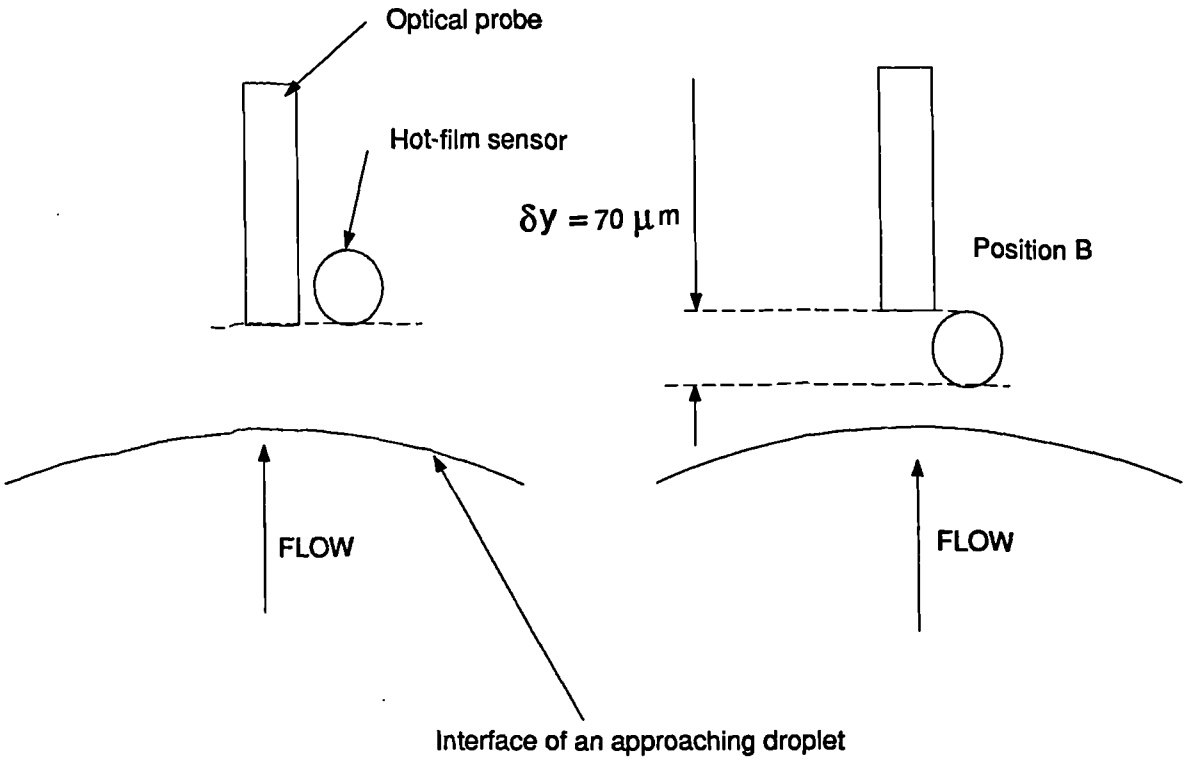

Figure 4.15: A diagram illustrating error in axial direction of positioning leading optical probe with respect to hot-film sensor

4.3.2 Testing of the hot-film and optical probe to measure continuous phase velocity

In order to justify the mapping of the optical signal onto the hot-film signal, feasibility tests were conducted to view the signals from the two probes. The errors in locating the leading optical probe in relation to the hot-film wire were also investigated. With reference to Figure 4.15, consider a 5mm diameter droplet approaching the hot-film sensor and the leading optical probe. The sampling rate was set to 8192Hz (see Section 5.4) so that each data point corresponds to a time increment of $122\mu s$. Let the droplet travel at $1ms^{-1}$ towards the probes and let the time at which the droplet comes into contact with the hot-film be t. If the optical probe was situated at position B , then the time taken before the droplet comes into contact with the optical probe will be at $t+70\mu s$; this is assuming that the droplet does not deform in shape. One can see that this time $(t+70\mu s)$ is less than the sampling rate, hence within a single data point resolution. However, consider the same droplet travelling at $0.1ms^{-1}$. Now the difference in time at which the interface comes into contact

with the optical probe will be $t + 700\mu s$. Hence the number of data points taken before the interface reaches the optical probe will be approximately 6. In order to calculate the total error in mapping the optical signal onto the hot-film signal, one has to estimate the time spent in the droplet. For a 5mm droplet travelling at $0.1 ms^{-1}$, the time spent will be 0.05seconds. Hence the total number of points recorded during the passage of the droplet will be 410. This will cause an error of 1.5% in the estimation of the start and finish points on the hot-film signal which is non-cumulative. In order to minimise the error in estimating the start and the finish positions, the distance between the optical probe and the hot-film sensor was measured. If the optical probe tip was above or below the hot-film wire then, the optical probe was re-aligned with the wire.

Another source of error was encountered when considering the radial distance (δz) between the optical probe and the hot-film sensor. With reference to Figure 4.16, consider a droplet, of a known size, approaching the two probes and making contact with the probes off centre. As illustrated, the droplet will make contact with the optical probe before making contact with the hot-film sensor. The time difference between impacting the optical probe and the hot-film probe is dependant on the droplet size and the position at which the probes made contact with the droplet. Figure 4.17, illustrates how the impact distance ($X2$) varies with the distance before impacting the second probe (Δy). Consider a 5mm droplet travelling at $1 ms^{-1}$ which impacts the probes at position $X2 = 2$mm; the value of Δy is 0.125mm, assuming that $\delta z = 0.1$mm. This will cause an error of 5% in mapping the optical signal onto the hot-film signal. If one was to increase the distance δz to 1mm, then for the same conditions as above, the error will be 32%. It is therefore important to minimise the radial distance between the optical and the hot-film probe. Figure 4.18 shows the recorded signals from the leading optical probe and the hot-film probe during the penetration of an oil droplet (the distance $\delta z = 0.1$mm). One can see that the signal at which the droplet impacts and leaves the optical probe matches with the hot-film signal.

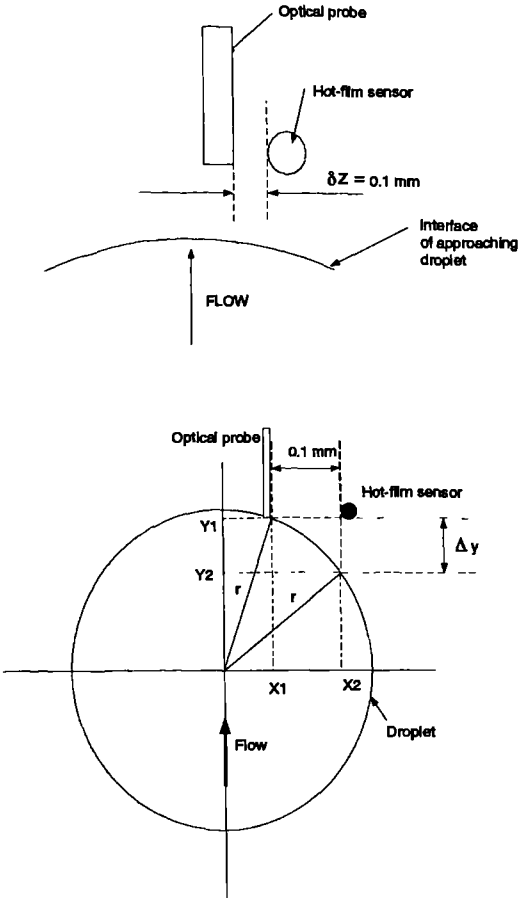

Figure 4.16: A diagram to aid error analysis for positioning the optical probe radially in relation to the hot-film sensor

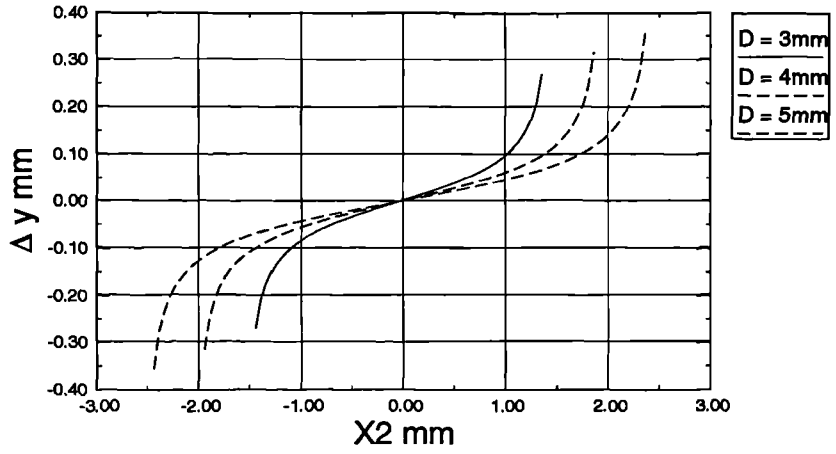

Figure 4.17: A diagram illustrating how Δy varies with X2

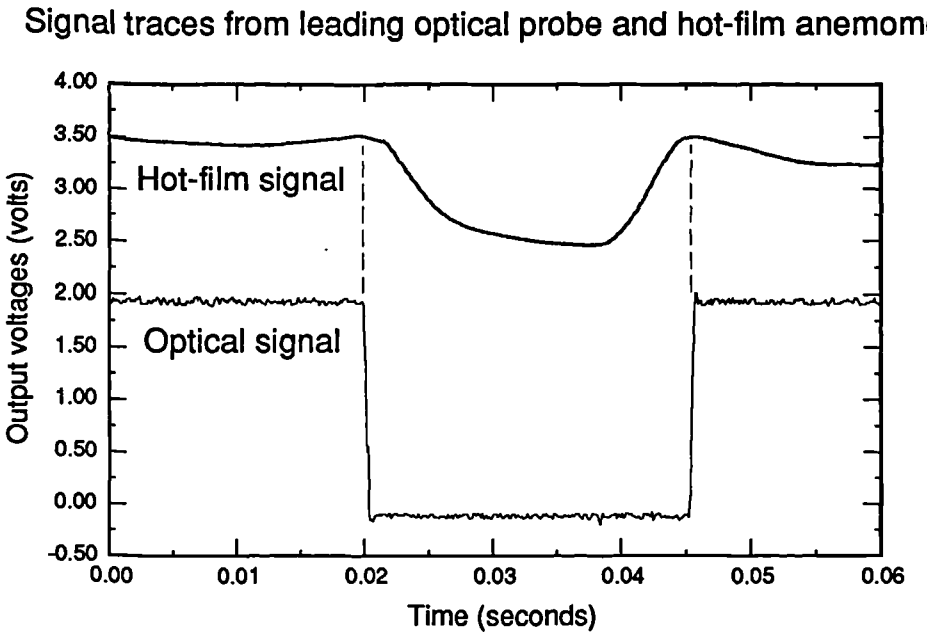

Figure 4.18: Signals from the leading optical probe and the hot-film anemometer

4.3.3 Testing of dual optical probe for measuring the dispersed phase velocity

The dispersed phase velocity is calculated by using two axially separated optical probes. The analysis of the optical signals to produce the dispersed phase velocity is given in Section 6.2.2. In order to aid the signal analysis, tests were carried out in the small test section (see Figure 4.5). Oil droplets were injected at the base and the signals from the optical probes were recorded on a computer. Two methods of analysing the optical signals were employed. These were the 'time of flight' method and the 'cross correlation' method. In all of the cases below, consider the twin optical signal outputs from a single droplet interaction. The tangential distance, δx, between the two optical probes was set to 0.1mm and the axial distance, y, was set to 1mm. With reference to Figure 4.19, consider a droplet of oil approaching the two probes axially and along the probes centre-line (CASE1). As the droplet penetrates probe 1, the signal will decrease down to a certain value determined by the reflective properties of the oil. At some time δt later, the oil droplet penetrates the second probe (probe 2). If the droplet penetrates both the probes along the probe centre-line, then the residence times Td_1 and Td_2 will be equal; this is assuming that the droplet does not deform after penetrating the first probe. Using the time of flight method, the droplet speed is given by the ratio of the distance between the two probes and the time delay δt. The time delay is calculated from the leading edges of the signals as shown. The trailing edge of the signals was also considered and is further discussed in Section 6.2.2.

Now consider a droplet approaching the probes off centre (CASE2). Let the droplet size be 5mm diameter and have a speed of $1ms^{-1}$. Using Figure 4.17 let $X2$ = 2mm hence Δy= 0.125mm. This implies that the true distance travelled by the droplet before impacting the second optical probe (probe 2) is 1.125mm. Using the time of flight method to calculate the droplet speed, the error in the speed calculation will be -11%. If the tangential distance, δx, between the two optical probes was increased to 1mm, the error in the speed calculation will be -87% for the same droplet size and position of impact. It is therefore crucial to minimise the tangential distance between the two optical probes.

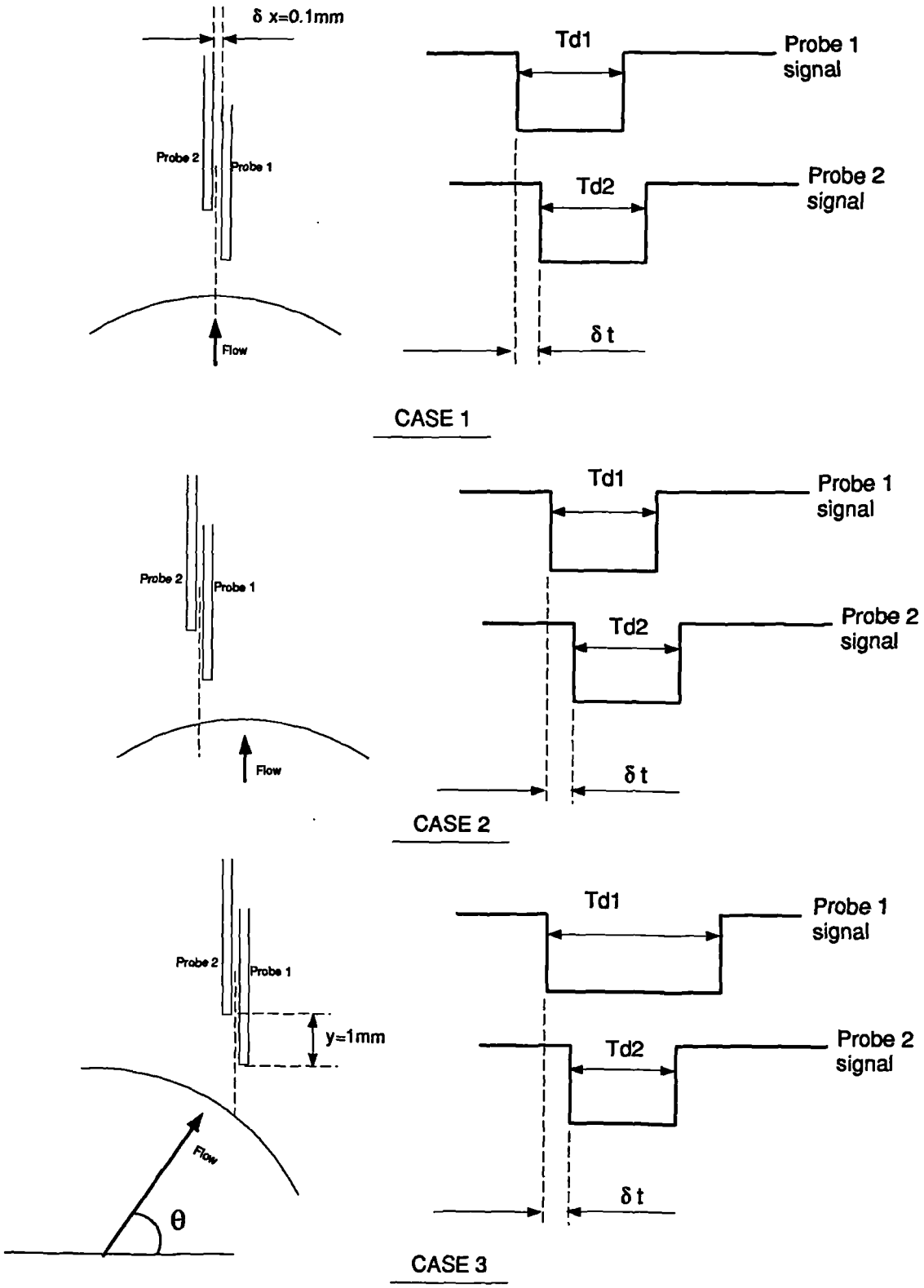

Figure 4.19: Possible sources of errors when calculating the dispersed phase velocity

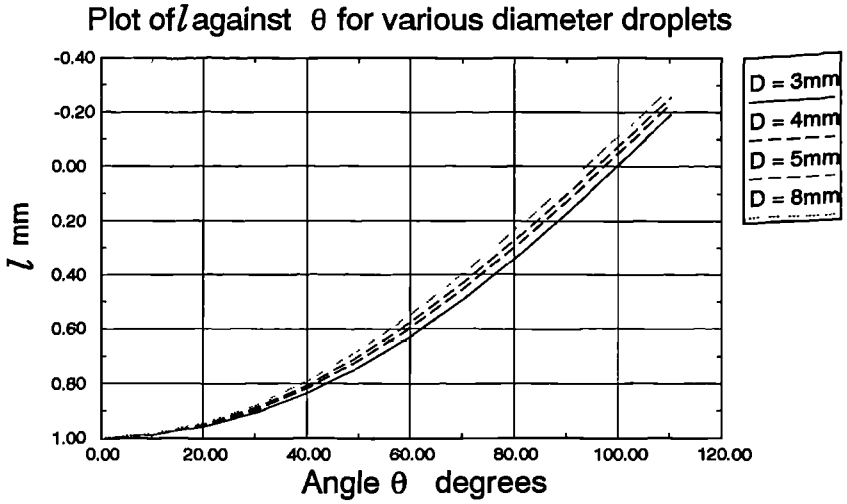

Figure 4.20: Plot to show possible errors in calculating the droplet speed

Another source of error occurs when a droplet approaches the optical probes at an angle θ (CASE3). There will be an error in the speed calculation since the distance travelled before impacting the second probe is not necessarily equal to the distance between the two optical probes (y). The residence times will not necessarily be equal because different chordal lengths will be cut by the two probes. It should be noted that, the cross correlation method utilises the entire time series to calculate the droplet speed whereas the time of flight method utilises the time difference between the leading and trailing edges of the signals. Since the true distance travelled is not known and that different residence times are encountered from the two signals, the error in calculating the droplet speed using the cross correlation method is larger than that for the time of flight method. This statement is verified in Section 6.2.2. In order to quantify the errors involved in measuring the dispersed phase velocity, an impact analysis theory was computed. This can be seen in Appendix A.

Figure 4.20 shows how l (distance travelled by droplet before impacting probe 2) varies as a function of θ (angular trajectory of droplet). As an example, consider a 5mm diameter droplet travelling at $1ms^{-1}$ and impacting the two probes at an angle of $\theta = 40°$. The distance travelled would be underestimated by 20% and hence the speed would be overestimated by 25%.

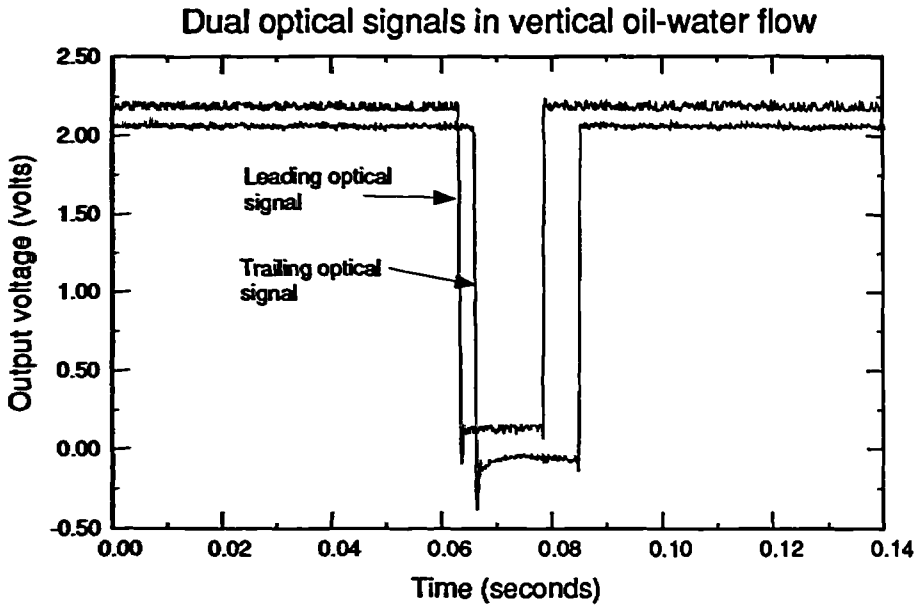

Figure 4.21: Optical signals in vertical oil-water flow

Figure 4.21, shows the recorded signals from the two optical probes in vertical oil-water flow. The baseline level for leading optical probe (probe 1) was adjusted for presentation purposes. From the illustration one can see that there is a definite time difference between the two signals and that the residence times for the two signals are not equal. This shows that two different chordal paths were cut by the optical probes. Also one can see that overshoots exist in the optical signal. These overshoots will be discussed in Section 6.2.1.

4.4 Final assembly of the dual probe

With reference to Figure 4.22, and recommendations made in Section 4.3, the assembly of the dual probe was carried out in three stages:

1. Initially, the two optical probes were adhered together with cyanoacrylate gel. This type of glue appears to be insoluble to oil. An offset of approximately 1mm (y) was set between the two fibres. A distance of 1mm was chosen because, the probes had to be close enough to detect the same droplets; other authors had used 1mm separation between probes e.g. Moujaes [1987], Dantec dual sensor probe (see Figure 2.5). The tangential distance δx between the two optical probes was kept to a minimum so as to minimise the error in computing the oil velocity (see Section 4.3.3). All of the distances between the two probes were measured using a light microscope with a micrometer gauge.

2. The hot film anemometer was placed into its holder (see Figure 4.1).

3. The two optical probes were glued (using cyanoacrylate gel) onto the stem of the hot-film anemometer. This part of the assembly was delicate and important in order to achieve the distances as in Figure 4.22. The final assembly operation was carried out under a large, well lit, microscope. Since the leading optical probe was to be used to de-convolve the hot-film signals, the optical probe had to be in line with the sensing area of the hot-film anemometer (see Section 4.3.2). By angling the two optical probes towards the hot-film sensor, a 0.1mm gap between the wire and the leading optical probe was achieved. A gap of approximately 0.1mm was chosen in order to minimise the error in the continuous phase measurement. This source of error is discussed in Section 4.3.2.

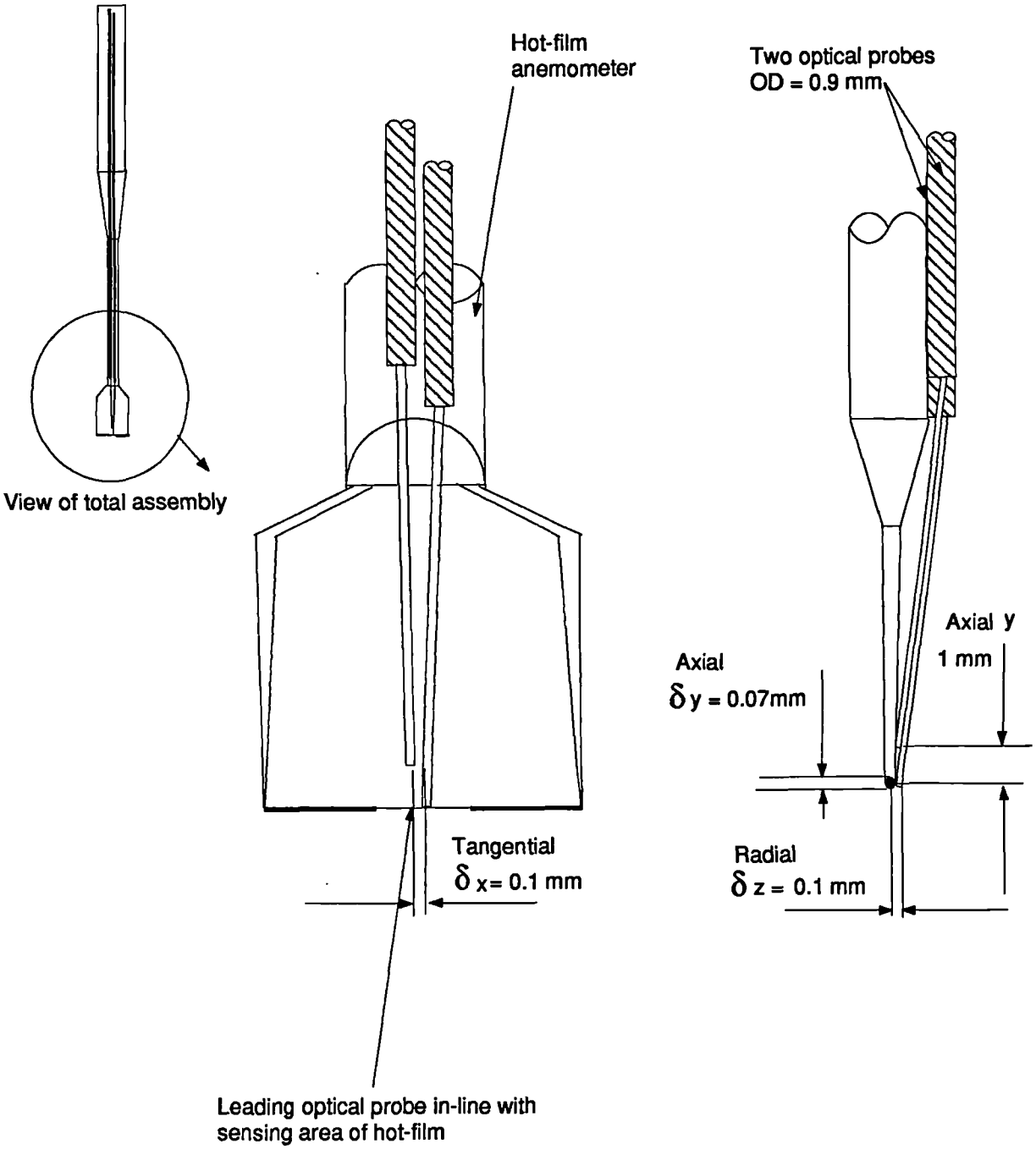

Figure 4.22: Assembly of the dual probe

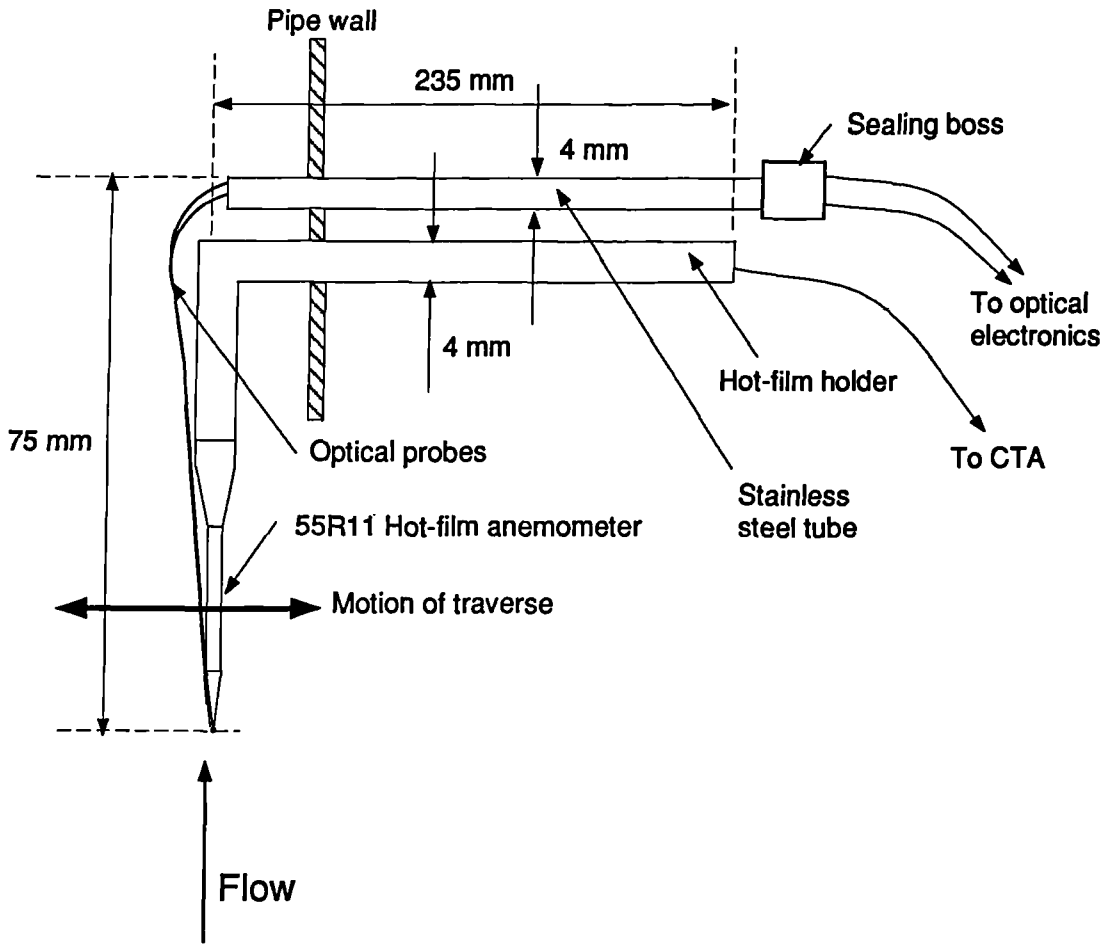

Figure 4.23: Final assembly of the dual probe

In order to use the dual probe in the flow loop (see Chapter 5), the final assembly was designed (see Figure 4.23). The inside diameter of the pipe section on the flow loop was 78mm. To mount the dual probe into the section, right-angled probe holders were used. The right angled holders orientated the dual probe axial to the flow. The holder for the hot-film is a standard commercial part whereas the optical probe holder was specially manufactured. Both the holders were 4mm diameter tubing. A photograph of the dual probe can be seen in Figure 4.24.

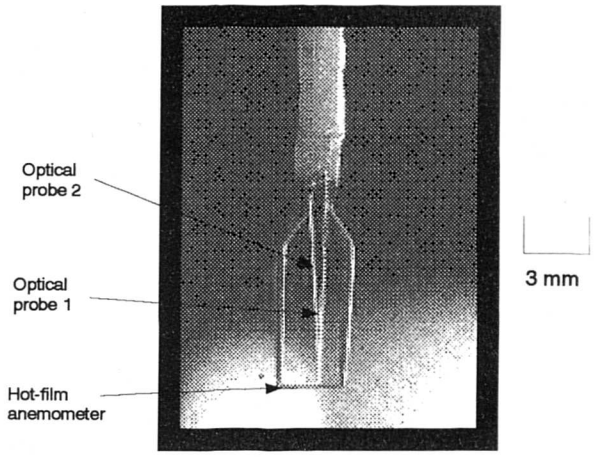

View on Arrow A

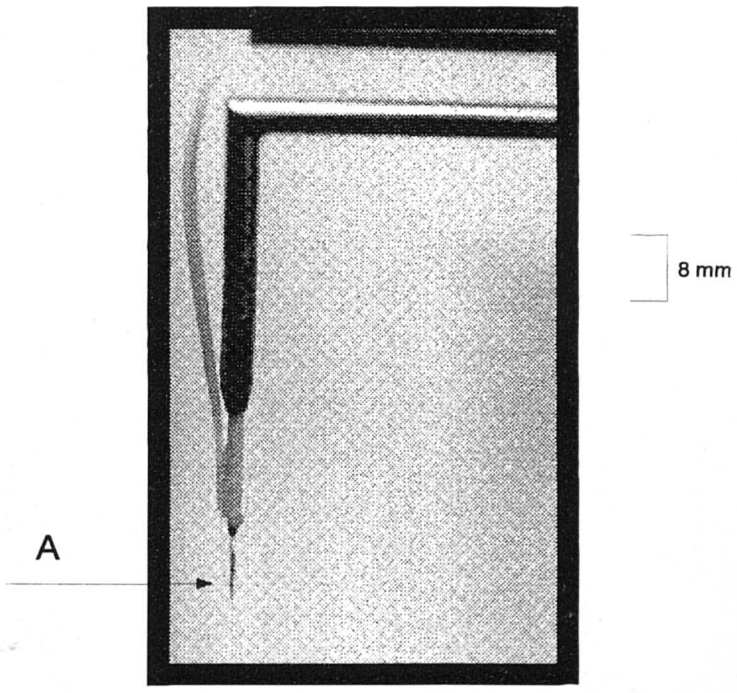

Figure 4.24: Photograph of dual probe sensing area and final assembly

4.5 Calibration of the hot-film anemometer

The calibration of the hot-film probe was carried out in the flow loop (see Chapter 5) with water as the flowing medium. The flow loop was always vertical when calibrating the hot-film probe. Measurements of the sensor output E and the water superficial velocity U_{ws} (see Section 5.3.1) were recorded for different radial positions of the probe. From the values of E and U_{ws}, the calibration constants were derived assuming a velocity-voltage relationship. The most commonly used relationship is King's law ([1914], [1915]) given by Equation 2.4 in Section 2.2. It should be noted that, the calibration model (Equation 2.4) does not include the overheat ratio (γ) (Equation 4.9). The overheat ratio provides the calibration constants $\mathcal{A}$ and $\mathcal{B}$ with a low sensitivity to the changes in ambient temperature of the flow, Smits [1991]. This is desirable because the data acquisition often extended over considerable time periods with a 1°C to 2°C change in flow temperature. It was found that calibrations made before and after experiments were more consistent with the model:

$$E^2 = \gamma(\mathcal{A} + \mathcal{B}\sqrt{U}) \tag{4.8}$$

than if a more simpler model was used (Equation 2.4 which does not use a temperature effect i.e. γ). If the overheat ratio was not included in the model, the voltage output from the hot-film E, would have been overestimated by 1.5%. The over heat ratio is defined as:

$$\gamma = \frac{R - R_o}{R_o} \tag{4.9}$$

where R is the sensor resistance at temperature T and R_o is the sensor resistance at ambient temperature T_o. The sensor resistance R at temperature T may be calculated from the manufactures data [Dantec] supplied with the probe. The sensor resistance is given by:

$$R = R_{20}[1 + \alpha_r(T - 20)] \tag{4.10}$$

where R_{20} is the sensor resistance at 20°C and α_r is the temperature coefficient of the hot-film probe.

The procedure for calibrating the hot-film probe was to set up a known volumetric flowrate of water and then to traverse the probe across a single diameter. The sensor voltage output E and the water volumetric flowrate Q_w (where Q_w is measured by a turbine meter, see Equation 5.1) were recorded

for 15 seconds at eight measuring positions (see Section 5.5.1) across the pipe diameter. Once the acquisition was complete for all eight positions, the water flowrate was increased to another known value and the sensor voltage was recorded. For each calibration test, eight different flowrates were investigated ranging from $2\text{m}^3\text{hr}^{-1}$ to $14\text{m}^3\text{hr}^{-1}$.

From Equation 4.8, let E_{ij} be the i^{th} time sample recorded at a probe position j, at some total flowrate, Q_w. The instantaneous velocity at position j, and time i, may be expressed as:

$$U_{ij} = \frac{1}{\mathcal{B}^2}\left(\frac{E_{ij}^2}{\gamma} - \mathcal{A}\right)^2 \tag{4.11}$$

The mean velocity at position j, is given by averaging Equation 4.11 over the number of samples, N_i:

$$\bar{U}_j = \frac{1}{N_i}\sum_{i=1}^{N_i}\frac{1}{\mathcal{B}^2}\left(\frac{E_{ij}^2}{\gamma} - \mathcal{A}\right)^2 \tag{4.12}$$

If it is further assumed that the mean velocity profile is radially symmetrical, then the total flowrate Q_w can be obtained by multiplying the mean water velocity, $\bar{U}_j$, by the annular area A_j associated with each probe position, hence:

$$Q_w = \sum_{j=1}^{N_j}\left\{\frac{A_j}{N_i}\sum_{i=1}^{N_i}\frac{1}{\mathcal{B}^2}\left(\frac{E_{ij}^2}{\gamma} - \mathcal{A}\right)^2\right\} \tag{4.13}$$

From Equation 4.13, all the quantities apart from the calibration constants, $\mathcal{A}$ and $\mathcal{B}$, are known or measured. A single traverse at a given flowrate yields an equation with two unknowns. If two different flowrates were investigated, then the two unknowns may be formulated. The final form of the Equation 4.13 was used in the analysis and is given by:

$$\mathcal{B}^2 = \left\{\sum_{j=1}^{N_j} A_j\left(\frac{1}{N_i\gamma^2}\sum_{i=1}^{N_i}E_{ij}^4 - \frac{2\mathcal{A}}{N_i\gamma}\sum_{i=1}^{N_i}E_{ij}^2 + \mathcal{A}^2\right)/Q_w\right\} \tag{4.14}$$

By solving Equation 4.14 for different flowrates, the calibrations constants $\mathcal{A}$ and $\mathcal{B}$ were determined. The hot-film probe was calibrated before and after experimental tests. Due to ambient temperature differences from day to day, the calibration constants were seen to have different values. The values for the calibration constants are as follows:

- $\mathcal{A} = 190 \pm 11\%$ and
- $\mathcal{B} = 240 \pm 11\%$

which were taken over a period of two years.

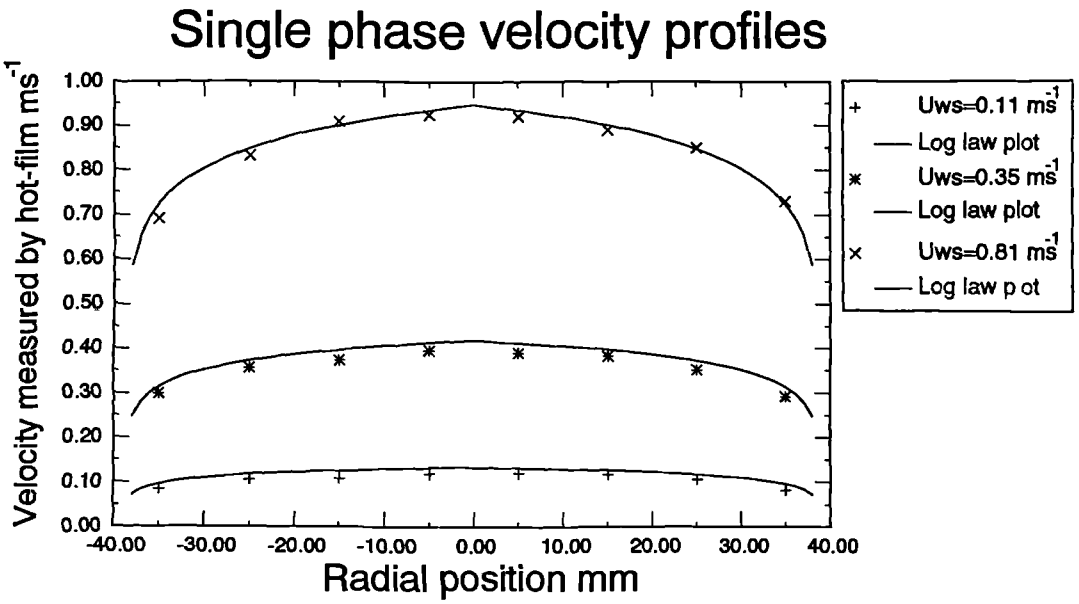

Figure 4.25: Example of velocity profiles for single phase water flows

The calibration constants were then substituted into Equation 4.12 to determine mean velocities for each measurement position across the pipe diameter. An example of the velocity profiles is given in Figure 4.25. Superimposed onto each measured water velocity profile, are the single phase 'log law' profiles calculated using Equation 4.17. At low water superficial velocities ($U_{ws} < 0.4\text{ms}^{-1}$), the log law predicted profiles and the experimental data do not compare as well at higher velocities. This will be further discussed in Section 5.3.2. As a check with different water flowrates, the water velocities (calculated from the hot-film) calculated at different positions across the pipe diameter were integrated over the pipe section to yield a mean flowrate, Q_{wp}, which is given by:

$$Q_{wp} = \sum_{j=1}^{N_j} A_j \bar{U}_j \tag{4.15}$$

The mean flowrate Q_{wp} was compared to the actual flowrate as measured by a turbine meter, (Q_w). The following equation was used for the comparison:

$$e_a = Q_{wp} - Q_w \tag{4.16}$$

where e_a is the actual error. Figure 4.26 shows a plot of the mean flowrate (reference turbine meter) against the actual error of reading e_a. The maximum relative error between the two readings is of the order of -8%, hence the confidence in velocities derived from the probe calibration cannot be better than this figure.

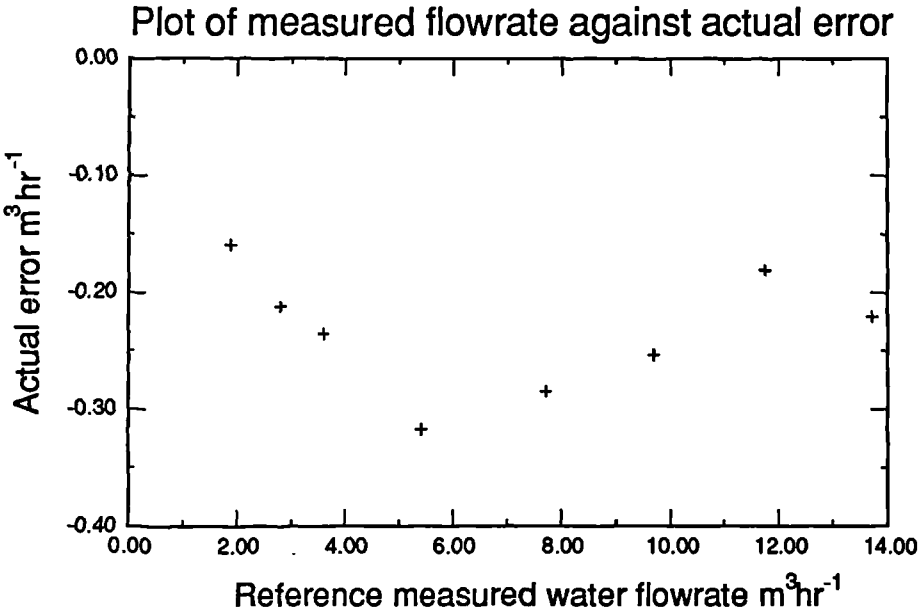

Figure 4.26: Plot of measured flowrate against actual error

4.6 The dual split-film probe

The dual split-film probe is another combination of a thermal anemometer (split-film anemometer) and optical probes. One of the advantages of using a split-film anemometer is that it provides both the magnitude and the direction of the continuous phase velocity normal to the split-film sensor.

4.7 Assembly of the dual split-film probe

With reference to Figure 4.27, the disadvantage of using this type of split-film anemometer was that it could not be held in a right-angled probe holder similar to that of the dual probe. A straight probe holder had to be utilised with film 1 being the leading sensor and film 2 the trailing sensor. Since the split-film probe was to be orientated perpendicular to the flow, the optical probes had to be mounted in such a way so that the tips of the probes were axial to the flow. Photographs of the dual split-film probe can be seen in Figure 4.28. During the construction of the dual split-film probe, similar considerations to that of Section 4.3.2 and Section 4.3.3 were applied.

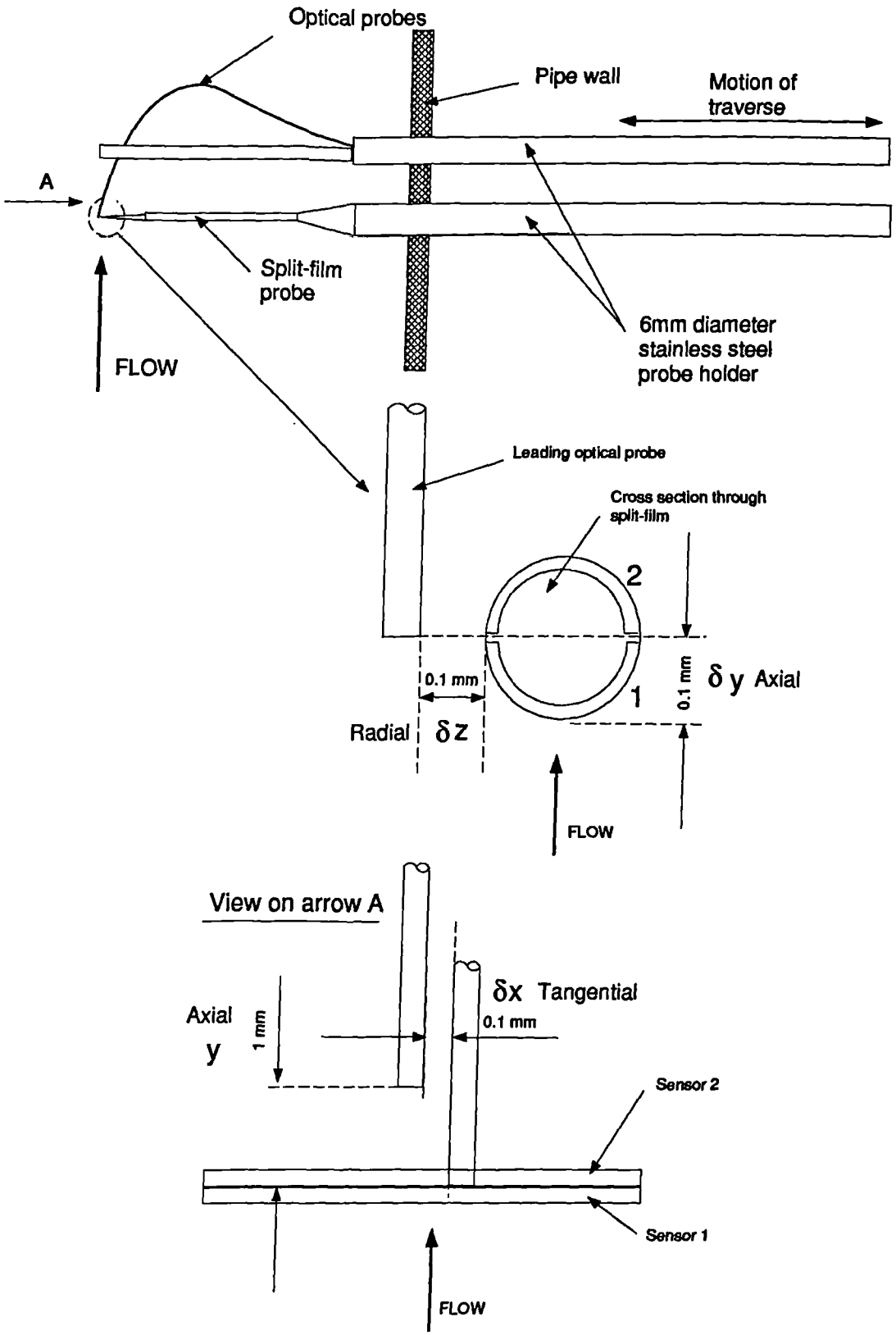

Figure 4.27: Assembly of the dual split-film probe

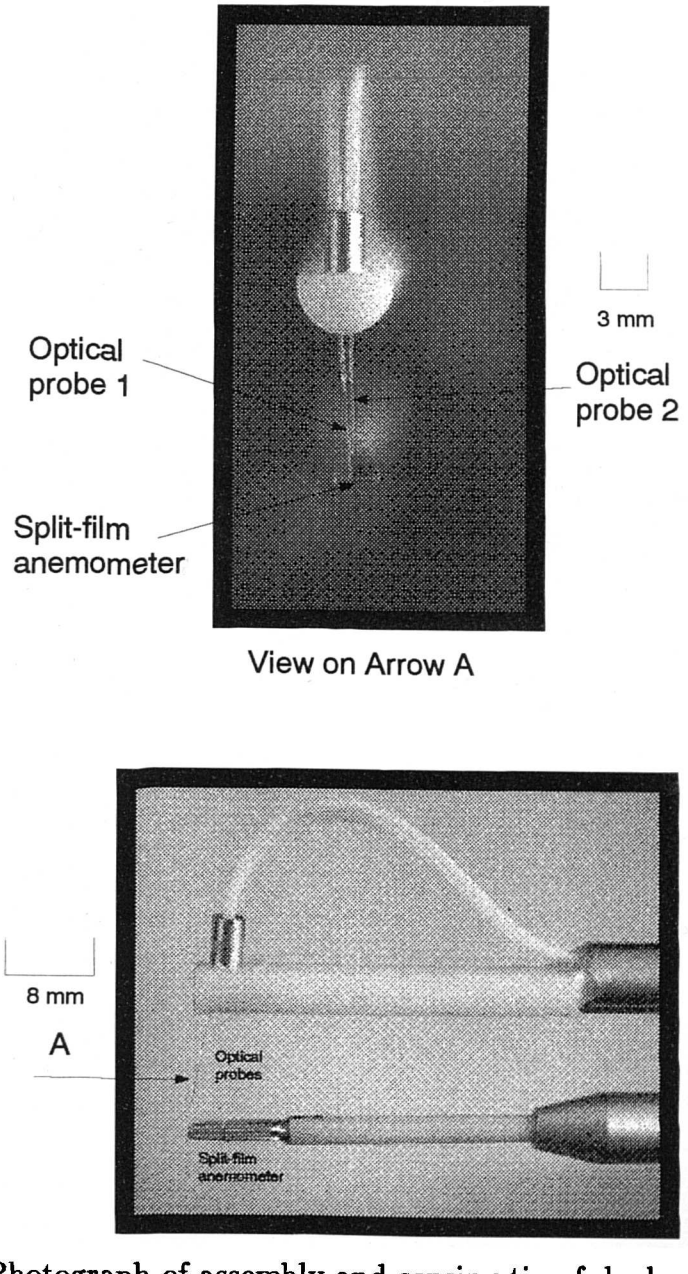

Figure 4.28: Photograph of assembly and sensing tip of dual split-film probe

4.8 Calibration of the split-film anemometer

The calibration of the split-film anemometer was conducted in a different manner to the hot-film anemometer. Split-film anemometers combine two nearly identical hot-film sensors on a common quartz fibre. The principle of operation of split-film probes is the variation of the local heat transfer with flow angle or flow pitch for a heated cylinder in a flow. Since the calibration of such probes is dependant on the direction of the flow, relative to the axis of the probe, a test section for calibrating the probe was designed. A diagram of the test section can be seen in Figure 4.29.

The test section was designed so that the split-film probe could be calibrated in the flow loop (see Chapter 5). In order to calibrate the sensors against flow angle, a flexible sealing joint was utilised; this allowed the axis of the probe to be pitched relative to the upward flow. The maximum and minimum pitch angles obtained using the flexible seal joint was $+40°$ and $-40°$ respectively. With reference to Figure 4.30, the split-film probe had to be calibrated between $+90°$ and $-90°$. By utilising a straight probe holder, the orientation of the sensors could be pitched from $+40°$ to $-40°$ and a right angled probe holder was used to obtain pitch angles from $\pm 50°$ to $\pm 90°$. One of the limitations of calibrating this type of probe in the flow loop was that it could not be traversed across the pipe section at a known pitch angle hence, the calibration was carried out with the probe positioned at the centre of the pipe. An assumption had to be made to relate the mean velocity across the pipe section to a centre line velocity.

With reference to Aziz and Govier [1972], the fully developed flow 'log law' equation was used to determine the centre line velocity, U, which is as follows:

$$U = \sqrt{\frac{\tau_w}{\rho}} \left\{ \frac{1}{k} \ln \left(\frac{y}{\nu} \sqrt{\frac{\tau_w}{\rho}} \right) + C \right\} \tag{4.17}$$

where τ_w is wall shear stress, ρ is the density of water, k was taken to be 0.41, y is the distance from the wall to the centre of the pipe, ν is the kinematic viscosity of water and C is a constant equal to 5.5.

Boerner and Leutheusser [1984], provided a novel calibration technique to be used with split-film probes. A 60m long water filled towing channel was used to calibrate the split-film probe. The split-film probe was attached to a shaft on a stepper motor which could pitch the fibre axis through 180°. The stepper motor was a part of the instrument carriage which was used to tow the split-

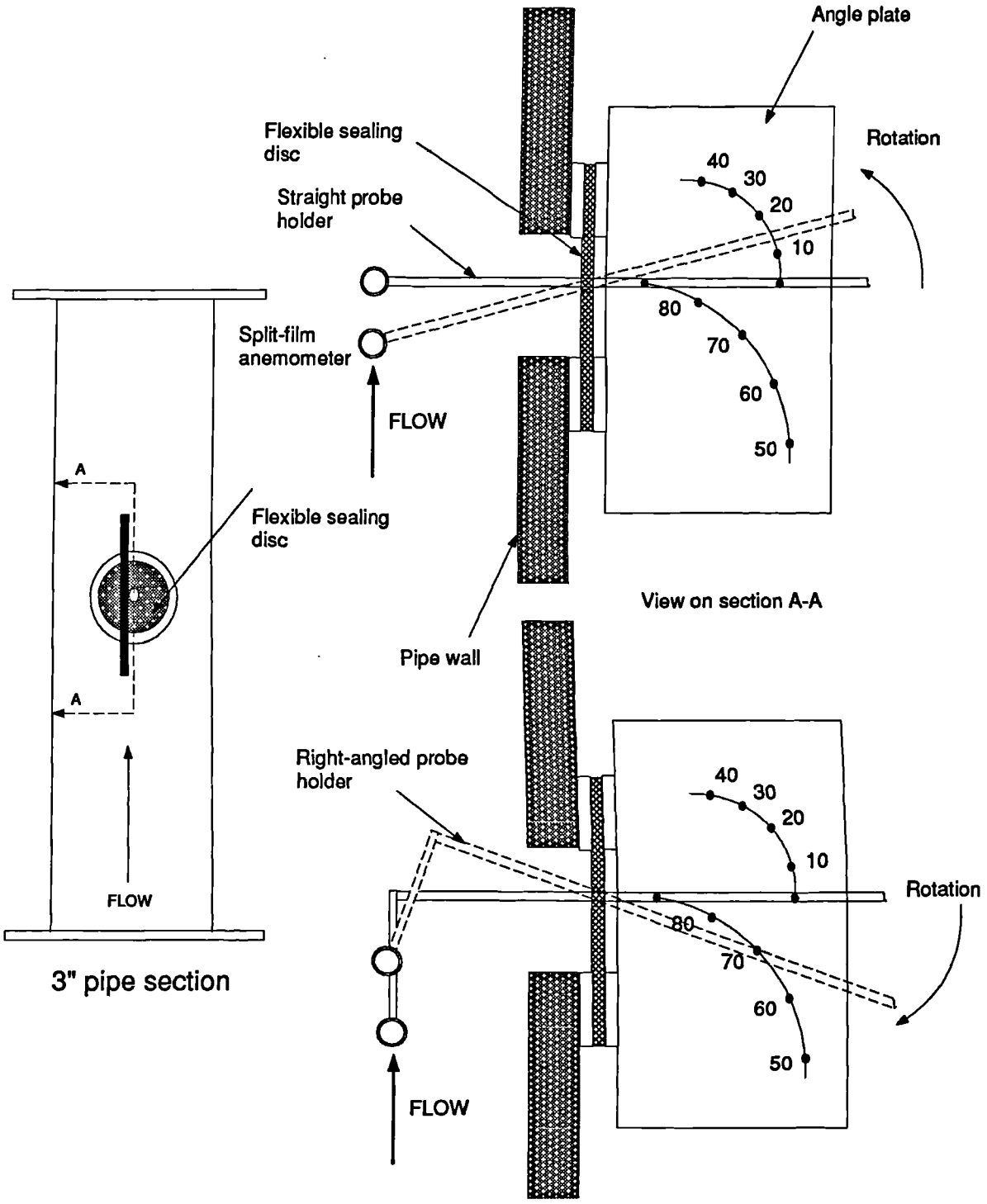

Figure 4.29: Test section used for calibrating the split-film probe

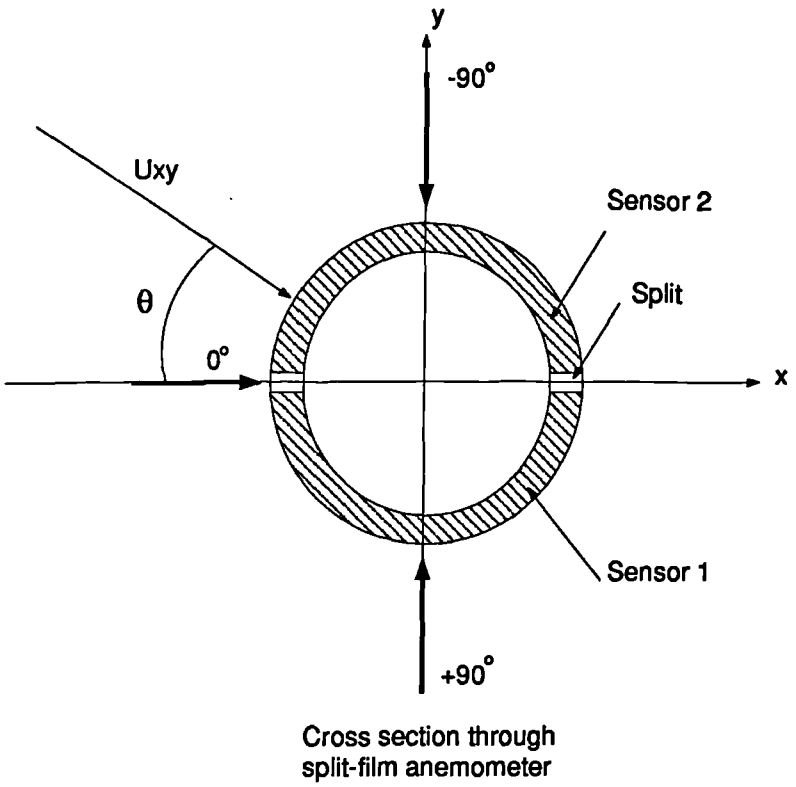

Figure 4.30: Orientation diagram for the split-film probe

film through the water filled channel up to $3ms^{-1}$. Boerner and Leutheusser stated that the sum of the heat transfer from the two sensors depends only on the velocity, while the difference depends on both the velocity and flow angle in the plane perpendicular to the two sensors. In order to calibrate the split-film, they described the heat transfer from the sensors in terms of the Nusselt number Nu:

$$Nu = \frac{E^2}{lR_w k\Delta T} \tag{4.18}$$

where E is the output of the sensor, l is the length of the sensor, R_w is the sensor resistance, k is the thermal conductivity of water and ΔT is the temperature difference between the probe and the fluid. Hence, the sum of the sensor outputs is given by:

$$\sum Nu = Nu_1 + Nu_2 = f(U_{xy}) \tag{4.19}$$

where Nu_1 corresponds to sensor 1, Nu_2 corresponds to sensor 2 and U_{xy} is the resultant instantaneous velocity in the xy plane (see Figure 4.30). The function $f(U_{xy})$ represents the first of two required calibration functions.

The second function, $g(\theta, U_{xy})$, required to calibrate the split-film probe is given by:

$$\Delta Nu = Nu_1 - Nu_2 = g(\theta, U_{xy}) \tag{4.20}$$

where θ is the flow angle. In order to calculate the flow angle, θ, Boerner and Leutheusser produced a single function:

$$\theta = \sin^{-1}\left(\frac{\Delta Nu}{\Delta Nu_{max}}\right)^h \tag{4.21}$$

where ΔNu_{max} is given by Equation 4.20 when $\theta = +90°$ and h is determined experimentally. Unfortunately, Boener and Leutheusser did not suggest a value for h. The value of h can be determined by rearranging Equation 4.21, hence:

$$\ln \sin\theta = h.\ln\left(\frac{\Delta Nu}{\Delta Nu_{max}}\right) + C \tag{4.22}$$

where C is a constant.

The procedure for calibrating the split-film probe was to set up a known water velocity and to measure the voltage outputs E_1 and E_2 from both sensors. Pitch angles from $+90°$ to $-90°$ in steps of $10°$ were investigated for mean velocities ranging from 0.05ms^{-1} to 1.05ms^{-1}. The sum of the Nusselt numbers (see Equation 4.19) for both sensors were plotted against centre line velocities for different pitch angles (see Figure 4.31). The second calibration curve was a plot of the difference in Nusselt numbers against the centre line velocity (see Figure 4.32) and finally Figure 4.33 shows a plot of ΔNu against θ using Equation 4.20. Using Equation 4.22, the determined value of h was 0.83 ± 0.02. One of the limitations of using the split-film anemometer was that it could not be calibrated before and after each experimental test. Since the calibration of this probe was time consuming it was decided to calibrate the probe after five experimental tests.

A check of the calibration of the split-film was carried out in the flow loop. A similar routine for the testing of the calibration of the hot-film anemometer (see Section 4.5) was used for the split-film anemometer. Eight measuring positions across a diameter were investigated in single phase vertical water flow. The velocity at a measuring position in the pipe section was calculated by using Figure 4.31. Examples of velocity profiles are given in Figure 4.34. Superimposed onto the velocity profiles are the 'log law' (see Equation 4.17) generated velocity profiles for the tested velocities.

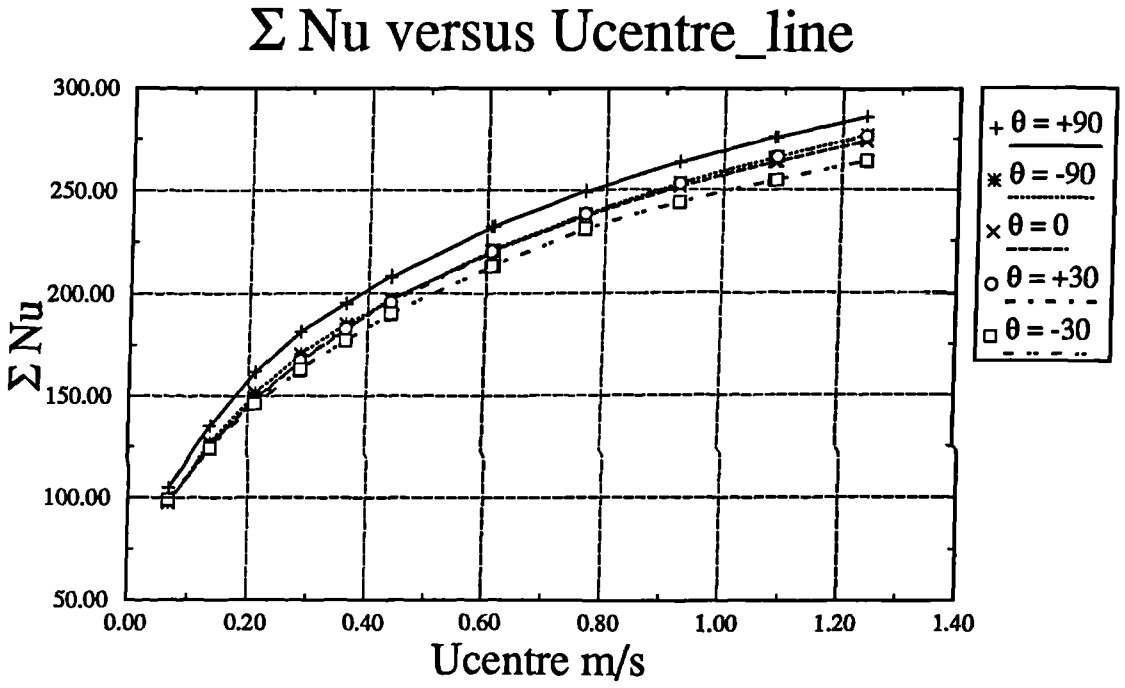

Figure 4.31: Sum of Nusselt numbers versus centre line velocity for single phase water

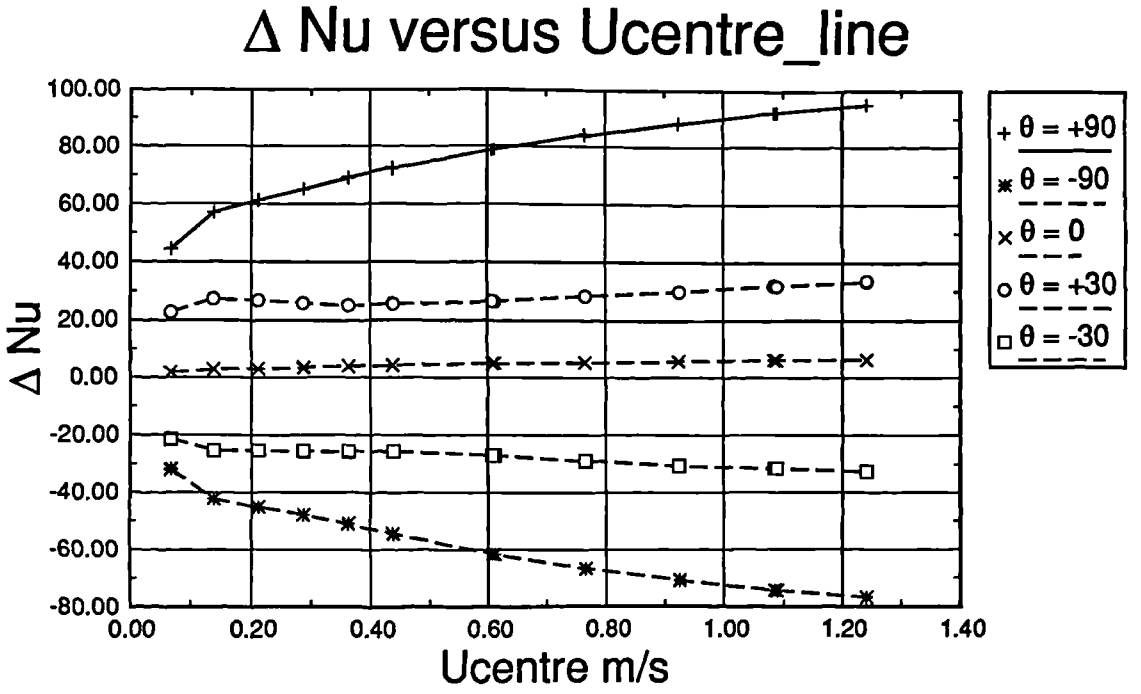

Figure 4.32: Difference of Nusselt numbers versus centre line velocity for single phase water

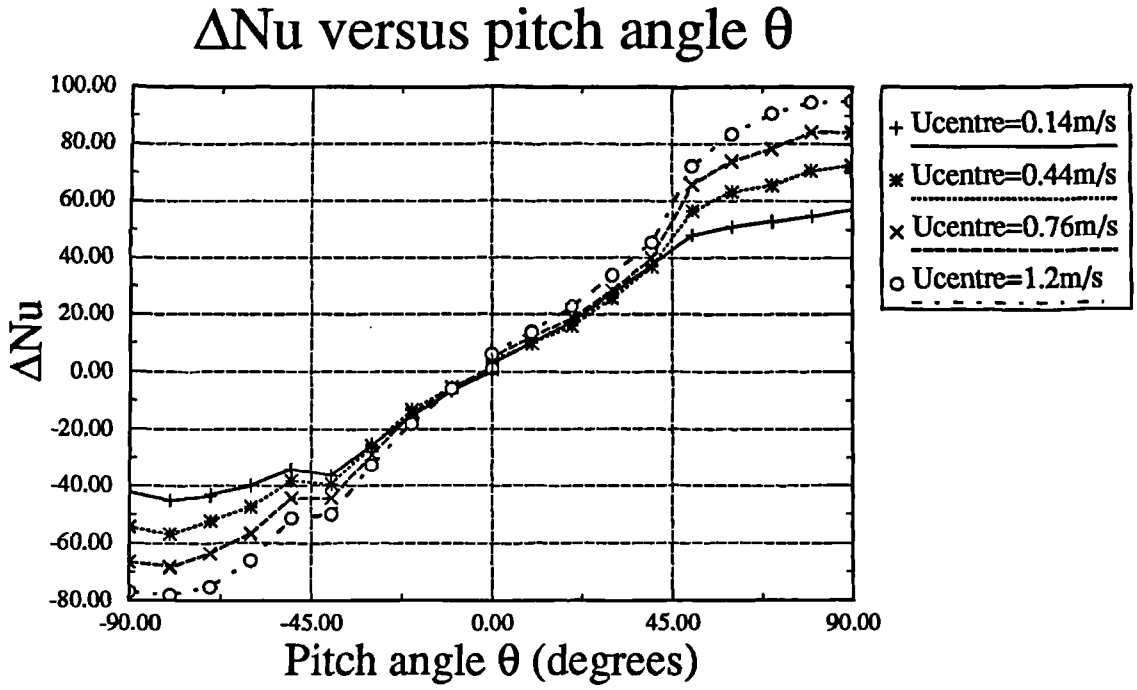

Figure 4.33: Difference of Nusselt numbers versus pitch angle for single phase water

As one can see, the experimental velocity profiles compare well with the predicted log law profile for velocities greater than 0.5ms^{-1}. However, at velocities lower than this value the comparison was unsatisfactory. A similar result was attained when calibrating the hot-film anemometer (see Section 4.5). This is further discussed in Section 5.3.2. By integrating the position velocities over the cross sectional area of the pipe, the mean flowrate (calculated from the probe) was calculated (see Equation 4.15). The mean flowrate as calculated by the split-film probe was then compared to the reference water turbine meter reading. The maximum relative error of reading was -7%, hence the confidence in the velocities as derived from the split-film cannot be better than this. Figure 4.35 shows a plot of the water turbine reference reading against the actual error of reading e_a (see Equation 4.16).

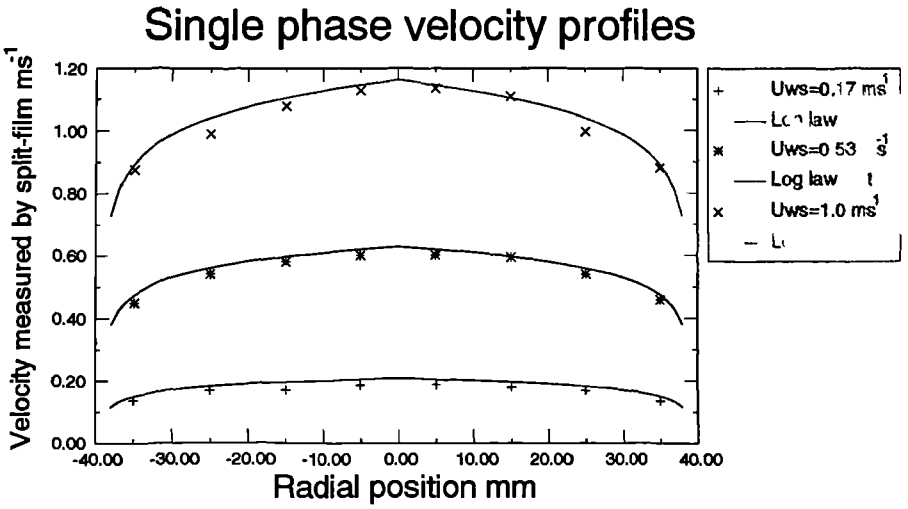

Figure 4.34: Examples of velocity profiles for single phase water flows

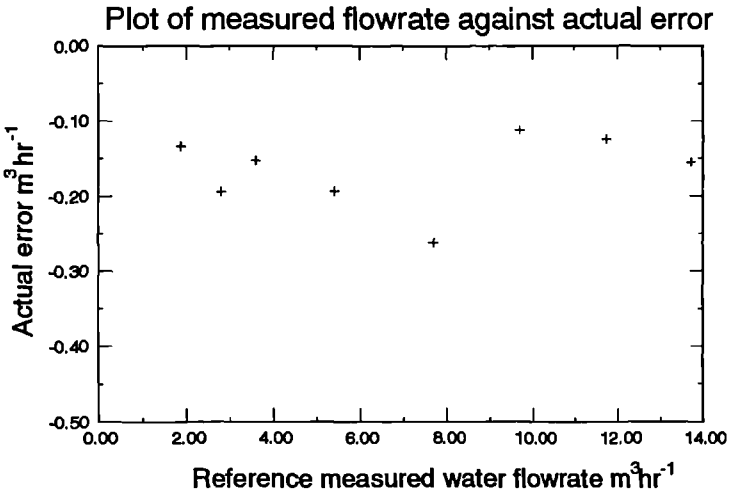

Figure 4.35: Plot of measured flowrate against actual error

Chapter 5

Experimental apparatus and procedure

5.1 Introduction

In this chapter, the experimental apparatus and procedure used for conducting the main series of tests using the dual probe and the dual split-film probe are described. In order to guide the reader through this chapter, a block diagram has been implemented with all the key headings. With reference to Figure 5.1, this chapter is divided in three parts. These are the experimental apparatus, the experimental procedure and the experimental investigations. Taking each section in turn, the experimental apparatus describes the multiphase flow loop where all of the experiments were carried out. This includes the reference measurements taken during the experiments in order to compare the dual probe results with the reference meter readings. The traversing mechanism used to 'map' the probes across the pipe section is described. Finally, the data acquisition procedure is described.

The experimental procedure section describes the initial tests carried out with the dual probe in the flow loop. These were performed to determine the number of measuring positions and sampling rates required to give satisfactory results. The final procedure for acquiring data from the entire dual probe experiments is described.

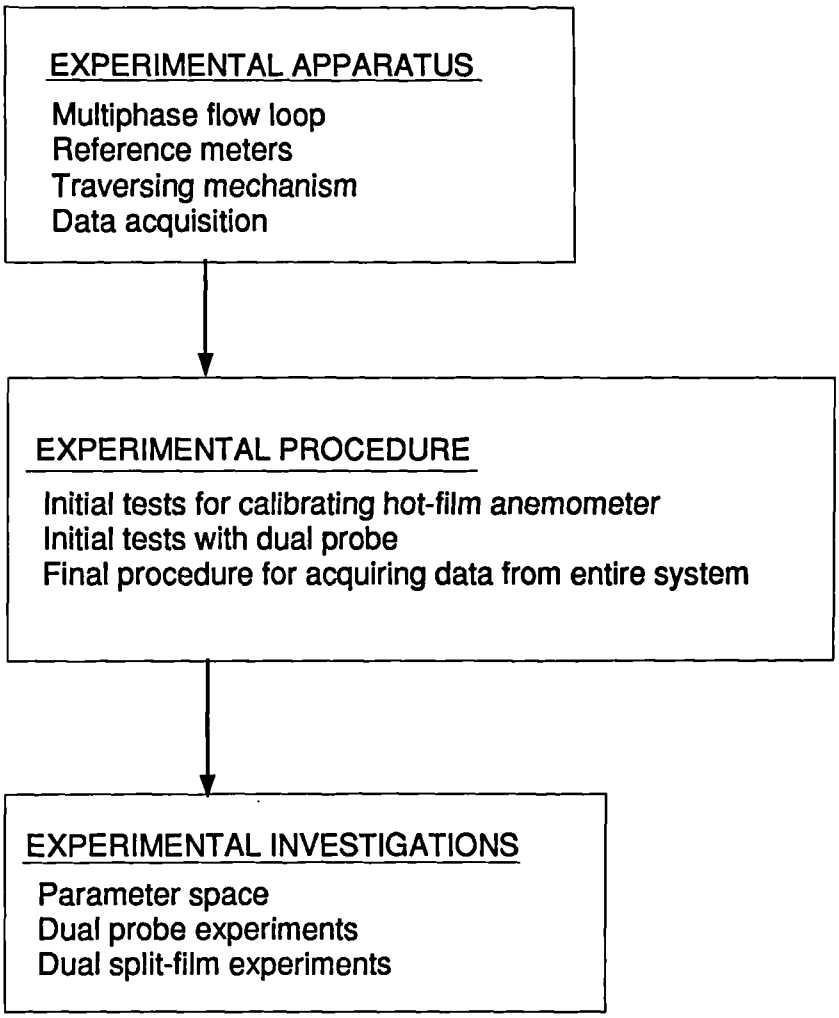

Figure 5.1: Block diagram to show the structure of this chapter

The final section, the experimental investigations, describes the parameter space over which the data from both the dual probe and the dual split-film probe were taken. The experimental investigations are given in a tabulated form.

5.2 Experimental apparatus

The testing of the dual probe and the dual split-film probe were carried out in the 3 inch (nominal diameter) multiphase flow loop based at the laboratories of Schlumberger Cambridge Research. The main feature of the flow loop is that it is inclinable between 0° and 45° to the vertical. The flow loop is capable of delivering three phase oil (kerosene)-water-air flows. Within the

scope of this work, only oil-water flows were investigated using the probes. The flow loop is a 'closed' loop where the oil and water are continually re-circulated. A diagram of the multiphase flow loop can be seen in Figure 5.2. A photograph of the flow loop can also be seen in Figure 5.3. The flow loop in this picture has been deviated to an angle of 15° from the vertical. A $3m^3$ separator is used to store the water and oil. Water and oil are pumped via separate centrifugal pumps through separate turbine meters. For both the oil and water phases, two turbine meters for each phase were provided. The small turbine meter (19mm diameter) had a flowrate range from 1 to $8m^3hr^{-1}$ and the large turbine meter (50mm diameter) had a flowrate range from 6 to $60m^3hr^{-1}$. The quoted accuracy and repeatability of the turbine meters are ±0.5% and 0.25% respectively. The turbine meters enable the volumetric flowrate, Q_l, of each liquid phase, to be calculated using calibration data for that particular turbine meter. The calibration data for the turbine meters provides a relationship between the frequency and the flowrate. The 'K' factor is defined as the ratio of the frequency output (Hz) to the flowrate (l/s) and has the units of pulses/litre. The K factor is usually given within the 'linear range' of the flow meter i.e. where the K factor remains within a pre-specified percentage of the mean K factor. Each turbine meter was supplied with its individual frequency to voltage (f/V) converter. The calibration of the frequency to voltage converters was performed on a tri-monthly basis to record the calibration drift. The drift varied from turbine meters ranging from 0.03% relative error on the small turbine meters to 0.6% relative error on the large turbine meters. These relative errors were well within the resolution of the acquisition system (see Section 5.4). By calculating the liquid volumetric flowrate Q_l, the single phase liquid velocity U_l, can be determined:

$$U_l = \frac{Q_l}{A} \tag{5.1}$$

where A is the cross sectional area of the test section. The liquid flow rates are set using a potentiometer controller which varies the pump speed. Computer control of the pump speed was also available and this was used during experiments.

Water is pumped into the working section, of the flow loop, via an inlet contraction as shown in Figure 5.2. Just upstream of the inlet contraction, a Mitsubishi (Miller [1983]) type flow conditioner was used to remove swirl and disturbed flow profiles. The flow conditioner was installed because two 90°

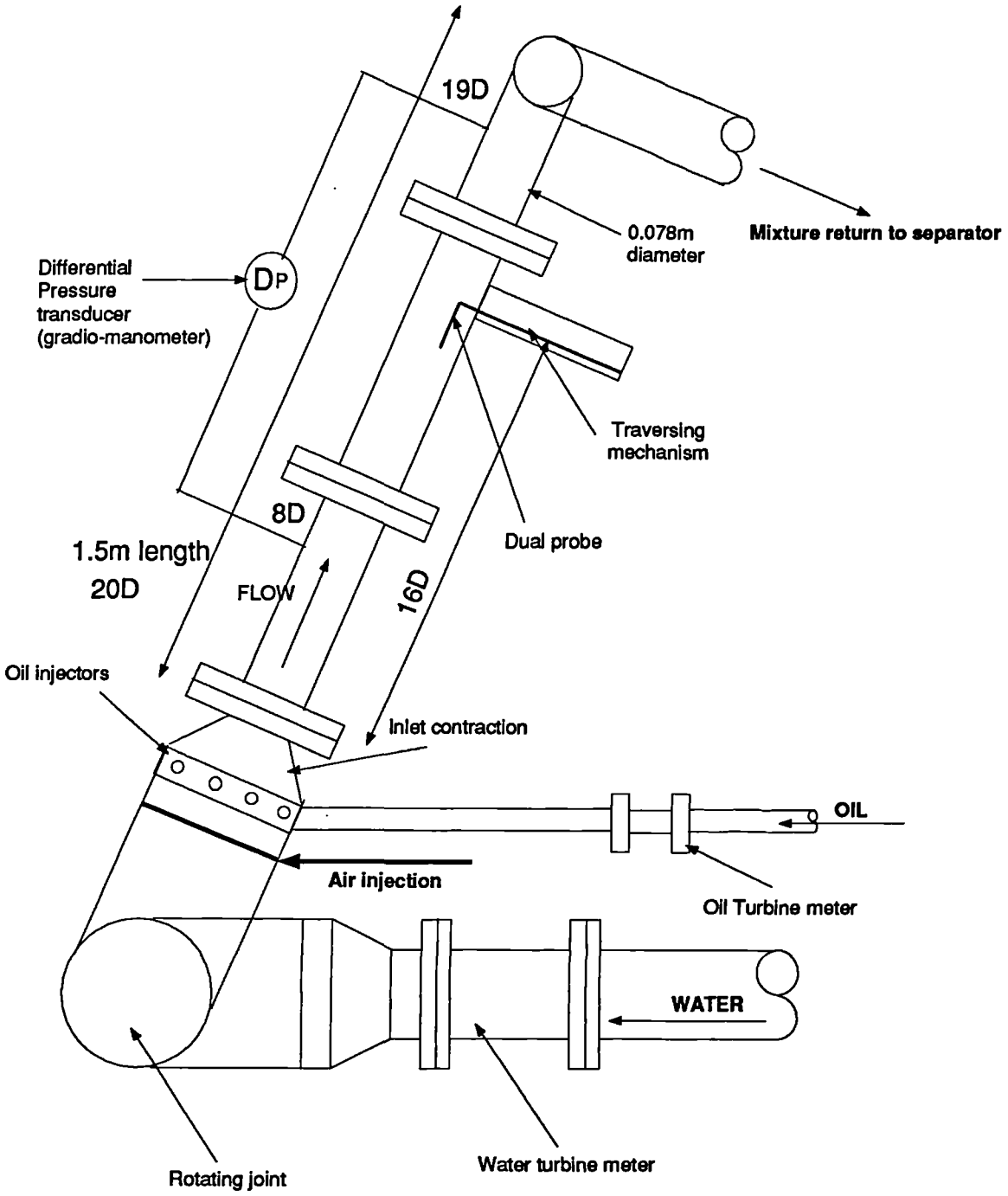

Figure 5.2: Diagram of the 3 inch multiphase flow loop

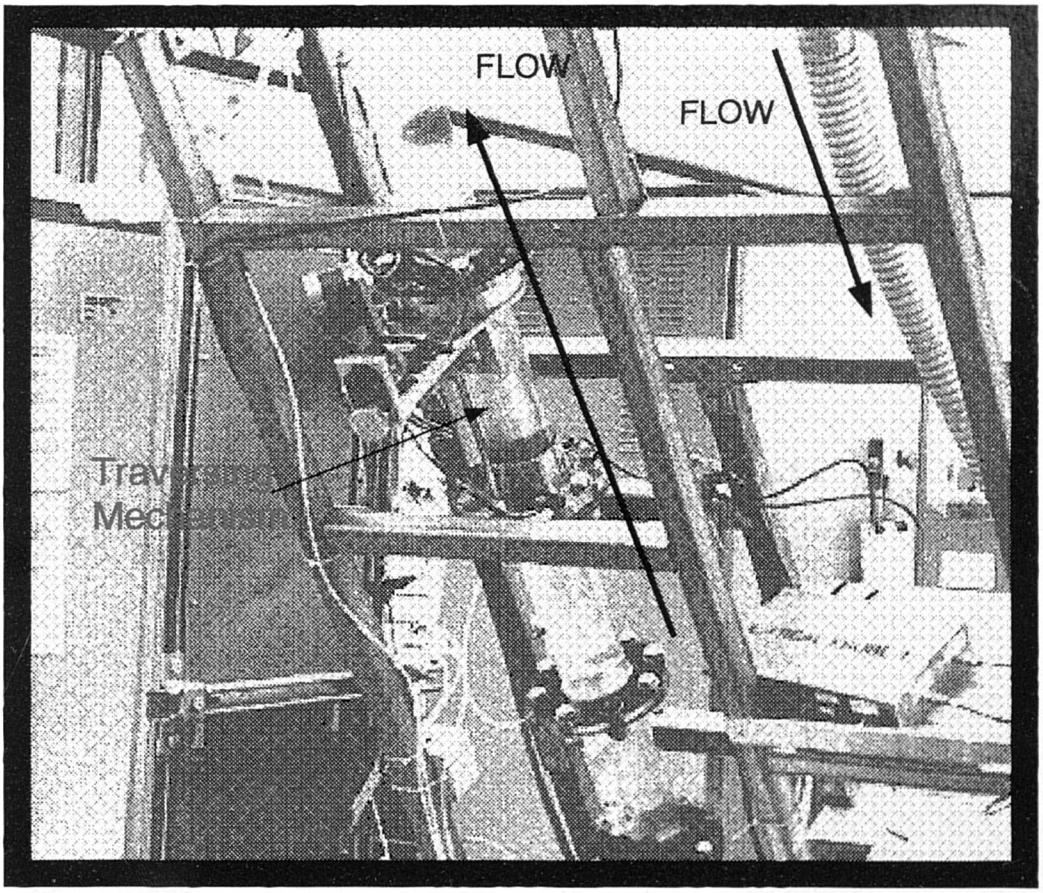

Figure 5.3: Photograph of the 3 inch multiphase flow loop

bends were encountered before reaching the inlet contraction. As a test, with the flow loop vertical, a single oil droplet was injected at the inlet contraction while flowing single phase water. It was observed that the oil remained in the centre of the pipe while flowing through the 1.5m working section. This showed that the swirl had been removed by the flow conditioner. During experiments, the oil was injected through port holes around the circumference of the inlet contraction, where both the water and oil are mixed. The mixture flows through the 78mm diameter perspex working section (perspex sections of pipe were used for flow visualisation).

The two phase mixture flows through a 1.5m length working section in which the gradio-manometer (used for measuring the differential pressure between two pressure tappings located on the pipe wall) is situated (see Section 5.3.2). A traversing mechanism, located between the pressure tappings of the gradio-manometer section, was used to traverse the probes across the working section (see Section 5.3.3). The flowing mixture then returns to the separator where the oil-water mixture is separated through knit-mesh cartridges.

5.3 Reference measurements

In the following subsections, the methods used to calculate the velocities and the average volume fraction in the working section are described. The equations given below relate to a two phase oil-water mixture with water as the continuous phase and oil as the dispersed phase.

5.3.1 Determining the superficial velocities in oil-water flows

In single phase flows, the mean velocity of the fluid is given by the ratio of the volumetric flowrate and the cross sectional area of the working section (see Equation 5.1). The mean velocity is calculated by measuring the flowrate with a turbine meter and calculating the cross sectional area of the test section. In two phase flows the cross sectional area of the flow is not entirely occupied by one phase. Consider a two phase oil-water flow with water as the continuous phase. The subscripts w and o refer to water and oil respectively.

From Aziz and Govier [1972] the average oil volume fraction, $\bar{\alpha}_o$, is given by:

$$\bar{\alpha}_o = \frac{A_o}{A} \tag{5.2}$$

where A_o is the area occupied by the oil and A is the total cross sectional area. By substituting Equation 5.2 into Equation 5.1, the oil superficial velocity U_{os} is given by:

$$U_{os} = \frac{Q_o \bar{\alpha}_o}{A_o} \tag{5.3}$$

hence

$$U_{os} = U_o \bar{\alpha}_o \tag{5.4}$$

where U_o is the actual velocity of oil. A similar exercise can be carried out to determine the water superficial velocity U_{ws}. From Equation 5.4, we may write:

$$U_{ws} = U_w \bar{\alpha}_w \tag{5.5}$$

where U_w is the actual velocity of water and $\bar{\alpha}_w$ is the mean water volume fraction. For a two phase oil-water system, the sum of the volume fractions for both phases must be equal to unity, hence:

$$\bar{\alpha}_o + \bar{\alpha}_w = 1 \tag{5.6}$$

By substituting Equation 5.6 into Equation 5.5, we get:

$$U_{ws} = U_w(1 - \bar{\alpha}_o) \tag{5.7}$$

In order to compute the superficial velocities, the mean oil volume fraction, α_o had to be calculated. This is described in Section 5.3.2. Another important definition is the homogeneous velocity, U_{hom}. This is given by the sum of the oil and water superficial velocities, hence:

$$U_{hom} = U_{ws} + U_{os} \tag{5.8}$$

5.3.2 Determining the volume fraction in the working section

For the purpose of providing a reference measurement, the mean oil volume fraction was determined by using a part of the test section i.e. the gradiomanometer, (see Figure 5.2) connected to a Honeywell differential pressure

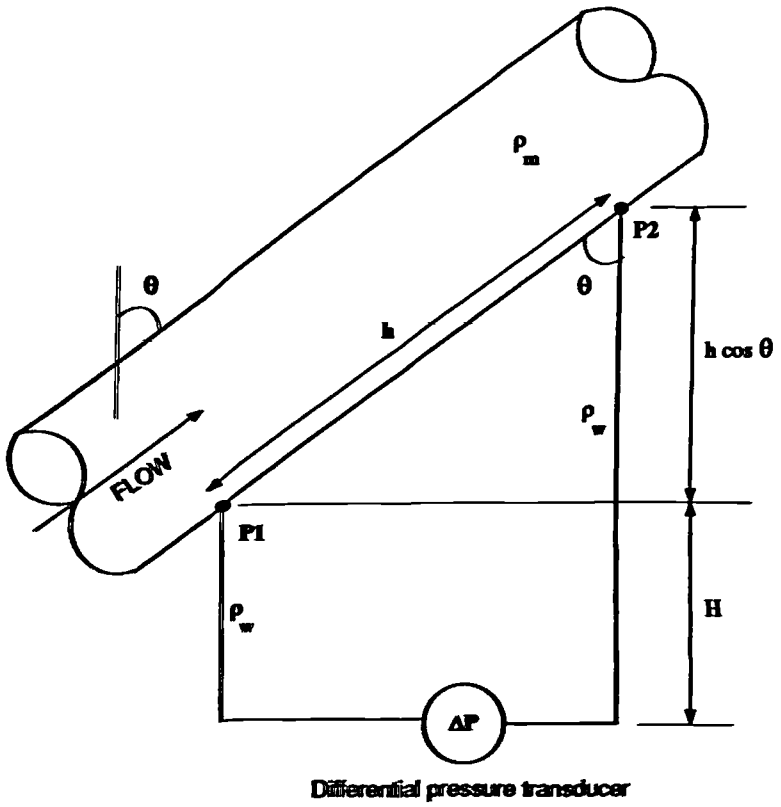

Figure 5.4: Diagram to assist determination of volume fraction

transducer. The differential pressure transducer was connected to the test section via water filled lines for reference purposes. This was required in order to have a stable reference density measurement. To maintain this stability, the pressure lines were flushed with water to remove contaminates e.g. air. The separation between the two tappings was 840mm. The first and the second pressure tapping points were 8 and 19 diameters downstream of the inlet contraction respectively.

Consider the performance of the differential pressure transducer in two phase flow when the working section is deviated at an angle θ from the vertical. With reference to Figure 5.4, we may write that the differential pressure ΔP measured by the differential pressure transducer is given by:

$$\Delta P = P_2 + (h\cos\theta + H)\rho_w g - H\rho_w g - P_1$$

hence

$$\Delta P = (P_2 - P_1) + \rho_w g h \cos\theta \qquad (5.9)$$

where ρ_w is the density of water in the pressure lines.

From the steady flow energy equation, we may write that:

$$P_1 + \frac{1}{2}\rho_m U_m^2 + H\rho_m g = P_2 + \frac{1}{2}\rho_m U_m^2 + \rho_m g(H + h\cos\theta) + P_l \qquad (5.10)$$

where ρ_m is the mixture density, U_m is the mixture velocity and P_l is a pressure loss term due to friction between the fluid and the pipe wall. By rearranging Equation 5.10:

$$P_1 - P_2 = P_l + \rho_m g h\cos\theta \qquad (5.11)$$

By substituting Equation 5.9 into Equation 5.11:

$$\Delta P = gh\cos\theta(\rho_w - \rho_m) - P_l \qquad (5.12)$$

Now, we may express the mixture density in terms of the two phases present in the test section i.e. water and oil. The equations below are written so that water is the continuous phase and oil is the disperse phase:

$$\rho_m = (1 - \bar{\alpha}_o)\rho_w + \bar{\alpha}_o\rho_o \qquad (5.13)$$

where ρ_o is the oil density, ρ_w is the water density and $\bar{\alpha}_o$ is the oil volume fraction. Substituting Equation 5.13 into Equation 5.12 gives:

$$\Delta P = \bar{\alpha}_o gh\cos\theta(\rho_w - \rho_o) - P_l \qquad (5.14)$$

In order to determine the value of P_l, it is necessary to carry out the following. The frictional pressure loss P_l in a single phase fluid is given by:

$$P_l = \frac{2U^2 hf\rho}{Dg} \qquad (5.15)$$

This is the Fanning formula where h is the distance between the pressure tappings, ρ is the fluid density, U is the flowing velocity, D is the diameter of the pipe and f is a dimensionless friction factor.

Aziz and Govier [1972] have stated that for two phase flows, Equation 5.15 is still valid provided that the terms are correctly interpreted. They indicate that flowing velocity U, should be replaced by U_{hom}, i.e.:

$$U = U_{hom} = U_{os} + U_{ws} \qquad (5.16)$$

Also, empirical results obtained by Hunt [1987] indicate that ρ should be replaced by the continuous phase density, ρ_w. By making these changes we get:

$$P_l = \frac{2U_{hom}^2 hf\rho_w}{Dg} \qquad (5.17)$$

The friction factor f remains unknown. To solve f, the following approach was taken.

Consider single phase water flow which is deviated at an angle of θ from the vertical. The frictional pressure loss is given by:

$$P_{ls} = \Delta P_s - \Delta P_{0s} \tag{5.18}$$

where ΔP_{0s} is the static and ΔP_s is the flowing differential pressure measurement in single phase flow.

Combining Equation 5.15 and Equation 5.18, and taking into account that we have single phase water flow, we get:

$$\Delta P_s - \Delta P_{0s} = \frac{2U_{ws}^2 h f \rho_w}{Dg} \tag{5.19}$$

or

$$f = \frac{Dg(\Delta P_s - \Delta P_{0s})}{2hU_{ws}^2 \rho_w} \tag{5.20}$$

Hence, by knowing ΔP_{0s} the friction factor can be determined from Equation 5.20, by measuring the flowing differential pressure, ΔP_s and the corresponding water superficial velocity U_{ws}, for single phase flows.

In order to compare the measured friction factor to theoretical models in single phase pipe flows, the Moody [1944] curves were superimposed onto the experimental data. With reference to Figure 5.5, at water velocities of less than 0.4ms^{-1}, the flow is not fully developed. This observation was seen during calibration of the hot-film and split-film anemometers since the velocity profiles at low water velocities ($\leq 0.4\text{ms}^{-1}$) did not compare well with the log law predicted velocity profiles (see Section 4.5 and Section 4.8). Figure 5.6 shows a 'log-log' plot of the experimental data. A linear fit to the data has produced the equation: $f = 0.0476Re^{-0.205}$ where f is the friction factor and Re is the Reynolds number. The Reynolds number is given by:

$$Re = \frac{UD}{\nu} \tag{5.21}$$

where U is the water velocity, D is the diameter of the working section and ν is the kinematic viscosity of water. The experimental equation for the friction factor ($f = 0.0476Re^{-0.205}$) was compared to the Blasius equation for a smooth pipe i.e. $f = 0.079Re^{-0.25}$. Unfortunately, the comparison was unsatisfactory, however, Knudsen and Katz [1958] state that for $3000 \leq Re \leq 10^5$, the friction factor is given by: $f = 0.046Re^{-0.2}$ which compares very well with the experimental data.

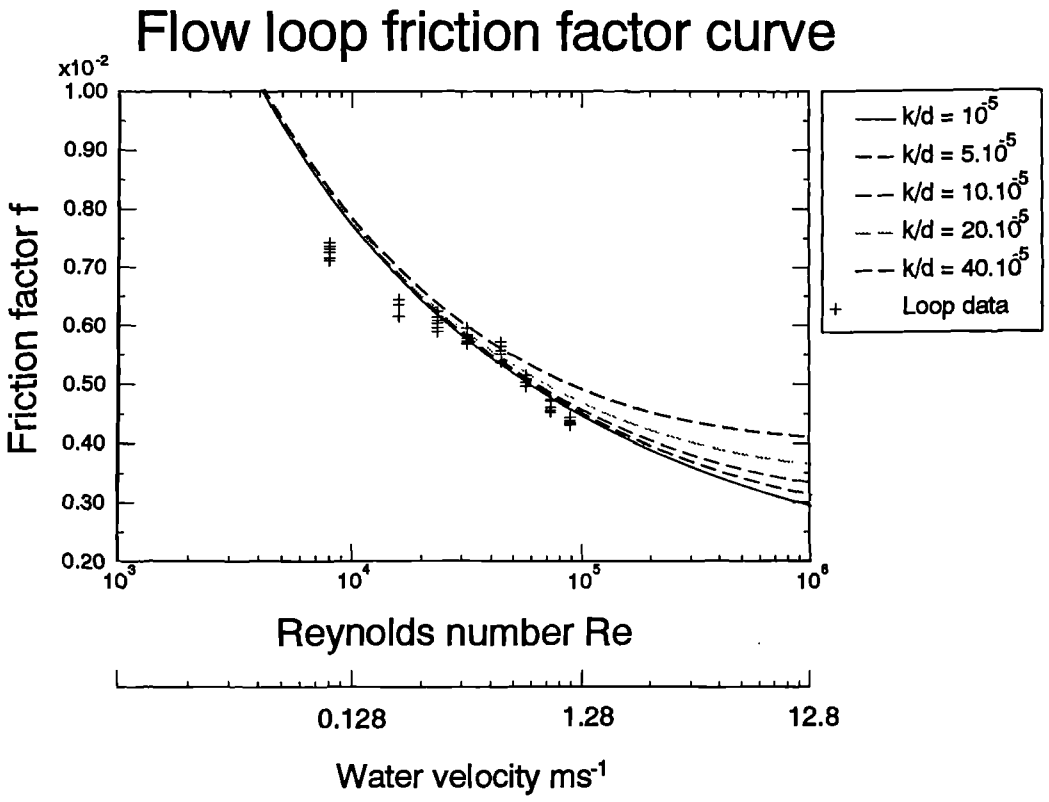

Figure 5.5: Friction factor curve for flow loop and Moody [1944] curves for a range of different pipe roughness (k/d)

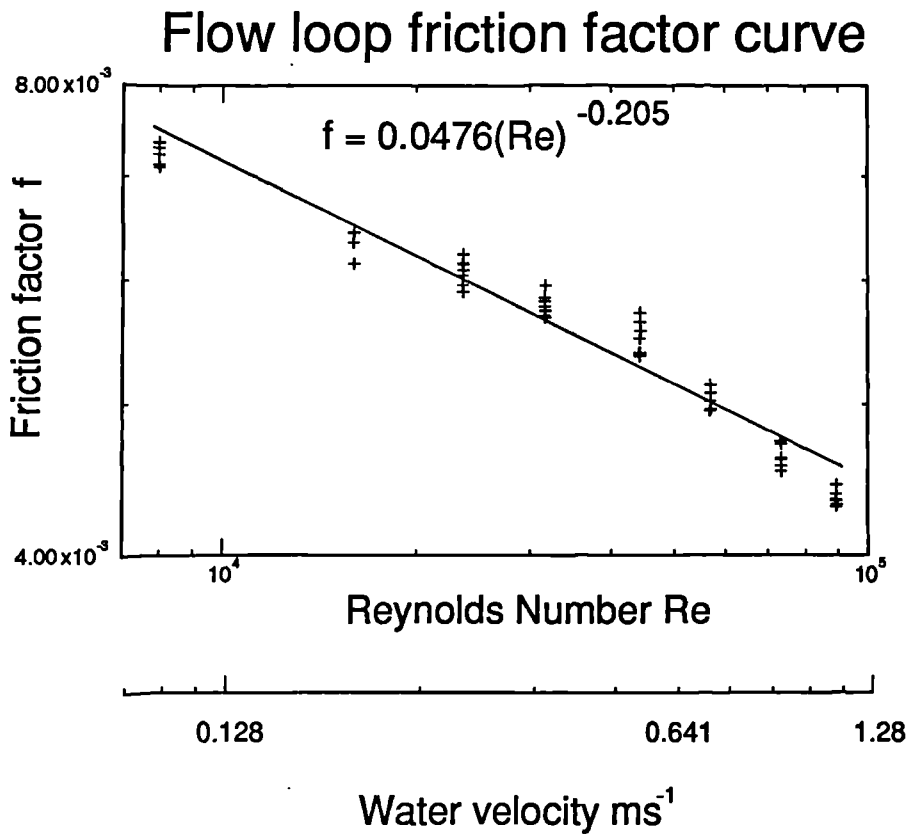

Figure 5.6: Friction factor curve for flow loop

Having estimated the friction factor, the oil volume fraction in a two phase oil-water flow can be determined. From Equation 5.14, the mean oil volume fraction, $\bar{\alpha}_o$, is given by:

$$\bar{\alpha}_o = \frac{\Delta P + P_l - \Delta P_0}{gh\cos\theta(\rho_w - \rho_o)} \tag{5.22}$$

where ΔP is the flowing differential pressure reading in oil-water flows, P_l is given by Equation 5.17 and ΔP_0 is the static differential pressure measurement in single phase water.

5.3.3 Traversing mechanism

A traversing mechanism was used to 'map' the dual probe and the dual split-film probe, over the pipe cross section, to measure the velocities and volume fractions. The traversing mechanism, located 16 diameters downstream of the inlet contraction (see Figure 5.2), was capable of rotational and radial motion using stepper motors. The accuracy of the motors were $\pm 3.25\%$ on a 1.8° step which was non-cumulative. One of the limitations of the traversing mechanism, when fixed onto the flow loop, was that the rotational arm could not be rotated through 360°. This was a constraint in the design of the traversing mechanism limiting the maximum rotation to 190°. This implied that only half of the cross sectional area of the working section could be investigated, at a time. With this limitation in mind, the zero degree position was defined as the start of the axis which symmetrically connected the bottom side of the pipe to the top side of the pipe. Vigneaux [1988] showed that, in deviated two phase oil-water flows, symmetry exists along the line which connects the top of the pipe to the bottom of the pipe. Figure 5.7 illustrates the position of the zero degree position in relation to the working section. With the dual probe fixed into the traversing mechanism, the maximum radial traverse from the centre of the pipe was limited to 37mm. This implied that data could not be taken very close to the wall. With reference to Figure 5.7, the dual probe was traversed from the centre of the pipe 'out' towards the nearest pipe wall (the black dots, on the directional arrows, represent the initial position of the probes at the centre of the pipe). Once a single radial traverse was complete, the probe was traversed back to the centre of the pipe and the traversing arm was rotated through 180°. The probe was then traversed 'out' towards the pipe wall. This implied that data could only be taken over half of the pipe cross sectional area in a

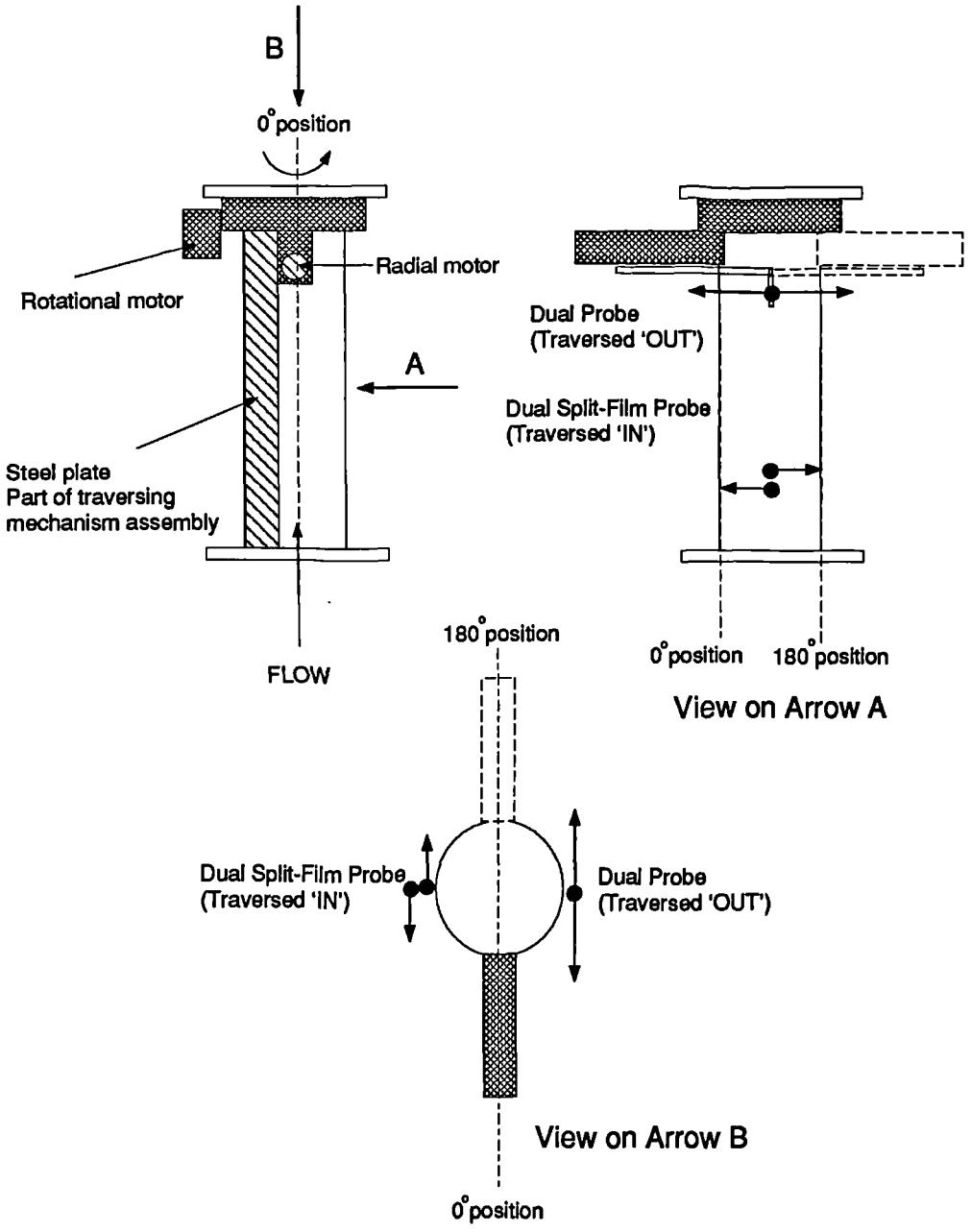

Figure 5.7: Diagram of the traversing mechanism at the zero position

single test (see Section 5.5.2). With reference to Figure 4.23, if the dual probe was to be traversed in the opposite direction i.e. 'into' the pipe, the optical probes would have collided with the pipe wall limiting the final radial traverse position to 5mm away from the wall. Similar restrictions were found using the dual split-film probe. With reference to Figure 5.7, instead of traversing 'out' towards the nearest pipe wall (dual probe), the dual split-film probe had to be traversed 'in' towards the furthest pipe wall. Again, this restricted the area over which the probe could be traversed in a single test. With reference to Figure 4.27, the dual split-film probe had to be traversed into the pipe because the optical probes would have collided with the pipe wall, hence restricting the final measuring position to 20mm from the wall.

5.4 Data acquisition system

The computer used for data collection and data manipulation was the Archimedes 540 computer. The computer was supplied with a 4Megabyte RAM, 120Megabyte hard disc and a 25MHz ARM3 processor. The computer was equipped with an IEEE card for communicating with low speed devices e.g. traversing mechanism, an Ethernet card which was used to transfer data to the main frame computers, and an ADC (analogue to digital converter) card which was used to capture high speed signals from the dual probes and low speed signals from the reference meters e.g. turbine meters, differential pressure transducer and platinum resistance thermometer (PRT). Figure 5.8 shows the acquisition system set up for the dual split-film probe experiments. A similar configuration was used for the dual probe experiments.

The ADC is a high speed 8 channel analogue input converter which could sample at 160kHz (maximum) for a single channel. The analogue input is converted into a 12 bit number between 0 to 4095 i.e. -5 volts corresponded to 0 and $+5$volts corresponded to 4095. The limitations of the ADC were that it sampled the input channels sequentially and the analogue input range was set to ± 5volts. In order to protect the ADC, 5.1volt zener diodes were used to limit the input voltage. All eight channels were calibrated against a precision power supply at known voltage inputs. Figure 5.9 shows the calibration of the ADC for a single channel. A linear fit to data provided the calibration constants for the ADC. The relative error (see Equation 5.23) between the calculated voltage and the true voltage was plotted against the true voltage.

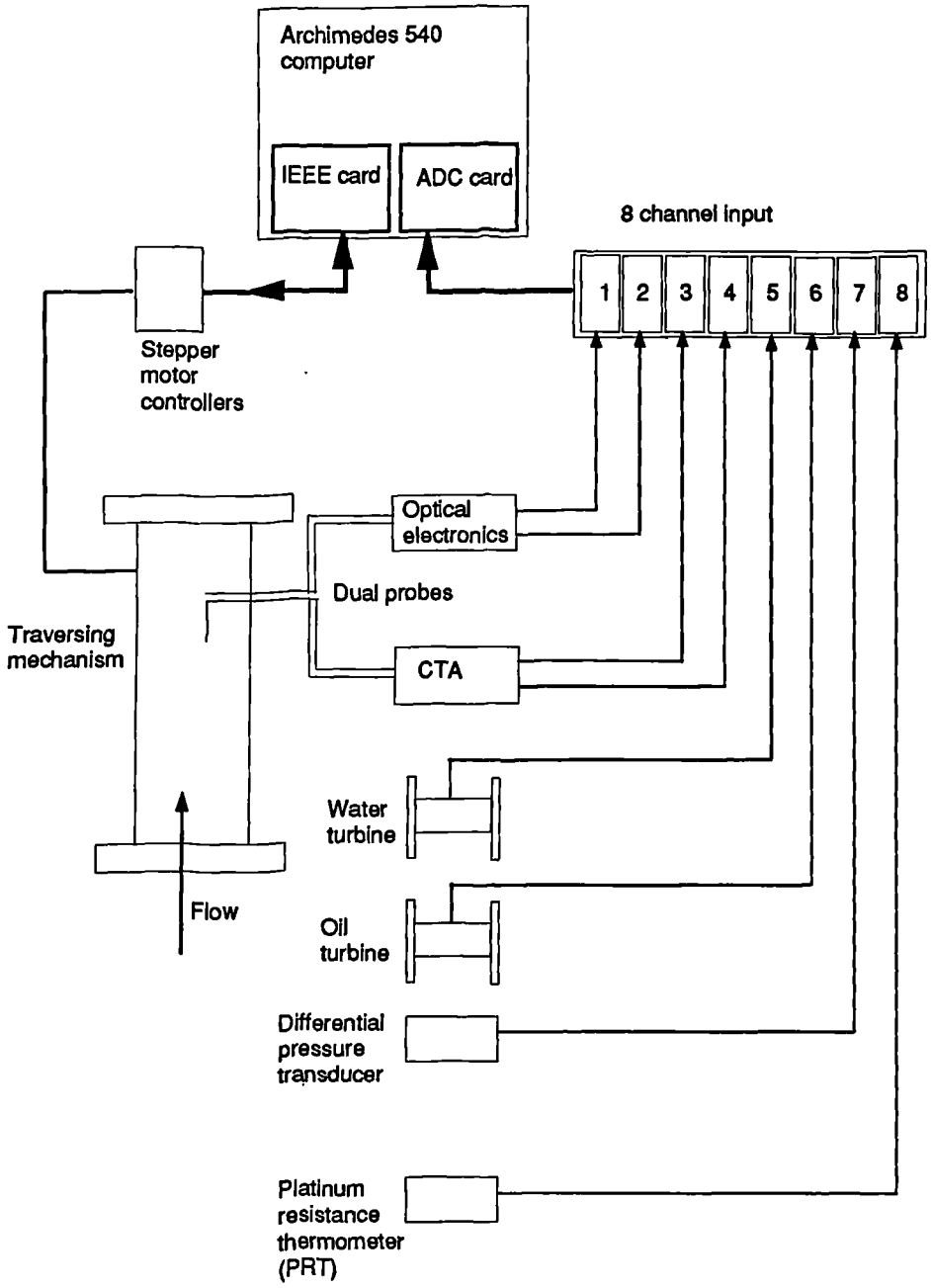

Figure 5.8: Experimental set up for data acquisition

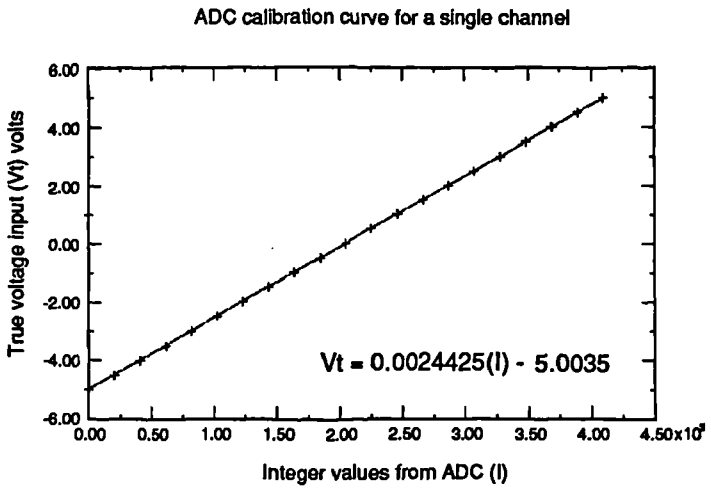

Figure 5.9: Calibration of ADC against known analogue input

With reference to Figure 5.10, the relative error was $\pm 0.1\%$. Also, the noise signals from each channel of the ADC were investigated. The input for each channel was grounded relative to the computer and data was recorded at 160kHz. Figure 5.11 shows the noise signal from a single channel. It should be noted that the noise signal are the integer values from the ADC.

The sampling rate and duration were estimated by initial testing of the probes in the flow loop (see Section 5.5). The reference meter readings were sampled at a low rate of 10Hz for 30 seconds (the frequency to voltage converters used with the turbine meters had a time constant of 0.2seconds). However the signals from the dual probe and the dual split-film probe had to be sampled at a higher frequency. In order to resolve the droplet velocity, consider a passing droplet travelling at $1ms^{-1}$. The time taken before the droplet penetrates the second optical probe will be 1ms after penetrating the leading optical probe. Hence the sampling rate has to be greater than 1kHz. Another consideration is the integration time or the total trace time. Authors in the past e.g. Vigneaux [1988], Farrar [1988] have used different time scales varying from 10 seconds to 1 minute. For all the experimental tests the sampling frequency used for acquiring data from the probes was set to 8192Hz for 20 seconds. The sampling rate of 8192Hz was chosen because this frequency was pre-programmed into the ADC hardware. The time over which the data was taken was restricted to 20 seconds because of the size of memory available on the computer. For a single position measurement in the flow, the size of one data file was approximately 1.3Megabytes.

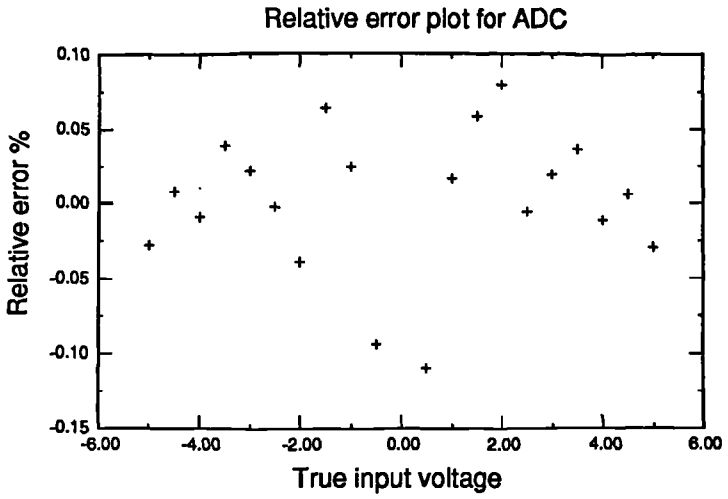

Figure 5.10: Relative error between calibration and true voltage input for the ADC

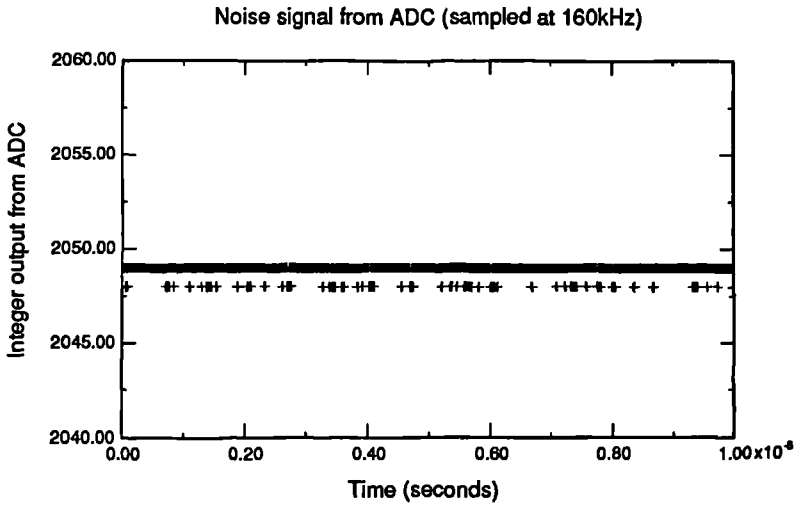

Figure 5.11: Noise signal from a channel of the ADC

5.4.1 Software acquisition procedure

Software was written in BBC Basic to control the traversing mechanism and to acquire data from the dual probe/dual split-film probe and reference meters. The acquisition software was written such that the data taking procedure was fully automated i.e. all of the measuring positions within the pipe section were pre-programmed into the software. A block diagram shown in Figure 5.12 illustrates the acquisition procedure. All of the data taken for one flow condition were saved onto the hard disc and then transferred over to a mass memory storage facility. The analysis of the data will be discussed in Chapter 6. The format of the saved data comprised a header where all the reference meter calculated values, the position of the dual probe, calibration constants and the deviation angle of the flow loop were stored. The raw signal traces from the dual probe were then saved after the header in either 3 or 4 data blocks (e.g. 3 data blocks were needed for the dual probe tests: 2 data blocks for the optical probe signals and 1 for the hot-film signals) depending on whether the dual probe or the dual split-film probe were being tested. The raw data from the probes were saved as binary numbers which reduced the amount of memory required to store all the data files.

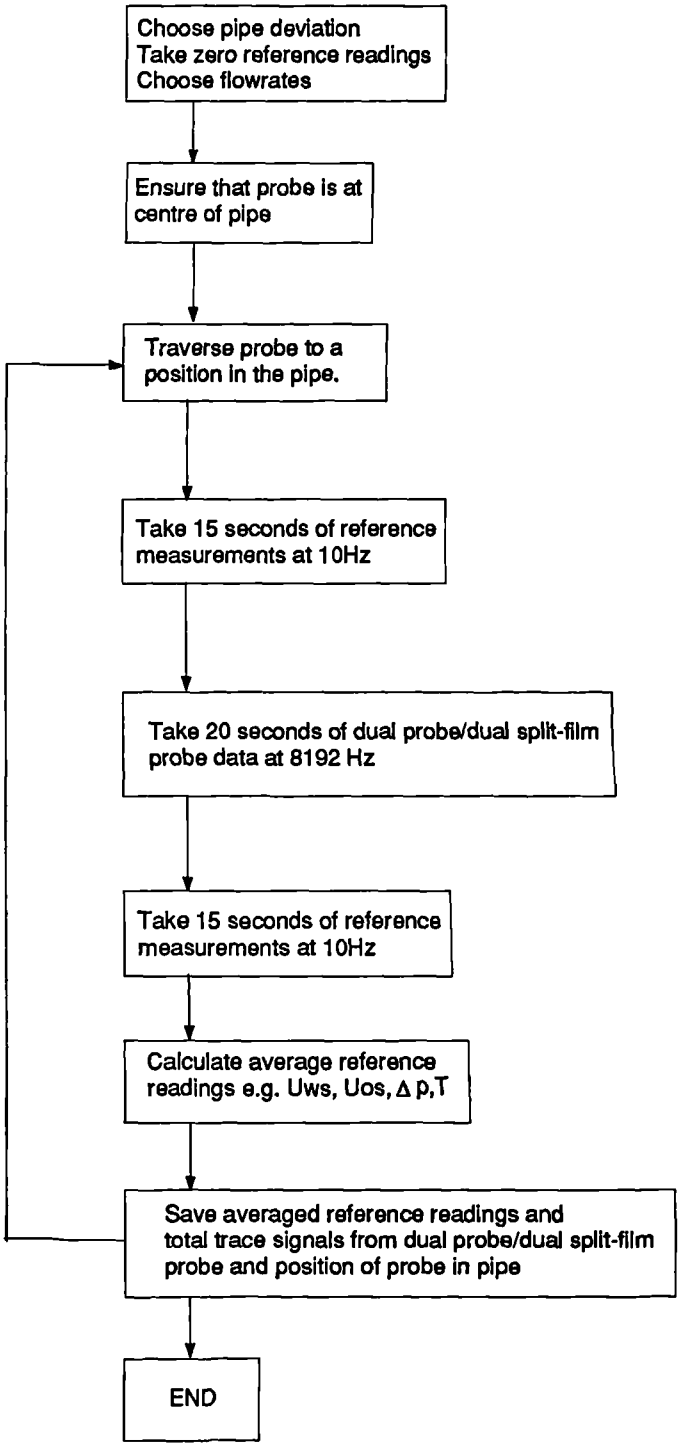

Figure 5.12: Block diagram of acquisition procedure

5.5 Experimental procedure

Initial tests were carried out in the flow loop before the main experimental programme was investigated. These initial tests were to gain experience in using all of the experimental apparatus and to calculate the most efficient procedure for acquiring data from the probes. These initial tests also provided an insight into how to analyse the data as a form of a check to see whether or not the data taken was comparable to the reference measurement.

5.5.1 Initial testing of the dual probe for calibrating the hot-film anemometer

The equations used for calibrating the hot-film anemometer can be seen in Section 4.5. The calibration of the hot-film anemometer was carried out in single phase vertical water flow. An even number of measuring positions were chosen and the hot-film anemometer calibration constants $\mathcal{A}$ and $\mathcal{B}$ were calculated. Eight different flow velocities i.e. 0.1ms^{-1} to 0.8ms^{-1}, were investigated to provide a wide range over which the calibration constants could be computed. A procedure similar to Section 4.5 was used to determine the mean water flowrate, Q_{wp}, as computed from the hot-film measurements. This was compared to the mean flowrate as calculated by the turbine meter. The number of measuring positions investigated varied from 4 to 16 across a single diameter. The distance between each measuring position was: 5mm for 16 positional traverse, 10mm for 8 positional traverse and 20mm for 4 positional traverse.

Figure 5.13 shows a plot of the actual errors (see Equation 4.16) against the measured water flowrate for different numbers of measuring positions across the pipe diameter. From the results, it was seen that 4 measuring positions were too few and no improvement was gained from taking 16 measuring positions. Hence, it was decided to use 8 measuring positions across a single diameter for calibrating the hot-film anemometer.

Having established the number of measuring positions, the sampling rate and duration were then calculated. Bearing in mind that the calibration of the hot-film anemometer was to be carried out before and after each experimental run, the duration and sampling rates were kept to a minimum. Initial experiments were carried out with different sampling frequencies ranging from 1kHz to 8kHz and for time scales ranging from 5 to 30 seconds. With reference

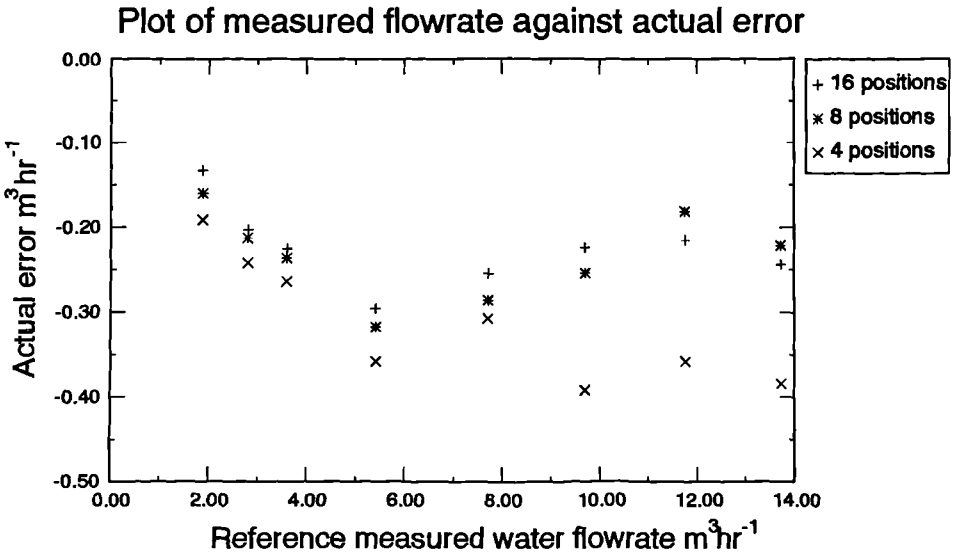

Figure 5.13: Plot of measured water flowrate against the actual error for different measuring positions

to Figure 5.14, the reference measured water flowrates are plotted against the actual error of reading (see Equation 4.16) for different sampling frequencies as stated on the graph, for a sampling duration of 15 seconds. One can see that the actual error of reading, when sampling at 1kHz or 8kHz, are not dissimilar. In order to maintain the calibration procedure to a minimum, it was decided to use a sampling frequency of 1kHz. Figure 5.15 shows that there are significant changes, in the actual error, between sampling durations of 5 seconds and 15 seconds (sampling frequency was 1kHz). No significant change was seen between sampling at 15 seconds and 30 seconds. It was decided to sample at 1kHz for 15 seconds per measuring position. The calibration of the hot-film took 30 minutes to complete. Examples of velocity profiles, after calibrating the hot-film anemometer, can be seen in Section 4.5.

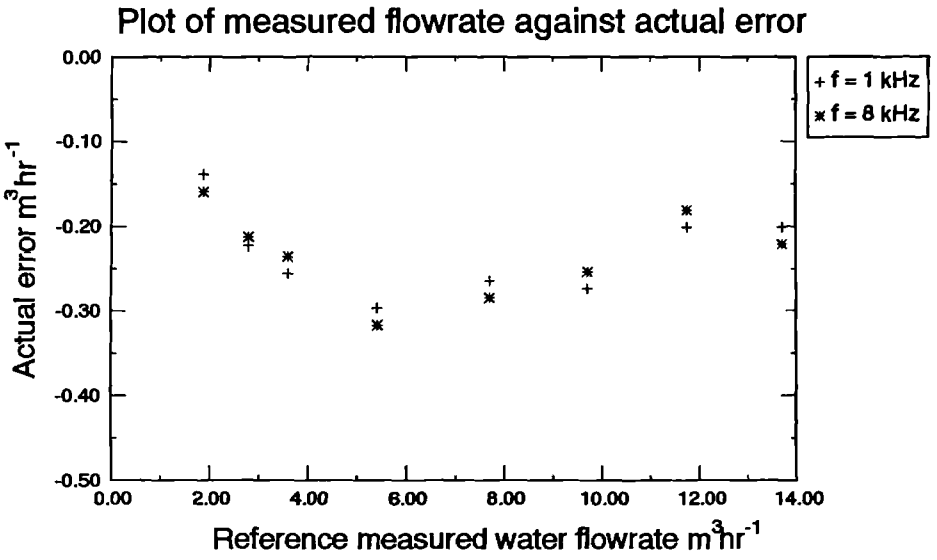

Figure 5.14: Plot of measured water flowrate against actual error (sampled at different frequencies)

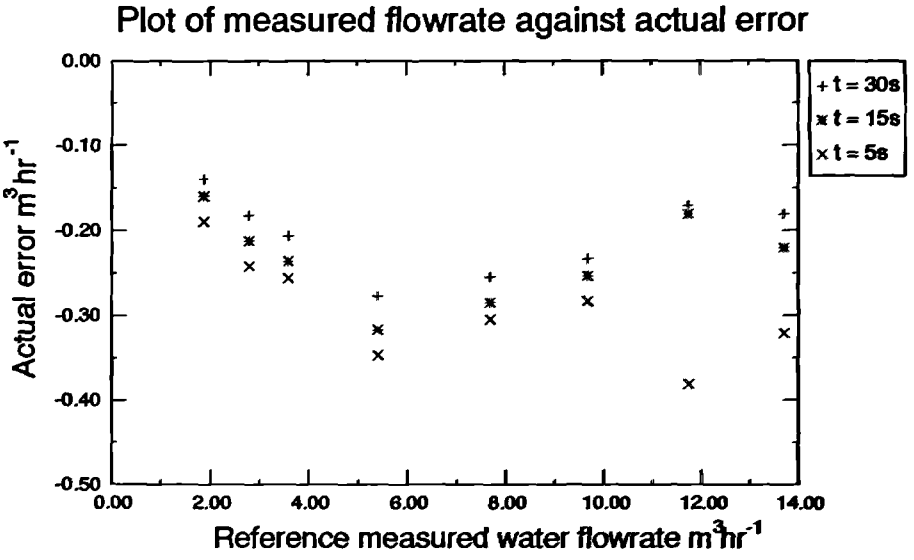

Figure 5.15: Plot of measured water flowrate against actual error (sampled at 1kHz at different durations)

5.5.2 Initial tests for the dual probe experiments

Preliminary testing of the dual probe was carried out in vertical oil-water flows. Water was the continuous phase with oil as the dispersed phase. The initial test was to calculate the number of measuring positions and rotational positions, required to achieve an uncertainty on the water superficial velocity (relative error) of better than 10%. Equation 5.23 defines the error of reading used for comparing the dual probe averaged results and the mean reference results:

$$e_x = \frac{(C_{px} - C_{rx})100}{C_{rx}} \tag{5.23}$$

where e_x is the relative error for the quantity x (e.g. consider the relative error of the quantity x, C_{px} is the integrated value of the quantity from the probe and C_{rx} is the calculated quantity from the reference meters). The relative error was calculated by integrating the probe results over the cross sectional area of the pipe and comparing it to the reference readings. A maximum relative error of 10% was assumed from the calibration of the hot-film anemometer where the confidence of the water velocity measurement was -8% (see Section 4.5). The sampling frequency used for acquiring data from the dual probe was set at 8192Hz for a time scale of 20 seconds (maximum duration see Section 5.4). Since two phase oil-water flows were being investigated, it was initially decided to use 16 measuring positions across a single diameter (calibration of the hot-film probe was carried out in single phase water with 8 measuring positions across a diameter). The number of rotational positions were initially set to three. Figure 5.16 illustrates the traversed positions investigated by the dual probe. Since the traversing mechanism was limited to 190° rotation (see Section 5.3.3), the data taken at the 90° position, had to be 'reflected' to provide data for the analysis routine and to conserve symmetry across the pipe section.

In order to justify the 'reflection' of different positional data values, the traversing mechanism was physically rotated through 180°. This implied that instead of traversing from 0° to 180°, the probe was rotationally traversed from 180° to 360°. With reference to Figure 5.16, data was initially taken for the 90° *set up traverse* and then data was taken for the 270° *set up traverse.* With the dual probe set in the 90° *set up traverse*, 15 different flow conditions were investigated with varying oil volume fractions from 5% to 25%. These flow conditions were chosen because they were a part of the experimental

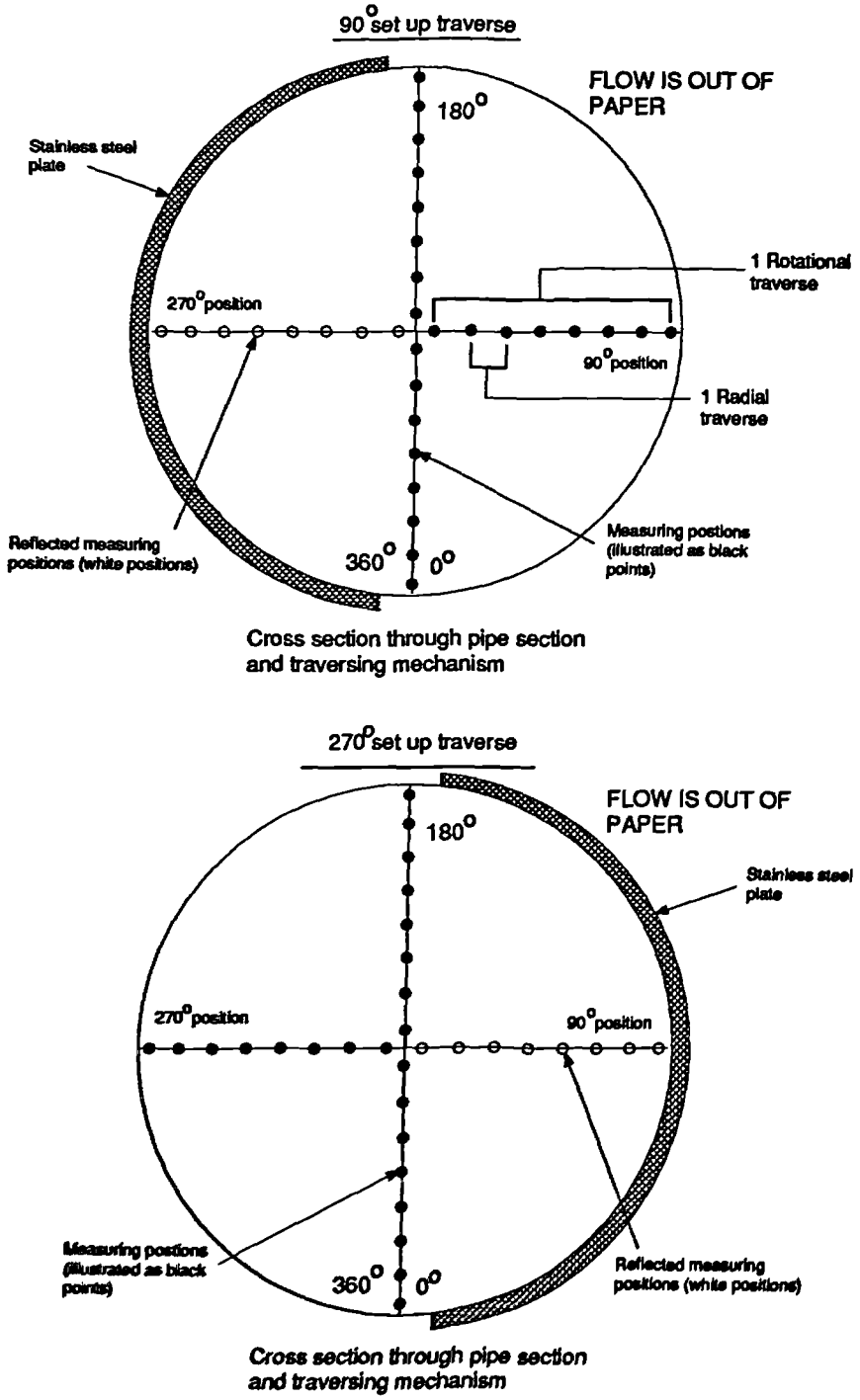

Figure 5.16: Radial and rotational positions initially investigated by the dual probe

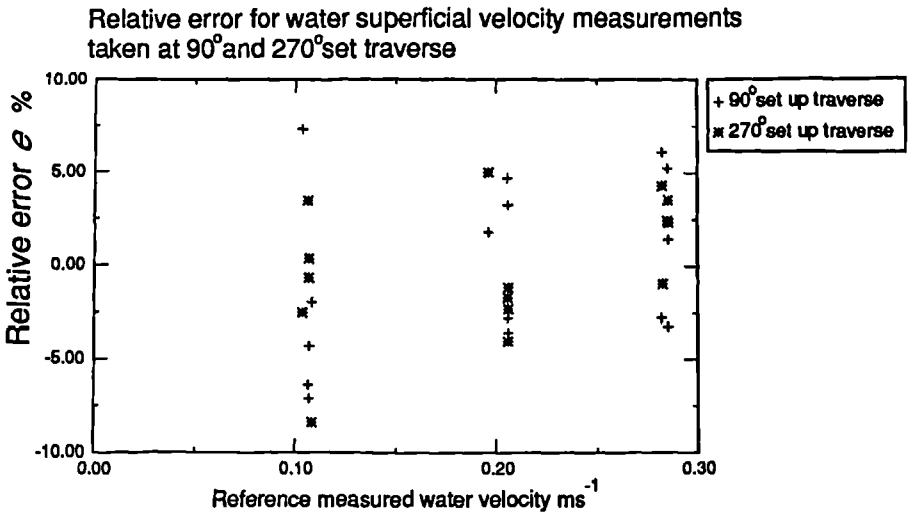

Figure 5.17: Relative error of water velocity against reference water turbine for different positions of the traversing mechanism

programme (see Section 5.6.1). The traversing mechanism was then physically rotated through 180° and mounted onto the flow loop for the 270° *set up traverse* and the same flow conditions were investigated. Figure 5.17 show plots of the relative errors from the experimental data taken against the reference meter readings, for the water velocity, for the different *set up traverse.* As one can see, for both positions of the traversing mechanism, the relative error of the water velocity as measured by the dual probe was approximately ±10% for both positions of the traversing mechanism. No significant clustering of the two data sets was seen, which is indicative of no systematic errors when the mechanism was physically rotated through 180° (mechanically moved). This result showed that reflection of the data was justifiable. Vigneaux [1988] also used the technique of reflecting data points where the Resistivity probe (RF) could not be traversed.

A similar exercise was carried out to investigate the number of radial traverses required to map (10% relative error) the flows in deviated pipes. The flow loop was deviated to 15° from the vertical and flowrates given in Section 5.6.1 for 15° deviation were used. Similar rotational traverses and measuring positions were also used for these tests (i.e. 3 rotational traverses and a reflected data set at 90° position). After the data had been collected and analysed, the mean integrated values as calculated from the dual probe (see Section 6.3) were compared to the reference meters. Figure 5.18 shows the

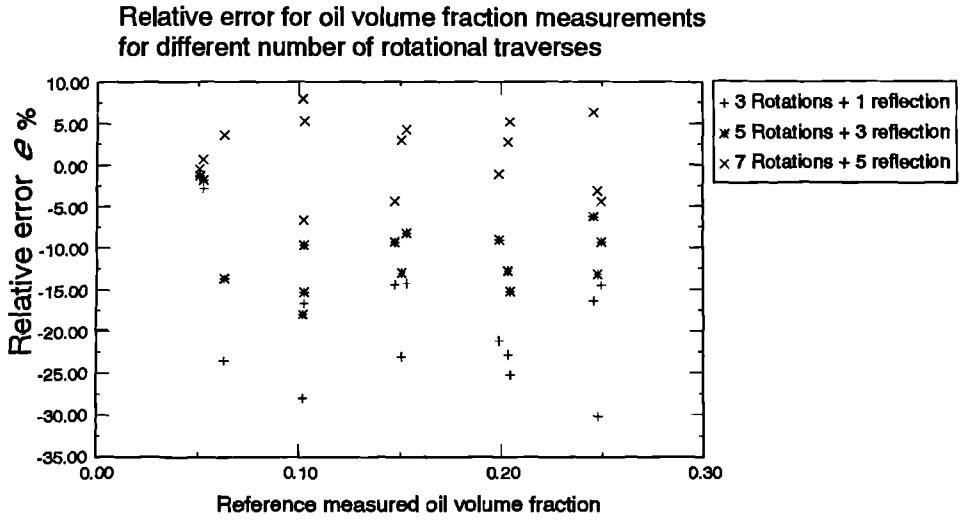

Figure 5.18: Relative error of oil volume fraction against reference meter reading for different rotational positions

relative error of oil volume fraction as calculated by the dual probe and the reference differential pressure transducer. As one can see from the graph, for 3 rotational traverses and 1 reflected data set, the relative error was approximately -25%. This implied that the number of rotational traverses had to be increased. The rotational traverses were decreased from a 90° step to a 45° step, doubling the rotational traverses i.e. 5 rotational traverses and 3 reflected data sets. The same flow conditions were investigated and an improvement in the relative errors between the reference reading and the integrated dual probe reading was seen (approximately -15%). However, this improvement was still outside of the limit set for the relative errors (10%). The rotational step was further decreased to a 30° step. The number of rotational traverses had increased to 7 with 5 reflected data sets. By investigating the same flow conditions and comparing the readings between the reference readings and the dual probe, it was seen that the relative errors were now within the 10% limit. It can be seen that the spread of the error data, taken at 5 rotations with 3 reflected data sets, are equal to the data taken at 7 rotations and 5 reflected data sets (approximately 20%). It was chosen to take data with 7 rotations and 5 reflected data sets since the spread of data is centred around 0.00. For all of the experiments carried out in the flow loop, the number of measuring positions was 8 on each radial traverse (or 16 across a diameter). The probes were rotated from 0° to 180° in steps of 30°. The total number of

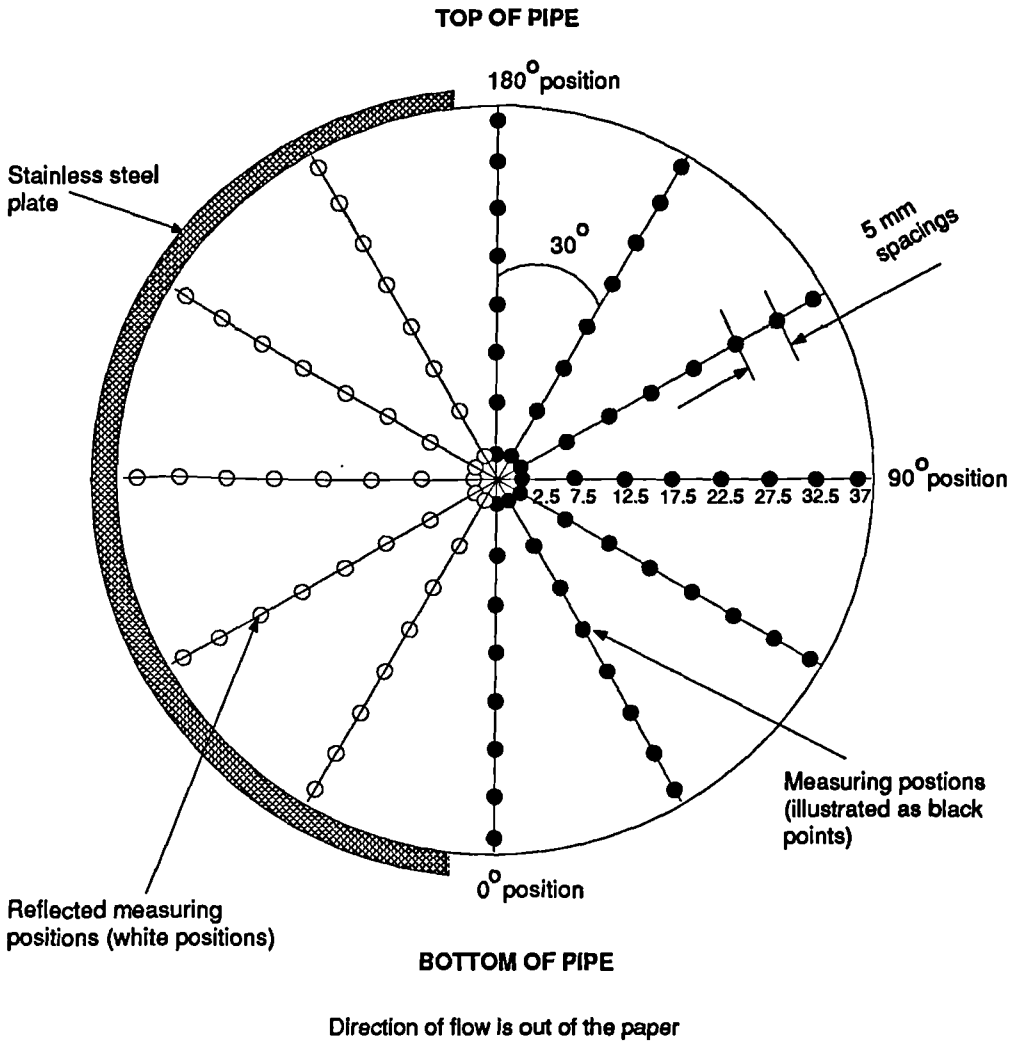

Figure 5.19: Measuring positions used to map flow loop using the dual probe

measuring positions where data were collected from the probes was 56 and the data collected at 40 positions (i.e. at rotational positions: $30°, 60°, 90°, 120°$ and $150°$) had to be 'reflected' so as to map the entire cross section of the pipe. Figures 5.19 shows the measuring positions where data were collected and reflected for all experiments carried out with the dual probe and the dual split-film probe. It should be noted that, along a single radial traverse, the initial probe position was 2.5mm away from the centre of the pipe. Each probe position was then incremented by a distance of 5mm until 32.5mm. The last measuring position was 37mm (2mm away from the pipe wall).

5.5.3 Experimental procedure used for acquiring data from the dual probe and the dual split-film probe

Prior to the start of any experimental tests, the hot-film anemometer was calibrated as described in Section 4.5. The dual split-film probe was calibrated after 5 experimental tests, since it was time consuming (see Section 4.8). The deviation angle of the flow loop was set and the differential pressure transducer and thermometer (PRT) 'zero' readings were taken in static single phase water. These zero readings were taken before and after each experimental run. The zero reading for the differential pressure transducer (ΔP_0) was used in the calculation of the mean oil volume fraction ($\bar{\alpha}_o$) within the working section (see Equation 5.22) and as an indication of the drift. A drift in the zero reading was sometimes encountered when fine droplets of oil were trapped in the pressure lines hence producing an uncertainty of the mean oil volume fraction. Since the oil volume fraction calculated from the dual probe was to be compared with the reference differential pressure transducer reading, it was important to ensure that the zero reading drift be kept to a minimum. Typically the difference in the differential pressure transducer zero reading was $\pm 1\%$ (full scale) before and after experiments. The thermometer (PRT) 'zero' reading was also required as a check for the hot-film and split-film calibration (see Sections 4.5 and 4.8). Typically, the temperature of the flowing fluids within the working section varied from 21°C to 23°C.

Once the zero readings were taken and stored, the water and oil flowrates were set. Section 5.6 discusses the experimental investigations carried out with the dual probe and the dual split-film probe. Before taking data at the first measuring position, the flows were allowed to stabilise for 2 to 5 minutes (see Vigneaux [1988]). An indication of the stability, of the flow, was seen by viewing the output from the differential pressure transducer. Once the flow had stabilised (stable output from differential pressure transducer), the probe was traversed to the first measuring position. A further 10 seconds were allowed for stabilisation between each radial traverse. Data collection commenced with taking reference readings for 15 seconds.

Data collection from the dual probe followed for 20 seconds and finally, a further 15 seconds of reference readings were taken. The data taken from the reference meters were then averaged over the number of samples to yield mean quantities e.g. water superficial velocity. The mean quantities and the raw

signal traces from the dual probe and the dual split-film probe were stored on the hard disc of the computer. The probe was then traversed to the next measuring position and data were acquired in a similar fashion as described earlier.

Once the collection of data was completed, the zero readings were taken from the differential pressure transducer and the PRT in static single phase water. The final zeros were noted and compared to the initial zero readings. The acquired data files were then analysed to compute the probe readings and to compare these readings with the reference meter readings. After analysing the data, all the data files were transferred using FTP (file transfer protocol) onto a mass storage facility for future analysis and reference.

5.6 Experimental investigations carried out in the flow loop

All of the flows investigated with the dual probe and the dual split-film probe were water continuous with oil as the dispersed phase. The parameter space over which the data from both of the probes were taken was calculated from the needs of the oil industry. In most producing oil wells, oil and water migrate through perforations and into the well (see Chapter 1). Most of the world oil wells are water continuous with oil as the dispersed phase ranging from 5% to 25% oil volume fraction. At the bottom of an oil well, low flow rates are usually encountered which range from 1000BPD to 5000BPD (Barrels per Day). By converting these values into total mean velocities in a 6inch pipe (6inch pipe is the typical oil well casing diameter), the velocities of interest are $0.1 ms^{-1}$ to $0.5 ms^{-1}$. The total mean velocity is given by the sum of the water and oil superficial velocities or homogeneous velocity (see Equation 5.8). These low flow rates are the most challenging to the oil industry since most of the worlds producing wells are low flow rate wells. Based on the needs of the oil industry, the parameter space was formulated. It must be noted that, the deviation angles of oil wells are usually between 15° and horizontal. Due to the limitation of the flow loop, the maximum deviation angle investigated was 45° from the vertical.

5.6.1 Dual probe experiments

It was decided to carry out experimental programmes where the deviations of the flow loop varied from, vertical to 30° in steps of 15°. Three different water superficial velocities were investigated at each deviation angle; these were 0.1, 0.2 and 0.3ms^{-1}. The oil superficial velocities were varied in order to produce different oil volume fractions within the test section. The mean oil volume fractions varied from 5% to 25% increasing in steps of 5%. Figure 5.20 summarises the experimental programme carried out using the dual probe. The oil volume fractions given in the table are nominal values.

Deviation Angle 0°					
Water Superficial Velocity ms^{-1}	Oil Volume Fraction				
0.1	0.05	0.1	0.15	0.2	0.25
0.2	0.05	0.1	0.15	0.2	0.25
0.3	0.05	0.1	0.15	0.2	0.25

Deviation Angle 15°					
Water Superficial Velocity ms^{-1}	Oil Volume Fraction				
0.1	0.05	0.1	0.15	0.2	0.25
0.2	0.05	0.1	0.15	0.2	0.25
0.3	0.05	0.1	0.15	0.2	0.25

Deviation Angle 30°					
Water Superficial Velocity ms^{-1}	Oil Volume Fraction				
0.1	0.05	0.1	0.15	0.2	0.25
0.2	0.05	0.1	0.15	0.2	0.25
0.3	0.05	0.1	0.15	0.2	0.25

Figure 5.20: Dual probe experiments

5.6.2 Dual split-film probe experiments

The experimental programme used to investigate the performance of the dual split-film probe was based on the dual probe experiments. Similar deviation angles and flowrates were investigated. Figure 5.21 summarises the experimental programme for the dual split-film probe. Again, the oil volume fractions given in the table are nominal values

Deviation Angle 15°					
Water Superficial Velocity ms^{-1}	Oil Volume Fraction				
0.1	0.05	0.1	0.15	0.2	0.25
0.2	0.05	0.1	0.15	0.2	0.25
0.3	0.05	0.1	0.15	0.2	0.25

Deviation Angle 30°					
Water Superficial Velocity ms^{-1}	Oil Volume Fraction				
0.1	0.05	0.1	0.15	0.2	0.25
0.2	0.05	0.1	0.15	0.2	0.25
0.3	0.05	0.1	0.15	0.2	0.25

Deviation Angle 45°					
Water Superficial Velocity ms^{-1}	Oil Volume Fraction				
0.1	0.05	0.1	0.15	0.2	0.25
0.2	0.05	0.1	0.15	0.2	0.25
0.3	0.05	0.1	0.15	0.2	0.25

Figure 5.21: Dual split-film probe experiments

Chapter 6

Application of the probes in oil-water flows

6.1 Introduction

In this chapter, the data analysis procedure and the experimental results will be discussed. The experimental results will be presented as contour plots and profile plots for each measured quantity. The contour plots are time averaged plots of the flowing structures within the pipe section. As an example, the contour plots, of the oil volume fraction, show the time averaged distribution of oil across the pipe section. The profile plots show the time averaged measured positional values across an axis which connects the top to the bottom of the pipe. Figure 6.1 shows an inclined pipe and defines the top and bottom of the pipe and shows the plane of the contour plots.

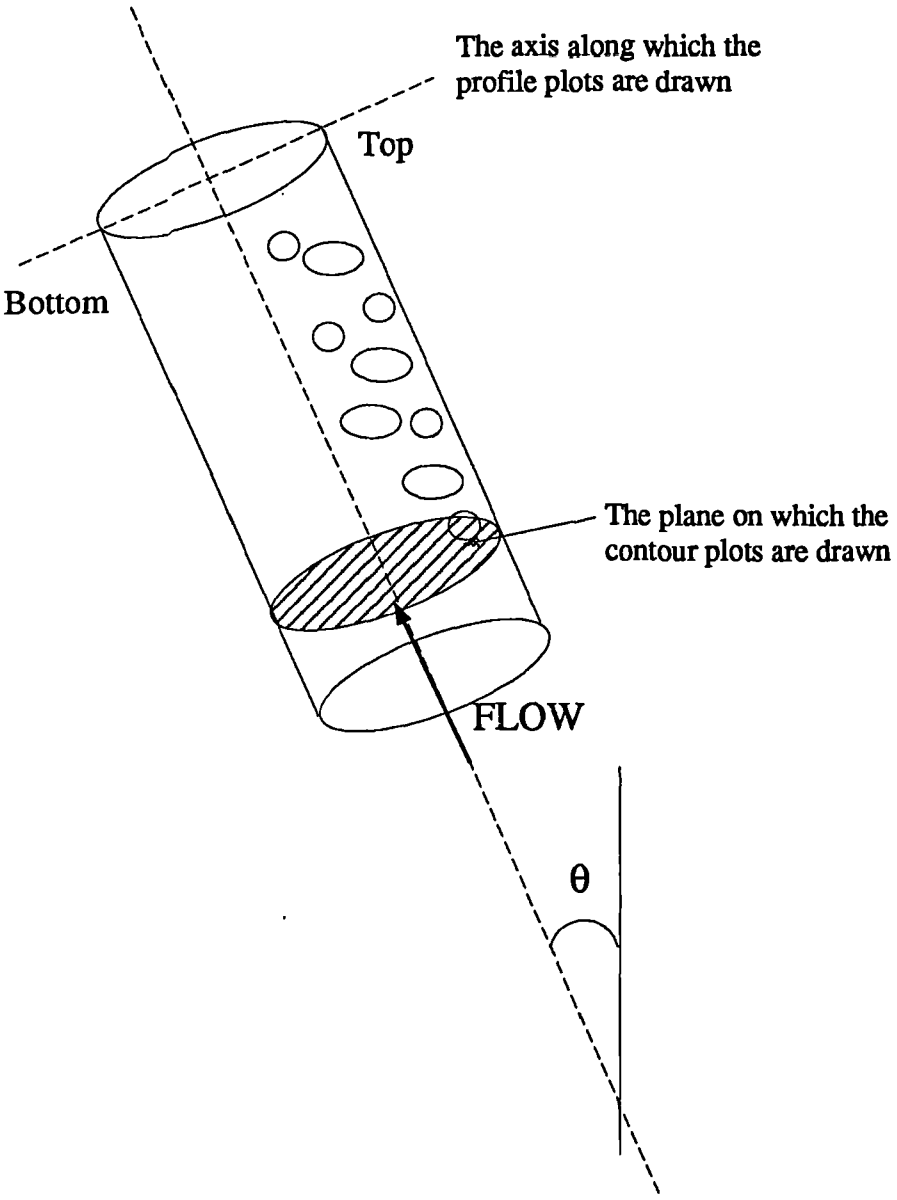

Figure 6.1: Notation diagram for presentation of results

6.2 Analysis technique

Once the data had been collected from the dual probe and the dual split-film probe, analysis routines were used to produce information about the flow. The analysis technique will be described in three parts. The determination of the oil volume fraction, the dispersed phase velocity and the continuous phase velocity will be described respectively.

6.2.1 Determination of the volume fraction

The volume fraction is calculated using the leading optical probe and/or the trailing optical probe. In this demonstration to calculate the volume fraction, the leading optical probe will be used.

Consider the leading optical probe in a two phase vertical oil-water flow. As oil droplets impact the probe, an output signal from the probe $X(t)$ will be seen. Figure 6.2 illustrates the residence time T_{di} of each droplet in the optical signal. The time averaged local volume fraction $\bar{\alpha}_j$, at a single position, j, in the flow, is given by:

$$\bar{\alpha}_j = \frac{\sum_{i=1}^{Nj} T_{dij}}{T} \tag{6.1}$$

where T_{dij} are the residence times for each droplet, T is the total averaging time and N_j is the number of droplets or events.

In order to calculate the oil volume fraction from the experimental optical signals, the start and finish of each oil droplet had to be extracted from the signals. A threshold technique was employed to distinguish between the dispersed phase and the continuous phase. The choice of threshold levels was computed by calculating the population density function (PDF) of the optical signal. Examples of PDF's, as computed from the leading and trailing optical probes, can be seen in Figures 6.3 and 6.4. As one can see, the two PDF curves are similar, however it should be noted that the baseline water level, on the trailing optical signal, has been adjusted to approximately -1volt for presentation. The amplitude of both PDF curves are dissimilar i.e. the amplitude of the water signal level for the leading optical probe is lower than that for the trailing optical probe. This implies that different residence times were recorded by the probes suggesting a difference in the oil volume fraction calculation. For this particular case, the calculated volume fraction from the leading probe was 0.056 and trailing probe was 0.051; hence the difference in

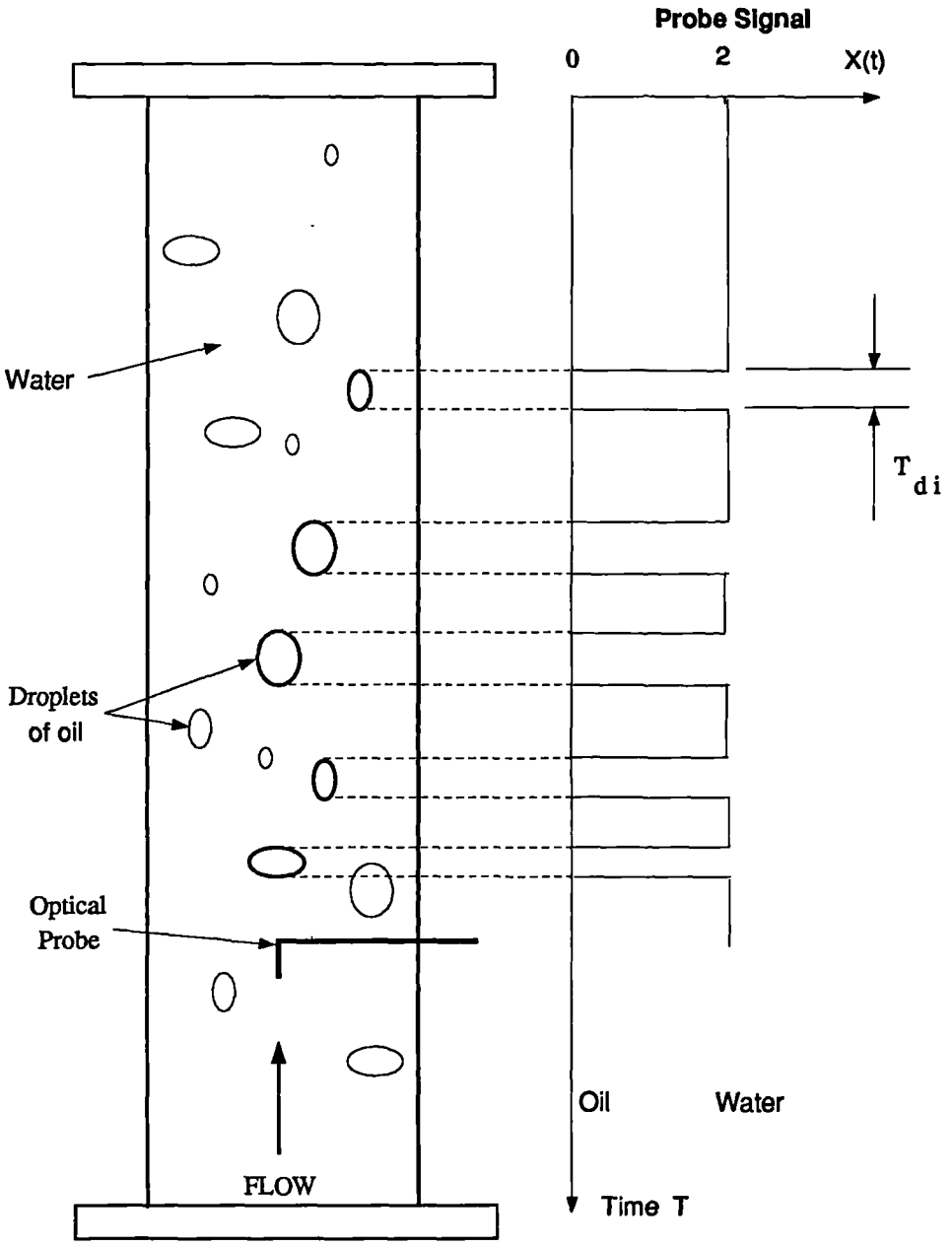

Figure 6.2: Schematic diagram to show determination of volume fraction

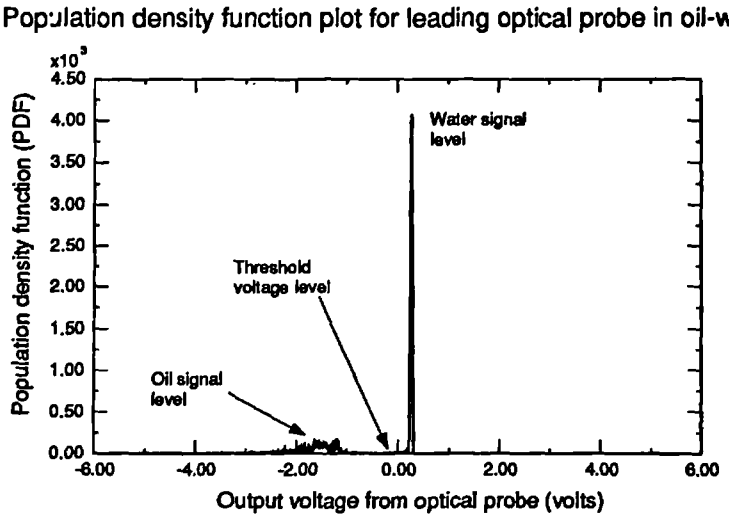

Figure 6.3: Population density function from leading optical probe signal in oil-water flow

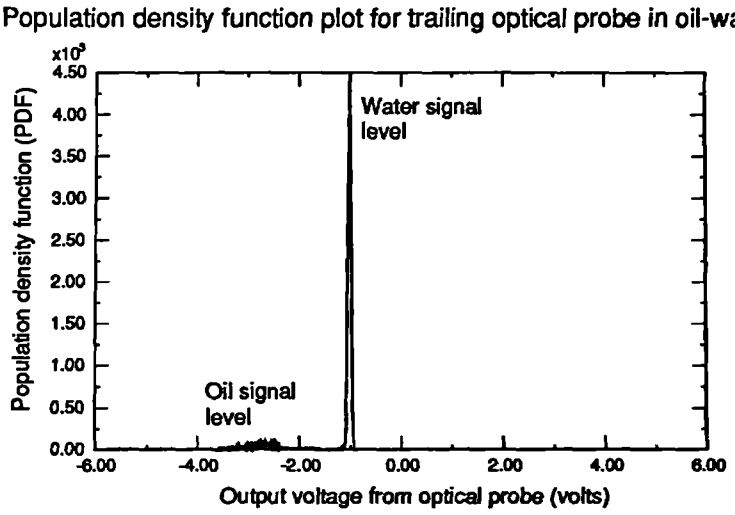

Figure 6.4: Population density function from trailing optical probe signal in oil-water flow

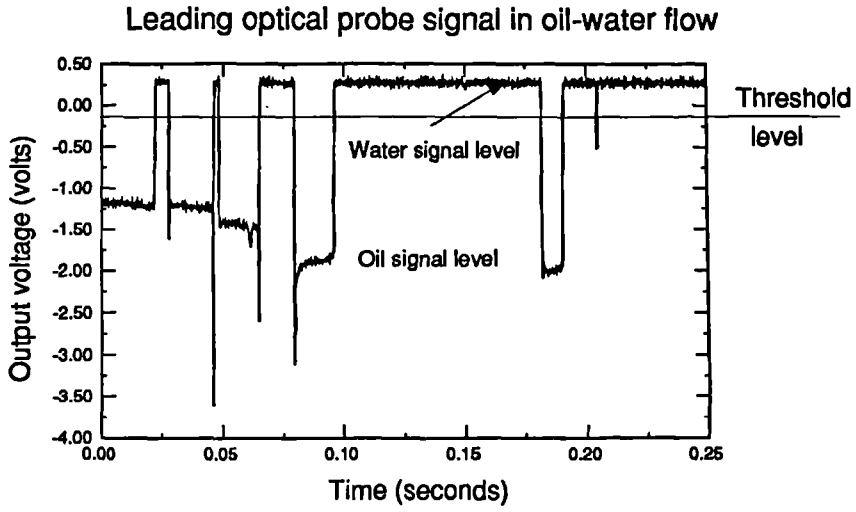

Figure 6.5: Calculation of the oil volume fraction using a thresholding method

reading was 9% (relative error). This dissimilarity between the two optical probes will be discussed shortly.

The two distinct peaks are the water signal level and oil signal level, the water signal level being larger than the oil (water continuous phase). The threshold level was computed by firstly calculating the maximum position of the water signal level i.e. the maximum water PDF and then choosing a level which was below the noise of the total optical signal. The noise of the total system was determined as described in Section 4.2.2 and was found to be 0.2volts. The threshold level taken was 0.4volts below the maximum PDF level for water which ensured that it was below the water baseline noise level and that it was above the minimum oil signal level. The threshold level was found to be a function of probe position and day, hence for each position in the flow, individual threshold levels were computed, for both optical probes.

Once the threshold level had been chosen (see Figure 6.5), this level was then used to compute the start and finish points of passing droplets. Each time the optical signal dropped below the threshold level, this was classed as the start of a droplet and as the signal rose above the threshold level, this was classed as the finish point of a droplet. The start and finish points were then converted into time (seconds) and the difference was summed. The ratio of the residence time (the time spent in the dispersed phase) and the total sampling time is an estimate of the oil volume fraction. The time averaged oil volume fraction is given by Equation 6.1.

With reference to Figure 6.5, an observation of the optical signals show that there are large overshoots in the signal, occurring at the oil signal level. These overshoots are suggested to be due to probe/droplet interactions which occur when the probe tip passes from water to oil or from oil to water i.e. at the start or finish points of the signals or even both. It should be noted that these overshoots are not due to the electronics since they occur randomly and that the amplitudes are not constant. Figure 6.6 shows a schematic diagram of a series of optical probe/droplet interactions. As an oil droplet impacts with the probe (1), high reflection intensities may occur from the lower side of the droplet as shown. These high reflection intensities will be transmitted through the optical fibre and into the photodiode where a large change in the signal will be detected. Similarly, as the droplet departs from the optical probe (2), high reflection intensities may occur from the lower side of the droplet. Figure 6.7, shows a diagram of the fibre-oil-water interface with all the corresponding transmitted and reflected intensities. All the intensities were calculated using Equation 4.3. One can see from the diagram that, when the optical probe is immersed in just oil, the total reflectance is 0.0002. However, if reflection from the water-oil interface occurs e.g. case 1 or 2 in Figure 6.6, the total reflected intensity is increased to approximately 0.015, hence producing an overshoot in the optical signal. It should be noted that, these overshoots always occurred at the oil baseline signal level which was sufficiently below the threshold level, hence not affecting the calculation of the start and finish positions of droplets. Furthermore, this does not affect the oil volume fraction calculation nor the droplet velocity calculation.

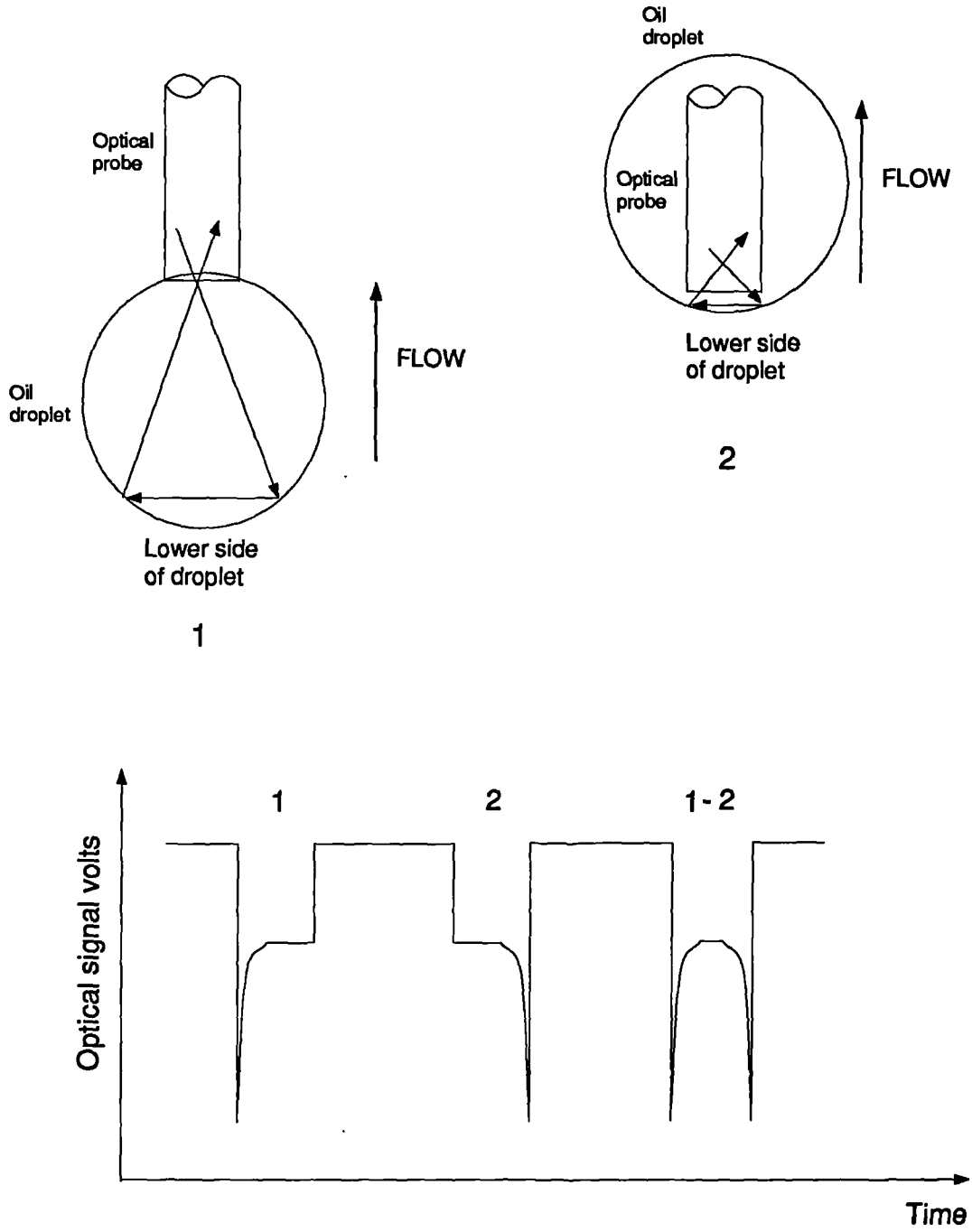

Figure 6.6: Schematic diagram to show cause of overshoots on optical signals

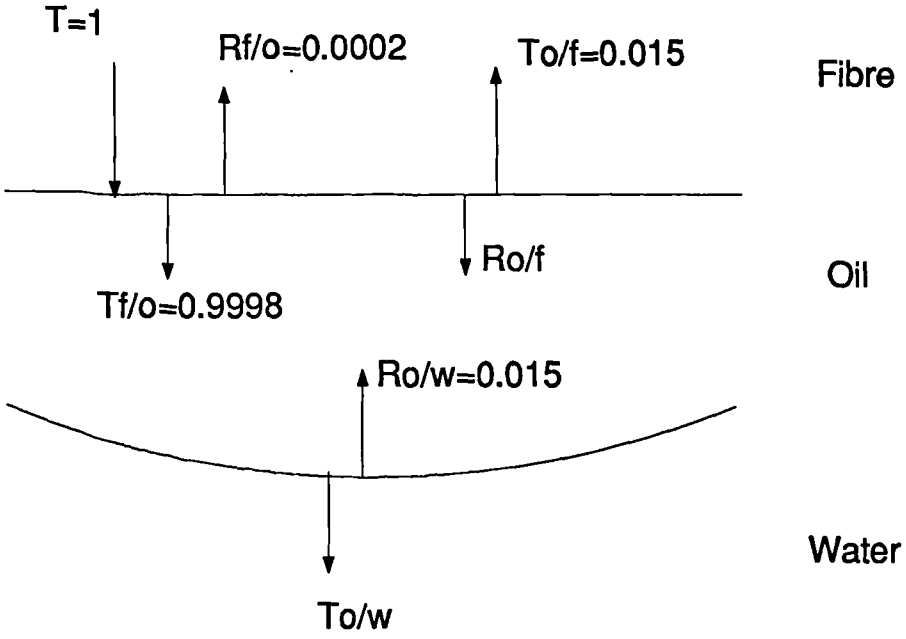

Figure 6.7: Diagram to show transmitted and reflected intensities

The oil volume fraction as calculated from the leading and trailing optical probe were compared. Figure 6.8 shows a plot of the reference measured oil volume fraction against the relative error for the oil volume fraction as calculated from the leading and trailing optical probes. The maximum region for the relative error of the oil volume fraction as calculated from the leading optical probe was +8% to −2%, where as for the trailing optical probe this error was +11% to −9%. Earlier in this section, the PDF's from both optical probes were investigated and it was shown that the oil volume fractions as calculated by both probes were dissimilar. This observation has been confirmed by the relative error results. This discrepancy in the results could be due to the probe/droplet interaction where the droplet deforms and retards while passing through the dual probe. In the following, the oil volume fraction was calculated using the leading optical probe.

6.2.2 Determination of dispersed phase velocity

The dispersed phase velocity was calculated using both optical probes. A similar exercise was carried out on the trailing optical probe signals in order to compute the start and finish points of droplets (see Section 6.2.1).

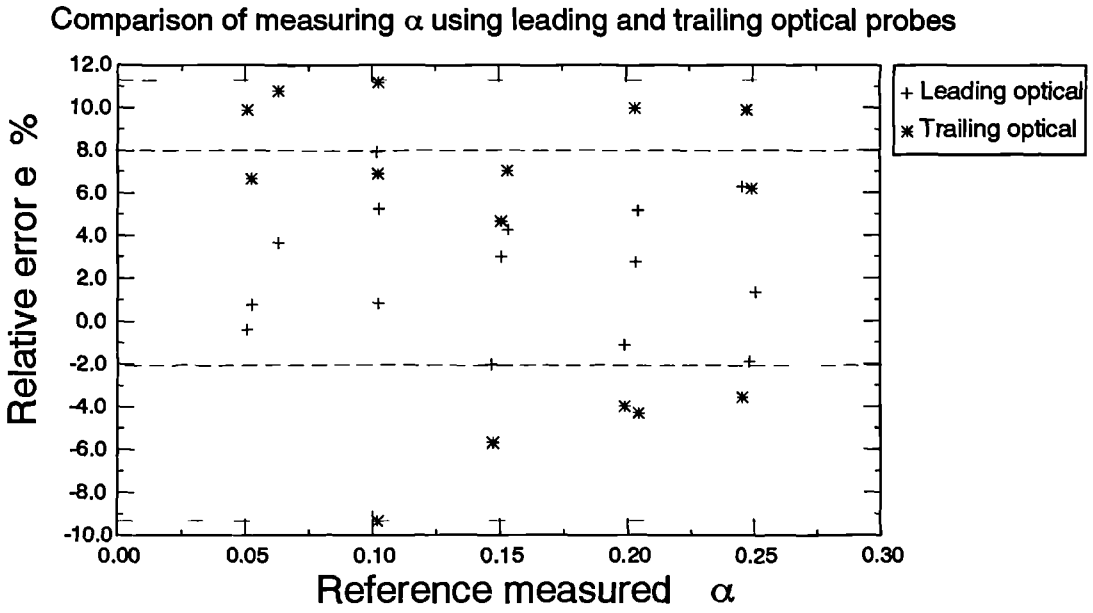

Figure 6.8: Comparison of the oil volume fraction computed by the leading and trailing optical probes

Again, a thresholding method was used for this computation. Two methods were employed to calculate the dispersed phase velocity. These were the time of flight method and cross correlation which are discussed respectively.

Time of flight method

Consider a two phase vertical oil-water flow. During flowing conditions, optical probes 1 and 2 produce signals $X(t)$ and $Y(t)$ respectively (see Figure 6.9). The dispersed phase velocity was computed by calculating the time delay δt_i, between the start points of each droplet. The instantaneous droplet velocity, U_i is given by:

$$U_i = \frac{y}{\delta t_i} \tag{6.2}$$

where y is the known separation between the two optical probes. This calculation was carried out with a droplet impacting both probes. For a significant part of the time series, the same droplets were seen to impact both probes. However, on occasions a droplet was seen to impact only one of the probes. A criterion was set so that if the leading edge of the droplet as detected by optical probe 2 was greater than 10ms (i.e. 0.1ms^{-1}), with reference to the leading edge of probe 1, this droplet would be disregarded from the calculation. An example where a droplet has made contact with the leading and not the

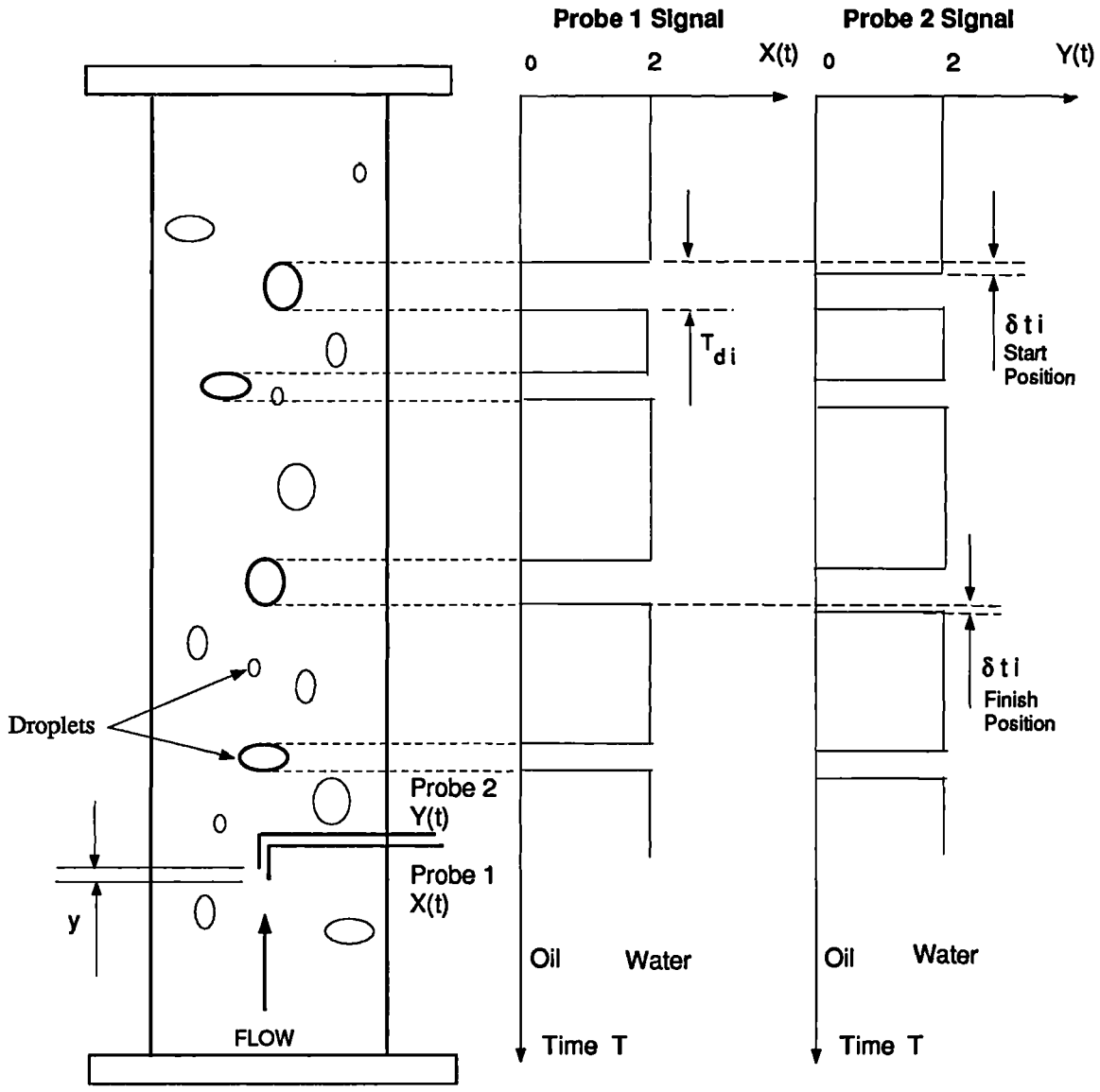

Figure 6.9: Schematic diagram to show determination of dispersed phase velocity

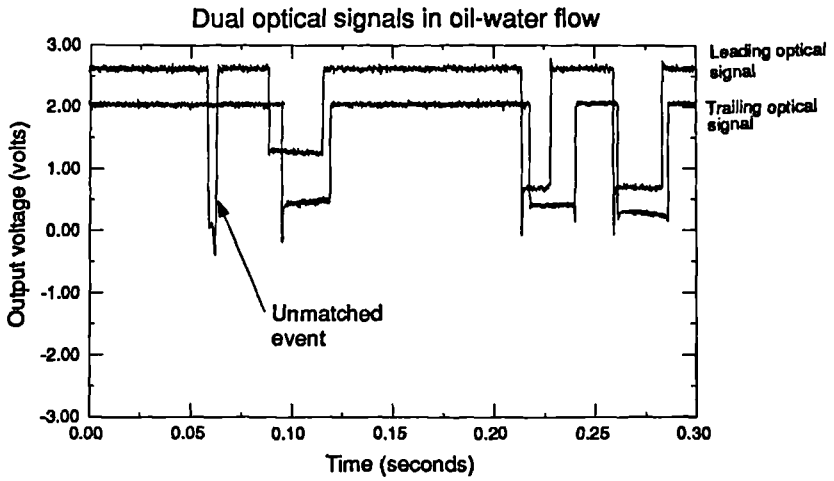

Figure 6.10: An example of a droplet hitting the leading probe and not the trailing probe

trailing optical probe, can be seen in Figure 6.10. The oil superficial velocity, $\overline{U_j^{ds}}$, at a position j in the flow, is given by:

$$\overline{U_j^{ds}} = \frac{1}{T}\sum_{i=1}^{N_i} U_{ij}T_{dij} \tag{6.3}$$

where T_{dij} are the residence times of each event and T is the total sampling time. The residence time for each event was computed from the leading optical probe signal and was used as a 'weighting' function. This ensured that each calculated droplet velocity was not biassed because of the droplet size. For instance, if a significant number of large droplets having a greater velocity than the mean oil velocity were detected, then the calculation of the mean oil velocity at that position would have been overestimated.

For comparison reasons, the time of flight method was also applied to the finish points of the signals to compute the dispersed phase velocity (see Figure 6.9). Figure 6.11 shows a plot of the reference measured oil superficial velocity against the relative error e for the oil superficial velocity as calculated using the start and finish points of the optical signals. The maximum region for the relative error of the oil superficial velocity as measured by the start points was $+7\%$ to -5% and the finish points was -3% to -14%. The regions plotted, for the start and finish points, show that the results are similar except that one region is overestimating and the other, underestimating. In order to gain a better estimate of the oil velocity, the average relative error between the start and finish points was calculated. As one can see, the region of relative error

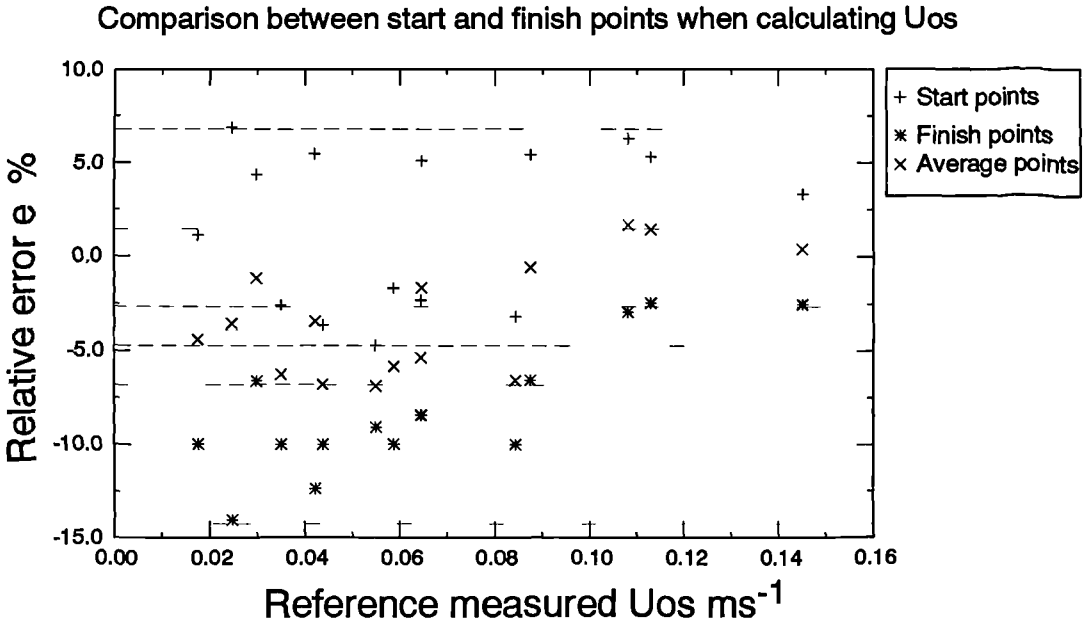

Figure 6.11: Comparison of time of flight method using start and finish points to compute the oil superficial velocity

has decreased to a range of $+2\%$ to -7%. In the following, the instantaneous droplet velocity, U_i, was calculated using both the start and finish points, of the optical signal, and averaging the calculated velocities, by using:

$$U_i = \frac{U_1 + U_2}{2} \tag{6.4}$$

where U_1 and U_2 are the instantaneous droplet velocities calculated using the start and finish points respectively (see Equation 6.2). This analysis technique is known as the averaged time of flight method.

Cross correlation method

The second method is the cross correlation technique. This signal analysis technique was used by other authors e.g. Moujaes and Dougall [1987]. With reference to Figure 6.9, the cross correlation function $\lambda_{xy}(\tau)$ derived from the two signals $X(t)$ and $Y(t)$ is defined as :

$$\lambda_{xy}(\tau) = \lim_{T\to\infty} \frac{1}{T} \int_0^T X(t)Y(t+\tau)dt \tag{6.5}$$

where τ represents an averaged time delay and T is an appropriate averaging time. Knowing the distance between the two optical probes, the dispersed

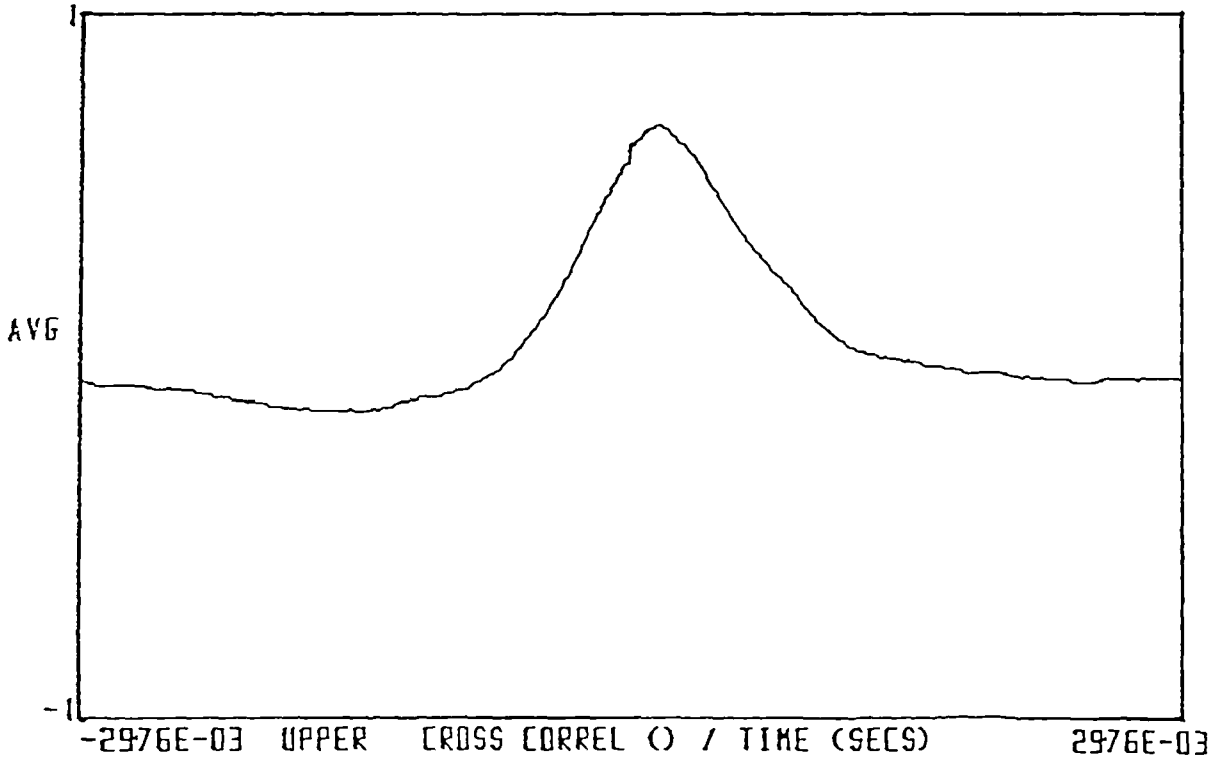

Figure 6.12: Magnitude of cross correlation function

phase velocity is given by:

$$U_j^x = \frac{y}{\tau_{maxj}} \tag{6.6}$$

where y is the distance between the two optical probes and τ_{maxj} is the mean transit time of the dispersed phase at position j in the flow. An example of a measured cross correlation function is given in Figure 6.12. In order to evaluate the techniques, the cross correlation method was compared to the averaged time of flight method. Figure 6.13 shows a plot of the reference measured oil superficial velocity against the relative error for both analysis techniques. The maximum region for the relative error of the oil superficial velocity as calculated using the averaged time of flight method was +2% to −7%. However, the maximum region for the relative error of the oil velocity as calculated using the cross correlation technique was +23% to −5%. One of the drawbacks in using the cross correlation technique is that the entire time series is integrated which results in overestimation of the oil velocity. Also, by using the cross correlation method, equal weighting of droplets is not taken into account compared to the averaged time of flight method.

The mean oil superficial velocity was calculated by using the averaged time of flight method (using start and finish points of the droplets, see Equation 6.3) for the data presented in the results section.

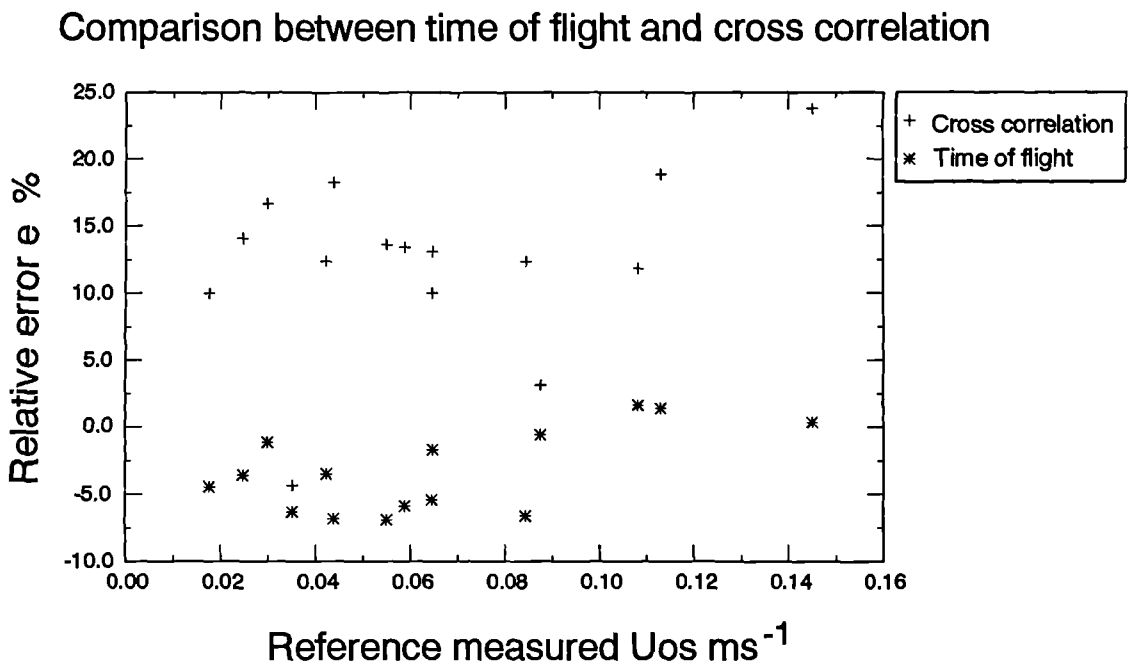

Figure 6.13: Comparison of cross correlation and time of flight analysis techniques to measure the oil superficial velocity

6.2.3 Determination of droplet cut chord length

In order to assess the 'size' distribution of oil droplets across the pipe section, the droplet cut chord length was calculated. Since the exact shape of the droplets and position at which the optical probe interacts with the droplet is not known, it has been assumed that the following calculation is an approximate estimation of the droplet size; hence the name droplet cut chord length. With reference to Figure 6.9, the droplet cut chord length for each droplet, C_i, is given by:

$$C_i = U_i T_{di} \tag{6.7}$$

where U_i is the averaged instantaneous droplet velocity, as calculated by the start and finish points of the signal, and T_{di} is the droplet residence time. The mean droplet cut chord length, at a position j in the flow, is given by:

$$\bar{C}_j = \frac{1}{N}\sum_{i=1}^{N} U_{ij} T_{dij} \tag{6.8}$$

where N is the total number of matched droplets.

6.2.4 Determination of the continuous phase velocity

This section is presented in two parts. The calculation of the water velocity using the dual probe and the dual split-film probe will be discussed respectively.

The dual probe

The continuous phase velocity is calculated using the signal from the hot-film anemometer $E(t)$ and the signal from the leading optical probe $X(t)$. The positioning of the leading optical probe in line with the hot-film anemometer allows the removal of the dispersed phase signal from the total hot-film signal. Once the dispersed phase signals have been removed, from the hot-film signal, the parts of the signals due to the continuous phase should remain. Consider a vertical two phase oil-water flow. With reference to Figure 6.14, the passages of droplets are illustrated by the points D. By removing the parts of the signal associated with the dispersed phase (D), the continuous phase signal will remain (curve C). Since the start and finish positions have been defined (see Section 6.2.1) from the leading optical signal, the same positions can be 'mapped' onto the hot-film signal. The start and finish points are illustrated by points b and a respectively. The part of the hot-film signal which lies in between points b and a are removed to leave the signal associated with the continuous phase velocity.

In order to use the above technique for analysing the hot-film signals in real oil-water flows, the maximum and minimum values of the hot-film signal at a single measuring position, were computed. The mid-point between the two values was calculated. This mid-point value was used for a check routine which will be described shortly. The start and finish points of each droplet, as computed by the leading optical probe, were mapped onto the hot-film signal, as described earlier. As a check, the maximum and minimum values were calculated for the remaining signals, after removal of the dispersed phase signal (curve C in Figure 6.14). The minimum value was then compared to the mid-point value, as calculated for the entire raw signal trace before analysing with the optical probe. If the minimum value fell below the mid-point value, this suggested that a droplet had not been detected by the optical probe. Since the distance between the optical probe and the hot-film sensor was of the order of 0.1mm (δz Figure 4.22), this occurrence was rare.

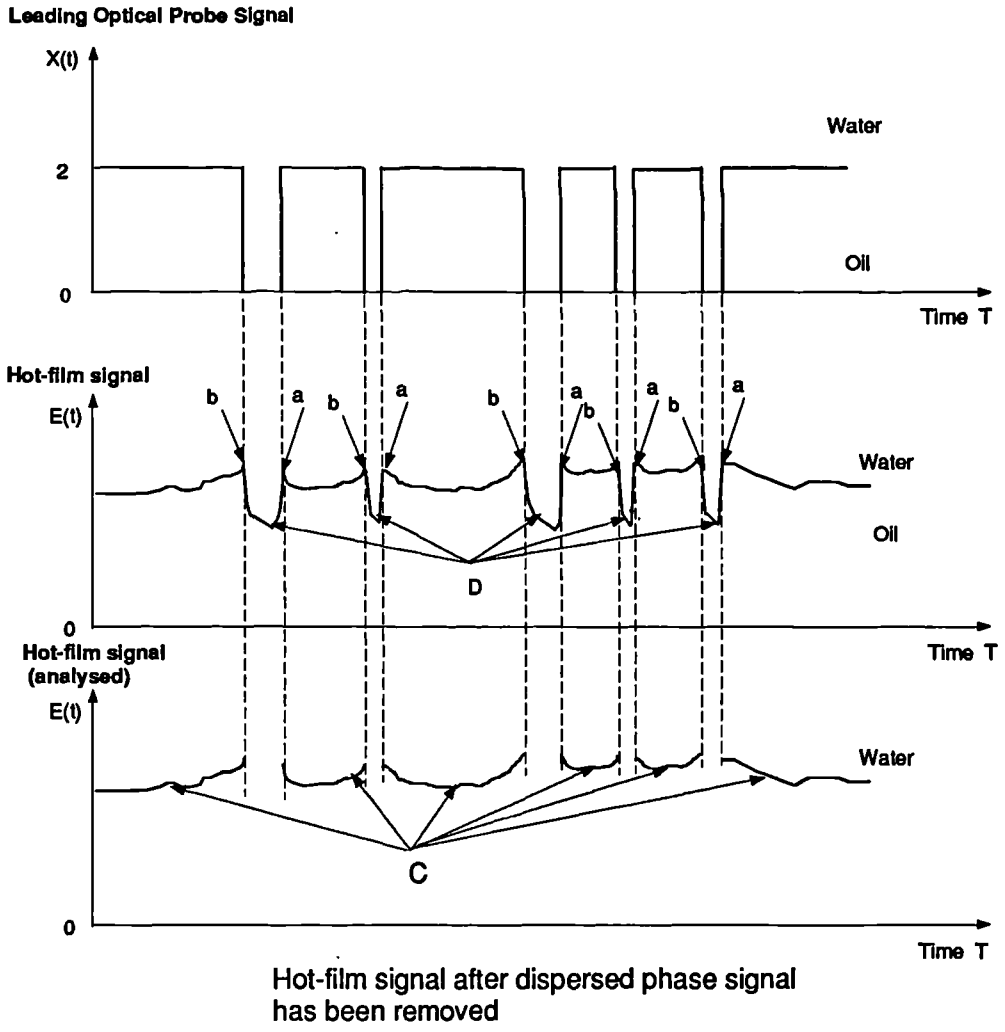

Figure 6.14: Schematic diagram to show determination of continuous phase velocity

For each data point voltage value, $E_j(t)$ (where j is the position of the probe within the pipe) of the remaining signal, the velocity of each data point was calculated using the calibration data for the hot-film anemometer (see Section 4.5). The velocity of each data point within the time trace of the remaining signal is given by:

$$U_j(t) = \frac{1}{\mathcal{B}^2}\left(\frac{E_j^2(t)}{\gamma} - \mathcal{A}\right)^2 \tag{6.9}$$

where $\mathcal{A}$ and $\mathcal{B}$ are the calibration constants and γ is the overheat ratio. Hence, the local mean actual continuous phase velocity $\overline{U_j^c}$ is given by:

$$\overline{U_j^c} = \frac{1}{N_j}\sum_{i=1}^{N_j}\frac{1}{(t_b - t_a)}\sum_{i=1}^{N_j}\int_{t_a}^{t_b} U_j(t).dt \tag{6.10}$$

where t_a and t_b are the start and finish points of the signal associated with the continuous phase, respectively. In order to compare the continuous phase velocity results from the hot-film anemometer and the water turbine meter, the water superficial velocity was calculated from the hot-film signal, $\overline{U_j^{cs}}$, and is given by:

$$\overline{U_j^{cs}} = \overline{U_j^c}(1 - \bar{\alpha}_j) \tag{6.11}$$

where $\overline{U_j^c}$ is given by Equation 6.10 and $\bar{\alpha}_j$ is given by Equation 6.1.

Figure 6.15 shows typical traces from the leading optical probe signal and the hot-film signal. One can see that the optical probe signal matches well with the hot-film signal hence justifying the mapping of the start and finish points of the dispersed phase onto the hot-film signal. Previous workers e.g. Farrar [1988], have used sophisticated software to analyse the complex hot-film signals in oil-water flows. Identification of passing droplets within an unstable background signal level (hot-film signals) is the major problem encountered when analysing hot-film signal. The advantage of using an optical probe is that it provides an 'on-off' signal driven by the phase present at the measuring optical tip. This provides a stable background level with clear discontinuities showing the passages of the dispersed phase. Hence the analysis of the optical signals are much simpler than for the hot-film signals and by utilising this simplicity, the complexity of identifying droplets on the hot-film signal is removed. In some cases of deviated flow (bottom side of the pipe see Section 6.4.2), there were no events recorded on the optical signals. If this type of optical signal was encountered (i.e. no oil droplets), then the entire hot-film signal was analysed to calculate the continuous phase velocity.

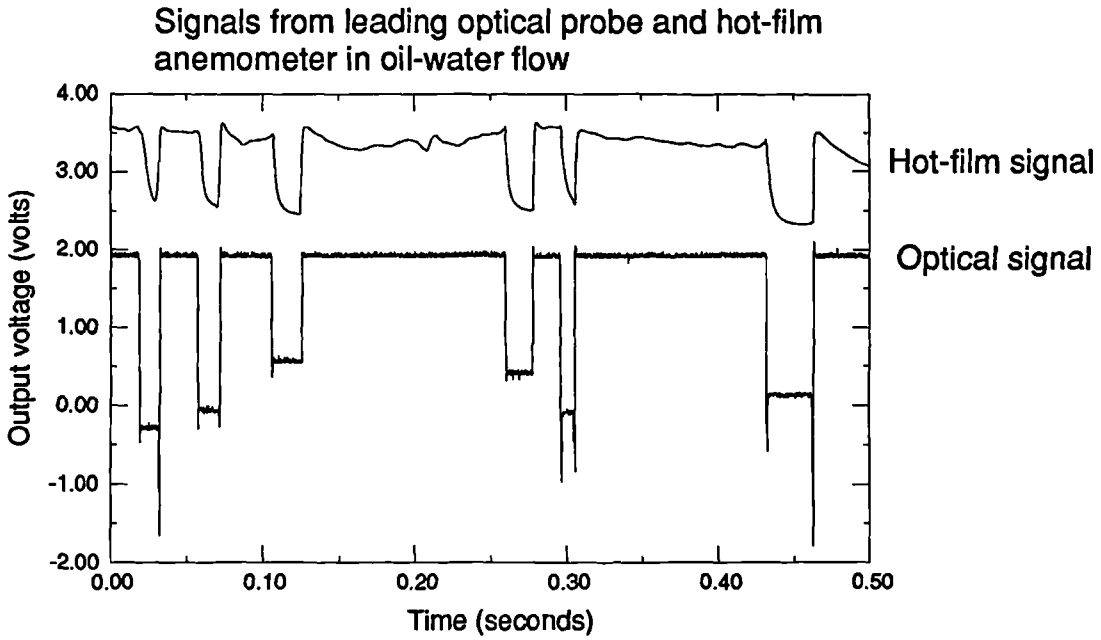

Figure 6.15: Example of the correlation between the leading optical probe and the hot-film anemometer

The dual split-film probe

The advantage of using a split-film anemometer is that it provides the magnitude and direction of the water velocity, axial to the sensors. An optical probe positioned close to the sensing area of the split-film sensor (see Figure 4.27) was used to remove the parts of the split-film signal associated with the dispersed phase (similar to hot-film signals). Consider a vertical two phase oil-water flow with water as the continuous phase. With reference to Figure 6.16, the passage of oil droplets is illustrated as the points D. As described earlier, the part of signal associated with the dispersed phase are mapped onto the split-film signals for removal. The parts of the signal, from the split-film, associated with the continuous phase will remain. Figure 6.17 shows, for real oil-water flow, output traces from the leading optical probe and the two split-film sensors. For each of the split-film sensors, the data points of the remaining signal are converted into Nusselt numbers (see Equation 4.18). Equation 6.12 gives the average Nusselt number, at a position j in the pipe, for the leading split-film sensor and is denoted by the number 1:

$$\overline{Nu_{1j}} = \frac{1}{N_j}\sum_{i=1}^{N_j}\frac{1}{(t_b - t_a)}\sum_{i=1}^{N_j}\int_{t_a}^{t_b} Nu_{1j}(t).dt \qquad (6.12)$$

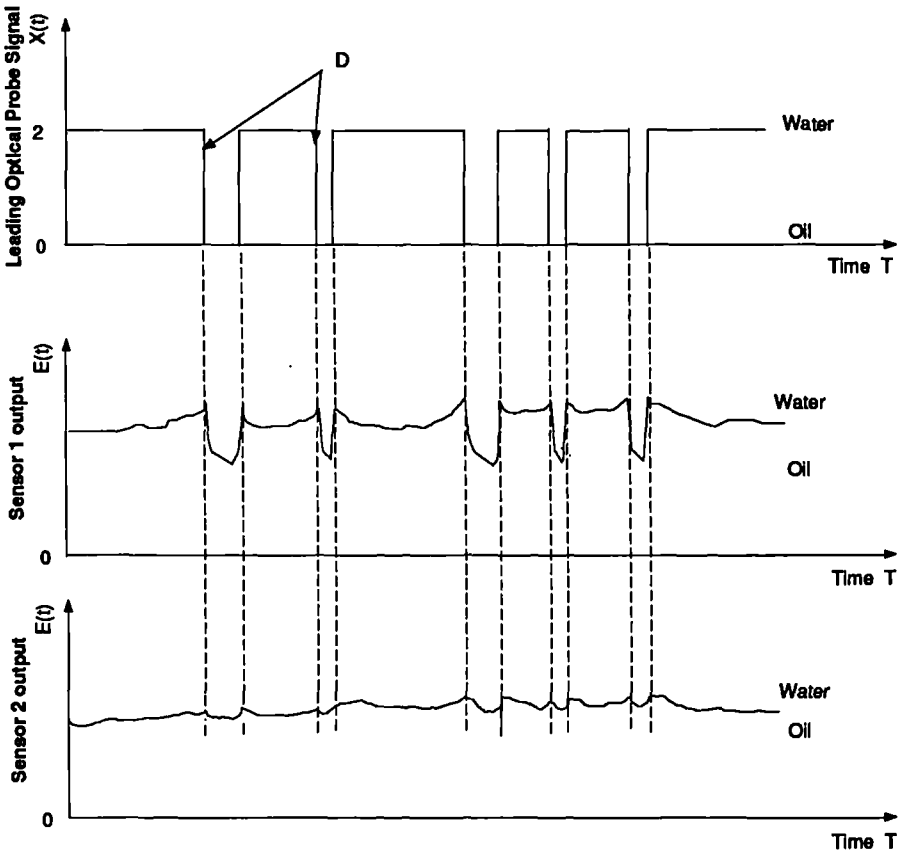

Figure 6.16: Schematic diagram to show determination of the continuous phase velocity from split-film signals

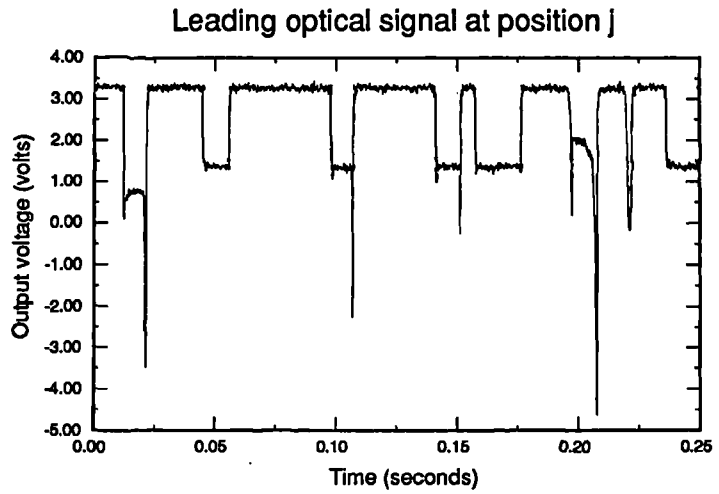

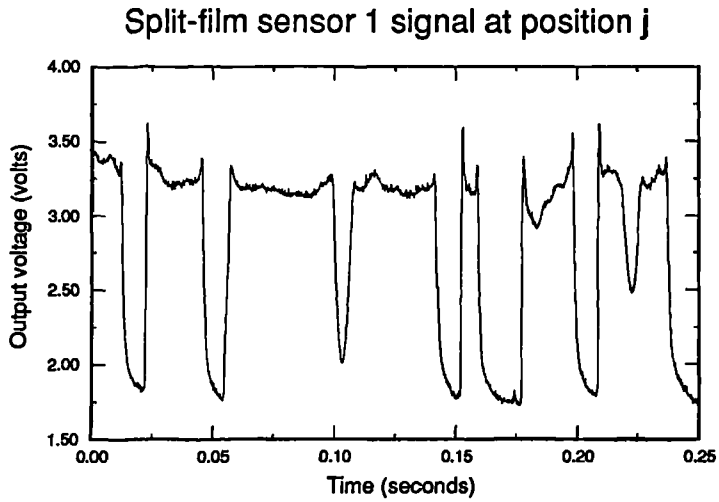

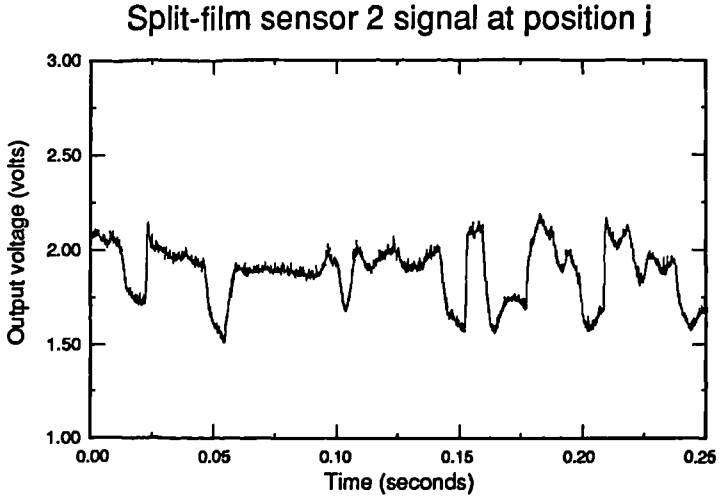

Figure 6.17: Traces from the dual split-film probe

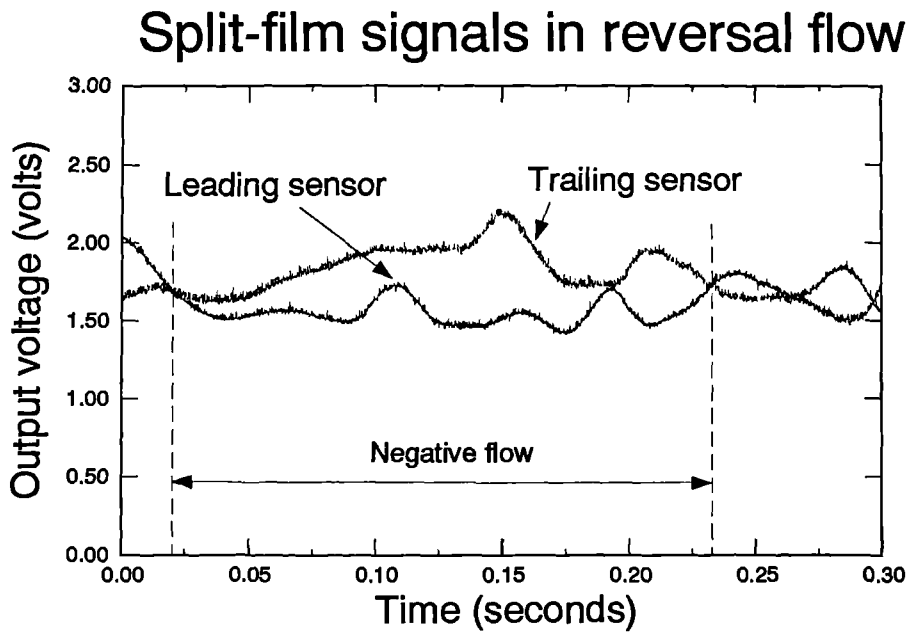

Figure 6.18: Illustration of back flow as indicated

Once the average Nusselt numbers had been computed for both sensors, the values were then summed. This is given by:

$$\sum Nu_j = \overline{Nu_{1j}} + \overline{Nu_{2j}} \tag{6.13}$$

The sum of the Nusselt numbers, $\sum Nu_j$, was then used to compute the magnitude of the continuous phase velocity by using the calibration of the split-film probe (see Section 4.8). The next step was to calculate the difference in Nusselt numbers which is given by:

$$\Delta Nu_j = \overline{Nu_{1j}} - \overline{Nu_{2j}} \tag{6.14}$$

The difference of the Nusselt numbers gave the direction of the flow with respect to the orientation of the split-film probe. Sensor 1 was always the leading sensor i.e. the sensor facing the flow. If ΔNu_j happened to be a negative number, this was regarded as a back flow. Figure 6.18 shows an instance where back flow was detected from $t = 0.02$s to $t = 0.23$s.

6.2.5 Determination of local slip velocities

In oil-water flows, the local slip velocity is defined as the relative velocity of oil to that of water. The mean local slip velocity, $\bar{U}_{sj}$, at a position j in the flow, is defined as:

$$\bar{U}_{sj} = \bar{U}_{oj} - \bar{U}_{wj} \tag{6.15}$$

where $\bar{U}_{wj}$ is the mean actual water velocity, given by Equation 6.10, and $\bar{U}_{oj}$ is the mean actual oil velocity which is given by:

$$\bar{U}_{oj} = \frac{\bar{U}_j^{ds}}{\bar{\alpha}_j} \tag{6.16}$$

where $\bar{U}_j^{ds}$ is given by Equation 6.3 and $\bar{\alpha}_j$ is given by Equation 6.1. In the literature, local slip velocities were not computed since there was no measure of either the water velocity or the oil velocity. Global slip velocities were computed by integrating the water or oil velocity over the pipe section and then to compute the other phase velocity via the turbine meter. As an example Vigneaux [1988] calculated the mean actual oil velocity over the pipe cross section by using a Resistivity probe. The actual water velocity was calculated from turbine meters, hence the global slip velocity was computed using Equation 6.15. Since the dual probe and the dual split-film probe can measure both the oil and water velocity, at the same time, the local slip velocities can be computed over the entire pipe cross section. To the present date, no one has been able to measure the local slip velocity.

6.3 Calculation of mean quantities over pipe cross-section

All the positional values of calculated oil volume fraction, water velocity and oil velocity were integrated over the pipe cross-section to yield their mean quantities. These mean quantities were then compared to the reference meters to calculate the relative error. The number of measuring positions were given in Section 5.5.3. Figure 6.19 shows the notational diagram used to calculate the areas associated with each measuring position. The area at a measuring position j is given by:

$$A_j = \frac{\pi}{12}\left(r_{j+1/2}^2 - r_{j-1/2}^2\right) \tag{6.17}$$

where $r_{j+1/2}$ and $r_{j-1/2}$ are the radial distances used to calculate the associated areas. The mean quantities, $\bar{x_A}$, integrated over the pipe cross-section is given by:

$$\bar{x}_A = \frac{1}{A}\sum_{j=1}^{N} \bar{x}_j A_j \tag{6.18}$$

where A is the total cross-sectional area, N are the total number of measuring and reflected positions (see Section 5.5.2) and the subscript j denotes the position. This equation was used to calculate, from the probes, the mean water superficial velocity, the mean oil superficial velocity, the mean oil volume fraction and the mean slip velocity.

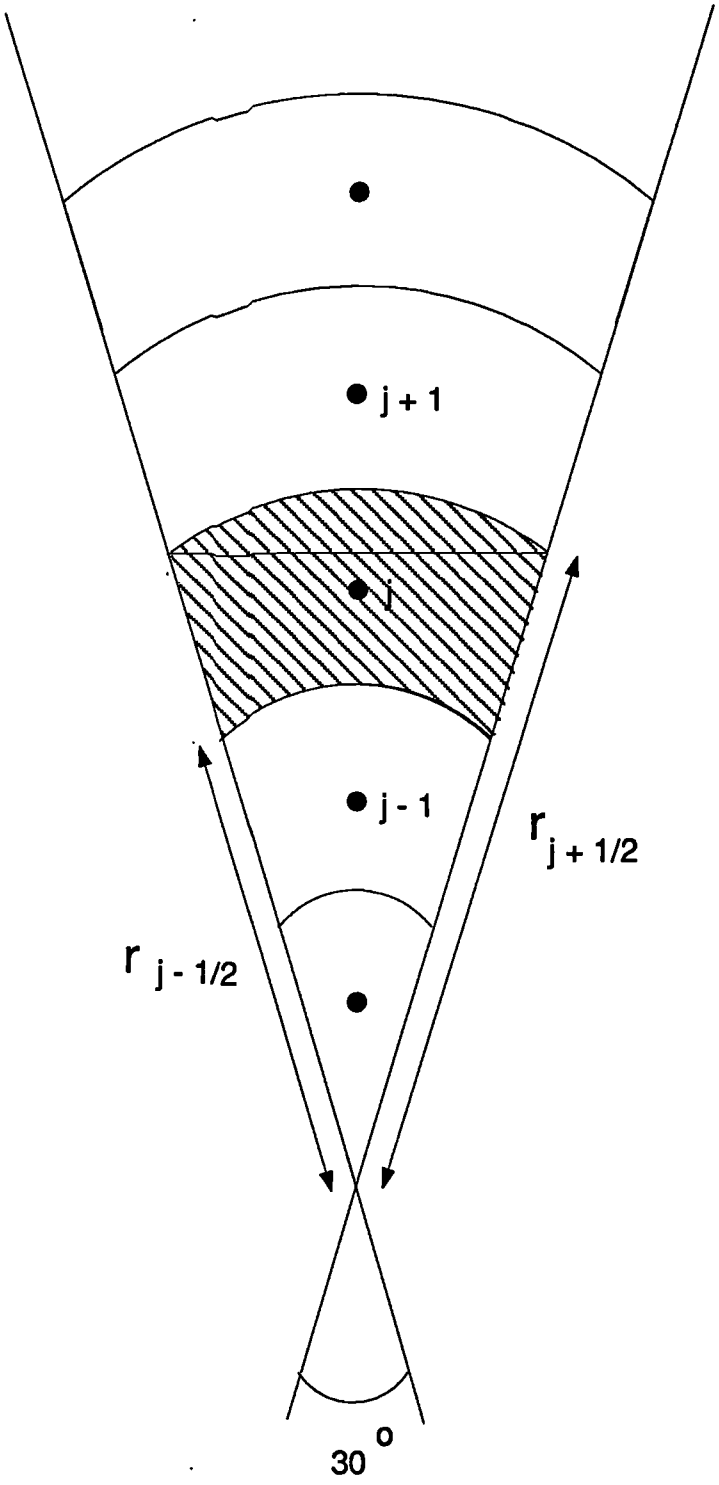

Figure 6.19: Notational diagram used for calculating sector areas

6.4 Results

In this section, the results obtained from both the dual probe and the dual split-film probe at various deviation angles are discussed. The experimental program carried out for both probes can be seen in Section 5.6. The results given below will be in the form of contour plots and profiles (see Figure 6.1). The profile plots show the measured profiles at measuring positions from the bottom side of the pipe (negative) to the top side of the pipe (positive) along a single diameter (zero is the centre of the pipe). As mentioned in Section 6.2, the integrated probe results were compared to the reference measurements. These results are tabulated below the profile and contour plots for that particular flow condition. The relative errors between the integrated results and the reference results are also given. For all relative error plots, plotted on the horizontal axes are the reference measurements and on the vertical axes are the relative errors. Horizontal lines are drawn to show the maximum region of the relative error data. Comparative results are given for the continuous phase velocity. As an example, reference to Figure 6.29, comparison of profile and contour plots for the continuous phase velocity as measured by the dual probe and the dual split-film probe are given.

6.4.1 Vertical flow

The tests in vertical flow were carried out using the dual probe. Figure 6.20 shows typical profile and contour plots measured from the dual probe in vertical oil-water flow. It should be noted that the oil velocity profiles given in Figure 6.20 are calculated using the time of flight method and the start and finish points of matched events (see Section 6.2.2). Also, the oil volume fraction is calculated using the leading optical probe (see Section 6.2.1). The results shown in Figure 6.20 were taken at a mean oil volume fraction $\bar{\alpha}$ of 0.1 or 10%. It can be seen that all profiles are rounded with their peak value at the centre of the pipe and minimum value at the walls. Similar shaped profiles were reported by Farrar [1988].

In order to evaluate the performance of the dual probe, the integrated results were compared to the reference meters. Figure 6.21 shows the plots of the reference measured velocity and oil volume fraction against the relative error results from the dual probe. There is a good agreement for all three measurements made by the dual probe against the reference meters.

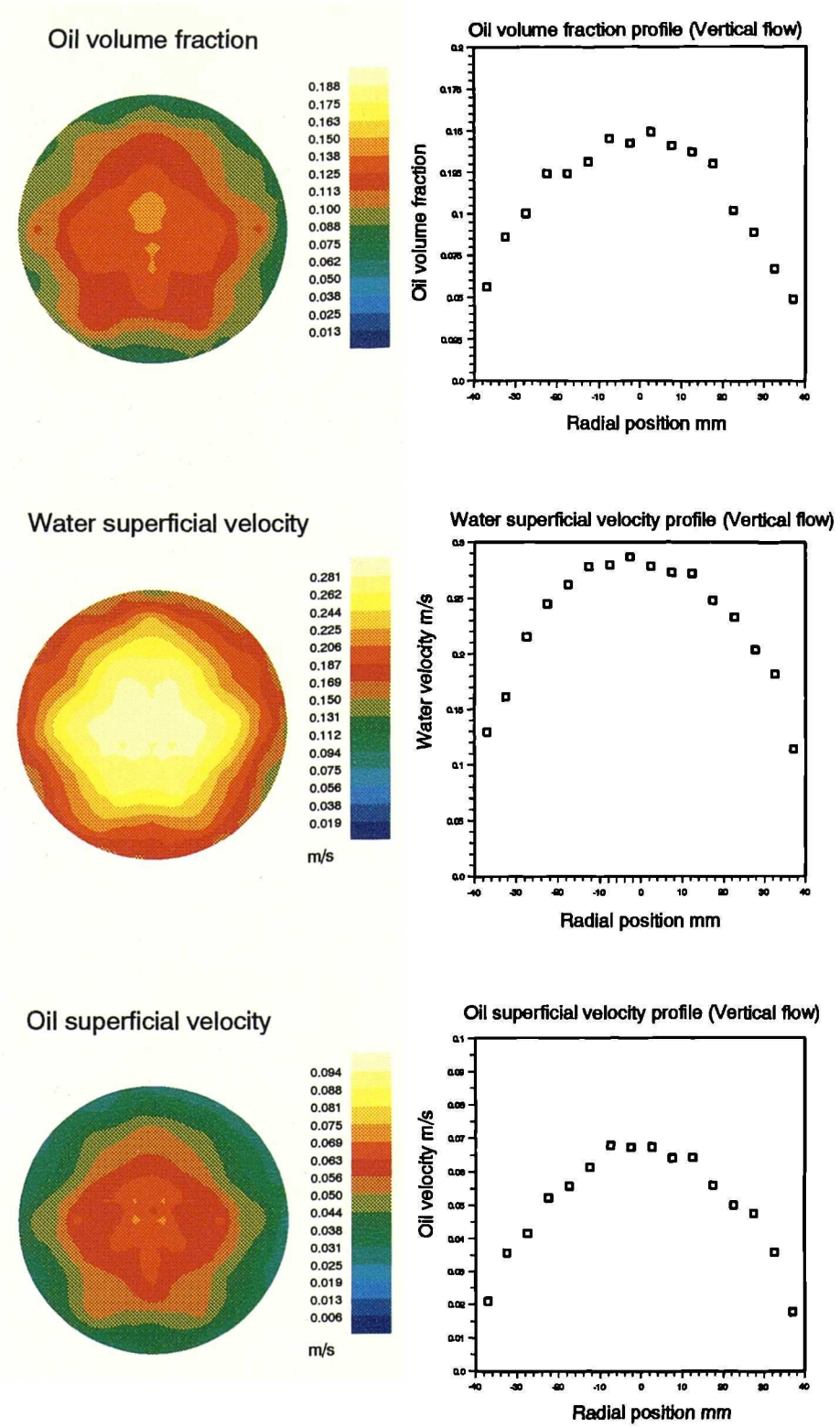

	Reference results	Integrated probe results
α	0.106	0.103
Uws m/s	0.201	0.196
Uos m/s	0.046	0.044

Figure 6.20: Measured velocity and volume fraction profiles in oil-water vertical flow (dual probe)

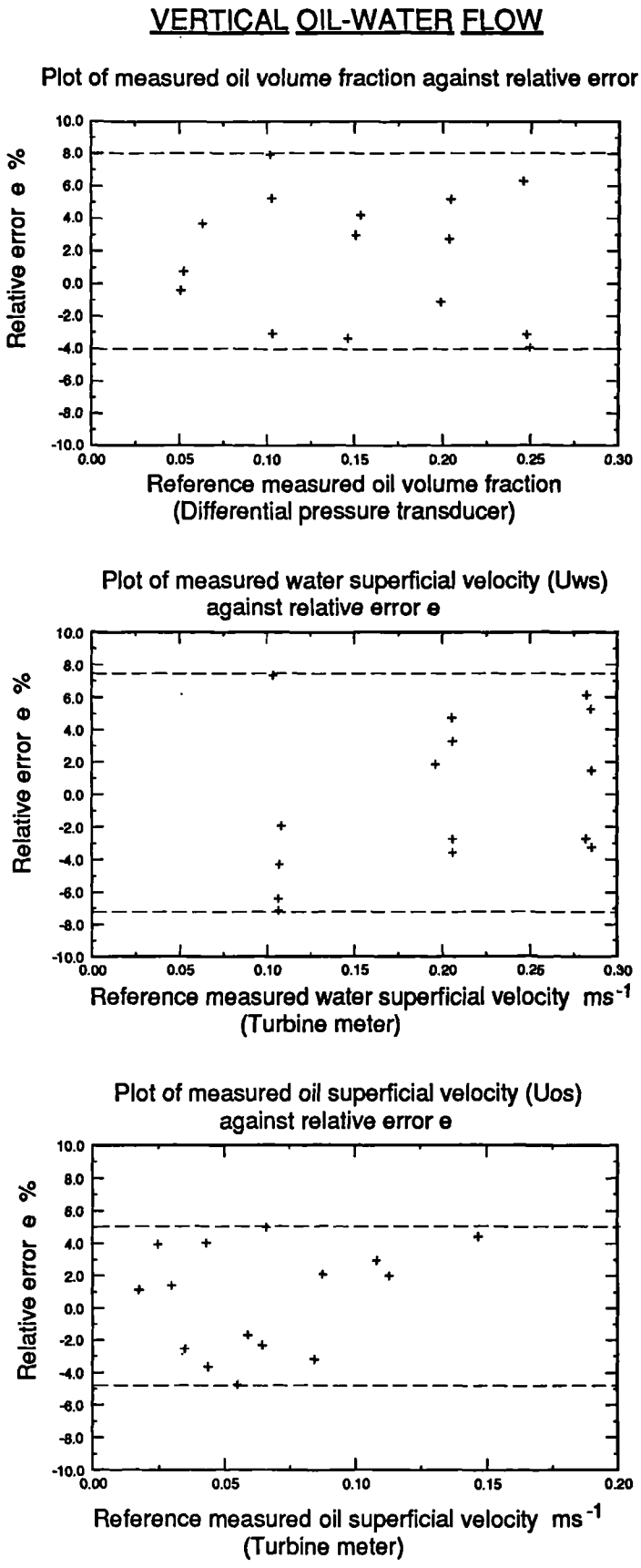

Figure 6.21: Comparison of reference measurements against integrated dual probe measurements (relative error)

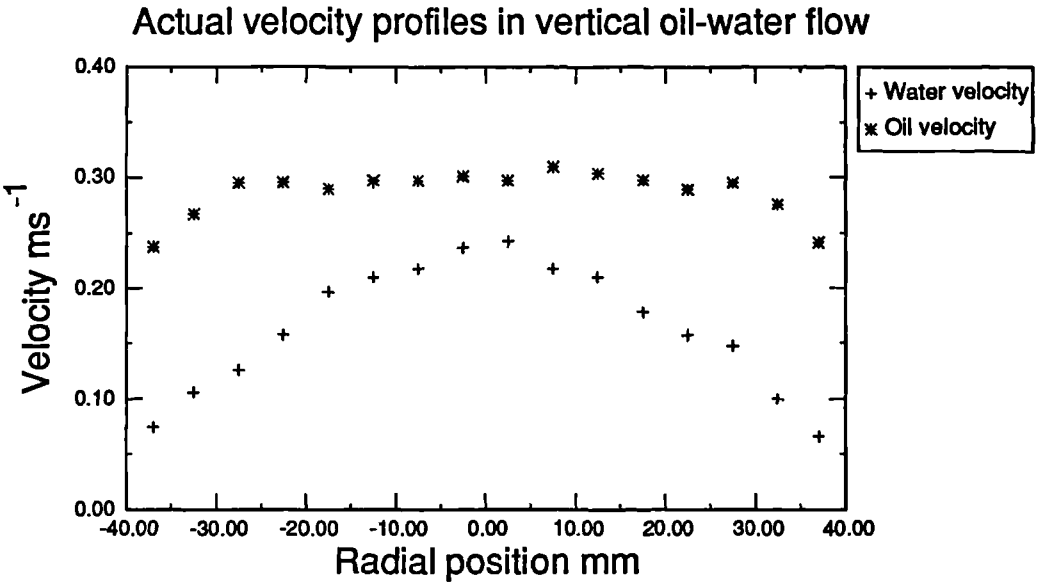

Figure 6.22: Actual velocity profiles in vertical oil-water flow

Typically, the maximum relative error for the oil volume fraction was +8% to −4%. A similar result of ±7% was attained for the water superficial velocity. The relative error for the oil superficial velocity was slightly lower at ±5%.

In order to aid discussions on slip velocity profiles, Figure 6.22 shows a profile plot of the actual water and oil velocities. For this particular case, the water superficial velocity was 0.1ms^{-1}, the oil superficial velocity was 0.042ms^{-1} and the oil volume fraction was 15%. The positional (local) slip velocity is given by the difference in the actual oil velocity and the actual water velocity, for that particular position (see Equation 6.15).

With reference to Figure 6.23, the slip velocities have been plotted as a function of radial position (similar to profile plots). Five graphs are presented, which vary as a function of oil volume fraction and water superficial velocity. Viewing the 5% oil volume fraction profile, one can see that as the water superficial velocity decreases, the slip velocity profile becomes more dipped at the centre. This trend was seen for all five plots. The reason for this trend is because as the water superficial velocity decreases, less turbulent mixing will occur and hence the droplets will tend to their natural rise velocity (approximately 0.15ms^{-1}). In order to assess how the slip velocity varies as a function of oil volume fraction, the global slip velocities were calculated using Equation 6.18, where $\bar{x_j}$ is the local slip velocity. With reference to Figure 6.24, the global slip velocities have been plotted against the reference measured oil

volume fraction. The curves have been banded with respect to the water superficial velocity. As one can see, at low oil volume fractions ($5-10\%$), the slip velocity is greater than that at higher oil volume fractions. As the oil volume fraction increases, the oil concentration within the pipe section increases hence producing closely packed oil droplets. Since the concentration has increased, this reduces the oil velocity hence the slip velocity. An interesting observation is that with increasing water superficial velocity, the slip velocity increases. It is thought that this is due to undeveloped flow and that the data set should collapse onto a single curve. In order to answer this suggestion, further work is required in developed flow; this is outside the scope of this thesis.

The global slip velocities are calculated from the locally measured water and oil velocities. To date, no data has been presented to suggest how the true slip velocity varies as a function of radial position or as a function of oil volume fraction. The curves presented in Figure 6.24 can be used to determine either the oil velocity or water velocity. As an example, if one was measuring the oil velocity using just optical probes and by measuring the global oil volume fraction (differential pressure transducer) and water superficial velocity (turbine meter), the actual water velocity can be computed. This computation of either the oil velocity or water velocity can be applied to deviated flows (see next sections).

With reference to Figure 6.25, the droplet cut chord length is plotted as a function of radial position across the pipe diameter. One can see that, as the oil volume fraction increases, the droplet cut chord length profiles become less peaked and tend to a constant droplet size of 4mm. It was seen from the slip velocity results, that as the oil volume fraction increases, the oil droplets become closely packed. This observation has been confirmed by the droplet cut chord length profiles since one sees a 'flatter' droplet size distribution across the pipe section.

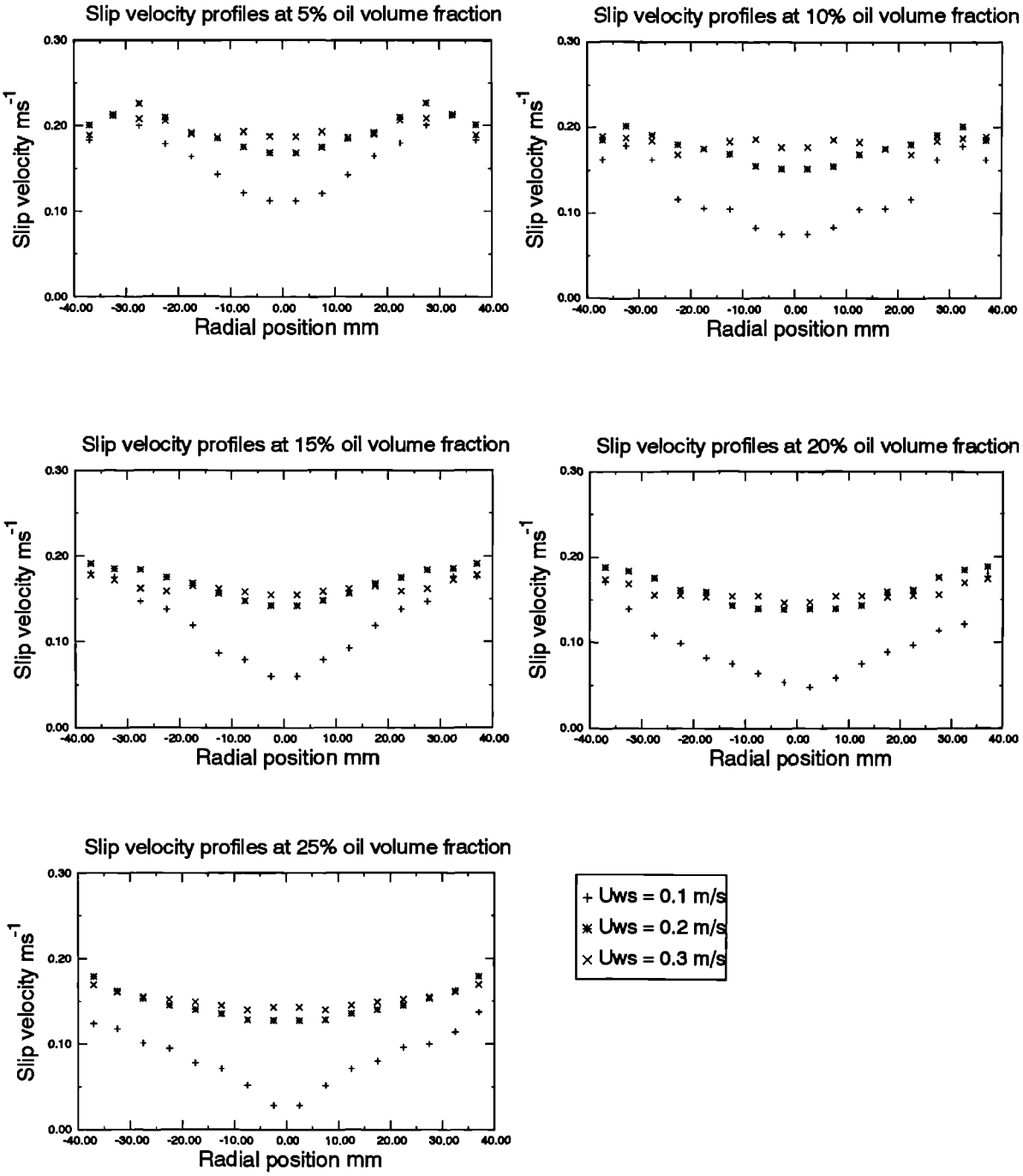

Figure 6.23: Plot of local slip velocities against radial position

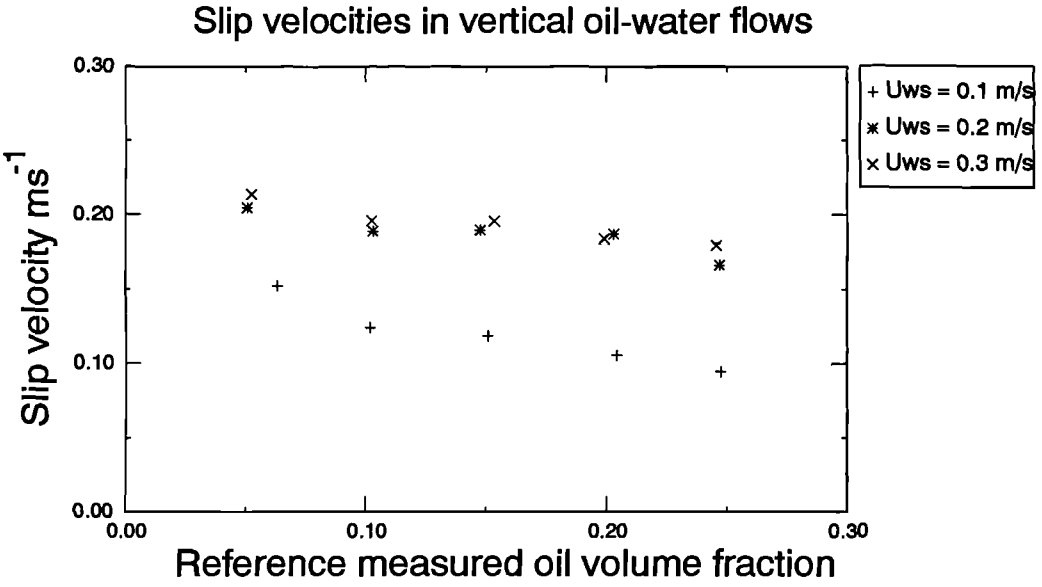

Figure 6.24: Plot of global slip velocities against reference measured oil volume fraction

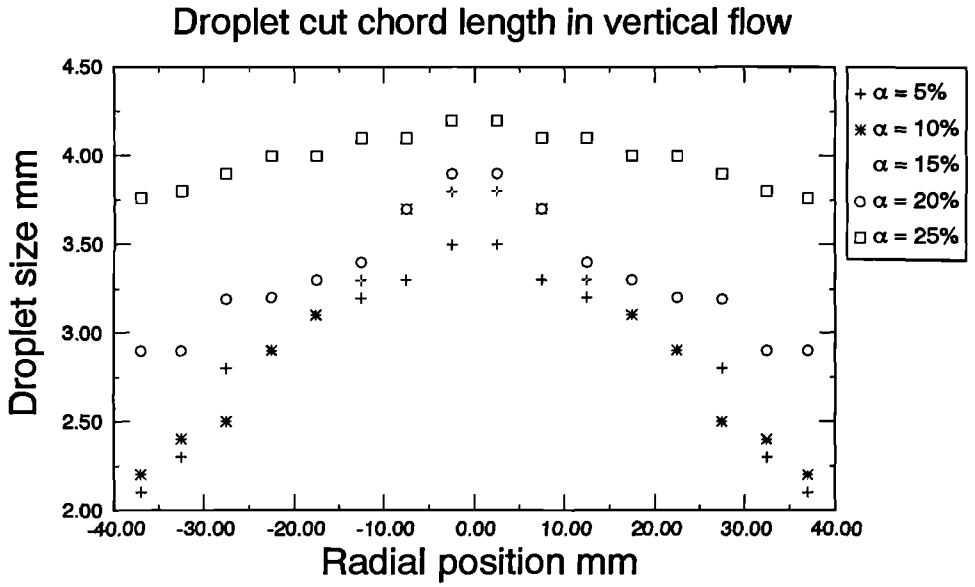

Figure 6.25: Plot of droplet cut chord length profiles

6.4.2 15° deviated flow

The flow loop was deviated to 15° from the vertical. The dual probe results and the dual split-film results are discussed respectively. In the following, low water velocities or low water flowrates refer to water superficial velocities of less than $0.3ms^{-1}$. Figure 6.26 shows typical profiles measured by the dual probe at a mean oil volume fraction of 0.1. As one can see from the profiles, most of the oil is concentrated near the top side of the pipe. This stratification of the two fluids is due to the density difference between the oil and water. The lighter phase (oil) always flows along the top side of the pipe and the heavier phase (water) flows on the bottom side of the pipe. These types of profiles have been observed and reported by Vigneaux [1988]. Figure 6.27 is a photograph of 15° deviated oil-water flow in the flow loop. This photograph shows that most of the oil droplets are situated near the top side of the pipe and the remainder is occupied by the water.

Once all the data had been taken with the dual probe, the relative error, e, from the dual probe results were compared to the reference meter results. Figure 6.28 shows the plots of the reference measured velocity and volume fraction against the relative error results from the dual probe. It was seen that the maximum region of relative error for the oil volume fraction varied from +10% to −5% and for the oil superficial velocity, the relative error varied from +7.5% to −6%. However, this was not the case for the water superficial velocity results. At low velocities ($0.1ms^{-1}$), it was seen that the maximum region for the relative error varied from 8% to 35% with increasing oil velocity. Observation in the flow loop showed that there were intermittent bursts of backward flowing oil droplets near the bottom of the pipe. These intermittent back flows were seen to occur at a low constant water flow rate and become more frequent as the oil flow rate increased. This is shown by the increase in the relative error plot. As mentioned earlier, the hot-film anemometer only measures the magnitude of the water velocity and not its direction. Hence, regardless of the flowing direction, the output from the hot-film will always be positive. This was one of the drawbacks of using the dual probe in deviated flow.

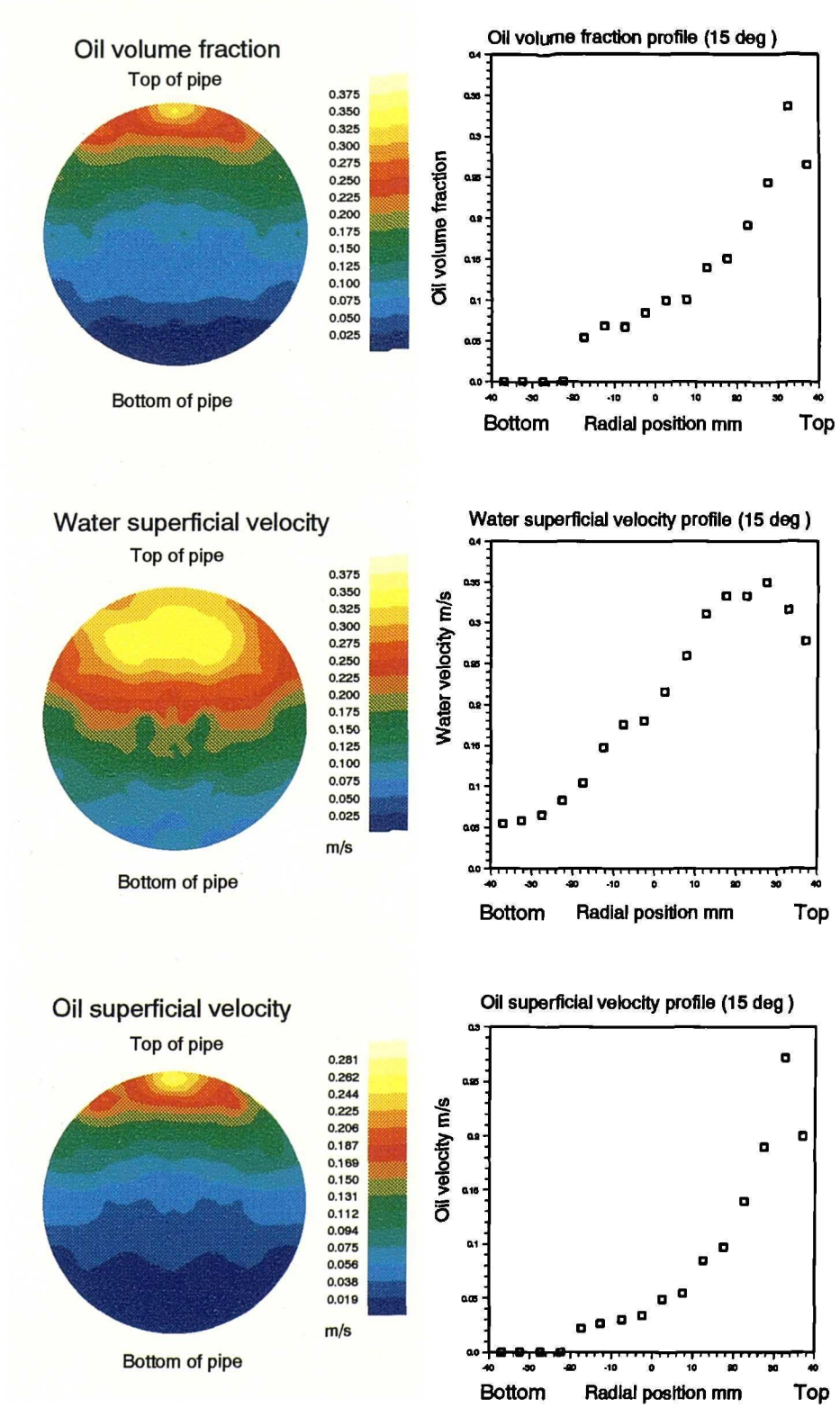

	Reference results	Integrated probe results
α	0.099	0.104
Uws m/s	0.196	0.191
Uos m/s	0.056	0.058

Figure 6.26: Measured velocity and volume fraction profiles in 15° deviated oil-water flow

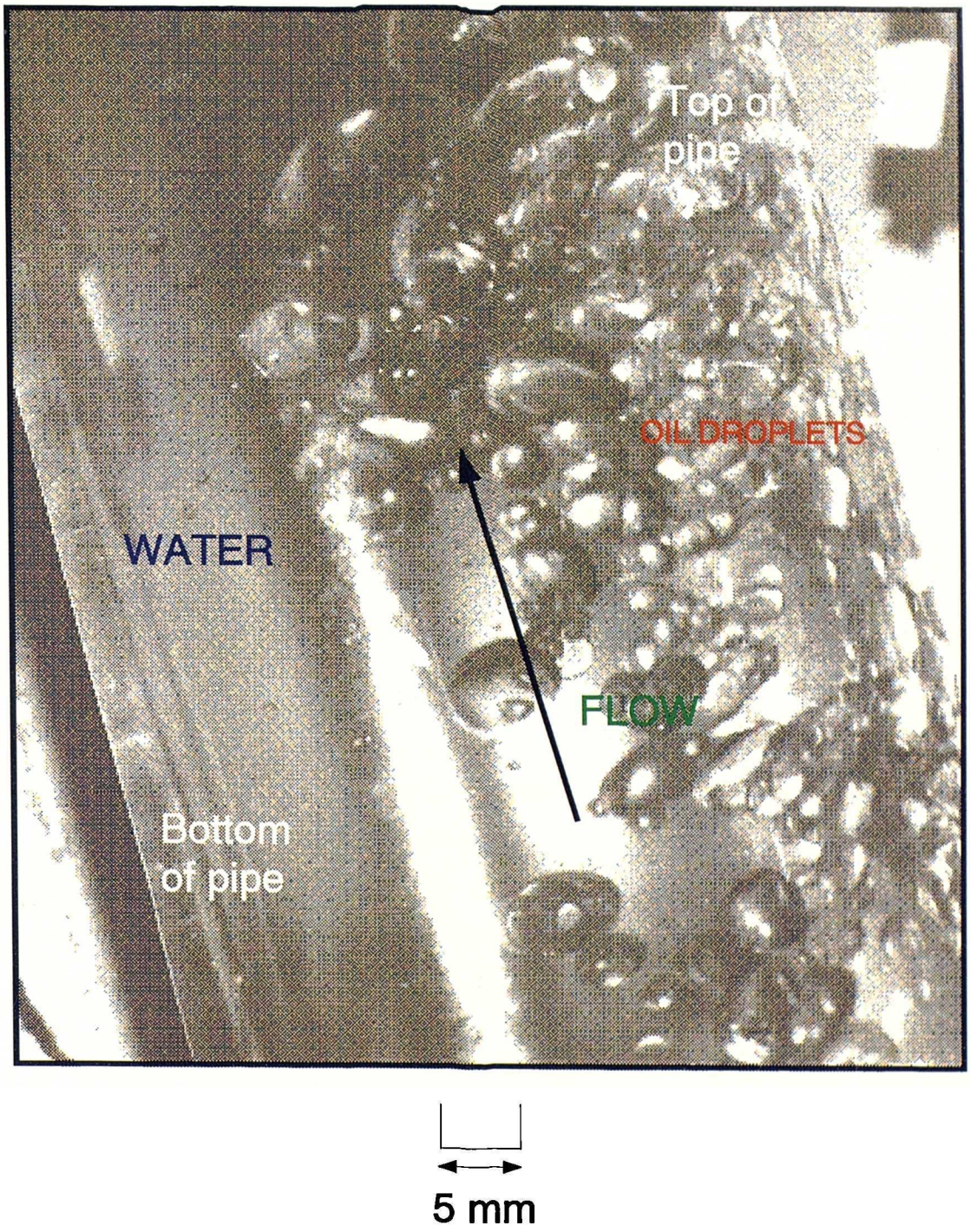

Figure 6.27: Photograph of 15° deviated oil-water flow

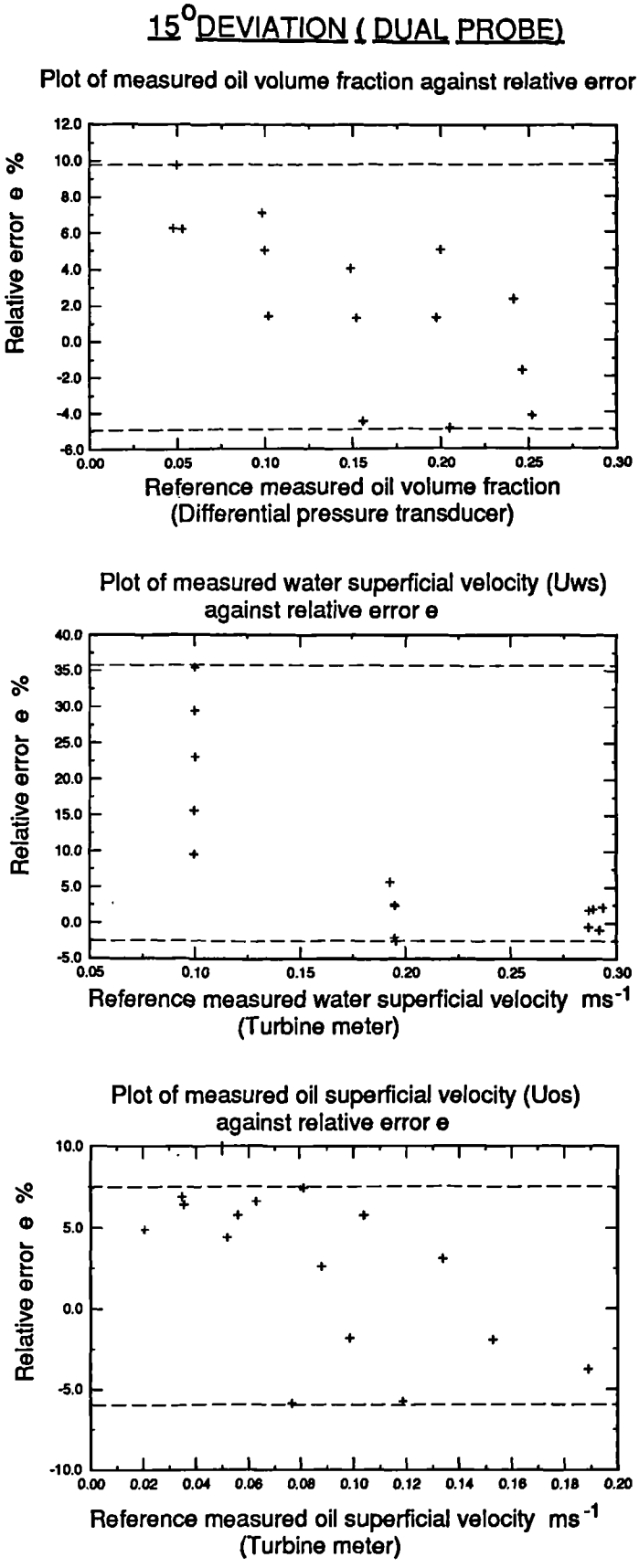

Figure 6.28: Comparison of reference measurements against integrated dual probe measurements (relative error)

The dual split-film probe was used at these low water flowrates to see whether or not the water velocity could be better measured. Figure 6.29 shows contour and profile plots of the water superficial velocity as measured by the dual probe and the dual split-film probe, at a water superficial velocity of $0.106 ms^{-1}$. One can see that the profile as measured by the dual probe exhibits an increase in the water velocity from radial positions -32.5mm to -37mm. This increase in velocity is due to water back flow. Comparing the two profiles, the dual split-film probe indicates clearly the region of back flow. This corresponds to the increase in velocity as seen by the dual probe. After testing the dual split-film probe, the performance of the probe was evaluated by comparing the integrated results against the reference meter results. Figure 6.30 shows the plots of the reference measured superficial velocities and oil volume fraction against the relative error results from the dual split-film probe. It can be seen that, there is a good estimation for all three measurements made by the dual split-film probe. Typically, the maximum region for the relative error of the oil volume fraction was $+9\%$ to -5%. A result of $+7\%$ to -8% maximum region for the relative error was attained for the water superficial velocity and a result of $+9\%$ to -7% relative error was attained for the oil superficial velocity. This result was promising for the performance of the dual split-film probe and it showed that a split-film anemometer was a more reliable instrument when measuring deviated flows at low water flowrates.

All of the relative error results taken with the dual probe and the dual split-film probe are summarised in Figure 6.31. The results obtained for the oil volume fraction compare significantly well between both probes. The slight variation in the results is due to different optical fibres being used on the probes (i.e. a different optical fibre, with the same specification, was used on both assembled probes). A similar result was obtained for the oil superficial velocities calculated by both probes. The combination of obtaining comparative results for both the oil volume fraction and the oil superficial velocities, implies that the sampling duration of 20 seconds (see Section 5.4) is sufficient, at a single measuring position. This result also shows the stability of the flow loop since the data taken with both probes were carried out on different days. The error in the water superficial velocity has been mentioned earlier.

15° DEVIATION

DUAL PROBE RESULT

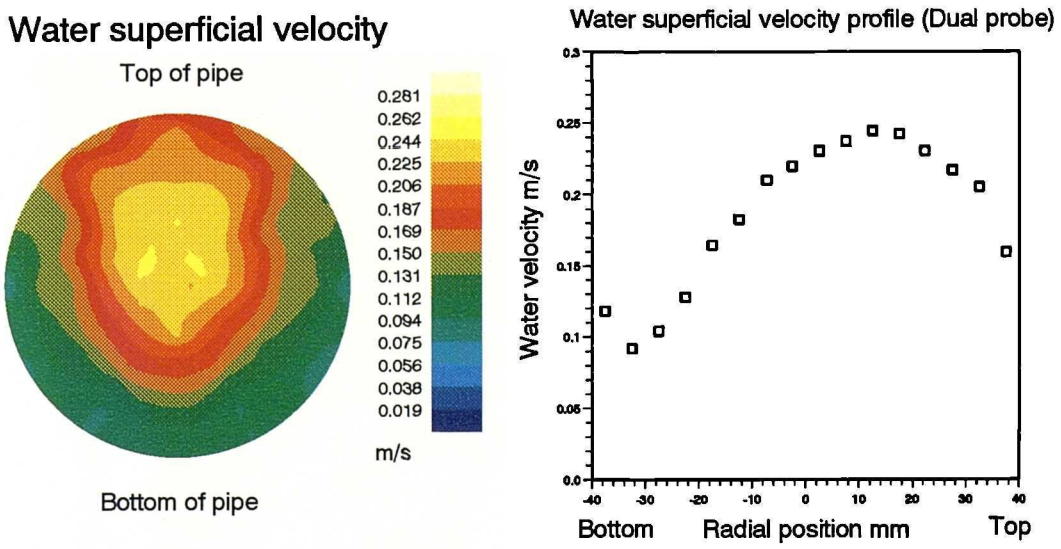

DUAL SPLIT-FILM PROBE RESULT

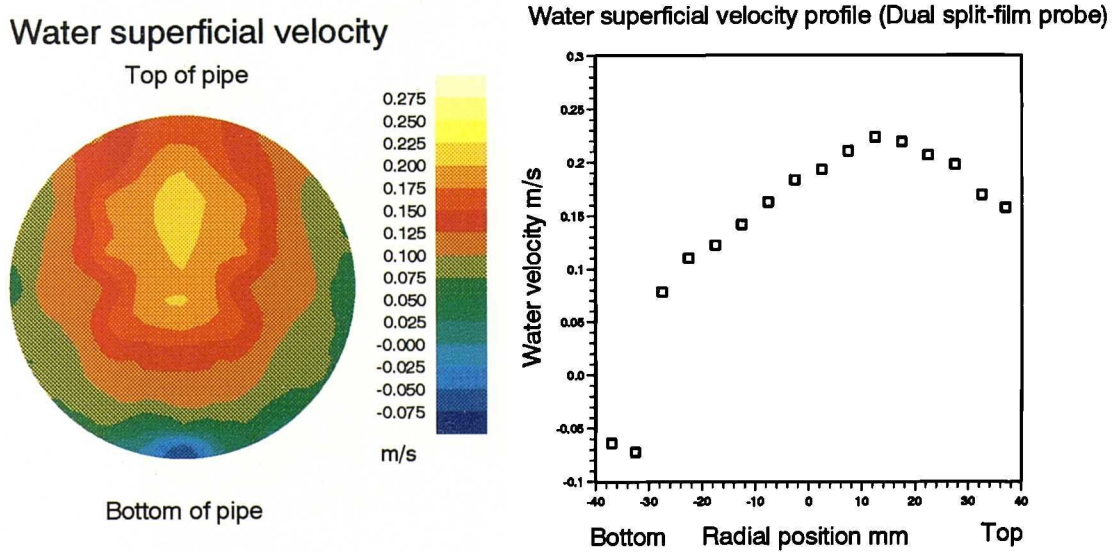

	Reference results	Dual probe estimation	Dual split film probe estimation
Uws m/s	0.106	0.136	0.110

Figure 6.29: Comparison of dual probe and dual split-film probe water superficial velocity results in 15° deviated oil-water flow

15° DEVIATION (DUAL SPLIT-FILM -PROBE)

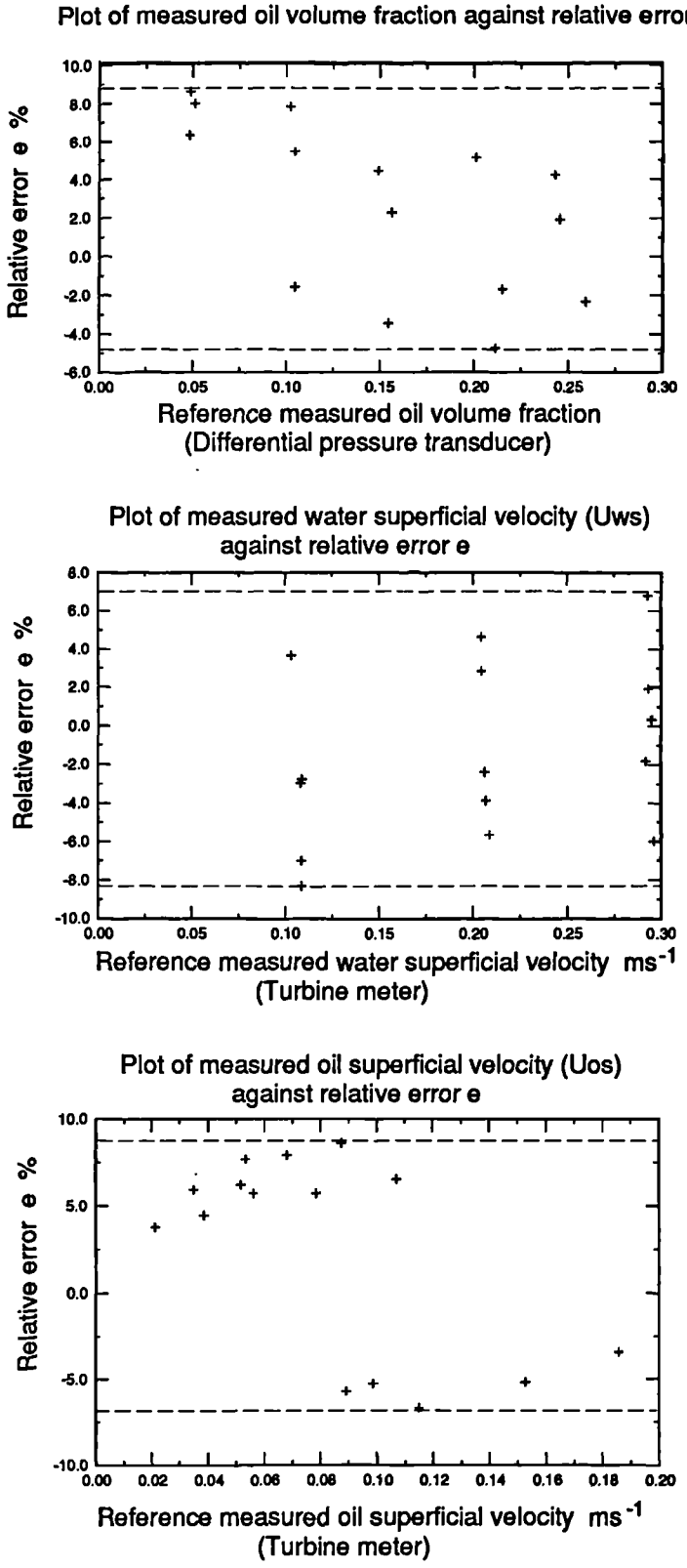

Figure 6.30: Comparison of reference measurements against integrated dual split-film probe measurements (relative error)

Quantity	Relative error range % DUAL PROBE	Relative error range % DUAL SF PROBE
Oil volume fraction	+10 to -5	+9 to -5
Water superficial velocity ms^{-1}	+35 to +8	+7 to -8
Oil superficial velocity ms^{-1}	+7.5 to -6	+9 to -7

Figure 6.31: Summary of relative error results in 15° deviated oil-water flow

Figure 6.32 shows actual velocity profiles for both oil and water. The water superficial velocity was $0.2ms^{-1}$, the oil superficial velocity was $0.035ms^{-1}$ and the oil volume fraction was 5%. The actual velocities of oil and water were used to compute the local slip velocities. With reference to Figure 6.33, the slip velocity has been plotted as a function of radial distance. One can see that discontinuities exist in the slip velocity profile plot. It has been shown earlier in this section, that at a low water superficial velocity, back flows exists near the bottom side of the pipe. As the water superficial velocity increases above $0.2ms^{-1}$, then back flows are not detected, hence a positive velocity profile. Applying this observation to the slip velocity profile, one can see that at low water superficial velocity ($0.1ms^{-1}$), the slip velocity is always positive. However at higher water velocities, the slip velocity profile is negative at the bottom side of the pipe. Since the slip velocity is defined as the relative velocity of oil to water, then negative slip velocities are encountered when the oil velocity is zero (no droplets). These types of slip velocity profiles were seen at all deviation angles.

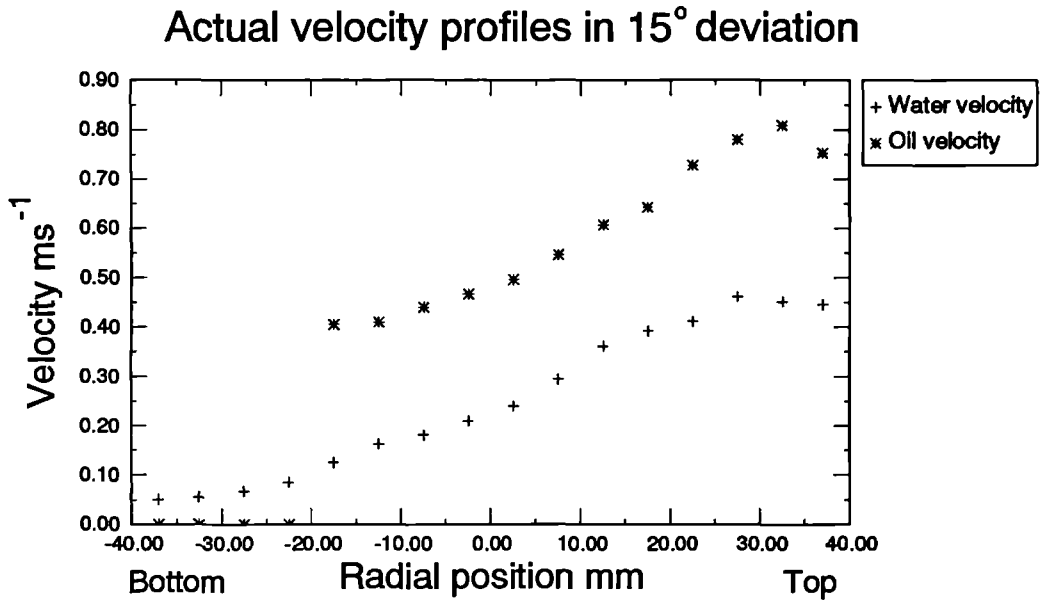

Figure 6.32: Actual velocity profiles in 15° deviated oil-water flow

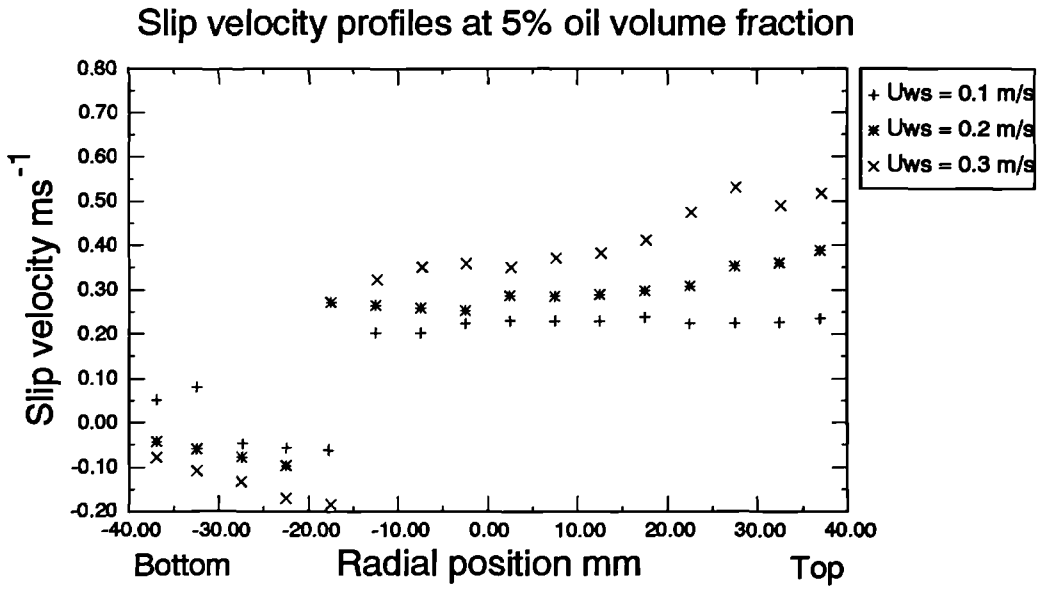

Figure 6.33: Plot of local slip velocities against radial position

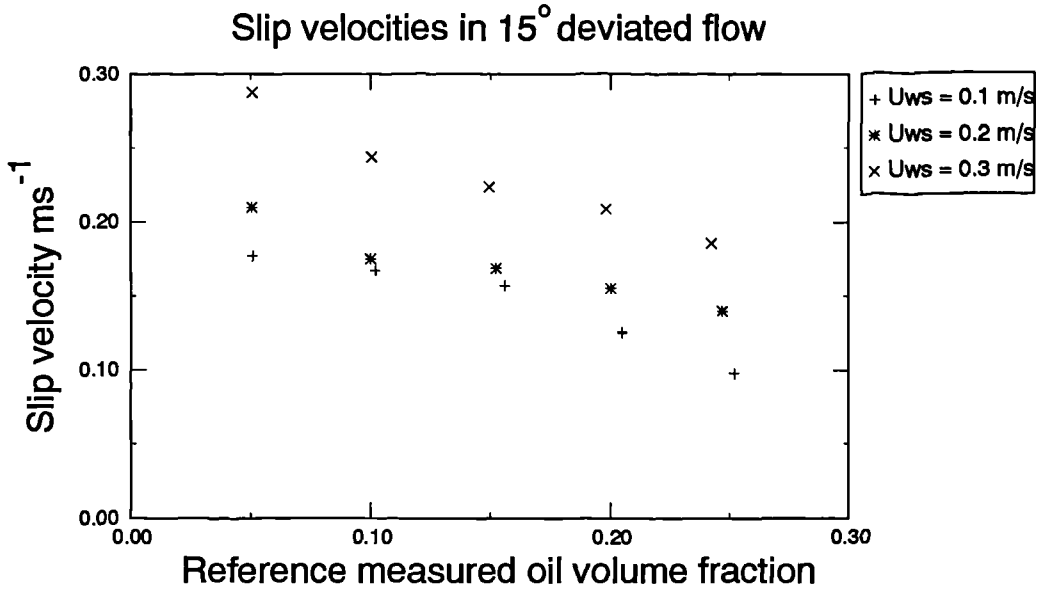

Figure 6.34: Plot of global slip velocities against reference measured oil volume fraction

With reference to Figure 6.34, the slip velocities have been plotted as a function of oil volume fraction. Similar curves were observed in vertical flow (see Figure 6.24). Again one can see that as the oil volume fraction increases, the slip velocities decrease. Vigneaux [1988] investigated slip velocities in deviated oil-water flows. He also showed that as the oil volume fraction increases, the slip velocity decreases.

In order to assess the oil droplet distribution, the droplet cut chord length was plotted across the diameter which connects the top to the bottom side of the pipe. With reference to Figure 6.35, one can see that the oil droplet size is relatively constant across the pipe diameter. Near the bottom side of the pipe where there are no oil droplets, the distribution falls to zero. Comparing Figure 6.35 to Figure 6.25, one can notice that the droplet size in deviated flow is larger ($\approx$ 5mm) than in vertical flow ($\approx$ 3mm). A possible suggestion for this difference is due to the level of turbulent mixing. In deviated flows, the turbulent mixing effect is more prominent that in vertical flows and this effect gives rise to a constant droplet size.

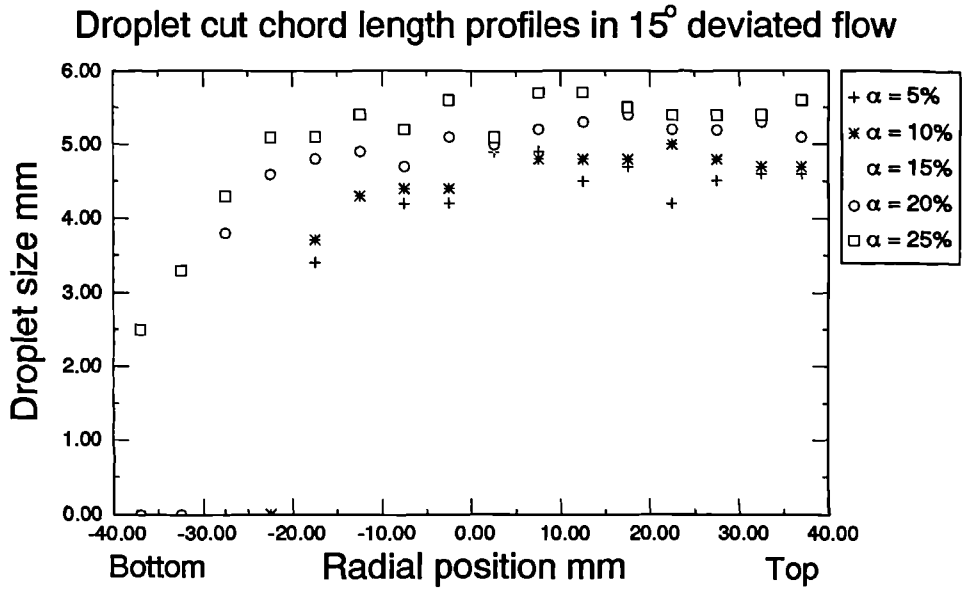

Figure 6.35: Plot of droplet cut chord length profiles

6.4.3 30° deviated flow

Figure 6.36 shows typical contour and profile plots of the oil volume fraction, water superficial velocity and oil superficial velocity with the pipe deviated at 30° to the vertical. The mean oil volume fraction was 0.1. Similar profiles can be seen to those taken at 15° deviation. Most of the oil is concentrated at the top of the pipe and the water at the bottom of the pipe. Once all the data had been taken with the dual probe, the integrated results from the dual probe were compared to the reference meters by calculating the relative error (see Equation 5.23). Figure 6.37 shows the plots of the reference measured superficial velocities and oil volume fraction against the relative error calculated from the dual probe results. Similar maximum region of relative errors were seen to those taken at 15° deviation for the oil volume fraction (+10% to −4%). A similar range of relative errors were seen comparing the 15° data to the 30° for the oil superficial velocity. The range of relative errors were +8.5% to −5%, for the 30° data, and +7.5% to −6%, for the 15° data.

With reference to Figure 6.37, large errors were seen in the water superficial velocity measurement, determined by the hot-film anemometer. At a water superficial velocity U_{ws} of 0.1ms^{-1}, the maximum relative error between the hot-film and the water turbine meter varied from +20% to +40% with increasing oil velocity. The cause of these large errors were due to water back flow.

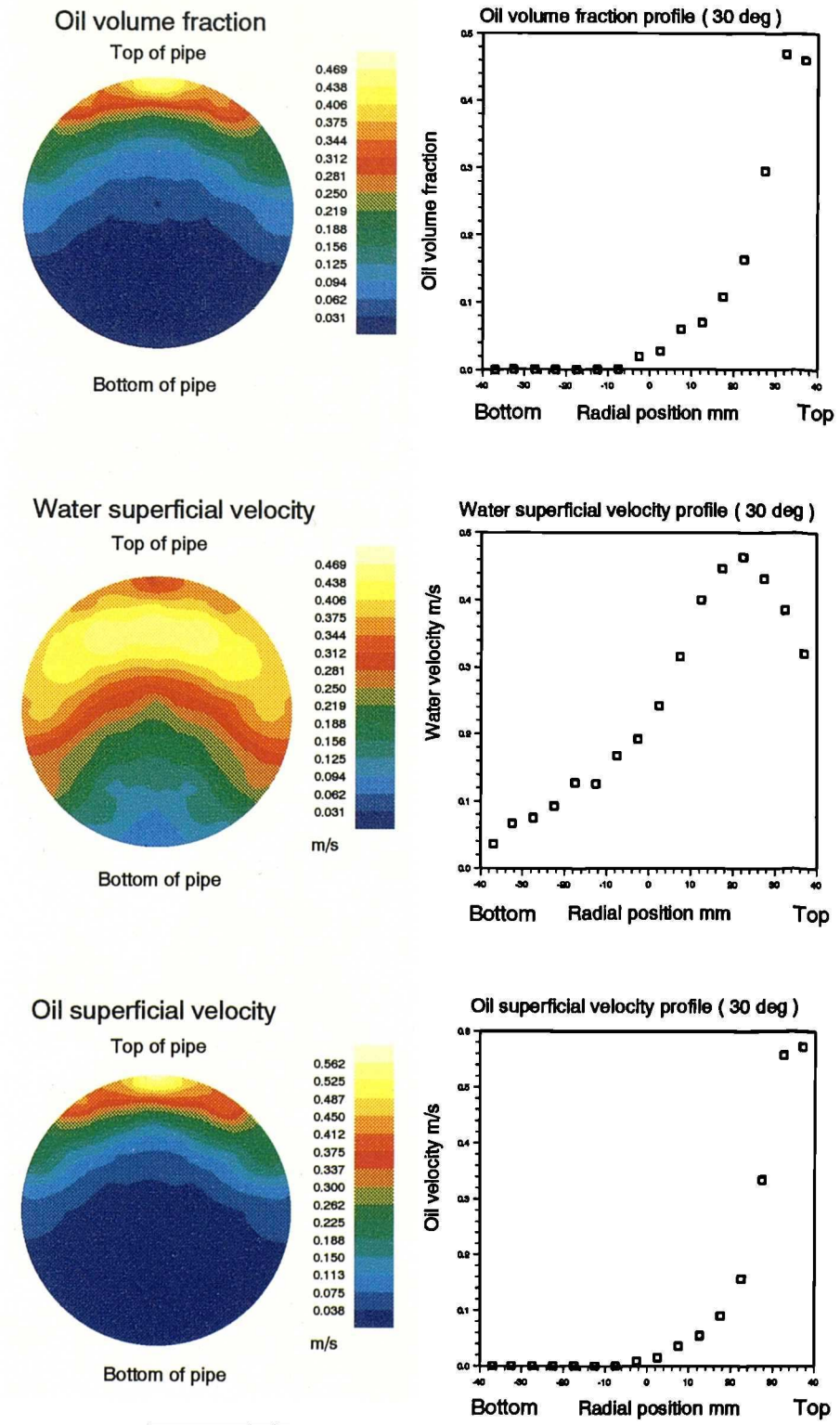

	Reference results	Integrated probe results
α	0.096	0.101
Uws m/s	0.288	0.293
Uos m/s	0.103	0.108

Figure 6.36: Measured velocity and volume fraction profiles in 30° deviated oil-water flow

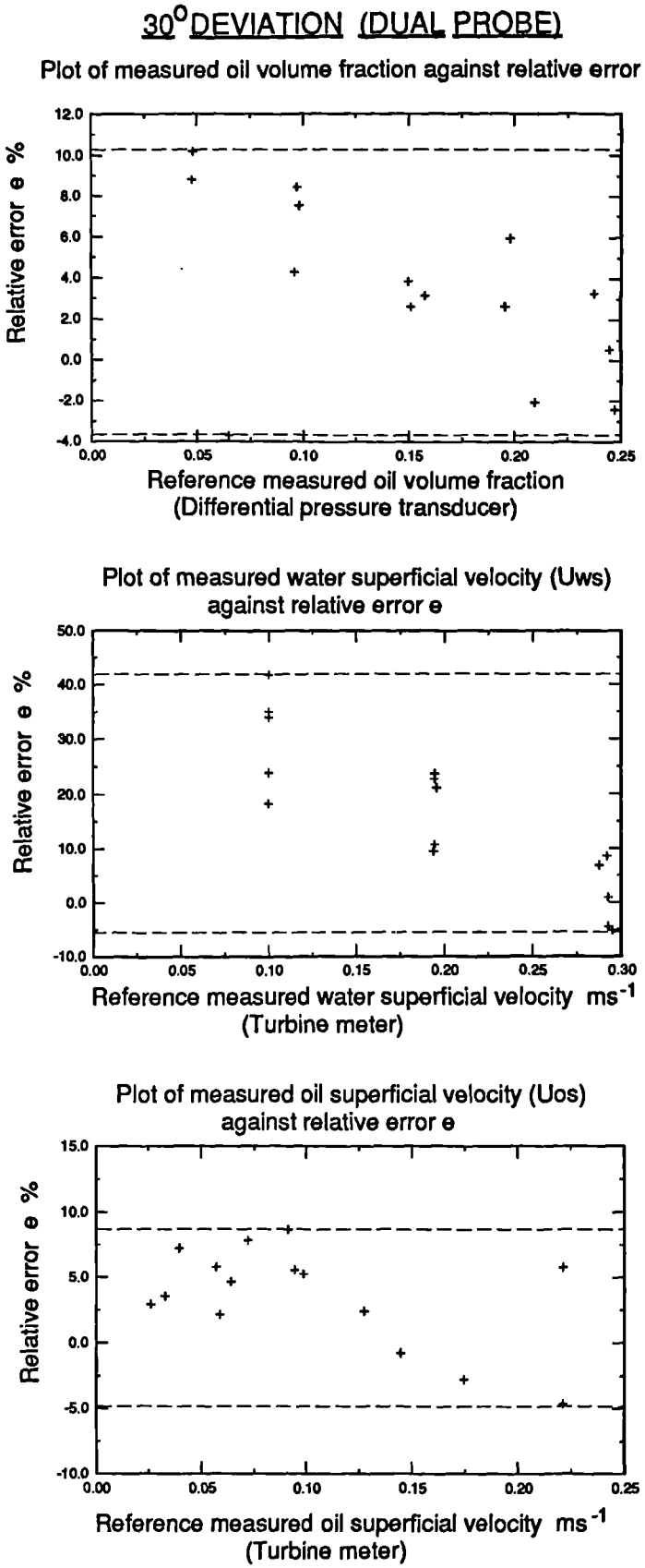

Figure 6.37: Comparison of reference measurements against integrated dual probe measurements (relative error)

At a water superficial velocity of 0.2ms^{-1}, the maximum relative error was seen to vary from +8% to +20% with increasing oil velocity. These errors were again due to back flow. However, at a water superficial velocity of 0.3ms^{-1}, the maximum region of the relative error decreased to +10% to −5%, hence back flows occur at $U_{ws} \leq 0.3\text{ms}^{-1}$.

The experimental conditions were repeated in order to test the dual split-film probe. Figure 6.38 shows contour and profile plots of the water superficial velocity as measured by the dual probe and the dual split-film probe. The water superficial velocity was 0.105ms^{-1}. One can see that there is an increase in measured water superficial velocity between radial positions −22.5mm to −37mm, from the dual probe results. This increase in water velocity has been seen in the 15° data and it is due to water back flow. At corresponding radial positions, the dual split-film probe has detected a water back flow. To evaluate the performance of the dual split-film probe, the relative errors were compared to the reference meter results. Figure 6.39 shows the plots of the reference measured velocity and volume fraction against the relative error from the dual split-film probe results. As one can see, there is a good agreement for all three measurements made by the dual split-film probe. The maximum region of the relative error for the oil volume fraction was +9% to −3% and for the water superficial velocity, the relative error was +9% to −7%. A result of +8% to −5% maximum region of relative error was attained for the oil superficial velocities. Similar to the dual probe results, the relative error of the oil superficial velocity calculated at 30° deviation, is larger than those seen at 15° deviation.

A summary of the relative error results are given in Figure 6.40. One can see the repeatability in the results obtained for both the oil volume fraction and oil superficial velocity as measured by both probes.

With reference to Figure 6.41, the slip velocities have been plotted as a function of oil volume fraction. Similar curves were seen for vertical and 15° deviated flow. Also the magnitudes of the slip velocities have increased with increasing deviation angle. As an example, viewing Figure 6.34, the slip velocity varies from 0.21ms^{-1} to 0.14ms^{-1} with increasing oil volume fraction, at a water superficial velocity of 0.2ms^{-1}. For the same conditions and viewing Figure 6.41, the slip velocity varies from 0.26ms^{-1} to 0.14ms^{-1}. This increase in slip velocity at low volume fraction (5%) is due to fast moving droplets near the top side of the pipe, causing an increase in the slip velocity. As the

30° DEVIATION

DUAL PROBE RESULT

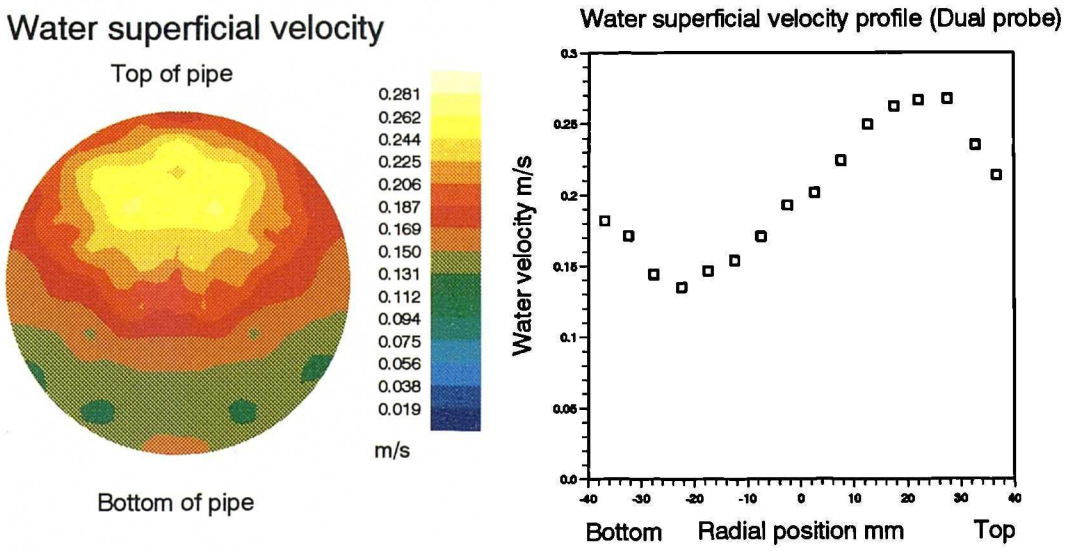

DUAL SPLIT-FILM PROBE RESULT

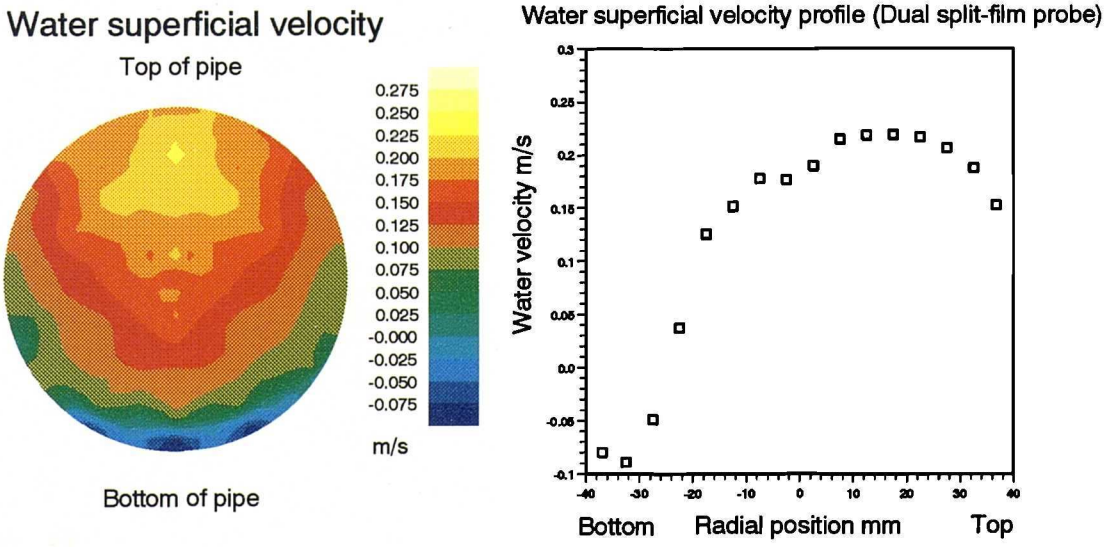

	Reference results	Dual probe estimation	Dual split film probe estimation
Uws m/s	0.105	0.142	0.112

Figure 6.38: Comparison of dual probe and dual split-film probe water superficial velocity results in 30° deviated oil-water flow

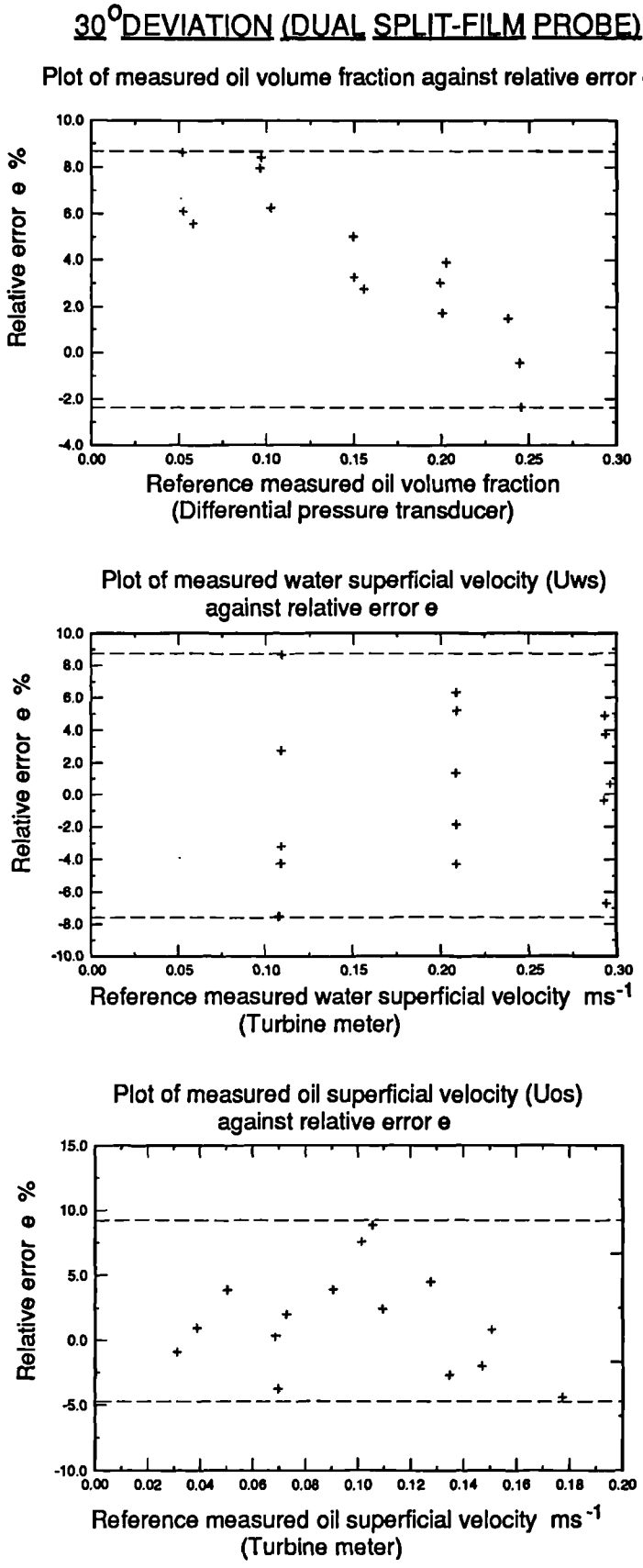

Figure 6.39: Comparison of reference measurements against integrated dual split-film probe measurements (relative error)

Quantity	Relative error range % DUAL PROBE	Relative error range % DUAL SF PROBE
Oil volume fraction	+10 to -4	+9 to -3
Water superficial velocity ms^{-1}	+40 to -5	+9 to -7
Oil superficial velocity ms^{-1}	+8 to -5	+9 to -5

Figure 6.40: Summary of relative error results in 30° deviated oil-water flow

oil volume fraction increases, slower moving re-circulating droplet swarms are observed hence back flowing droplets reduce the mean oil velocity. At large oil volume fractions, 25%, higher interaction between the oil droplets exist which in turn reduces the oil velocity. It has been seen from the superficial velocity profile plots, that at low constant water velocities, back flows exist and become more frequent as the oil volume fraction increases. This observation has been seen in the slip velocity curves.

With reference to Figure 6.42, the droplet cut chord length has been plotted as a function of radial position. Comparing the same plot at 15° deviation (see Figure 6.35), one can see that similar curves have been produced. This suggests that the droplet cut chord lengths are independent of the deviation angle. Also the droplet cut chord length is insensitive of the oil volume fraction.

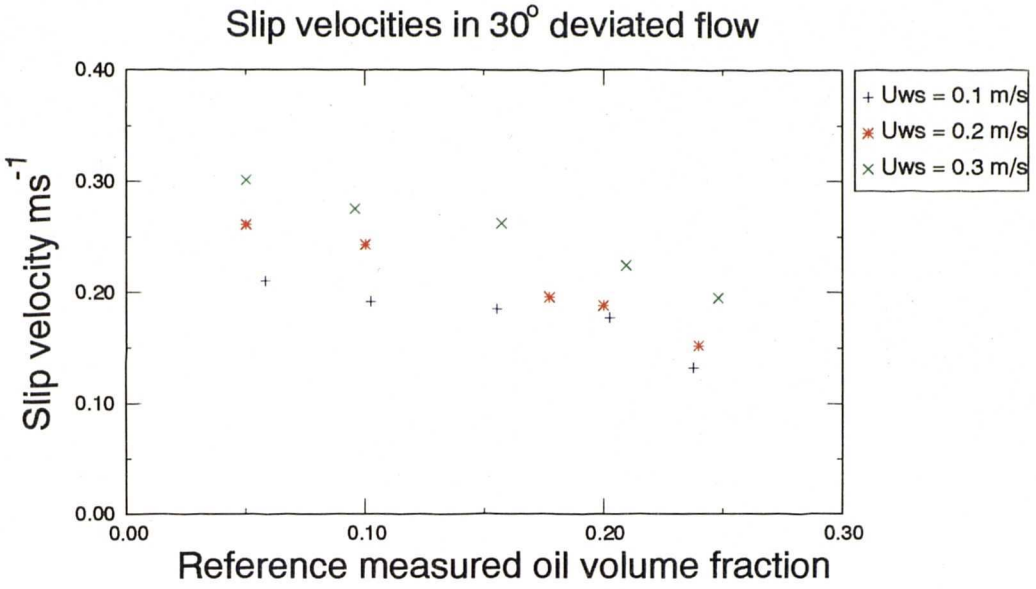

Figure 6.41: Plot of global slip velocities against reference measured oil volume fraction

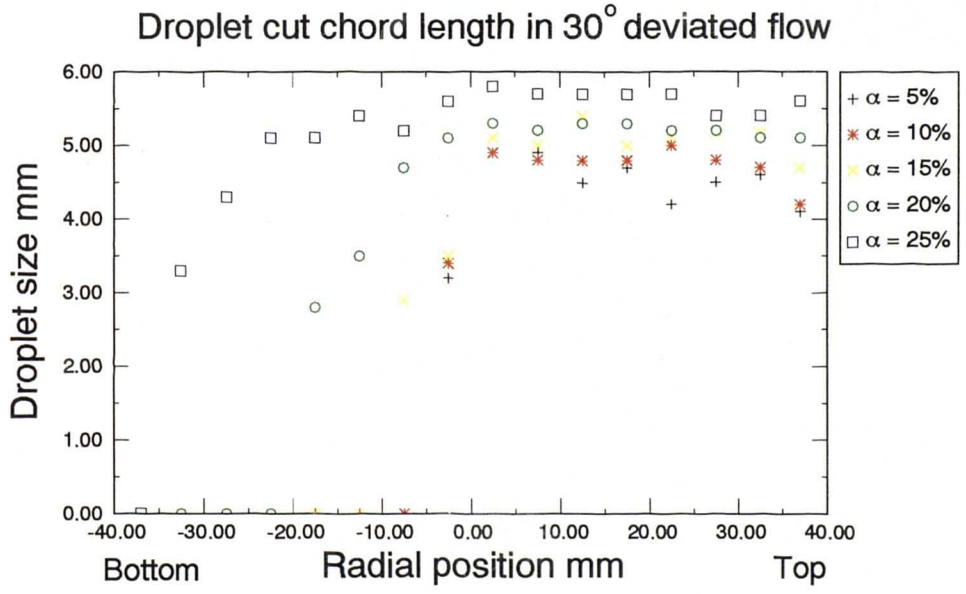

Figure 6.42: Plot of droplet cut chord length profiles

6.4.4 45° deviated flow

Tests were carried out at 45° deviation only using the dual split-film probe. From the results taken at the other deviation using the dual probe, it was decided not to use the dual probe, since its measurement of the water velocity was unsatisfactory at low water velocities. Figure 6.43 shows typical contour and profile plots for oil volume fraction, water superficial velocity and oil superficial velocity taken with the dual split-film probe. One can see that the area of back flow illustrated in the water velocity profile has increased compared to results shown at 30° and 15° deviations. The integrated results from the dual split-film probe were compared to the reference meters. Figure 6.44 shows the plots of the reference measured velocity and volume fraction against the relative errors from the dual split-film probe results. It can be seen that there is a good agreement for all three measurements made by the dual split-film probe. The maximum region of the relative error for the oil volume fraction was +10% to −6%. A result of ±8% maximum region of the relative error was attained for the water superficial velocity. The maximum region for the relative error of the oil superficial velocity was +7% to −8%. A similar result was obtained for 30° deviation oil superficial velocity.

The slip velocities are plotted as a function of oil volume fraction, see Figure 6.45. For all deviation angles, it has been seen that as the oil volume fraction increases, the slip velocity decreases. Also as the deviation angle increases, the magnitude of the slip velocities increase. With reference to Figure 6.46, the droplet cut chord length has been plotted as a function of radial position. Similar curves have been presented for 15° and 30° deviation.

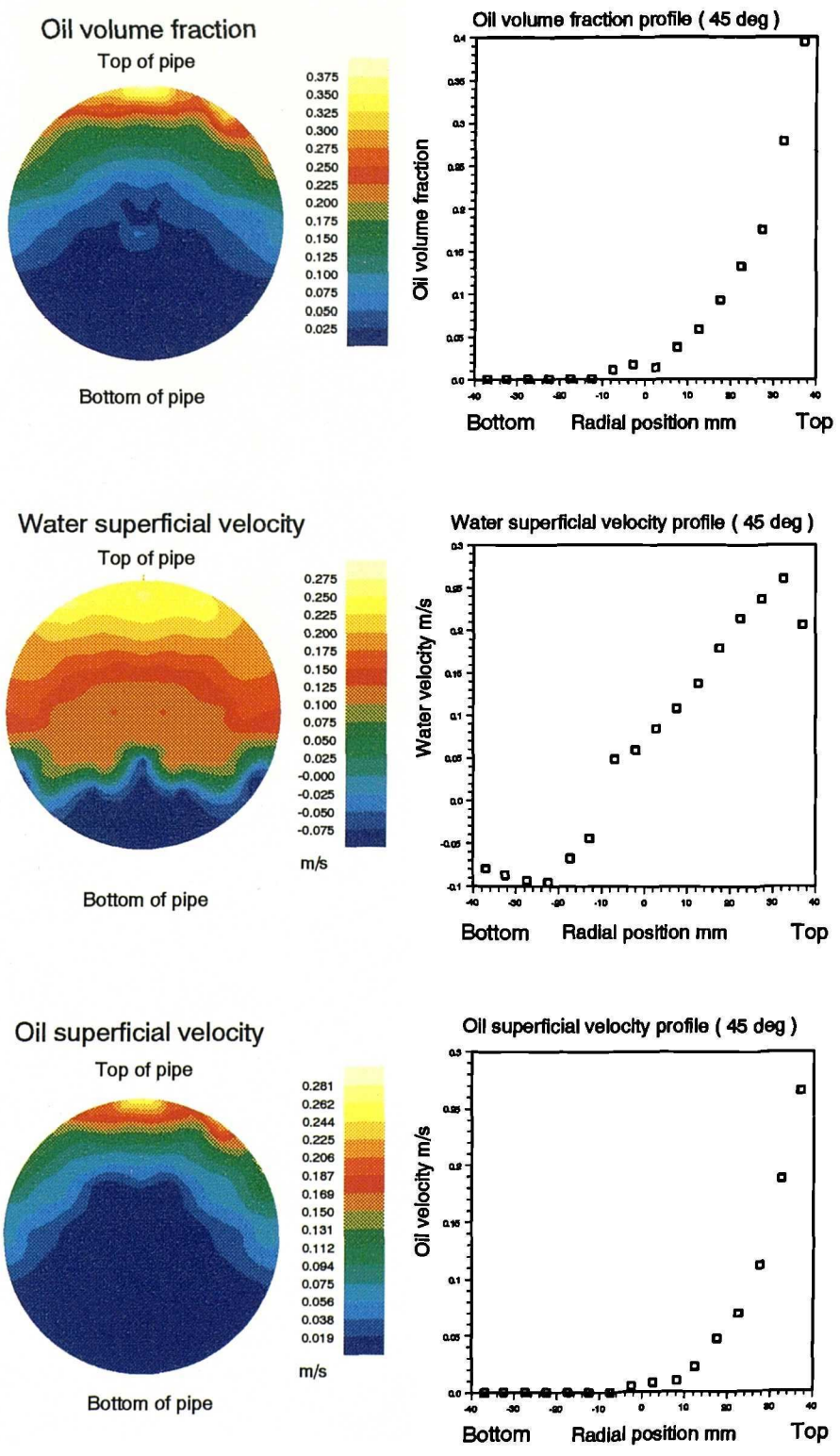

	Reference results	Integrated probe results
α	0.116	0.119
Uws m/s	0.105	0.112
Uos m/s	0.065	0.071

Figure 6.43: Measured velocity and volume fraction profiles in 45° deviated oil-water flow

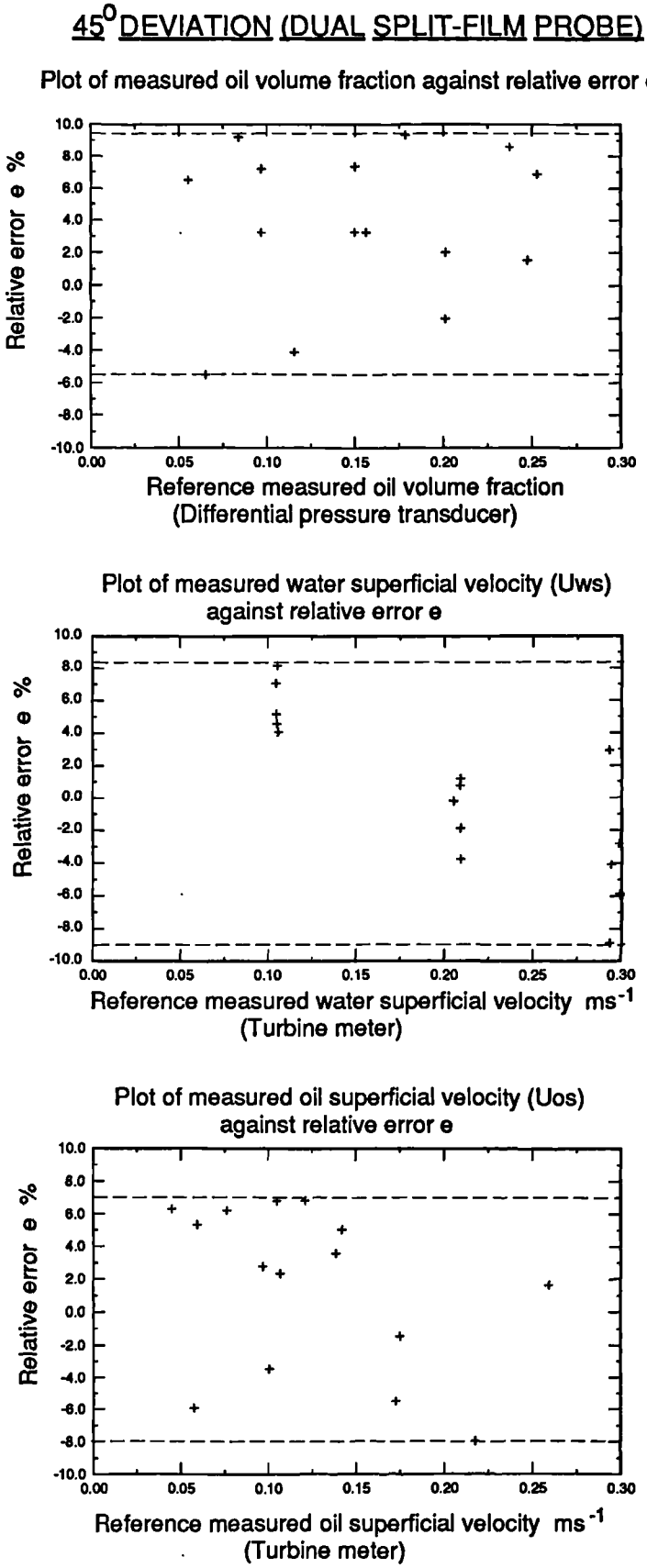

Figure 6.44: Comparison of reference measurements against integrated dual split-film probe measurements (relative error)

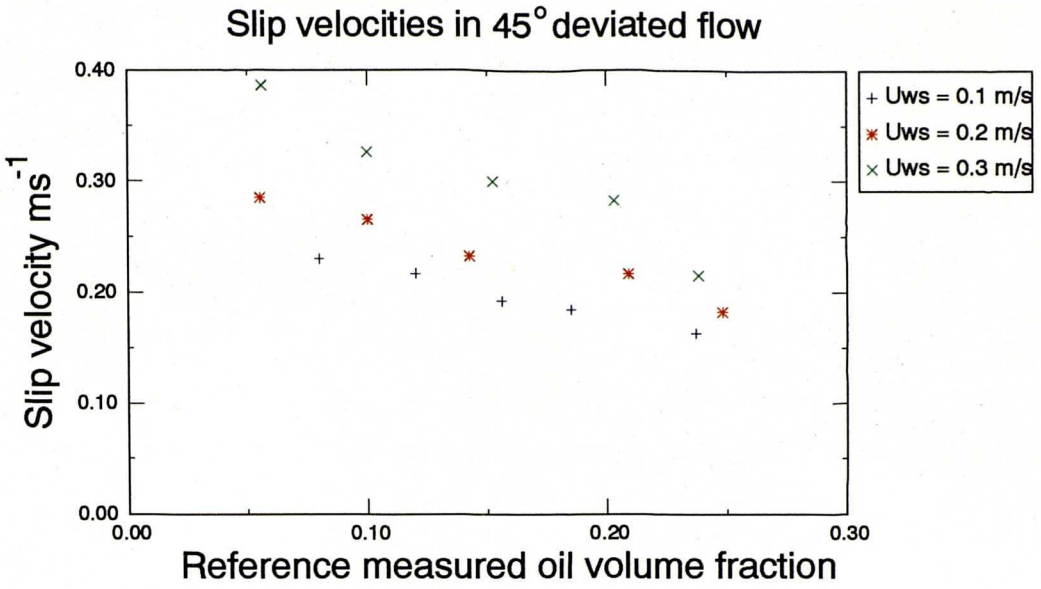

Figure 6.45: Plot of global slip velocities against reference measured oil volume fraction

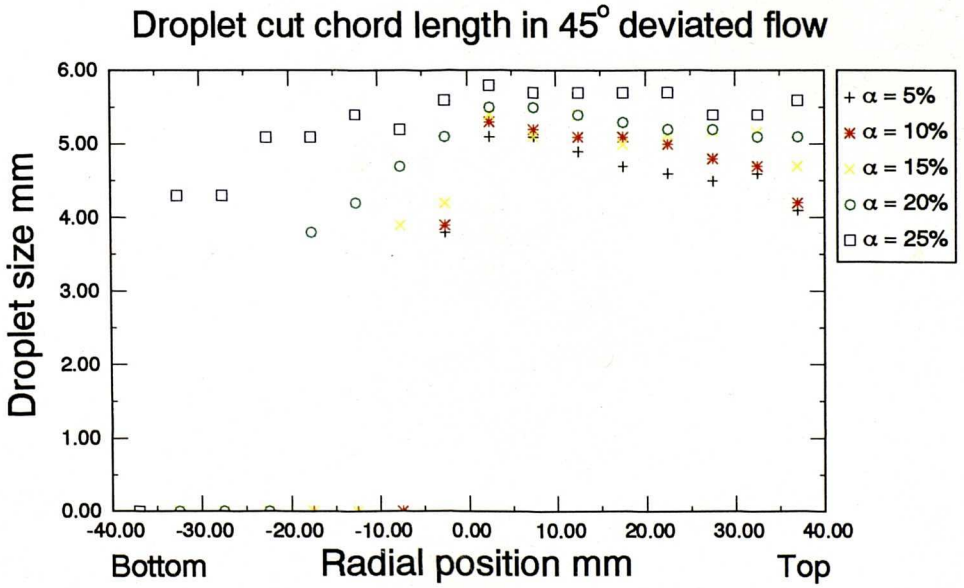

Figure 6.46: Plot of droplet cut chord length profiles

6.5 Summary

It has been shown, in vertical oil-water flow, that the dual probe is capable of measuring the water and oil superficial velocities and the oil volume fraction within a $\pm 10\%$ relative error range. The slip velocities were also investigated by the dual probe. It was shown that as the water superficial velocity increased, so did the slip velocity. It is thought that this observation is due to undeveloped flow. It was seen that, as the oil volume fraction increases, the slip velocity decreases. This is due to closely packed oil droplets which reduce the oil velocity. The droplet cut chord lengths were presented and it was shown that as the oil volume fraction increases, the droplet cut chord length profiles become flatter. It was found that the droplet cut chord length was approximately 4mm.

In deviated oil-water flows, the measured oil superficial velocities and the oil volume fractions where within a $\pm 10\%$ relative error range. Large relative errors were seen when measuring the water superficial velocity, using the dual probe. These large errors occured at water superficial velocities of less than $0.3 ms^{-1}$. Water back flows were observed near the bottom side of the pipe which affected the water velocity measurement. In order to measure these water back flows, the dual split-film probe was tested with success. By using this type of probe, the water superficial velocity was measured within a relative error range of $\pm 10\%$. The slip velocities were investigated in deviated flows. It was shown that with increasing oil volume fraction, the slip velocity decreases. Similar results were shown for vertical flow data. The droplet cut chord lengths were investigated and it was found that, in an oil region, the droplet cut chord length profiles were approximately constant. This showed that the droplet cut chord length in deviated flow was insensitive to changes in oil volume fraction (as seen for vertical flow). This was due to higher levels of turbulent mixing and buoyancy effects which lead to a constant droplet cut chord length of 5mm.

Chapter 7

Comparison of experimental results with a deviated oil-water flow model

7.1 Introduction

In this chapter, the use of a two phase flow model will be discussed. It has been found that only one theoretical model exists. This model enables the velocity profiles to be determined for a given set of flow conditions in a deviated oil-water flow. Previous approaches to describe the local volume fraction distributions and velocity profiles in deviated oil-water flows have used 'phenomenological' constants obtained in flow loops (see Tabeling *et al.* [1991]). The two phase flow model has been developed by Mobbs and Lucas [1993] at Schlumberger Cambridge Research. It solves the Navier-Stokes and continuity equations for two phase flows.

7.2 Results

In this section results will be presented from the model and measured profiles from the dual split-film probe. Three cases were investigated at 15°, 30° and 45° deviations. These will be discussed respectively. The presentation of the results will be in the form of profile plots. The axis which connects the top to the bottom of the pipe will be used where the homogeneous velocity

(see Equation 5.8) will be plotted. Superimposed is the model generated homogeneous velocity profile. To aid discussions, the water superficial and the oil superficial velocities, measured by the dual split-film probe, are also superimposed onto the profile plots. The radial position at 0m corresponds to the bottom of the pipe and 0.078m corresponds to the top of the pipe. The model was executed on a 'Sun' workstation where different pressure gradients (see Equation 7.1) were implemented in order to commence the development of the homogeneous velocity profile. For all the model generated profiles, the total development time had to be chosen so that the homogeneous velocity profile was not changing in shape or magnitude with respect to time. Figure 7.1, shows a set of model generated velocity profiles at 15° oil-water flow with water as the continuous phase. As one can see, after 5 seconds the predicted velocity profile is not changing, hence for this particular case, 5 seconds was chosen as the development time. For each predicted velocity profile given below, different development times were required. The maximum development time was found to be 10 seconds (45° deviated oil-water flow). For all deviation angles, the following conditions were used:

1. Slot width (pipe diameter) = 78mm.

2. Molecular viscosities of $10^{-4}m^2s^{-1}$ for the dispersed phase and $10^{-6}m^2s^{-1}$ for the continuous phase were used.

3. The densities of the dispersed (oil) and continuous (water) phases were $790kgm^{-3}$ and $1000kgm^{-3}$ respectively.

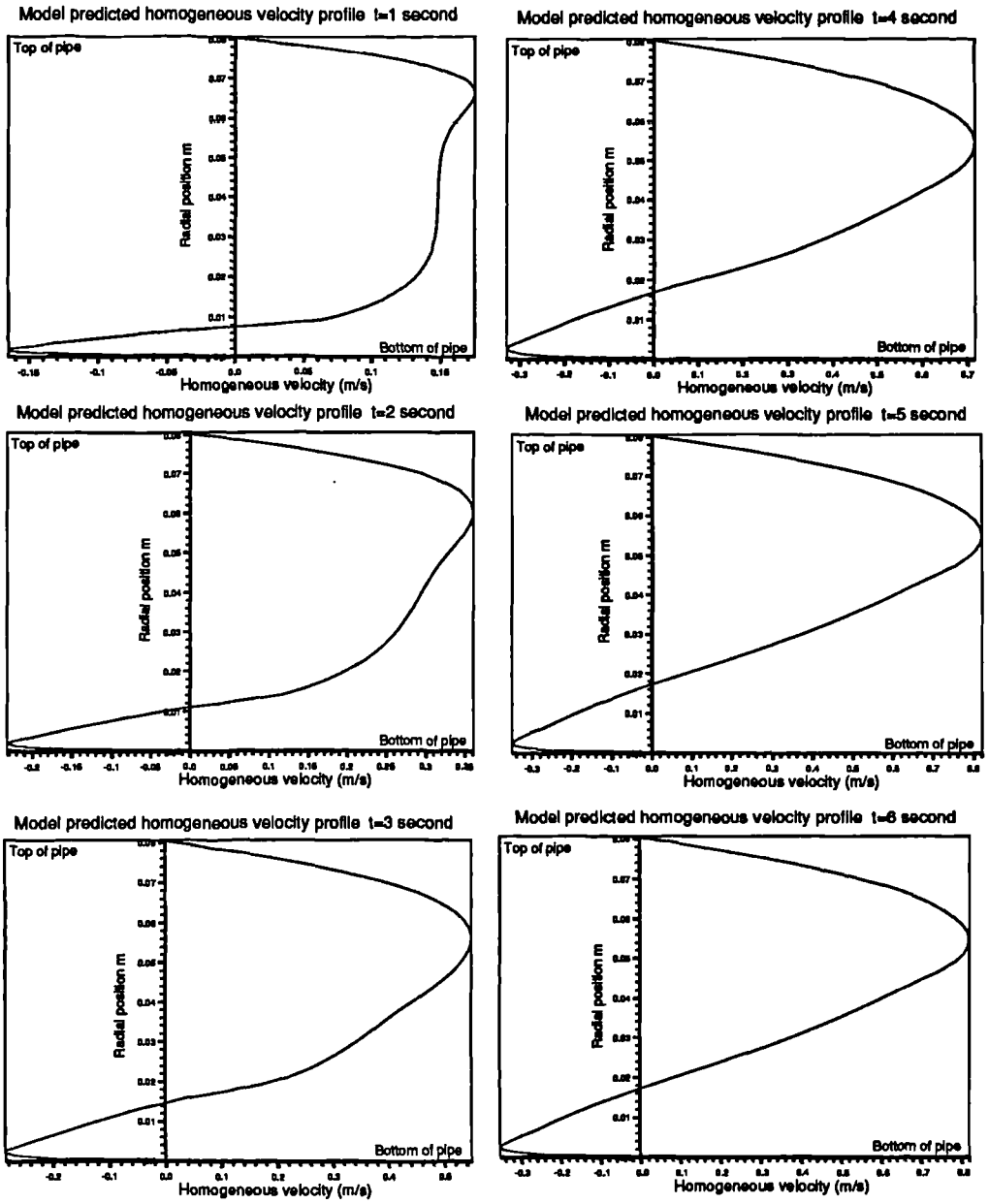

Figure 7.1: Evolution of homogeneous velocity profiles as predicted by the two phase model

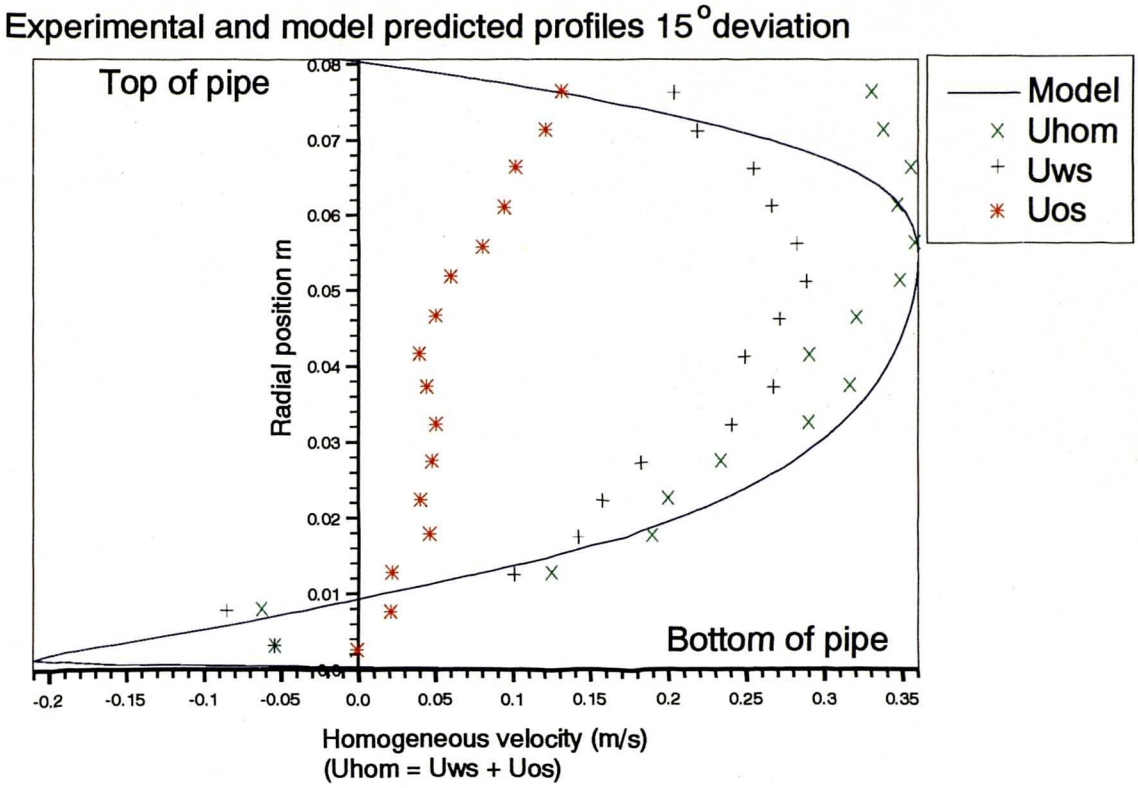

Figure 7.2: Model generated and probe measured velocity profiles

7.2.1 15° deviation

Figure 7.2 shows the model predicted homogeneous velocity profile and the measured superficial and homogeneous velocity profiles by the dual split-film probe. For this particular case, the mean water superficial velocity was, $U_{ws} = 0.108\text{ms}^{-1}$ and a mean oil volume fraction across the pipe section $\bar{\alpha}_o = 0.25$. In order to commence the one dimensional model, a pressure gradient had to be chosen. The pressure gradient $\frac{dp}{dx}$ is given by:

$$\frac{dp}{dx} = -\rho_m g \cos\theta \tag{7.1}$$

where ρ_m is the mixture density which is given by Equation 5.13, g is the acceleration due to gravity and θ is the pipe deviation. The imposed pressure gradient used for the simulation was -9000Pam^{-1}. It can be seen that the model and the measured homogeneous profiles show similar shaped velocity profiles. However, near the top wall, the model and the measured homogeneous profiles are dissimilar. As mentioned in Chapter 5, the final probe position was 2mm away from the wall. This was assumed to be close enough to the wall to show a distinct boundary layer. By inspecting the water superficial velocity

profile, U_{ws}, one can see that this profile shows the effect of the pipe wall on the velocity profile similar to that seen on the model predicted profile. However, this effect of the wall is not seen on the oil superficial velocity, U_{os}, profile. Since the homogeneous velocity profile is the combination of the water superficial and oil superficial velocities, this produces a profile which has a reduced effect due to the pipe wall near the top of the pipe.

In order to investigate the reasons for the oil superficial velocity profiles not being affected by the pipe wall, a set of experiments was carried out in the flow loop at 5° and 10° deviation. The water superficial velocity was maintained at 0.12ms^{-1} and the oil superficial velocity was increased to attain a maximum of 0.25 oil volume fraction. Figure 7.3 shows the homogeneous velocity profiles measured across a single diameter connecting the top to the bottom of the pipe. Four different profiles are shown, varying from single phase water velocity ($\alpha = 0$) to two phase oil-water flow at an oil volume fraction (α) of 0.25. For the two phase flow data set, one can see that the profiles are affected by the pipe wall since they exhibit curvature near the top wall. These types of profiles were not seen at 15° deviation, hence one can conclude that the absence of the boundary layer is a real effect in deviated pipes greater than 5° and that it is due to the presence of oil. A similar set of data was taken at 10° deviation to confirm the effect of the boundary layer. The same water superficial velocity was used as the 5° tests with varying oil volume fractions up to 0.25. Figure 7.4 shows four different homogeneous velocity profiles varying from single phase water flow to two phase oil-water flow. For the two phase data set, one can see that as the oil volume fraction increases, the homogeneous profiles show less curvature near the top wall as compared to the 5° tests. These profiles are similar to those seen at 15° deviated flow (see Figure 7.2). It has been shown that, as the deviation angle increases and with increasing oil volume fraction, the homogeneous velocity profile tends to 'flatten' near the top of the pipe not showing the boundary layer due to the pipe wall. One can conclude, from the above findings, that the two phase flow model is not capable of predicting the effects due to the presence of oil near the top side of the pipe. This is a deficiency of the model which will be investigated at a later date.

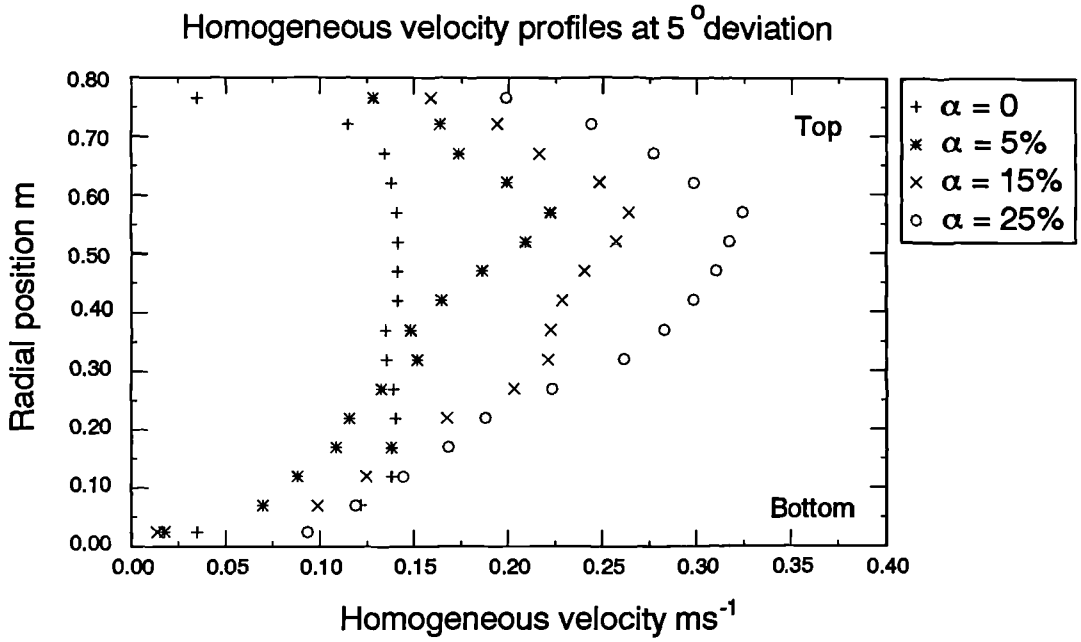

Figure 7.3: Homogeneous velocity profiles taken at 5° deviation

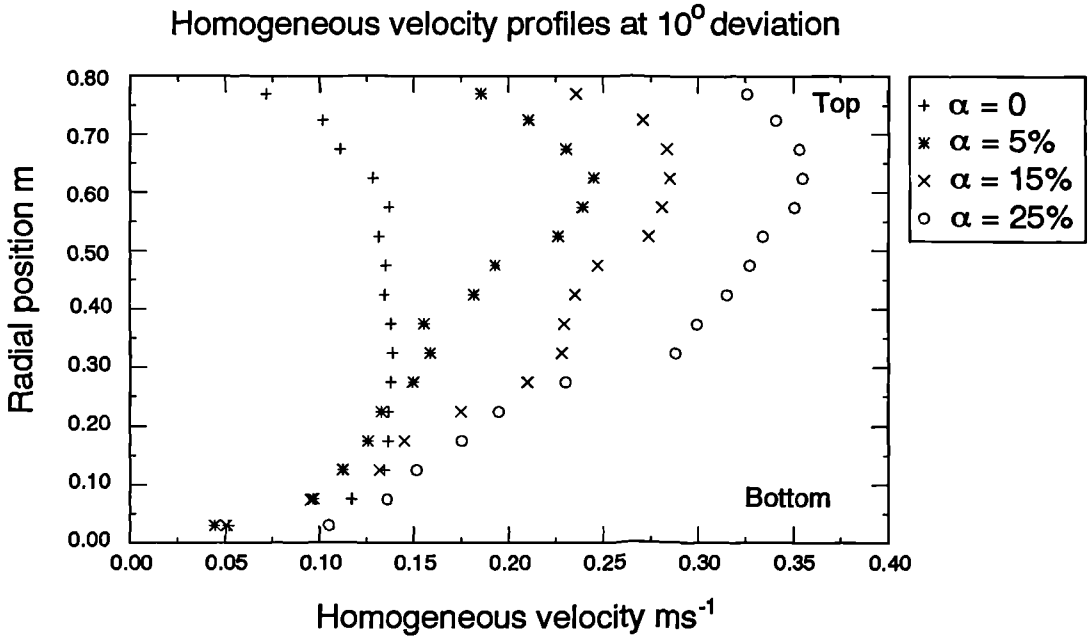

Figure 7.4: Homogeneous velocity profiles taken at 10° deviation

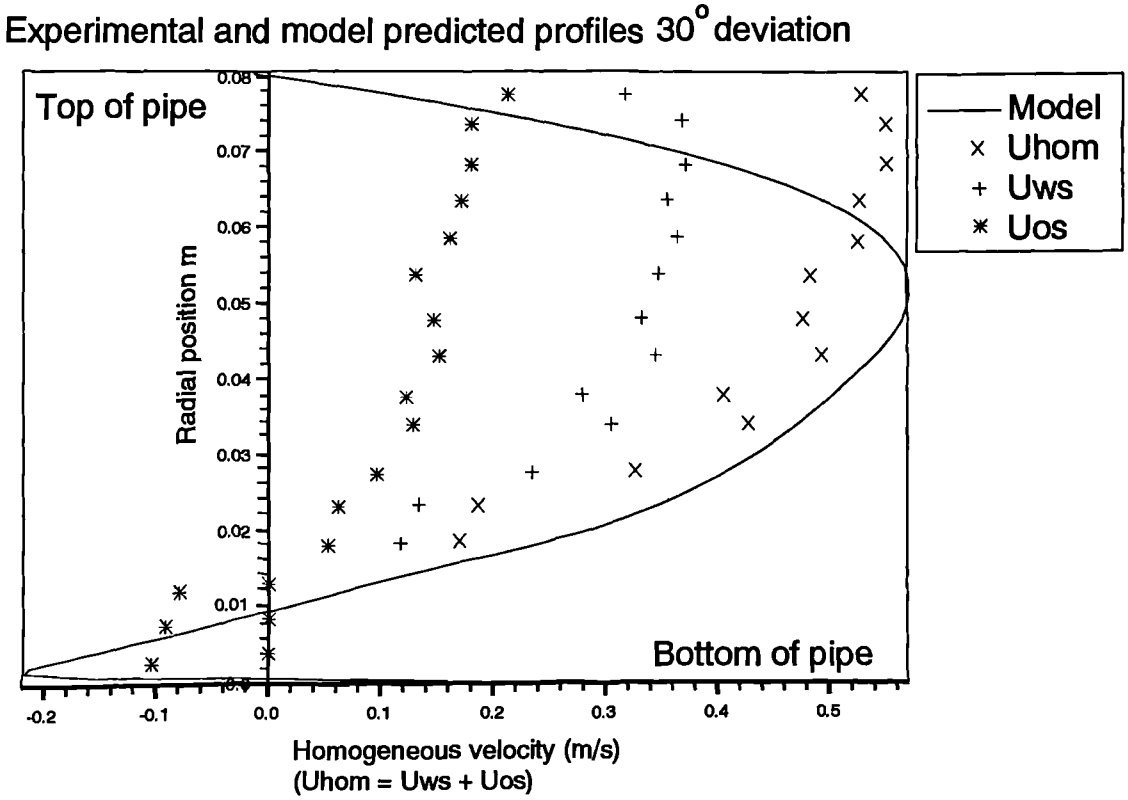

Figure 7.5: Model generated and probe measured velocity profiles

7.2.2 30° deviation

Figure 7.5 shows the model predicted homogeneous velocity profile and the measured superficial velocity profiles from the dual split-film probe. The flow conditions were, $U_{ws} = 0.2\text{ms}^{-1}$ and $\bar{\alpha}_o = 0.2$. The imposed pressure gradient for the model was -8120Pam^{-1} (see Equation 7.1). Both the model predicted and the measured homogeneous velocity profiles exhibit similar shapes. However, similar to the 15° results, the boundary layer near the top wall was not seen on the measured profile. This effect was discussed earlier.

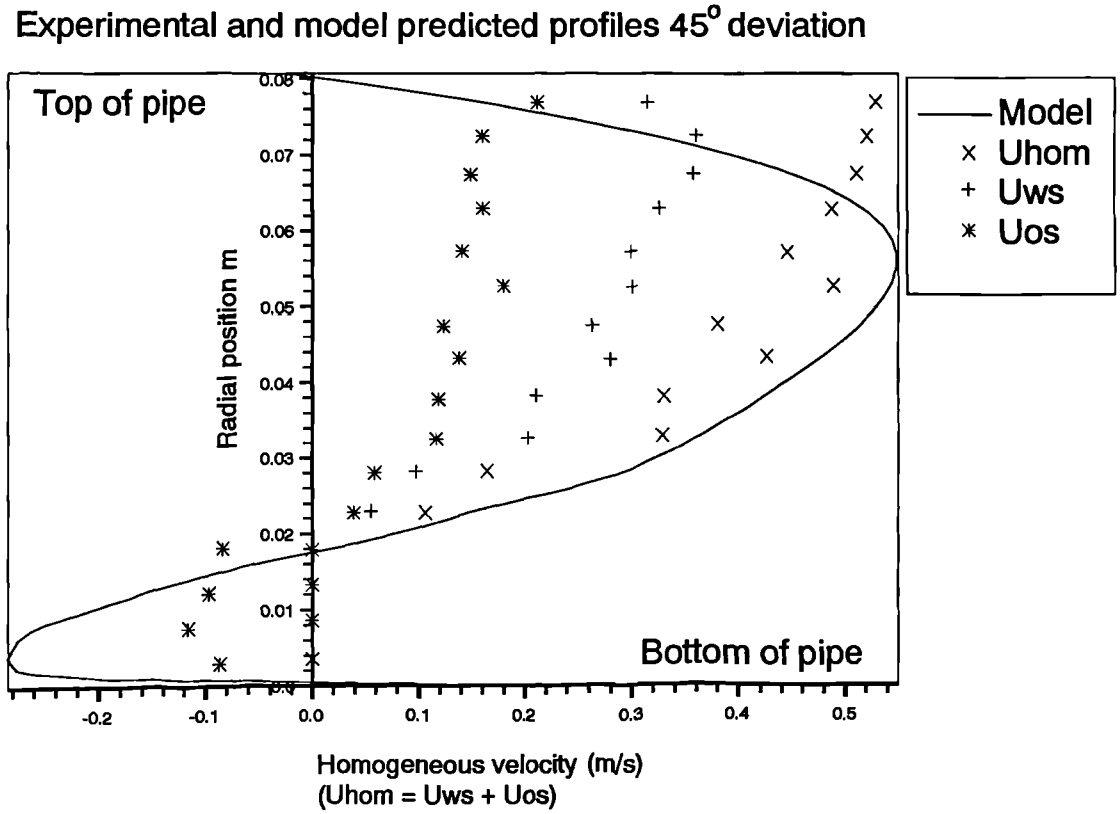

Figure 7.6: Model generated and probe measured velocity profiles

7.2.3 45° deviation

Figure 7.6 shows the model predicted homogeneous velocity profile and the measured superficial velocity profiles from the dual split-film probe. The flow conditions were, $U_{ws} = 0.2\text{ms}^{-1}$ and $\bar{\alpha}_o = 0.12$. The imposed pressure gradient for the model was -6700Pam^{-1}. Again, both profiles exhibit similar shapes. However, similar to the 15° and 30° result, the boundary layer effect due to the top wall was not seen on the measured profile. It has also been noticed that as the deviation angle increases, the top part of the measured homogeneous velocity profile (dual split-film probe) becomes increasingly flatter and slants forward. This again is due to the presence of oil on the top side of the pipe.

7.3 Summary

A two phase flow model was used to compare the measured homogeneous velocity profiles from the dual split-film probe and the model predicted homogeneous velocity profiles. The model showed good agreement with the velocity profiles predicted by the probe. However, near the top wall, the effect of the boundary layer was not observed with the measured homogeneous velocity profiles (probe). This is caused by the presence of oil on the top side of the pipe. It has been shown that as the deviation angle increases, the homogeneous velocity profile, near the top wall, tends to flatten and slants forward. This disagreement is due to the model which will be resolved at a later date.

Chapter 8

Conclusions

An intrusive instrument has been developed that is capable of measuring both the time dependent and steady state parameters in two phase deviated oil-water flows. It has generated extensive data on the time averaged structures of deviated oil-water flows that is of a much higher quality than hitherto obtained. The instrument is capable of providing the continuous (water) and the discontinuous (oil) phase velocities and the volume fraction. The work presented in this thesis has been concerned with the development and testing of measuring instruments (dual probe and dual split-film probe). Research of deviated oil-water flows is still a relatively new concept and to date, there is a lack of experimental data.

Intrusive measuring probes e.g. hot-film anemometers, optical probes, have been used in the past to measure liquid-liquid and liquid-gas flows in vertical pipes. It has been seen that the hot-film anemometer can provide information such as the continuous phase velocity, provided the signals are analysed correctly. One of the limitations of using this type of probe in oil-water flows, has been the complexity of identifying the start and finish points of a passing oil droplet within a fluctuating background water signal. Furthermore, it has been seen that the hot-film anemometer could not measure water back flows, which are encountered in deviated pipes.

Optical probes have been used to measure the gas volume fraction in liquid-gas flows. The reflected light from an optical probe tip when immersed in two phase flows, produces an '$on-off$' type of signal. One signal level represents the continuous phase (usually the upper level) and the other, the dispersed phase signal level. The continuous phase (water) signal level is a steady base-

line level which is not affected by changes in water velocity as is seen from the hot-film signals (fluctuating background signal). Furthermore, optical probes have been used to measure the dispersed phase (air) velocity by positioning a second optical probe some distance downstream of the first. By using appropriate signal analysis routines, the dispersed phase velocity can be determined.

The dual probe is the combination of a hot-film anemometer and two optical probes. The leading optical probe was orientated such that the measuring tip was laterally in line with the sensing area of the hot-film wire. This implied that the signals from the droplets detected by the optical probe could be mapped onto the hot-film signals and by removing these parts of the hot-film signal, the background continuous phase signal would remain. This provided a simple analysis technique for analysing the hot-film signals. A second optical probe was placed 1mm downstream of the leading optical probe so as to compute the dispersed phase velocity.

One of the requirements from the dual probe results was to compare the measured results with the reference measurements e.g. comparison of the continuous phase velocity as measured by the dual probe and the water turbine meter. In order to perform this comparison, the time averaged data taken over the cross sectional area were integrated to yield the mean averaged values. After testing the dual probe in vertical oil-water flows, it was found that the instrument was capable of measuring all three quantities (water velocity, oil velocity and oil volume fraction) accurately within an error range of $\pm 10\%$. During the vertical oil-water tests, comparisons were made between analysis techniques to compute the oil volume fraction and the oil superficial velocity. It has been shown that the leading optical probe produces a better estimate of the oil volume fraction compared to the trailing optical probe. This was due to the deformation of the oil droplet after passing through the leading optical probe and the hot-film anemometer. Two different analysis methods were used to measure the dispersed phase velocity. These were the 'time of flight' and 'cross correlation'. It has been found that the time of flight method provides a better estimate of the oil superficial velocity compared to the cross correlation method.

Similar tests were carried out in deviated oil-water flow where it was shown that the dual probe was capable of measuring the oil volume fraction and the oil superficial velocity accurately. However, the hot-film anemometer, which is part of the dual probe, proved to be unsuccessful at measuring the water

superficial velocity at low water velocities (i.e. less than $0.2ms^{-1}$ to $0.3ms^{-1}$, depending on deviation angle). This was due to water back flow.

In order to measure these water back flows, the dual split-film probe was designed and implemented. The dual split-film probe is similar in design to the dual probe except that it uses a split-film anemometer instead of a hot-film anemometer. The dual split-film probe was tested in deviated oil-water flows successfully. It was found that at low water velocities ($\leq 0.3ms^{-1}$), the split-film anemometer was capable of measuring these water back flows, hence producing accurate water velocity results. The dual split-film probe proved to be the preferred instrument for measuring the water velocity, at low flow rates, in deviated oil-water flows. After testing the dual split-film probe, it was found that similar results were obtained, to those observed from the dual probe, for the oil volume fraction and the oil superficial velocities. This showed that the results obtained from the two optical probes were repeatable.

It must be noted that regardless of the recommendation of using the dual split-film probe, the dual probe is still an excellent instrument for measuring oil-water flows. Firstly, the dual probe is much cheaper than the dual split-film probe and assembly of the dual probe is less complicated. One of the major advantages of using the dual probe is that the calibration of the hot-film anemometer is less time consuming compared to calibrating the split-film anemometer. If vertical oil-water flows or deviated high oil-water flows (greater than $0.3ms^{-1}$) are to be investigated, then it is recommended to use the dual probe.

The slip velocities and droplet cut chord lengths were also investigated. It was found that as the oil volume fraction increased, the slip velocity decreased which was independent of deviation angle. The decrease in slip velocity was due to higher interaction between oil droplets and slower moving oil droplet swarms hence reduction in the oil velocity. As the deviation angle increased i.e. from 0° to 45°, and at low oil volume fractions ($5-10\%$), the magnitude of the slip velocities increased. This was due to fast moving oil droplets near the top side of the pipe which increase the oil velocity and in turn the slip velocity. To date, no one has been able to measure local slip velocities. The droplet cut chord lengths were investigated at all deviations. In vertical flow, the droplet cut chord length profiles were seen to become less peaked at the centre of the pipe with increasing oil volume fraction. The droplet cut chord length varied between $2-4mm$. In deviated flows, the droplet cut chord length

profiles showed that the droplet size did not vary significantly where oil was present. For all deviations, the droplet cut chord length was approximately 5mm.

8.1 Further Work

One of the limitations of both the dual probe and the dual split-film probe is that they can resolve only velocities which are normal to the sensing wire. In order to measure radial and tangential components of the continuous phase velocity, one has physically to re-mount the probes to resolve the component velocities. This would be unsatisfactory since the velocities will not be simultaneously measured. To overcome such a problem, three orthogonally mounted split-films could measure all three components at the same time. This does have its drawbacks; the main disadvantage would be the cost of such a system and also the size of such a probe.

Another disadvantage encountered when using the probes was that of the droplet/probe interaction. This has always been the case when using an intrusive instrument to measure flows. In order to resolve this problem, further work should be carried out to measure/visualise the droplet/probe interaction and the effects of the probe assembly on the flow e.g. blockage effects. This will render an insight into the problems encountered during calculation of the oil volume fraction and the oil superficial velocity using the two optical probes.

The wetting film present on the cleaved optical probe needs investigating. A simple analysis has been made to show that a thin water film is always present on the optical probe tip. A model could be implemented to show how the signals vary as a function of film thickness. The overshoots in the optical signal, as the probe tip pierces an oil droplet, should be further investigated. These overshoots may provide information such as the droplet size, since the overshoots are reflections from the bottom side of the oil droplet.

It has been shown that the two phase flow model, (see Chapter 7), was deficient in predicting the velocity profile near the top wall. The experimental data showed that near the top wall, the effect of the boundary layer is not seen, due to the presence of oil. The experimental data can be used to improve the model in these regions.

The success of the dual probe and the dual split-film probe has lead to an objective of designing an alternative dual split-film probe to be used in actual oil wells. This implies designing and developing a 'ruggedised' version of the existing probe. As mentioned in the conclusions, a further part of this work is to extend the data set so as to cover many more flowrates and deviations.

Bibliography

Abuaf, N., Jones, O.C. and Zimmer, G.A. (1978). Optical Probe for Local Void Fraction and Interface Velocity Measurements, *Rev. Sci. Instrum.* 49(8), American Institute of Physics.

Aziz, K. and Govier, G.W. (1972). The Flow of Complex Mixtures in Pipes, Krieger, Malabar Florida.

Akagawa, K. (1963). A Study of Fluctuating Characteristics of the Void Fraction in Gas-Liquid Two-Phase Flow, *Trans. Japan Soc. Mech. Eng.* 29 pp.924-931.

Beck, M.S. and Plaskowski, A. (1987). Cross Correlation Flowmeters, Their Design and Application. Hilger.

Boerner, T., Martin, W.W. and Leutheusser, H.J. (1982). Comparative Measurements in Bubbly Two-Phase Flow using Laser-Doppler and Hot-Film Velocimetry, Proceedings of the 1982 Annual Meeting of the A.I.Ch.E., L.A., CA.

Boerner, T. and Leutheusser, H.J. (1984). Calibration of Split-Fibre Probe for Use in Bubbly Two-Phase Flow, *DISA Info.* No. 29, pp.10-13.

Born, M. and Wolf, E. (1980). Principles of Optics, Pergamon Press, Sixth Edition, pp.60-64, ISBN $0-08-026481-6$.

Bremhorst, K.and Gilmore, D.B. (1976). Response of Hot-Wire Anemometer Probes to a Stream of Air Bubbles in a Water Flow, *J.Phys. E: Sci. Instrum.*, 9, pp.347-352.

Bruun, H.H. and Farrar, B. (1988). Hot-Film Probe Studies of Kerosene/Water and Gas/Liquid Flows, Proceedings of the First World Conference on Experimental Heat Transfer, Fluid Mechanics and Thermodynamics, 4-9 Sept. 1988, Dubrovnik, Yugoslavia, Elsevier Science Pub., pp.371-379.

Canstar Ltd., 3900 Victoria Park Ave., North York, Toronto, Ontario. M2H 3H7, Canada

Cartellier, A. (1989). Optical Probes for Local Void Fraction Measurements: Characterisation of performance, *Rev. Sci. Instrum.* American Institute of Physics, Vol.61, No.2 pp.874-886.

Cartellier, A. and Achard, J.L. (1990). Local Phase Detection Probes in Fluid/Fluid Two-Phase Flows. *Rev. Sci. Instrum.* 62(2), American Institute of Physics, pp.279-303.

Cartellier, A. (1992). Simultaneous Void Fraction Measurement, Bubble Velocity, and Size Estimate using a Single Optical Probe in Gas-Liquid Two-Phase Flows. *Rev. Sci. Instrum.* 63(11), American Institute of Physics, pp.5442-5453.

Danel, F. and Delhaye, J.M. (1971). Sonde Optique pour Mesure du Taux de Presence Local en Ecoulement Diphasique. Mesures, 99 – 101.

Dantec Electronics Ltd. Techno House, Redcliffe Way, Bristol BS1 6NU.

Delhaye, J.M. (1969). Hot-Film Anemometry in Two-Phase Flow, Proc. 11th Nat. ASME/AIChE Heat Transfer Conf. on Two-Phase Flow Instrumentation, Minneapolis, Minnesota, pp.58-69.

Farrar, B. (1988). Hot-Film Anemometry in Dispersed Oil-Water Flows, Ph.D. Thesis, University of Bradford.

Franz, K., Boerner, T., Kantorek, H.J. and Buchholz, R. (1984). Flow Structures in Bubble Columns, German Chemical Eng. 7, pp.365-374.

Hecht, E. and Zajac, A. (1980). Optics, Addison-Wesley Publishing comp., Fifth Edition, pp.71-79

Hinata, S. (1972). A Study on the Measurement of the Local Void Fraction by the Optical Fibre Glass Probe, *Bull. J.S.M.E.* 15, pp.1228-1235.

Horowitz, P. and Hill, W. (1989). The Art of Electronics (second edition), Cambridge University Press.

Hsu, Y.Y, Simon, F.F, and Graham. R.W. (1963). Application of Hot-Wire Anemometry for Two Phase Flow Measurements such as Void Fraction and Slip Velocity, Proc. ASME Winter meeting, Philidelphia, pp.26-34.

Hunt, A. (1987). The Venturi Meter - Theory. Schlumberger Cambridge Research, Cambridge, UK. (Personal communication)

King, L.V. (1914). Convection of Heat from Small Cylinders in a Stream of Fluid, *Phil. Trans. Roy. Soc. (London)*, 214, pp.373 – 432.

King, L.V. (1915). Precision Measurement of Air Velocity by means of the Linear Hot-Wire Anemometer, *Phil. Mag.*, Series 6, 29, pp.599 – 604.

Knudsen, J.G. and Katz, D.L. (1958). Fluid Dynamics and Heat Transfer, McGraw and Hill Book Co., New York. 1958.

Kobayashi, K. and Irino, Y. (1973). Phase Velocities and Slip Ratios in Gas/Liquid Two-Phase Flows, Proc. 10th Japan Heat Transfer Symp, pp.41-44

Ling, S.C. and Hubbard, P.G. (1956). The Hot-Film Anemometer: A New Device for Fluid Mechanics Research, *J. Aero Sci.*, 23, pp.890 – 891.

Middlebrook, G.B. and Piret, E.L. (1950). Hot-Wire Anemometry, *Ind. Eng. Chem.*, 42, pp.1511-1513.

Miller, N. and Mitchie, R.E. (1969). The Development of a Universal Probe for Measurement of Local Voidage in Liquid/Gas Two Phase Flow Systems, Proc. 11th Nat. ASME/AIChE Heat Transfer Conf. on Two Phase Flow Instrumentation, Minneapolis, Minnesota, pp.82 – 88.

Miller, R.W. (1983). Flow Measurement Engineering Handbook, McGraw-Hill Book Group, pp.5 – 45, ISBN 0 – 07 – 042045 – 9.

Mobbs, S.D. and Lucas, G.P. (1993). A Turbulence Model for Inclined, Bubbly Flows, *Applied Scientific Research*, 51 : 263 – 268, FTM Nieuwstadt (ed.), Advances in Turbulence IV, Kluwer Academic Publishers.

Moody, L.F. (1944). Friction Factors for Pipe Flow, *Trans. Am. Soc. Mech. Engrs*, Vol.66, pp.671-684

Morris, D., Teyssedou, A., Lapierre, J. and Tapucu, A. (1987). Optical Fibre Probe to Measure Local Void Fraction Profiles, Applied Optics, Vol.26, No.21, pp.4660-4664.

Moujaes, S. and Dougall, R.S. (1987). Experimental Investigation of Cocurrent Two-Phase Flow in a Vertical Rectangular Channel, Canadian J. of Chem. Eng., Vol.65, pp.705-715.

Moujaes, S. (1990). Testing of a Spherical Dual-Tipped Optical Fibre Probe for Local Measurements of Void Fraction and Gas Velocity in Two-Phase Flows, Canadian J. of Chem. Eng., Vol.68, pp.504-510.

Nassos, G.P. and Bankoff, S.G. (1967). Local Resistivity Probe for Study of Point Properties of Gas Liquid Flows, *Can. J. Chem. Eng*, 45, pp.271-274.

Neal, L.G. and Bankoff, S.G. (1963). A High Resolution Resistivity Probe for Determination of Local Void Properties in Gas Liquid Flow, *AIChE J.*, 9, pp.490-494.

Rasmussen, C.G. (1967). The Air Bubble Problem in Water Flow Hot-Film Anemometry, *DISA Info.* No.5, pp.21-26.

Sekoguchi, K. and Sato, Y. (1975). Liquid Velocity Distribution in Two Phase Bubble Flow, *Int. J. Multiphase Flow*, 2 pp.79-95.

Serizawa, A., Kataoka, I. and Michiyoshi, I. (1974). Turbulence Structure of Air-Water Bubbly Flow, parts I-III, *Int. J. Multiphase Flow*, 2, pp.221-259.

Serizawa, A., Tsuda, K. and Michiyoshi, I. (1983). Real-Time Measurements of Two Phase Turbulence Using Dual Sensor Anemometry, in: *Measuring Techniques in Gas-Liquid Two Phase Flows,* ed. by J.M. Delhaye and G. Cognet, Symp., Nancy, France, July 5-8 1983, Springer Verlag, 1984, pp.495-523.

Simonian, S. (1991). Patent for Dual probe and Dual split-film probe. Application No. 9210212.8. Schlumberger Cambridge Research, Cambridge, UK.

Smits, A. (1991). Hot-Film Anemometry Study of Two-Phase (Oil Dispersed in Water) Flows, Schlumberger Cambridge Research, Cambridge, UK. (Personal Communication).

Tabeling, P., Pouliquen, O., Theron, B. and Catala, G. (1991). Oil Water Flows in Deviated Pipes: Experimental Study and Modelling, Elsevier Science Publishers.

Toral, H. (1981). A Study of The Hot-Wire Anemometer for Measuring Void Fraction in Two Phase Flow, *J. Phys. E: Sci Instrum.*, 14, pp.822 – 827.

Vigneaux, P. (1988). Liquid-Liquid Flows in Inclined Pipes. AIChE Journal Vol.34, No.5, pp.781-789.

Weske, J.R. (1943). A Hot-Wire Circuit with Very Small Time Lag, NASA Tech. Note No.881.

Appendix A

Calculation of possible errors in the dispersed phase measurement

The following is a geometrical calculation to show the effect of an oil droplet impacting both optical probes at an acute angle.

Consider a droplet approaching the two optical probes as shown in Figure A.1. The droplet is travelling at a speed V at an angle of θ to the vertical. The droplet impacts the first optical probe at an angle $\theta + \alpha$ to the vertical. The angle α is the impact angle and the droplet has a radius of a. The residence time Td_1 is equal to l_1/V and Td_2 is equal to l_2/V. The time of flight δt is equal to l/V. It is the length l that has to be computed correctly so as to minimise the error in calculating the dispersed phase velocity. The author will define some terms used in the calculation of l. Let $\lambda_1 = l_1/2a$, $\lambda_2 = l_2/2a$ and $\lambda = l/L$ where L is the distance between the first probe and the second probe. The coordinates of the point M is given by:

$$M = (-a\sin(\alpha+\theta)), (-a\cos(\alpha+\theta)) \tag{A.1}$$

The equation of the circle is given by:

$$a^2 = (x + a\sin(\alpha+\theta))^2 + (y + a\cos(\alpha+\theta))^2 \tag{A.2}$$

The equation of the line BD is given by:

$$y = \cot\theta x + \rho \tag{A.3}$$

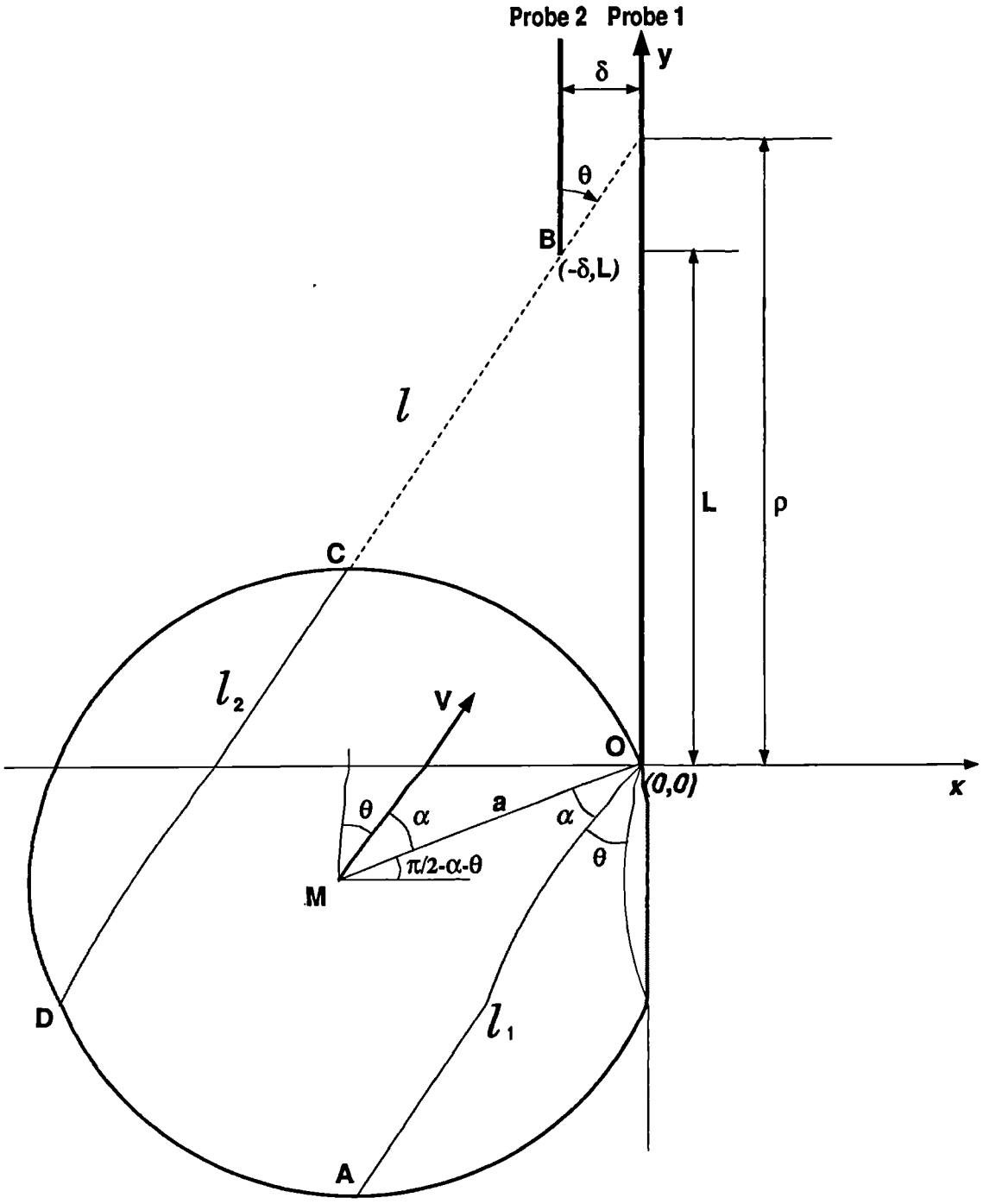

Figure A.1: Notational diagram for angular impact on the two optical probes

By substituting the coordinates for the point $B(-\delta, L)$ into Equation A.3, then:

$$\rho = L + \delta \cot\theta \tag{A.4}$$

Now one can calculate the point at which the line BD and the circle intersect.

$$a^2 = (x + a\sin(\alpha+\theta))^2 + (\cot\theta x + \rho + a\cos(\alpha+\theta))^2 \tag{A.5}$$

$$\frac{x^2}{\sin^2\theta} + x\left[\frac{2a\cos\alpha}{sin\theta} + 2\rho\cot\theta\right] + \rho^2 + 2a\rho\cos(\alpha+\theta) = 0 \tag{A.6}$$

Define $\chi = \frac{x}{\sin\theta}$, then from Equation A.6:

$$\chi^2 + \chi\left[2a\cos\alpha + 2\rho\cos\theta\right] + \rho^2 + 2a\rho\cos(\alpha+\theta) = 0 \tag{A.7}$$

Let

$$\Delta = (2a\cos\alpha + 2\rho\cos\theta)^2 - 4\rho^2 - 8a\rho\cos(\alpha+\theta) \tag{A.8}$$

hence

$$\Delta = 4a^2 - 4(\rho\sin\theta - a\sin\alpha)^2 \tag{A.9}$$

Hence the solution of χ is given by:

$$\chi = -p \pm \sqrt{\Delta'} \tag{A.10}$$

where $\Delta' = a^2 - (\rho\sin\theta - a\sin\alpha)^2$ and $p = a\cos\alpha + \rho\cos\theta$. Now one can calculate the distance BC: The coordinates of the points B and C are given by:

$$B = (-\delta, L) \tag{A.11}$$

and

$$C = ((-p + \sqrt{\Delta'})\sin\theta, (-p + \sqrt{\Delta'})\cos\theta + \rho) \tag{A.12}$$

hence

$$l^2 = \left[\left(-p + \sqrt{\Delta'}\right)\sin\theta + \delta\right]^2 + \left[\left(-p + \sqrt{\Delta'}\right)\cos\theta + \rho - L\right]^2 \tag{A.13}$$

$$l^2 = \left(-p + \sqrt{\Delta'}\right)^2 + 2\delta\sin\theta\left(-p + \sqrt{\Delta'}\right) + 2(\rho - L)\cos\theta\left(-p + \sqrt{\Delta'}\right) + \delta^2 + (\rho - L)^2 \tag{A.14}$$

Substitute Equation A.4 into Equation A.14. hence:

$$l^2 = \left[\left(-p + \sqrt{\Delta'}\right) + \frac{\delta}{\sin\theta}\right]^2 \tag{A.15}$$

Now substitute for p and Δ'

$$l^2 = \left[-a\cos\alpha - \rho\cos\theta + \sqrt{a^2 - (\rho\sin\theta - a\sin\alpha)^2} + \frac{\delta}{\sin\theta}\right]^2 \tag{A.16}$$

Now

$$\frac{\delta}{\sin\theta} - \rho\cos\theta = \frac{\delta}{\sin\theta} - L\cos\theta - \frac{\delta\cos^2\theta}{\sin\theta} = -L\cos\theta + \delta\sin\theta \tag{A.17}$$

It follows that:

$$l = -\left[\sqrt{a^2 - (\rho\sin\theta - a\sin\alpha)^2} + \delta\sin\theta - L\cos\theta - a\cos\alpha\right] \tag{A.18}$$

As defined earlier $\lambda = \frac{l}{L}$, hence:

$$\lambda = -\sqrt{\left(\frac{a}{L}\right)^2 - \left(\frac{\rho\sin\theta}{L} - \frac{a\sin\alpha}{L}\right)^2} - \frac{\delta\sin\theta}{L} + \cos\theta + \frac{a\cos\alpha}{L} \tag{A.19}$$

Now, we want the term ρ as a function of δ

$$\frac{\rho\sin\theta}{L} = \left(1 + \frac{\delta\cot\theta}{L}\right)\sin\theta = \sin\theta + \frac{\delta\cos\theta}{L} \tag{A.20}$$

Hence

$$\lambda = -\sqrt{\left(\frac{a}{L}\right)^2 - \left(\sin\theta + \frac{\delta\cos\theta}{L} - \frac{a\sin\alpha}{L}\right)^2} - \frac{\delta\sin\theta}{L} + \cos\theta + \frac{a\cos\alpha}{L} \tag{A.21}$$

If we now assume that the impact angle $\alpha = 0$, then

$$\lambda = \sqrt{\left(\frac{a}{L}\right)^2 - \left(\sin\theta + \frac{\delta\cos\theta}{L}\right)^2} + \frac{\delta\sin\theta}{L} - \cos\theta - \frac{a}{L} \tag{A.22}$$

Now we know that $\lambda = l/L$ hence

$$\frac{l}{L} = \frac{a}{L}\left(\sqrt{1 - \left(\frac{L\sin\theta}{a}\right)^2} - 1\right) - \cos\theta \tag{A.23}$$

and

$$l = a\beta - a - L\cos\theta \tag{A.24}$$

where $\beta = \sqrt{1 - \left(\frac{L\sin\theta}{a}\right)^2}$.